

# **Mechanical Engineering:**

# **The Selective Laser Melting of Metals and**

# **In-situ Aluminium Matrix Composites**

**2008-2012**

The Exeter Partnerships:  
An Insider's Comments on Effectiveness

Submitted by **Sasan Dadbakhsh** to the **University of Exeter**  
as a thesis for the degree of  
**Doctor of Philosophy in Engineering**  
In May 2012

This thesis is available for Library use on the understanding that it is copyright material and that no quotation from the thesis may be published without proper acknowledgement.

I certify that all material in this thesis which is not my own work has been identified and that no material has previously been submitted and approved for the award of a degree by this or any other University.

Signature: .....

## **Abstract**

Selective laser melting (SLM) is an additive manufacturing technique to produce complex three-dimensional parts through solidifying successive layers of powder materials on top of each other, from the bottom to top. The powder base nature allows the SLM to process a wide variety of materials and their mixtures and fabricate advanced and complicated composite parts. However, the SLM is a newly established process and seeks detailed scientific studies to develop new materials systems for the consumption of industry. These scientific studies are particularly important because of many issues associated with the SLM process, such as porosity, balling, delamination, thermal stress, etc, which can be varied from one material system to another.

This PhD project aims to elucidate the fundamental mechanisms governing the microstructure and mechanical properties of the metallic and in-situ Al matrix composite parts made by SLM. The research starts with a preliminary study on SLM of stainless steel in order to explore the usage of SLM machine and related parameters. It illustrates the effect of part layout on the quality of products.

The main research focuses on the in-situ formation of particulate reinforced Al matrix by using SLM of Al/Fe<sub>2</sub>O<sub>3</sub> powder mixture. It is a pioneering research to integrate in-situ interaction with laser melting to produce advanced Al composites. It investigates the mechanisms governing SLM assisted in-situ reaction and also the effects of various parameters such as SLM layer thickness, laser power and scanning speed as well as the proportion of Fe<sub>2</sub>O<sub>3</sub>. It examines the influence of Al alloy powder and it describes the effect of hot isostatic pressing (HIP) post-treatment. The physical, mechanical, and metallurgical properties of the products are extensively assessed using various techniques. The processing windows of the process are sketched. The findings demonstrate unique microstructural features due to combined in-situ reaction and laser rapid consolidation, and contribute to provision of an in-depth scientific understanding of novel Al matrix composites by using SLM assisted in-situ processes.

As part of this PhD project, industrial collaborative research has also been conducted to characterise the surface finish, metallurgical quality, process accuracy and mechanical properties of various SLM made metallic parts using Al, Ti, stainless steel, and super alloys. This part of research has generated scientific data and results for industrial applications of metallic fabrication using SLM.

# Acknowledgement

---

For the great opportunity of working in such exciting project accompanied with the extreme guidance, support and trust, I would like to thank my supervisor Dr Liang Hao.

For supervision, developing the custom software for the Realizer, helping for my settlement and moral advices, I would like to thank Dr Neil Sewell.

For training the SLM machine and for being a wonderful housemate and colleague, I would like to thank Dr Peter Jerrard.

For the great collaboration, I would like to thank all AVLAM partners: TWI Ltd, EADS UK, Bombardier Aerospace plc, TISICS Ltd and Materialise UK.

For the financial support of the AVLAM project, I would like to thank Technology Strategy Board (TSB).

For the help and good advices, I would like to thank Ed James.

For the assistance and companion, I would like to thank the people in the room 252 especially Kent McClymont.

For the provision of the research facilities, I would like to thank Exeter Advanced Technologies (X-AT).

For the help with carrying out many experiments, I would like to thank Dr Lesley Wears.

For the preparation of many official documents during my stay, I would like to thank Elizabeth Roberts.

For the inspiration and help, I would like to thank Dr Iva Kavcic.

And for their non-stop support, I would like to thank my parents and my brother.

# List of Publications

---

## Published Journal Articles:

- Dadbakhsh, S., Hao, L. , Jerrard, P.G.E., & Zhang, D.Z. (2012) Experimental investigation on selective laser melting behaviour and processing windows of in situ reacted Al/Fe<sub>2</sub>O<sub>3</sub> powder mixture, *Powder Technology*, 231, 112–121.
- Dadbakhsh, S. & Hao, L. (2012) Effect of Al alloys on the selective laser melting of in-situ formed particle reinforced composites, *Journal of Alloys and Compounds*, 241, 328–334.
- Dadbakhsh, S. & Hao, L. (2012) Effect of hot isostatic pressing (HIP) on Al composite parts made from laser consolidated Al/Fe<sub>2</sub>O<sub>3</sub> powder mixtures, *Journal of Materials Processing Technology*, 212, 2474–2483.
- Dadbakhsh, S. & Hao, L. (2012) In situ formation of particle reinforced Al matrix composite by selective laser melting of Al/Fe<sub>2</sub>O<sub>3</sub> powder mixture. *Advanced Engineering Materials*, 14, 45-48.
- Dadbakhsh, S., Hao, L. & Sewell, N. (2012) Effect of selective laser melting layout on the quality of stainless steel parts. *Rapid Prototyping Journal*, 18, 241-249.
- Dadbakhsh, S., Hao, L. & Kong, C. Y. (2010) Surface finish improvement of LMD samples using laser polishing. *Virtual and Physical Prototyping*, 5, 215-221.
- Hao, L. & Dadbakhsh, S. (2009) Materials and process aspects of selective laser melting of metals and metal matrix composites: A review. *Zhongguo Jiguang/Chinese Journal of Lasers*, 36, 3192-3203.
- Hao, L., Dadbakhsh, S., Seaman, O. & Felstead, M. (2009) Selective laser melting of a stainless steel and hydroxyapatite composite for load-bearing implant development. *Journal of Materials Processing Technology*, 209, 5793-5801.
- Jerrard, P. G. E., Hao, L., Dadbakhsh, S. & Evans, K. E. (2011) Consolidation behaviour and microstructural characteristics of Al and a mixture of Al-Cu alloy powders following selective laser melting processing. *Lasers in Engineering*, 22, 371-381.

## Conferences:

- Dadbakhsh, S., Hao, L. & Kong, C. Y. (2010) Surface Finish Improvement of LMD Samples Using Laser Polishing. *Proceedings of the 11th National Conference on Rapid Design, Prototyping and Manufacturing*, 79-86.
- Dadbakhsh, S., Hao, L. & Sewell, N. (2009) A test procedure for mechanical qualification of additive layer manufacturing parts. *Proceedings of the 10th National Conference on Rapid Design, Prototyping and Manufacturing*, 53-61.
- Dadbakhsh, S., Hao, L., Sewell, N. & Jerrard, P. (2009) Direct fabrication of an in-situ Al composite using selective laser melting process. *Innovative Developments in Design and Manufacturing - Advanced Research in Virtual and Rapid Prototyping*, 319-325.

Hao, L., Raymond, D., Strano, G. & Dadbakhsh, S. (2010) Enhancing the sustainability of additive manufacturing. *IET Conference Publications*. 565 CP ed., 390–395.

Jerrard, P. G. E., Hao, L., Dadbakhsh, S. & Evans, K. E. (2010) Consolidation behaviour and microstructure characteristics of pure aluminium and alloy powders following Selective Laser Melting processing. *Proceedings of the 36th International MATADOR Conference*, 487-490.

\* Presenting my work in 2<sup>nd</sup> and 3<sup>rd</sup> (2009 and 2010) EADS Airbus PhD seminar on Additive Layer Manufacturing - *Airbus/EADS Filton, UK*

### **Submitted Journal Articles:**

Dadbakhsh, S. & Hao, L. Microstructural evolution of Al/5wt.%Fe<sub>2</sub>O<sub>3</sub> powder consolidated parts by selective laser melting: Part I. Effect of layer thickness in conjunction with laser power and scanning speed, under submission.

Dadbakhsh, S. & Hao, L. Microstructural evolution of Al/Fe<sub>2</sub>O<sub>3</sub> powder consolidated parts by selective laser melting: Part II. Effect of Fe<sub>2</sub>O<sub>3</sub> content in conjunction with laser power and scanning speed, under submission.

# Contents

---

<i>Abstract</i> .....	2
<i>Acknowledgement</i> .....	3
<i>List of Publications</i> .....	4
<i>Contents</i> .....	6
<i>List of Figures</i> .....	10
<i>List of Tables</i> .....	17
<i>Introduction</i> .....	18

## **Part One: Background Theory and Literature Review.....21**

<i>Chapter 1: Background</i> .....	22
1.1. Laser Materials Processing .....	22
1.1.1. Principles of laser operations .....	22
1.1.2. Industrial lasers .....	23
1.1.3. Industrial applications of laser materials processing.....	24
1.2. Additive Layer Manufacturing (ALM) .....	26
1.2.1. Principles of ALM .....	26
1.2.2. ALM processes .....	26
1.3. Selective Laser Melting (SLM) and Applications .....	29
1.3.1. Principles of SLM .....	29
1.3.2. Benefits and disadvantages of SLM process.....	31
1.4. Application of Additive Layer Manufacturing, Especially SLM.....	31
 <i>Chapter 2: SLM Processing Aspects</i> .....	34
2.1. Powder Consolidation Mechanisms.....	34
2.2. Process Parameters.....	35
2.2.1. Material parameters .....	35
2.2.1.1. Composition .....	35
2.2.1.2. Powder density and particle shape and size .....	36
2.2.1.3. Microstructure .....	37
2.2.1.4. Flow properties.....	37
2.2.2. Laser and scan parameters .....	38
2.2.2.1. Energy density input: laser power, scan speed, scan line spacing, and layer thickness .....	38
2.2.2.2. Spot size .....	42
2.2.2.3. Scanning strategy .....	42
2.2.3. Environment.....	43
2.3. Effects of Laser-Material Interaction.....	44
2.3.1. Laser induced compression and vaporisation.....	44
2.3.2. Laser absorption.....	44
2.4. Powder Consolidation.....	46
2.4.1. Sintering.....	46
2.4.2. Melting pool, rapid solidification, and potential defects.....	48
2.4.2.1. Formation of the melting pool.....	49
2.4.2.2. Effect of rapid cooling and solidification on microstructure.....	50
2.4.2.3. Potential defects in the SLM parts .....	52
2.4.2.3.1. Porosity formation .....	52

2.4.2.3.2. Hot tearing.....	53
2.4.2.3.3. Balling .....	53
2.4.3.2.3. Residual stress .....	56
2.5. Characterisation of Density and Porosity.....	58
2.5.1. Calculating the density from dimension and mass.....	60
2.5.2. Methods based on Archimedes' principle to measure density.....	60
2.5.3. Porosity measurement on the basis of metallographic examinations.....	61
2.5.4. Non-destructive testing (NDT) to measure porosity .....	61
<i>Chapter 3: Developments of SLM of Metal Alloys and MMCs</i> .....	63
3.1. SLM of Advanced Metal Alloys.....	63
3.2. SLM of MMCs.....	68
3.2.1. SLM of MMCs through ex-situ techniques .....	68
3.2.2. SLM of MMCs through in-situ techniques .....	70
3.3. Research Hypothesis: SLM of Al MMCs from Powder Mixture of Al/Fe <sub>2</sub> O <sub>3</sub> .....	72
<b>Part Two: Materials, Experimental Procedures, and Preliminary Experiments.....</b>	<b>74</b>
<i>Chapter 4: Materials and Experimental Procedures</i> .....	75
4.1. Materials and SLM Experimental Setup.....	75
4.1.1. SLM powders.....	75
4.1.1.1. 316L stainless steel .....	75
4.1.1.2. Pure aluminium and iron oxide .....	76
4.1.1.3. Al6061 and AlSi10Mg and Iron Oxide .....	77
4.1.2. SLM machinery setup and processing apparatus .....	78
4.2. Hot Isostatic Pressing (HIP) Post-Treatment .....	82
4.3. Experimental Measurements and Characterisations .....	82
4.3.1. Density and porosity measurements .....	82
4.3.2. Hardness .....	82
4.3.3. Tensile, compression, and shear-punch testing.....	82
4.3.4. Surface roughness measurements .....	83
4.3.5. Metallographic analysis .....	84
4.3.6. X-ray diffraction (XRD) and CT scanning .....	85
<i>Chapter 5: Preliminary Experiments on SLM of 316L Stainless Steel.....</i>	86
5.1. Introduction.....	86
5.2. Experimental Procedures .....	87
5.3. Results and Discussion .....	88
5.3.1. Primary inspections on quality of SLM process .....	89
5.3.2. Mechanical properties investigations.....	91
5.3.3. Cross sectional analyses.....	96
5.4. Conclusions.....	97
<i>Chapter 6: Preliminary Experiments to Fabricate In-Situ Al Matrix Composite through SLM of Al/Fe<sub>2</sub>O<sub>3</sub>.....</i>	99
6.1. Single Layer SLM Preliminary Experiments on an In-Situ Al Composite.....	99
6.1.1. Introduction.....	99
6.1.2. Experimental procedure .....	100
6.1.3. Results and discussion .....	100
6.1.3.1. SLM processing .....	100
6.1.3.2. Visual inspection during SLM process.....	101
6.1.3.3. Visual inspection after SLM process.....	102

6.1.3.4. Microstructural investigations .....	106
6.1.3.5. Phase analysis by X-ray diffraction (XRD) measurement .....	107
6.1.4. Conclusions.....	108
6.2. Preliminary Multilayer SLM Experiments on In-Situ Formation of Particle Reinforced Al Matrix Composite .....	109
6.2.1. Introduction.....	109
6.2.2. Experimental procedure .....	109
6.2.3. Results and discussion .....	110
6.2.3.1. Multilayer part processing.....	110
6.2.3.2. Microstructural characterisation and phase identification.....	110
6.2.4. Conclusions.....	112

### **Part Three: In-situ Fabrication of Al Matrix Composites by Using Selective Laser Melting of Al/Fe<sub>2</sub>O<sub>3</sub> Powder Mixture ..... 113**

#### *Chapter 7: Experimental Investigation on Selective Laser Melting Behaviour and Processing Windows of In-Situ Reacted Al/Fe<sub>2</sub>O<sub>3</sub> Powder Mixture ..... 114*

7.1. Introduction.....	114
7.2. Materials and Experiments .....	114
7.3. Results.....	115
7.3.1. Visual inspections .....	115
7.3.2. Surface roughness .....	117
7.3.3. Density .....	118
7.3.4. Hardness .....	119
7.3.5. Optical microscopy results.....	121
7.4. Discussion.....	124
7.4.1. Visual condition, surface roughness, density, hardness and microstructure .....	124
7.4.2. Material properties in relation to laser energy and processing window .....	126
7.5. Conclusions.....	131

#### *Chapter 8: Effect of Layer Thickness on Microstructural Evolution of Al/5wt%Fe<sub>2</sub>O<sub>3</sub> Powder Consolidated Parts Made by Selective Laser Melting at Different Laser Powers and Scanning Speeds ..... 132*

8.1. Introduction.....	132
8.2. Materials and Experiments .....	132
8.3. Results.....	133
8.3.1. Hardness properties.....	133
8.3.2. Microstructural characterisation and phase identification using XRD.....	134
8.3.2.1. Single layer specimens made by SLM on a thick powder bed .....	134
8.3.2.2. Multilayer parts with layer thickness of 75 µm .....	135
8.3.2.3. Multilayer parts with layer thickness of 50 µm .....	138
8.4. Discussion.....	140
8.4.1. In-situ interaction initiation.....	140
8.4.2. Effect of layer thickness, laser power, and scanning speed on oxide formation .....	140
8.4.3. Microstructures, phases, and microhardness.....	141
8.4.4. In-situ combined SLM phenomena.....	145
8.5. Conclusions.....	146

#### *Chapter 9: Effect of Fe<sub>2</sub>O<sub>3</sub> Content on Microstructural Evolution of Al/Fe<sub>2</sub>O<sub>3</sub> Powder Consolidated Parts Made by Selective Laser Melting at Different Laser Powers and Scanning Speeds ..... 147*

9.1. Introduction.....	147
------------------------	-----

9.2. Results.....	148
9.2.1. Hardness measurements .....	148
9.2.2. Microstructural characterisation and phase identification using XRD.....	149
9.2.2.1. Al/5wt%Fe <sub>2</sub> O <sub>3</sub> .....	149
9.2.2.2 Al/10wt%Fe <sub>2</sub> O <sub>3</sub> .....	152
9.2.2.3. Al/15wt%Fe <sub>2</sub> O <sub>3</sub> .....	154
9.3. Discussion.....	156
9.3.1. In-situ combined SLM reaction .....	156
9.3.2. Microstructures, phases, and microhardness.....	157
9.3.3. Effect of Fe <sub>2</sub> O <sub>3</sub> content, laser power, and scanning speed on microstructural evolution.....	159
9.3.4. In-situ combined SLM mechanisms in dependence of Fe <sub>2</sub> O <sub>3</sub> content, laser power, and scanning speed .....	161
9.4. Conclusions.....	162
<i>Chapter 10: Effect of Hot Isostatic Pressing (HIP) on Al Composite Parts Made from Laser Consolidated Al/Fe<sub>2</sub>O<sub>3</sub> Powder Mixtures.....</i>	164
10.1. Introduction.....	164
10.2. Materials and Experiments .....	165
10.3. Results.....	165
10.3.1. Density, hardness and microhardness .....	165
10.3.2. CT scan observations .....	166
10.3.3. Microstructural characterisation and phase identification using XRD.....	167
10.3.3.1. As manufactured SLM parts (before HIP treatment) .....	167
10.3.3.2. HIP post-treated SLM parts.....	170
10.4. Discussion.....	173
10.5. Conclusions.....	176
<i>Chapter 11: Effect of Al Alloys on the Selective Laser Melting of In-Situ Formed Particle Reinforced Composites.....</i>	178
11.1. Introduction.....	178
11.2. Materials and Experiments .....	178
11.3. Results and Discussion .....	179
11.3.1. Visual observation of SLM behaviour and physical phenomena.....	179
11.3.2. Porosity analysis using CT scanning.....	180
11.3.3. Density, hardness and microhardness, and compressive strength .....	181
11.3.4. Microstructural characterisation and phase identification using XRD.....	183
11.4. Conclusions.....	188
<b>Part Four: Industrial Case Studies and Applications .....</b>	<b>189</b>
<i>Chapter 12: SLM Case Studies and industrial Applications.....</i>	190
12.1. Surface Finish Improvement of LMD Samples Using Laser Polishing.....	190
12.1.1. Introduction.....	190
12.1.2. Material and experimental procedure.....	191
12.1.3. Results and discussion .....	193
12.1.4. Conclusions.....	198
<i>Future Work Recommendations .....</i>	200
<i>References.....</i>	202

## List of Figures

Fig. 1.1: The interaction of a two-level atom with radiation leads to stimulated transitions, in addition to the spontaneous decay of the upper level (Foot, 2006) .....	22
Fig. 1.2: Simplified schematic of a typical laser (Silfvast, 1996). (b) Helium-Neon laser at the Kastler-Brossel Laboratory at Paris VI: Pierre et Marie Curie. ....	23
Fig. 1.3: Range of five laser processing methods of metals and alloys (regions bounded by solid boundaries) and contours of energy density (broken lines) (Ion, 2005a) .....	24
Fig. 1.4: (a) A schematic of the process zone during laser cladding, and (b) coating of oil drilling tools by laser cladding (Toyserkani et al., 2005). ....	25
Fig. 1.5: Schemes of two types of stereolithography setups. Left: a bottom-up system with scanning laser. Right: a top-down setup with digital light projection (Melchels et al., 2010). ....	27
Fig. 1.6: Schematic of Fused deposition modelling (FDM) (McNulty et al., 1998).....	28
Fig. 1.7: (a) The LENS process performing a single-line build (Hofmeister et al., 1999) and (b) fabrication of a blade by Laser Engineering Net Shaping (LENS) (Toyserkani et al., 2005).....	28
Fig. 1.8: A schematic of selective laser sintering (SLS) process (Nelson et al., 1993). ....	29
Fig. 1.9: Diagram showing (a) how the SLM system works (Li et al., 2009) and (b) laser scanning and corresponding melting of powders (Gu et al., 2011a, Osakada and Shiomi, 2006).....	30
Fig. 1.10: Some parts manufactured by SLM process; (a),(b) Ti alloy prototype of the resurfacing hip arthroplasty (RHA) endoprosthesis with the original multi-spiked connecting scaffold taken directly from the SLM machine (Uklejewski et al., 2011), (c),(d) 316L stainless steel and Ti6Al4V parts with internal structures (Yasa et al., 2011) and (e),(f) heat exchanger designs and the miniature cooler part with extremely intricate inner geometry (Neugebauer et al., 2011). ....	32
Fig. 1.11: Some parts manufactured by SLM process; (a),(b) synthetic and porous bone structures made from 316L stainless steel available at Centre for Additive Layer Manufacturing (CALM) - University of Exeter, (c),(d) Al alloy aerospace part made by EADS UK, and (e),(f) Al composite sandwich panel part manufactured by the author (designed by Nunzio Palumbo, University of Exeter). ....	33
Fig. 2.1: Laser-based powder consolidation mechanisms (Kruth et al., 2007). ....	34
Fig. 2.2: Effect of powder particle size on the fractional density of laser-sintered iron at the scan line spacing of 0.2 mm. $D_{50}$ is particle size at 50% of the cumulative particle size distribution ( $\mu\text{m}$ ) and $S_w$ is particle size distribution slope (Simchi, 2006). ....	36
Fig. 2.3: The schematic of the effects from combinations of different sizes (Zhu et al., 2007). ....	37
Fig. 2.4: Density of 316L stainless steel cubic parts made by direct metal laser re-melting (DMLR) as a function of energy density (when $v = 100 \text{ mm/s}$ ) for variation in scan spacing (Morgan et al., 2004). ....	39
Fig. 2.5: SLM process parameter study for Ti-6Al-4V. Used energy density, measured part density and one micrograph are shown for six parameter sets (Vandenbroucke and Kruth, 2007).....	39
Fig. 2.6: (a) Delamination of the sintered iron layers and (b) formation of large horizontal cracks in laser sintered iron ( $D_{50} = 51 \mu\text{m}$ ) due to applying a high value of laser energy ( $P = 215 \text{ W}$ , $v = 50 \text{ mm/s}$ , $s = 0.1 \text{ mm}$ , $t = 0.05 \text{ mm}$ ) (Simchi, 2006). ....	40
Fig. 2.7: SEM micrographs show the surface morphology of laser sintered iron. $P = 215\text{W}$ , $v = 50 \text{ mm/s}$ , $t = 0.1 \text{ mm}$ , and (a) $s = 0.3 \text{ mm}$ and (b) $s = 0.1 \text{ mm}$ (Simchi, 2006).....	40
Fig. 2.8: Polished but non-etched microstructure of CuSn/Cu/CuP composite samples, laser sintered with laser power of 375 W, scan speed of 0.05 m/s, layer thickness of 0.30 mm, and varied scan line spacing of (a) 0.30 mm (showing much porosity) and (b) 0.15 mm (showing a reduced porosity) (Gu et al., 2006). ....	41
Fig. 2.9: Schematic pattern of different scan spacing (Aiyiti et al., 2006). ....	41
Fig. 2.10: Schematic of scanning patterns used in the mentioned study for direct laser sintering of iron powder (the scan line distance in X- and Y- direction is equal): (a) short raster pattern in X-direction; (b) long raster	

pattern in Y-direction; (c) alternating from layer to layer, starting with a short raster pattern for the first layer (Simchi and Pohl, 2003).....	42
Fig. 2.11: Effect of scan vector length on the fractional density of laser sintered iron ( $D_{50} = 41 \mu\text{m}$ ) (Simchi, 2006).....	43
Fig. 2.12: Laser induced shock waves using Q-switched laser light (O'Neill et al., 1999).....	44
Fig. 2.13: Physical model of melt removal from the interaction zone (Chang and Na, 2002).....	44
Fig. 2.14: Some of the mechanisms which increase the absorptivity of real engineering surfaces: (a) typical cross section of an engineering surface; (b) high angle absorptance and multiple reflections due to surface roughness and (c) multiple reflections within an oxide layer (Bergström et al., 2007).....	45
Fig. 2.15: SEM images showing typical microstructures of laser sintered tracks at different laser powers: (a) $P = 350 \text{ W}$ ; (b) $P = 400 \text{ W}$ . Fixed parameters are $v = 0.04 \text{ m/s}$ and $t = 0.25 \text{ mm}$ (Gu and Shen, 2009b).....	46
Fig. 2.16: Schematic of sintering by coalescence phenomenon caused by limited liquid formation (Gu and Shen, 2009b).....	47
Fig. 2.17: SEM characterisation of laser sintered tracks at different scan speeds: (a) $v = 0.05 \text{ m/s}$ ; (b) $v = 0.07 \text{ m/s}$ ; (d) $v = 0.10 \text{ m/s}$ . (c) is local magnification of (b). (e) and (f) are local magnifications of (d). $P = 400 \text{ W}$ and $t = 0.25 \text{ mm}$ are constant (Gu and Shen, 2009b).....	48
Fig. 2.18: Schematic drawing of (a) laser surface melting (Mohanty and Mazumder, 1998) and (b) the central longitudinal section of the molten pool and resultant laser trace (Takeshita and Matsunawa, 2001).....	49
Fig. 2.19: Schematic mechanism of (a) convection arise from shape of keyhole, leading to (b) unsteady and discrete solidification conditions (Mohanty and Mazumder, 1998) .....	50
Fig. 2.20: Effect of temperature gradient $G$ and growth (solidification) rate $R$ on (a) the formation of various solidification microstructures (Chowdhury et al., 2011), and (b) absolute stability in change from planar to unstable growth: at low growth (interface velocity) rates, the solute destabilises the planar front growth, whereas, at higher growth rates, surface energy has a stabilising effect (Lavernia et al., 1992) .....	51
Fig. 2.21: The type of microstructure observed (solid lines) and predicted (dashed lines) in an Al-Fe binary alloy as a function of solidification rate and Fe content (Gilgien et al., 1995, Toyserkani et al., 2005). ....	52
Fig. 2.22: Three-dimensional high-resolution X-ray tomography of a shrinkage porosity formed in an Al-4.5 wt% Cu alloy (Asta et al., 2009). .....	53
Fig. 2.23: Associated wetting angle and interfacial free energies: a) high dilution, well wetting, and ideal for full melting b) ideal clad, c) no dilution, and non-wetting (Toyserkani et al., 2005). .....	54
Fig. 2.24: SEM micrographs of iron powder after single line laser scanning ( $P = 215 \text{ W}$ , $v = 50 \text{ mm/s}$ , $\text{N}_2$ atmosphere, ambient powder bed temperature): (a) top view and (b) side view of metallic balls (Simchi and Pohl, 2003). .....	54
Fig. 2.25: Result of line scanning test (Klocke and Wagner, 2003). .....	55
Fig. 2.26: Effect of laser power on balling mechanism ( $v = 50 \text{ mm/s}$ , square dimension: $10 \times 10 \text{ mm}^2$ ) (Klocke and Wagner, 2003). .....	55
Fig. 2.27: Process window for selective laser melting of iron-based powder in continuous wave operation (Kruth et al., 2004). .....	56
Fig. 2.28: (a) Temperature gradient mechanism, (b) different temperatures through different scan vector lengths (Kruth et al., 2004). .....	57
Fig. 2.29: The six different scanning strategies used in the comparison (Kruth et al., 2004). .....	57
Fig. 2.30: Effects of density on mechanical properties of as-sintered 4% nickel steel. The processing includes pre-sintering and re-pressing of material above $6.6 \text{ g/cm}^3$ (ASM International Handbook Committee, 1998).59	59
Fig. 2.31: Array of cubes produced in an experimental run. Cubes are produced at varying laser pulse repetition frequencies to study density of material (Morgan et al., 2004). .....	60
Fig. 2.32: Method for weighing in water (ASTM Standard B311, 2005).....	61

Fig. 2.33: Schematic of the basic elements of a radiographic system showing the method of sensing the image of an internal flaw in a plate of uniform thickness .....	62
Fig. 2.34: A typical radiographic picture.....	62
Fig. 3.1: Optical etched microstructures taken from below the lased surface of the 316L steel samples with: (a) 0wt% 17-4PH, (b) 25wt-% 17-4PH, (c) 50wt-% 17-4PH, (d) 75wt-% 17-4PH, (e) 100wt-% 17-4PH ..	64
Fig. 3.2: (a) SLM cubic aluminium specimens on aluminium SLM build substrate, and (b) wall delamination of SLM Al6061 specimen .....	66
Fig. 3.3: Optical and SEM micrographs of an Al6061 sample; (A) sample after polishing and etching with Keller's reagent; (B) deep etched with NaOH solution.....	66
Fig. 3.4: (A) Marangoni convection in the melt pool. (B) Oxide disruption and solidification of the melt pool .....	67
Fig. 3.5: Densities by means of cross sections of SLM samples depending on scanning velocity and laser power.....	67
Fig. 3.6: Produced Al-part with 1 kW laser power, Courtesy of Festo AG & Co. KG.....	68
Fig. 3.7: Typical SEM view of (a) stainless steel/hydroxyapatite and (b) 316L stainless steel microstructure	69
Fig. 3.8: (a) Photograph of SLM parts made by various processing parameters from SiC/Ti powder system. (b) Influence of laser energy density on density and microstructure of SLM-processed composite parts ....	71
Fig. 4.1: The typical SEM images of 316L stainless steel powder.....	75
Fig. 4.2: (a) Iron (III) oxide powder sample with a dark red colour. (b) The uniform and reddish colour of Al/5wt%Fe <sub>2</sub> O <sub>3</sub> . ....	76
Fig. 4.3: The pure Al/Fe <sub>2</sub> O <sub>3</sub> particle interaction; (a) Al/5wt%Fe <sub>2</sub> O <sub>3</sub> powder mixture, (b) the previous picture with higher magnification, and (c) Al/10wt%Fe <sub>2</sub> O <sub>3</sub> powder mixture (the chemical composition was acquired by EDS). ....	77
Fig. 4.4: The SLM Realizer installed at the University of Exeter: 1) argon cylinder, 2) interface PC, 3) interim PC and motor controller, 4) laser unit, 5) storage cabinet, 6) status monitor, 7) build chamber, and 8) gas regulator.....	78
Fig. 4.5: Close up view of the build chamber.....	78
Fig. 4.6: Example of the SLM process in action on Al/5wt%Fe <sub>2</sub> O <sub>3</sub> powder mixture: (a) a deposited powder layer, ready for laser scanning, (b) laser melting of rectangular parts, and (c) end of the first scanning and starting the second scanning.....	79
Fig. 4.7: Schematic pattern of scanning strategy for single and additive layers.....	80
Fig. 4.8: (a) The forward movement of loader 2 to start powder deposition. (b) Demonstration of a shaft with slots, used to deposit powder in loader 1 and 2. ....	81
Fig. 4.9: (a) Compression testing setup and (b) shear-punch testing die.....	83
Fig. 4.10: The surface roughness tester at the University of Exeter; (a) surface roughness machine and (b) close up of the machine when a part is being scanned by laser probe apparatus.....	84
Fig. 4.11: (a) Optical and (b) SEM microscopy equipments at the University of Exeter.....	84
Fig. 5.1: Schematic layouts of parts regarding the gas direction; (a) parallel and (b) perpendicular to gas flow. ....	87
Fig. 5.2: Different samples for different testing methods.....	88
Fig. 5.3: A set of cylindrical parts fabricated parallel to gas flow showing the decrease of delamination with the gas direction as well as fabrication sequence; (a) front and (b) right view.....	89
Fig. 5.4: The thermal image of the bed showing temperature distribution at the end of process.....	90
Fig. 5.5: A set of cylindrical parts fabricated perpendicular to gas flow showing no delamination; (a) front and (b) right view.....	90

Fig. 5.6: Material porosity of the samples fabricated parallel and perpendicular to gas flow.....	91
Fig. 5.7: Tensile properties of the SLM parts produced parallel and perpendicular to gas flow. For comparison, tensile properties of a conventionally manufactured annealed bar is given from references (ASM International Handbook Committee, 1990).....	92
Fig. 5.8: Shear strength of the specimens produced parallel and perpendicular to gas flow (for comparison, the estimated shear strength of a conventionally manufactured annealed bar is ~ 250 MPa). .....	93
Fig. 5.9: (a) Compression properties of the parts produced parallel and perpendicular to gas flow; and typical apparent rupture of a compression specimen produced (b) parallel and (c) perpendicular to gas flow.....	95
Fig. 5.10: Typical cross sectional micrograph of samples produced parallel to gas flow; (a) XY section and (b) transversal section. ....	97
Fig. 5.11: Typical cross sectional micrograph of samples produced perpendicular to gas flow; (a) XY section and (b) transversal section. ....	97
Fig. 6.1: The visual process development to fabricate single layer parts from (a) Al and (b) Al/5wt%Fe <sub>2</sub> O <sub>3</sub> mixture using laser power of 39 W and scanning speed of 72 mm/s within the second step. Reddish colour of Al/5wt%Fe <sub>2</sub> O <sub>3</sub> powder mixture in comparison with silver colour of Al powder is evident in the background. ....	102
Fig. 6.2: The visual process development to fabricate single layer parts from (a) Al and (b) Al/5wt%Fe <sub>2</sub> O <sub>3</sub> mixture using laser power of 17 W and scanning speed of 921 mm/s.....	102
Fig. 6.3: The visual appearance of the parts fabricated from (a) Al and (b) Al/5wt%Fe <sub>2</sub> O <sub>3</sub> mixture using first set of parameters. Balling is evident especially in the parts made from Al/5wt%Fe <sub>2</sub> O <sub>3</sub> . ....	103
Fig. 6.4: The visual appearance of the parts fabricated from Al/Fe <sub>2</sub> O <sub>3</sub> mixture using fifth set of parameters. ....	105
Fig. 6.5: Typical optical microstructural view of the Al part fabricated using laser power of 82 W and scanning speed of 80 mm/s.....	106
Fig. 6.6: (a) Typical optical microstructural views of the part fabricated from Al/5wt%Fe <sub>2</sub> O <sub>3</sub> mixture using laser power of 82 W and scanning speed of 168 mm/s and (b) an image of higher magnification. ....	107
Fig. 6.7: XRD diffraction pattern of the of the part fabricated from Al/5wt%Fe <sub>2</sub> O <sub>3</sub> mixture using laser power of 82 W and scanning speed of 168 mm/s.....	107
Fig. 6.8: The typical multilayer cubic parts (10 mm × 10 mm × 6 mm) produced by SLM of Al/5wt%Fe <sub>2</sub> O <sub>3</sub> powder mixture.....	110
Fig. 6.9: Typical microstructural views of the SLM part fabricated from Al/5wt%Fe <sub>2</sub> O <sub>3</sub> mixture; a) optical microscopy image showing random grain structure, b) SEM overall view of grain structure and c) previous image with higher magnification showing fine particles formed inside grains and boundaries (overall chemical composition was acquired by EDS).....	111
Fig. 6.10: The XRD pattern of the SLM sample shown in previous figure (in addition to present phases, the weak peaks of Al <sub>13</sub> Fe <sub>4</sub> may be observed in the sample spectrum). .....	112
Fig. 7.1: The visual appearance of parts being fabricated from (a) Al/5wt%Fe <sub>2</sub> O <sub>3</sub> and (b) Al/15wt%Fe <sub>2</sub> O <sub>3</sub> powder mixture using $P = 82$ W and $v = 0.33$ m/s. The surface appearance of final parts manufactured from (c) Al/5wt%Fe <sub>2</sub> O <sub>3</sub> and (d) Al/15wt%Fe <sub>2</sub> O <sub>3</sub> powder mixture. ....	116
Fig. 7.2: The visual appearance of parts fabricated from (a) Al/5wt%Fe <sub>2</sub> O <sub>3</sub> , (b) Al/10wt%Fe <sub>2</sub> O <sub>3</sub> , and (c) Al/15wt%Fe <sub>2</sub> O <sub>3</sub> powder mixture ( $P = 39\text{-}91$ W and $v = 0.5\text{-}0.14$ m/s). ....	117
Fig. 7.3: Surface roughness properties of the SLM parts made from Al powder mixed with (a) 5 wt%, (b) 10 wt% and (c) 15 wt% Fe <sub>2</sub> O <sub>3</sub> powder in different laser powers and scanning speeds.....	118
Fig. 7.4: Density of the SLM parts fabricated from (a) Al/5wt%Fe <sub>2</sub> O <sub>3</sub> , (b) Al/10wt%Fe <sub>2</sub> O <sub>3</sub> and (c) Al/15wt%Fe <sub>2</sub> O <sub>3</sub> powder mixture vs. laser power in various scanning speeds. ....	119
Fig. 7.5: Hardness of the SLM parts fabricated from (a) Al/5wt%Fe <sub>2</sub> O <sub>3</sub> , (b) Al/10wt%Fe <sub>2</sub> O <sub>3</sub> and (c) Al/15wt%Fe <sub>2</sub> O <sub>3</sub> powder mixture vs. laser power in various scanning speeds. ....	120

Fig. 7.6: Visual appearance of the cross section in SLM samples made from I) Al/5wt%Fe <sub>2</sub> O <sub>3</sub> ( $P = 82$ W, $v = 0.25$ m/s), II) Al/10wt%Fe <sub>2</sub> O <sub>3</sub> ( $P = 82$ W, $v = 0.2$ m/s), and III) Al/15wt%Fe <sub>2</sub> O <sub>3</sub> ( $P = 70$ W, $v = 0.14$ m/s). .....	121
Fig. 7.7: The micrographs of the SLM sample fabricated from Al/5wt%Fe <sub>2</sub> O <sub>3</sub> mixture ( $P = 82$ W, $v = 0.25$ m/s); (a) polished surface (along XY section), (b) random grain structure (along XY section), (c) higher magnification of boundaries composed of fine particulate phases, and (d) grain structure along SLM building direction.....	122
Fig. 7.8: The micrographs of the Al/10wt%Fe <sub>2</sub> O <sub>3</sub> SLM sample (cut along XY section - fabricated by $P = 82$ W and $v = 0.20$ m/s); (a) polished surface, (b) random grain structure with thick boundaries, (c) particulate phases spread in microstructure, and (d) dark-field image of previous picture. ....	123
Fig. 7.9: (a) Polished surface and (b) particulate phases spread in microstructure appearing in Al/15wt%Fe <sub>2</sub> O <sub>3</sub> part (cut along XY section - fabricated by $P = 70$ W and $v = 0.14$ m/s).....	123
Fig. 7.10: Material surface roughness parameter as a function of laser energy density for (a) Al/5wt%Fe <sub>2</sub> O <sub>3</sub> and (b) Al/15wt%Fe <sub>2</sub> O <sub>3</sub> . The confidence and prediction bands are uncertainty in estimated data occurrence with no and with observational error respectively.....	127
Fig. 7.11: Material density as a function of laser energy for (a) Al/5wt%Fe <sub>2</sub> O <sub>3</sub> and (b) Al/15wt%Fe <sub>2</sub> O <sub>3</sub> . .....	128
Fig. 7.12: Material hardness as a function of laser energy density for Al mixed with 5 and 15 wt% Fe <sub>2</sub> O <sub>3</sub> . .....	129
Fig. 7.13: SLM processing window for the SLM parts fabricated from (a) Al/5wt%Fe <sub>2</sub> O <sub>3</sub> , (b) Al/10wt%Fe <sub>2</sub> O <sub>3</sub> and (c) Al/15wt%Fe <sub>2</sub> O <sub>3</sub> powder mixture.....	130
Fig. 8.1: Microhardness of the multilayer parts fabricated with layer thicknesses of 50 μm and 75 μm and scanning speeds of 0.14 m/s and 0.5 m/s vs. laser power.....	134
Fig. 8.2: The typical SEM microstructural views of the part fabricated on a thick powder bed using (a) $P = 17$ W and $v = 0.14$ m/s (showing granular structure including sintered lines), and (b) $P = 51$ W and $v = 0.14$ m/s (showing a granular structure). The overall chemical composition was acquired by EDS. (c) X-ray diffraction pattern of the part shown in previous image.....	135
Fig. 8.3: (a) Overall view of microstructure, (b) higher magnification of coralline-like and fuzzy appearance of boundaries in previous image, and (c) XRD pattern of the SLM part fabricated when $P = 39$ W, $v = 0.5$ m/s, and $t = 75$ μm.....	136
Fig. 8.4: (a) Overall view of microstructure, (b) higher magnification of boundaries seen in previous image, and (c) XRD pattern of the part fabricated when $P = 39$ W, $v = 0.14$ m/s, and $t = 75$ μm. ....	136
Fig. 8.5: (a) Overall appearance of microstructure, (b) the interior seen in previous image, and (c) XRD pattern of the part fabricated when $P = 61$ W, $v = 0.14$ m/s, and $t = 75$ μm. ....	137
Fig. 8.6: (a) Overall appearance of the grain structure, (b) higher magnification of coralline-like and fuzzy appearance in previous image, and (c) XRD pattern of the part fabricated when $P = 82$ W, $v = 0.5$ m/s, and $t = 75$ μm. ....	138
Fig. 8.7: (a) Microstructure containing (b) porous feature around interior, and (c) XRD pattern of the part made by $P = 91$ W, $v = 0.5$ m/s, and $t = 50$ μm. ....	139
Fig. 8.8: a) View of grain structure, b) fine particles formed inside grains and boundaries (close-up of previous image), and (c) XRD pattern of the part made by $P = 91$ W, $v = 0.14$ m/s, and $t = 50$ μm. ....	139
Fig. 9.1: Microhardness of the parts fabricated from Al/5-15wt%Fe <sub>2</sub> O <sub>3</sub> powder mixtures as a function of laser power in conjunction with various scanning speeds.....	148
Fig. 9.2: SEM micrographs of Al/5wt%Fe <sub>2</sub> O <sub>3</sub> when $P = 39$ W and $v = 0.5$ m/s; (a) overall view of solid formations and microstructure, and (b) high magnification of coralline-like appearance of boundaries (around spectrum 2). (c) X-ray diffraction pattern of the corresponding part.....	149
Fig. 9.3: (a) Overall view of microstructure, (b) details around a pore and particulate format of phases inside matrix, and (c) XRD pattern of the Al/5wt%Fe <sub>2</sub> O <sub>3</sub> part when $P = 51$ W and $v = 0.14$ m/s.....	150
Fig. 9.4: (a) Microstructural overall view, (b) mixture of coralline-like feature and fine particles developing in matrix, and (c) XRD pattern of the Al/5wt%Fe <sub>2</sub> O <sub>3</sub> part when $P = 82$ W and $v = 0.5$ m/s.....	151

Fig. 9.5: (a) Overall view of microstructure, (b) large semi-particulate features around spectrum 1, (c) smooth area around spectrum 3, and (d) XRD pattern of the Al/5wt%Fe <sub>2</sub> O <sub>3</sub> part when $P = 82$ W and $v = 0.14$ m/s.....	151
Fig. 9.6: The SEM micrographs of Al/10wt%Fe <sub>2</sub> O <sub>3</sub> (when $P = 39$ W and $v = 0.5$ m/s) showing a single phase matrix having an orange peel appearance.....	152
Fig. 9.7: The typical microstructure of Al/10wt%Fe <sub>2</sub> O <sub>3</sub> when $P = 51$ W and $v = 0.14$ m/s showing a coarse orange peel appearance.....	152
Fig. 9.8: (a) Microstructural overall view, (b) particulate format of coarser area around zone I, (c) firmly adhered particles forming around zone II, and (d) XRD pattern of the Al/10wt%Fe <sub>2</sub> O <sub>3</sub> part when $P = 82$ W and $v = 0.5$ m/s. ....	153
Fig. 9.9: a) Microstructural overall view, (b) particles formed on cracked area, and (c) XRD pattern of the Al/10wt%Fe <sub>2</sub> O <sub>3</sub> part when $P = 91$ W and $v = 0.14$ m/s.....	154
Fig. 9.10: Relatively smooth appearance of microstructure embedding tiny particles in Al/15wt%Fe <sub>2</sub> O <sub>3</sub> part when $P = 39$ W and $v = 0.5$ m/s. ....	154
Fig. 9.11: (a) Overall view of microstructure showing a rough area developing throughout the matrix, (b) very fine particulate nature of the rough area (around spectrum 1) and (c) XRD pattern of the Al/15wt%Fe <sub>2</sub> O <sub>3</sub> part when $P = 61$ W and $v = 0.14$ m/s. ....	155
Fig. 9.12: (a) Microstructure containing agglomerated and piled up particulate phases on cracks, and (b) XRD pattern of the Al/15wt%Fe <sub>2</sub> O <sub>3</sub> part when $P = 70$ W and $v = 0.5$ m/s. ....	156
Fig. 10.1: (a) Density, and (b) hardness and microhardness of the SLM parts fabricated from Al/5wt%Fe <sub>2</sub> O <sub>3</sub> ( $t = 50$ and 75 $\mu\text{m}$ ), Al/10wt%Fe <sub>2</sub> O <sub>3</sub> and Al/15wt%Fe <sub>2</sub> O <sub>3</sub> powder mixtures. ....	166
Fig. 10.2: CT scan exhibition of the part (made from Al/15wt%Fe <sub>2</sub> O <sub>3</sub> ) (a) before and (b) after HIP post-treatment.....	166
Fig. 10.3: As-manufactured Al/5wt%Fe <sub>2</sub> O <sub>3</sub> SLM part when $t = 75$ $\mu\text{m}$ ; (a) overall view of solids, (b) typical microstructure with a mixture of coralline-like and particulate appearance, and (c) higher magnification of tiny features. (d) XRD pattern of the corresponding part. ....	167
Fig. 10.4: As-manufactured Al/5wt%Fe <sub>2</sub> O <sub>3</sub> SLM part when $t = 50$ $\mu\text{m}$ ; (a) overall view of solids, (b) microstructure composed of semi-particulate phases, and (c) higher magnification of the attached phases with a semi-particulate appearance. (d) XRD pattern of the corresponding part.....	168
Fig. 10.5: (a) Overall view of solids, (b) microstructure with a particulate appearance, (c) higher magnification of the particles resolved in matrix, and (d) XRD pattern of as-manufactured Al/10wt%Fe <sub>2</sub> O <sub>3</sub> SLM part. ....	169
Fig. 10.6: (a) Overall view of solids, (b) microstructure showing fine particles placed in matrix, and (c) XRD pattern of as-manufactured Al/15wt%Fe <sub>2</sub> O <sub>3</sub> SLM part. ....	169
Fig. 10.7: (a) Overall view of solids, (b) microstructure with a rough and coarse coralline-like appearance, (c) higher magnification of rough and coarse corallines, and (d) XRD pattern of HIP treated Al/5wt%Fe <sub>2</sub> O <sub>3</sub> SLM part when $t = 75$ $\mu\text{m}$ . ....	170
Fig. 10.8: (a) Overall view of cross section, (b) porous microstructure composed of very tiny particles, and (c) XRD pattern of HIP treated Al/5wt%Fe <sub>2</sub> O <sub>3</sub> SLM part when $t = 50$ $\mu\text{m}$ .....	171
Fig. 10.9: (a) The cross section, (b) porous microstructure composed of agglomerated fine particles, and (c) XRD pattern of HIP treated Al/10wt%Fe <sub>2</sub> O <sub>3</sub> SLM sample.....	172
Fig. 10.10: (a) The cross section, (b) microstructure resulting from abundant, coarse and mixed phases, and (c) XRD pattern of HIP treated Al/15wt%Fe <sub>2</sub> O <sub>3</sub> SLM sample. ....	172
Fig. 11.1: The visual appearance of SLM process during first and secondary scanning of each layer for (a) Al/15wt%Fe <sub>2</sub> O <sub>3</sub> , (b) Al6061/15wt%Fe <sub>2</sub> O <sub>3</sub> , and (c) AlSi10Mg/15wt%Fe <sub>2</sub> O <sub>3</sub> . ....	180
Fig. 11.2: The CT scan exhibition of the SLM part made from (a) Al/15wt%Fe <sub>2</sub> O <sub>3</sub> , (b) Al6061/15wt%Fe <sub>2</sub> O <sub>3</sub> , and (c) AlSi10Mg/15wt%Fe <sub>2</sub> O <sub>3</sub> . ....	181
Fig. 11.3: Density and relative density of the SLM parts. The density was measured by dimensional method while relative density was achieved according to CT scanning experiments. ....	182

Fig. 11.4: Hardness and microhardness of the Al alloy and Al matrix composite parts. The hardness of Al alloys (Al and Al6061 in their annealed state, and AlSi10Mg (comparable to A360.0) in die casting state) was picked from references.....	183
Fig. 11.5: Compressive strength of the SLM parts made from Al alloy mixed with 15 wt% Fe <sub>2</sub> O <sub>3</sub> .....	183
Fig. 11.6: (a) Typical microstructure containing (b) very fine particles observed in the SLM part made from Al/15wt%Fe <sub>2</sub> O <sub>3</sub> (the chemical composition was acquired by EDS system). (c) XRD pattern of the corresponding part.....	184
Fig. 11.7: (a) Microstructure containing very fine particles with a rough appearance observed in the SLM part made from Al6061/15wt%Fe <sub>2</sub> O <sub>3</sub> . (b) XRD pattern of the corresponding part .....	185
Fig. 11.8: SEM micrographs of AlSi10Mg/15wt%Fe <sub>2</sub> O <sub>3</sub> ; (a) microstructure containing very fine particles with a rough appearance, (b) close view of microstructure containing particles around 100 nm, and (c) clear view of ultrafine (or even nanoscale) dendritic nature of matrix. (d) XRD pattern of the corresponding part. ....	186
Fig. 12.1: The schematic of LMD process, in which the deposition is undertaken at the tool centre point, courtesy of TWI.....	191
Fig. 12.2: Visual appearance of the surface finish after laser polishing of Inconel LMD parts (sample 18 is the reference with no surface polishing). .....	193
Fig. 12.3: 2D (Ra) and 3D (Sa) roughness parameters of laser polished surface (sample 18 (Ref.) is the sample that was untouched after fabrication). .....	194
Fig. 12.4: Typical 2D and 3D roughness profiles of (a) and (c) sample 18 (Ref.), and (b) and (d) sample 3, respectively.....	195
Fig. 12.5: Linear roughness predicted using Design Expert software, using beam spot size of (a) 1.0 mm, (b) 0.7 mm and (c) 0.3 mm .....	196
Fig. 12.6: Roughness characteristics of the surface as a function of laser energy density .....	197

## List of Tables

Table 4.1: Chemical composition (in weight %) of the standard alloys used in this work .....	77
Table 6.1: Summary of different steps to improve parameters .....	100
Table 8.1: Summary of microstructural evolution in dependence of layer thickness, laser power and scanning speed .....	144
Table 9.1: Summary of microstructural evolution in dependence of $\text{Fe}_2\text{O}_3$ content, laser power and scanning speed .....	160
Table 10.1: Summary of microstructural characteristics before and after HIP post-treatment....	173
Table 12.1: The laser parameters used for surface polishing of LMD parts .....	192

---

# Introduction

---

## Research Background

With the rapid growth of laser applications and the reduced cost of laser systems, laser material processing has gained a high importance in a variety of industries. Automotive, aerospace, navy, defence, and many other sectors are widely adapting laser technology for welding, cutting, and hardening (Toyserkani et al., 2005). Among laser industrial applications, ‘Additive Layer Manufacturing’ (ALM) processes have received significant attention in recent years allowing us to manufacture parts in polymers, ceramics and metals for a variety of applications. ALM family includes a variety of techniques. Selective Laser Melting (SLM), as one of ALM techniques, generate complex three-dimensional parts from metals, metal alloys, and metal matrix composites (Childs et al., 2004, Kruth et al., 2007, Reeves, 2008, Savalani et al., 2006). The principle of SLM is relatively simple, working by building-up and solidifying the required geometry from powder material, layer-by-layer on top of each other (Childs et al., 2004, Kruth et al., 2007).

Metal matrix composites (MMCs) are increasingly demanded from a variety of applications in the ground transportation (auto and rail), aerospace, thermal management, recreation markets, etc. Attractive characteristics include very good specific strength, stiffness, tailorable strength, coefficient of thermal expansion (CTE), thermal conductivity, and excellent wear resistance (Ibrahim et al., 1991). Discontinuously reinforced MMCs also provide isotropic properties and moderate cost. The MMCs are now broadly applied and represent an important established class of metallic materials. However, a dramatic expansion of applications is also expected from the significant additional improvements, which are still available in this relatively new class of materials (Ibrahim et al., 1991, Miracle et al., 2004, Tjong and Ma, 2000). For example, the aerospace industries seek to enhance the performance of commercial and military aircraft by further usage of metal-matrix composites (MMCs), especially, aluminium composites. Aluminium composites may possess excellent combination of demanded properties such as high thermal conductivity, high strength, low density, relative low-cost, etc (Rawal, 2001, Yan et al., 2008). Despite the wide application of Al MMCs, there is no report to demonstrate their

production using SLM process. Therefore, the ability of SLM process to manufacture Al MMCs and the relevant challenges are unclear and require to be assessed. This appears as a very promising and valuable subject in this field.

## **Research Objectives and Tasks**

This PhD project aims to develop selective laser melting (SLM) process for the fabrication of advanced metals and Al matrix composites. The key objectives include material/process behaviour (e.g. material-laser interaction; laser consolidation) and characterisation of novel microstructures and properties in dependence of process parameters (e.g. laser power; scanning speed; layer thickness).

This research first gathers the relevant background theory and literature review for this subject. Then, it explains the material and experimental procedure used in this work and explores the characteristics of the SLM machine through preliminary experiments on 316L stainless steel.

The main part of the PhD focuses on the production of in-situ particulate reinforcements inside Al matrix by using SLM process in the powder mixture of Al/Fe<sub>2</sub>O<sub>3</sub>. It successfully fabricates single-layer and multi-layer parts from in-situ formed particle Al matrix composites. It investigates the fundamental mechanisms governing SLM assisted in-situ reaction and also the effects of various parameters such as SLM layer thickness, laser power and scanning speed as well as proportion of Fe<sub>2</sub>O<sub>3</sub>. It examines the influence of Al alloy powder and it describes the effect of hot isostatic pressing (HIP) post-treatment. The physical, mechanical, and metallurgical properties of the products are extensively assessed using various techniques such as CT scanning, hardness, tensile and compression and shear-punch tests, optical and electron microscopy, XRD, etc. The processing windows of the process are sketched for various proportions of Al/Fe<sub>2</sub>O<sub>3</sub> powder mixture. The results contribute to provision of an in-depth scientific understanding of novel Al MMCs by using SLM assisted in-situ processes, and to develop new manufacturing technique to fabricate net-shape Al matrix composite parts by using less energy consumption and low-cost additives.

Moreover, this study is associated with an industrial collaborative research on developing laser assisted additive manufacture methods for the rapid manufacturing of new

classes of high value metallic parts composed of Al, Ti, stainless steel, and super alloys. So, part of this PhD study collaborate with industrial partners to establish a SLM processing window for individual metallic powder material and characterise the surface finish, metallurgical quality, process accuracy and mechanical properties of the SLM products.

## Thesis Organisation

*Part I. Background Theory and Literature Review:* This part includes 3 chapters about the relevant literature, background and state of the art of ALM processes, the processing aspects of SLM, and developments of metal alloys and MMCs by SLM, and research hypothesis for SLM of Al MMCs from Al/Fe<sub>2</sub>O<sub>3</sub> powder Mixture.

*Part II. Materials, Experimental Procedures, and Preliminary Experiments:* This part (in three chapters) explains the materials and experimental setup which were used for obtaining the results, and the preliminary studies on SLM of 316L stainless steel as well as single layer and multilayer parts made from Al/Fe<sub>2</sub>O<sub>3</sub> powder mixture. The preliminary studies illustrate the challenges and capabilities of SLM to manufacture parts from different materials as well as the parameters affecting the results.

*Part III. In-situ Fabrication of Al Matrix Composites by Using Selective Laser Melting of Al/Fe<sub>2</sub>O<sub>3</sub> Powder Mixture:* This part demonstrates the major results of this PhD research and is presented in five chapters. It initially illustrates the SLM behaviour, properties, and processing windows of consolidated Al/Fe<sub>2</sub>O<sub>3</sub> powder mixtures. It then describes the effect of SLM layer thickness and Fe<sub>2</sub>O<sub>3</sub> contents in conjunction with laser power and scanning speed on microstructural evolution of produced Al composites. It also explains the effect of hot isostatic pressing (HIP) as a post-treatment on densification and microstructure. It finally examines the effect of various Al alloys on SLM behaviour of powder mixtures and in-situ formation of particles in manufactured composites.

*Part IV. Industrial Case Studies and Applications:* Since this research is associated with an industrial collaborative project, this part presents an example of our collaborations, i.e., development of laser metal polishing which was carried out with the help of industrial partners.

# **Part One: Background Theory and Literature Review**

---

# Chapter 1: Background

---

## 1.1. Laser Materials Processing

### 1.1.1. Principles of laser operations

Atomic systems such as atoms, ions, and molecules can exist only in discrete energy states. A change from one energy state to another, called a transition, is associated with either the emission or the absorption of a photon (Koechner, 2006). Electrons of atoms with two levels of energies,  $E_1$  and  $E_2$ , as shown in Fig. 1.1, can be stimulated by absorption of energy to move to upper level of energy. Subsequently, the electron can transit from the upper to lower levels via radiation, when the electron is not in equilibrium condition. This radiation of beam is fundamental in laser operation. A large population of atoms in upper state will result in a dominated stimulated emission. This emission may appear as a light of a given wavelength. The spectrum of the light emitted by an element is a characteristic of the element (Foot, 2006).

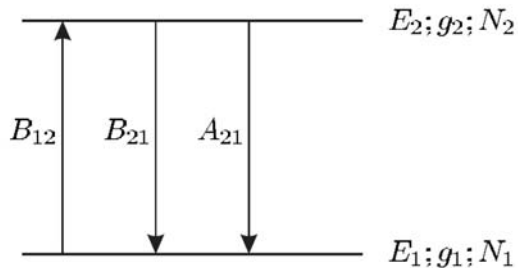


**Fig. 1.1:** The interaction of a two-level atom with radiation leads to stimulated transitions, in addition to the spontaneous decay of the upper level (Foot, 2006).

**Overall Design:** The basic laser consists of a cavity with two parallel mirrors in which light would oscillate back and forth between the mirrors forever if it is not prevented by some mechanism such as absorption (Steen and Mazumder, 2010). Between the mirrors, there is a gain or amplifying medium, where stimulated emission occurs. The mirrors guide the light back into the amplifying medium repeatedly for continued growth of the developing beam (Silfvast, 1996). The optical arrangement is shown in Fig 1.2.

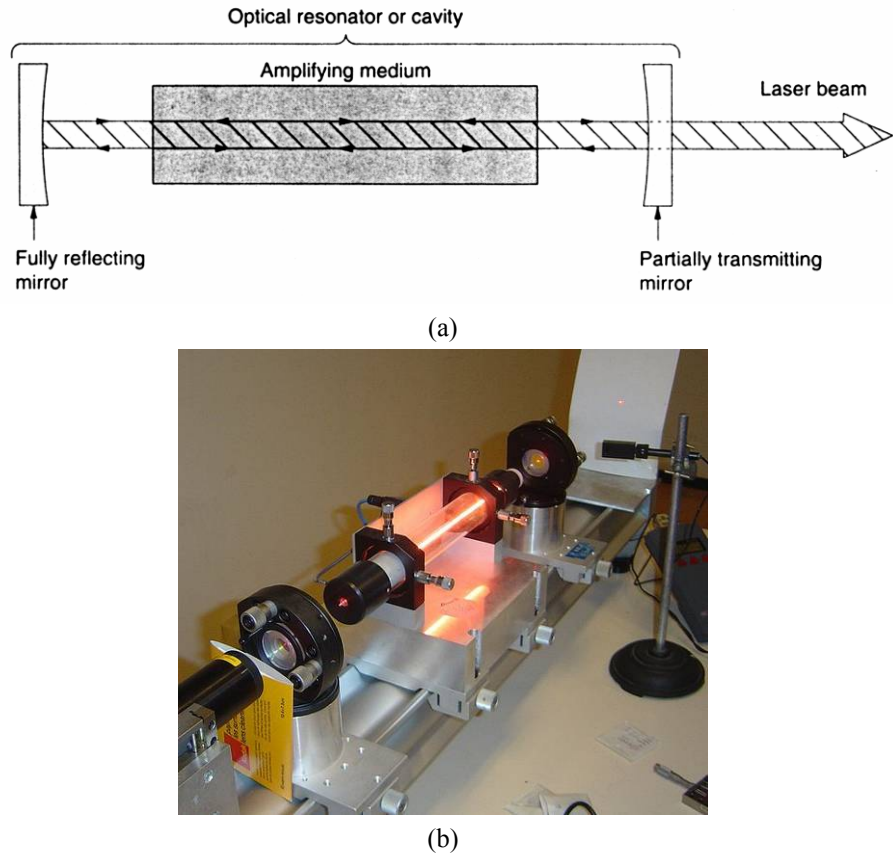


**Fig. 1.2:** Simplified schematic of a typical laser (Silfvast, 1996). (b) Helium-Neon laser at the Kastler-Brossel Laboratory at Paris VI: Pierre et Marie Curie.

### 1.1.2. Industrial lasers

Different types of lasers are used for powder-bed based additive layer manufacturing: CO<sub>2</sub>, Nd:YAG (lamp pumped, diode pumped, or Qswitched), fibre lasers, disc lasers, Cu-vapour lasers. Type of laser has a significant influence on the consolidation of powder particles due to several reasons: (i) laser absorption of various materials greatly depends on the laser wavelength, (ii) the possible consolidation mechanism highly depends on features like energy density, and (iii) laser mode (continuous, pulsed, Q-switched, and...) has a large influence on consolidation (Kruth et al., 2007).

One example of common lasers is fibre laser system. Fibre laser systems are solid-state lasers where the light is guided in optical fibres. The fibres, guiding the light, can be very thin, may be around 100 µm. Owing to the small cross section and long length of the fibre, efficient operation with good beam quality can be achieved, e.g., a beam quality 10 times

better than that of a standard Nd:YAG laser. Erbium and ytterbium ions are common in such laser systems (Koechner, 2006, Steen and Mazumder, 2010).

### 1.1.3. Industrial applications of laser materials processing

Regarding the capability of laser to produce a controlled energy, it can be utilised in various processes as illustrated in Fig. 1.3. Fig. 1.3 also indicates that the energy density of the laser beam plays an important role in the processing mechanism. Some examples of laser applications are further explained below:

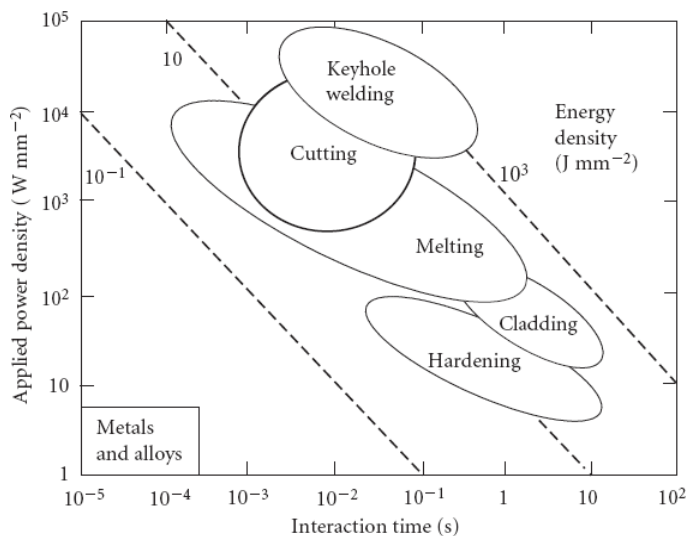


**Fig. 1.3:** Range of five laser processing methods of metals and alloys (regions bounded by solid boundaries) and contours of energy density (broken lines) (Ion, 2005a).

### Laser Surface Treatment

The laser can be efficiently used in surface heating. The electromagnetic radiation of a laser beam is absorbed within the first few atomic layers for opaque materials such as metals, while there are no hot gas jets, eddy currents or even radiation spillage outside the optically defined beam area. In fact the applied energy can be placed precisely on the surface only where is needed. Surface treatment is very important nowadays, offering the chance to save strategic materials and idealise surfaces and bulk properties.

### Laser Welding

Laser welding is a welding technique used to join multiple pieces of metal through the use of a laser. The laser welding show important advantages compared to other techniques

such as the low heat input, the high localisation ability, the high welding speed, the high flexibility, the high weld quality and the high production rate. The focussed laser beam is one of the highest power density sources available for industry today, producing a power density similar to an electron beam. At these high power densities all materials will evaporate. Accordingly, a hole is usually formed by evaporation. This "hole" is then traversed through the material with the molten walls sealing up behind it. The result known as a "keyhole" weld is recognised as instability arise from laser welding (Sánchez-Amay et al., 2009, Steen and Mazumder, 2010).

## Laser Cladding

The objective in laser cladding is to fuse an alloy layer or coating, of enhanced mechanical and chemical properties, into the surface of a substrate with the minimum of dilution from the substrate into the alloy (Sexton et al., 2002). Repair by cladding is a common and standard practice in the die and mould industries, where the life of loaded die elements and vital tool parts can be successfully extended by the timely repair of damaged surfaces (Capello and Previtali, 2006). Fig. 1.4 shows a schematic and one of the applications of laser cladding for coating of oil drilling tools, which are subjected to significant wear in their operation.

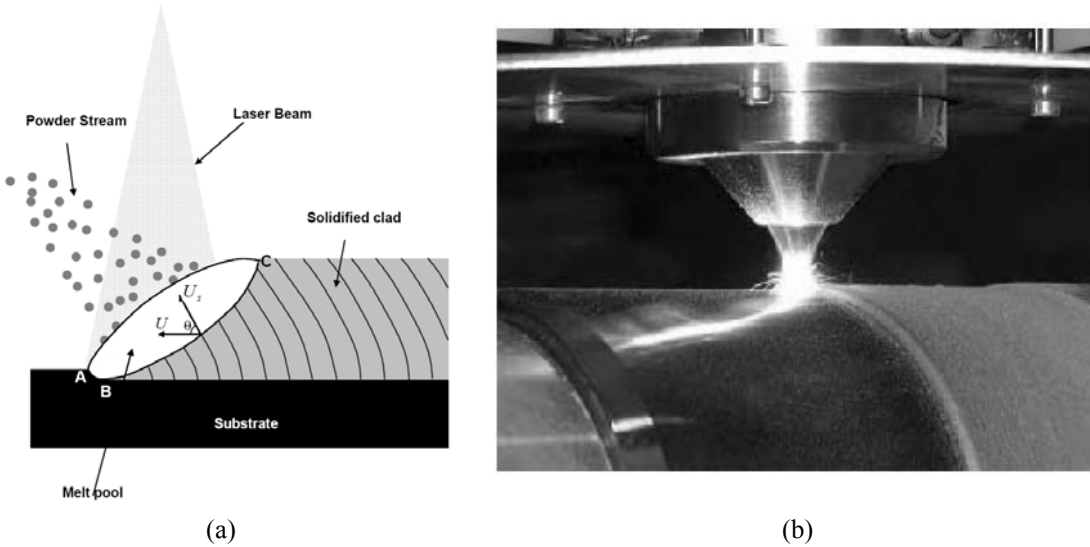


**Fig. 1.4:** (a) A schematic of the process zone during laser cladding, and (b) coating of oil drilling tools by laser cladding (Toyserkani et al., 2005).

## **1.2. Additive Layer Manufacturing (ALM)**

### **1.2.1. Principles of ALM**

The principle of additive layer manufacturing is relatively simple. In contrast with machining, where material is removed from a solid block, or casting where material is melted and forced into a cavity, additive processes work by ‘building-up’ the required geometry particle-by-particle, layer-by-layer, from the bottom to up (Reeves, 2008).

### **1.2.2. ALM processes**

There are many different mechanisms for both production a single layer and bonding several layers together. In some simple systems, layers are cut from sheet material and bonded using adhesives or ultrasonic welding type processes. In other systems, layers are produced by melting fine powders using a laser or electron beam, and consolidating the new layer on previous layer by remelting. Generally, there are over 30 various ALM processes marketed by over 40 different companies around the world. The majority of these systems have been focused on polymeric materials, though the ALM processes of metallic systems are growing day by day (Kruth et al., 1998, Reeves, 2008, Yan et al., 2009). Some ALM techniques have been briefly explained below. Each of these technologies have their own unique benefits; including materials flexibility, cost of ownership, the speed of build cycle, cycle time between jobs, build envelope capacity, layer thickness, part accuracy and repeatability, surface finish and metallurgical properties. Some processes build within a heater chamber to reduce residual stresses, whilst other build parts onto strong base plates which can be post heat-treated to remove build stresses. In some processes the parts can literally be broken away from the build plate, whilst in other processes they require removal using wire erosion (Reeves, 2008).

#### Stereolithography (SL)

Like most solid freeform fabrication techniques, SL is an additive fabrication process that allows the fabrication of parts from a computer-aided design (CAD) file. The CAD-file describes the geometry and size of the parts to be built. The SL manufacturing is based on the controlled solidification of a liquid resin by photo-polymerisation. Using a laser beam or a digital light projector, a pattern is illuminated on the surface of a resin. Then, the SL

elevator platform moves down by a single layer thickness and the built layer is recoated with liquid resin. A pattern is then cured in this second layer. These steps (the movement of the platform and the curing of an individual pattern in a layer of resin) are repeated constructing a solid 3D object. After draining and washing-off excess resin, an as-fabricated (or green) structure is obtained. This structure is usually incomplete, and post-curing with ultraviolet light is often required to improve mechanical properties.

Fig. 1.5 shows schematic diagrams of two types of stereolithography setups. In both systems objects are built in a layer-by-layer manner by controlled photo-polymerisation of a liquid resin; differences are in the build orientation and in the method of illumination (Melchels et al., 2010).

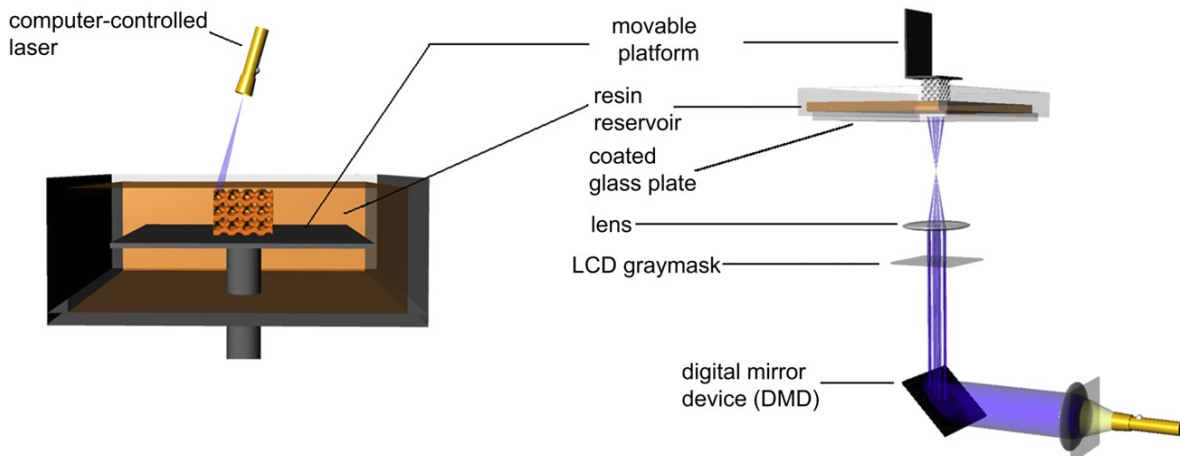


**Fig. 1.5:** Schemes of two types of stereolithography setups. Left: a bottom-up system with scanning laser. Right: a top-down setup with digital light projection (Melchels et al., 2010).

### Fused deposition modelling (FDM)

FDM is an additive manufacturing technology in which a spool of thermoplastic filament feeds into a heated FDM extrusion head. Inside the flying extrusion head, the filament is melted into liquid (above the melting temperature) by a resistant heater. The head traces an exact outline of each cross-section layer of the part when the head moves horizontally in x and y axes. After finishing of one layer, the extrusion head moves up a programmed distance in z direction for building the next layer. Each layer is bonded to the previous layer through thermal heating. Figure 1.6 shows the working principle of FDM (Yan and Gu, 1996).

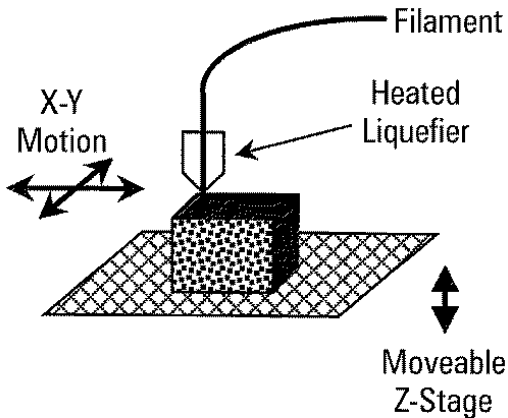


**Fig. 1.6:** Schematic of Fused deposition modelling (FDM) (McNulty et al., 1998).

#### Laser-engineered net shaping (LENS)

LENS process is a laser-assisted, direct metal manufacturing process which incorporates features from stereolithography and laser surfacing, and controls the forming process by a computer file. Powder-metal particles are delivered in a gas stream into the focus of a laser to form a molten pool. The part is then driven on to generate a three-dimensional part by layer-wise, additive processing (Hofmeister et al., 1999). Fabrication of parts by LENS process has been shown in Fig. 1.7.

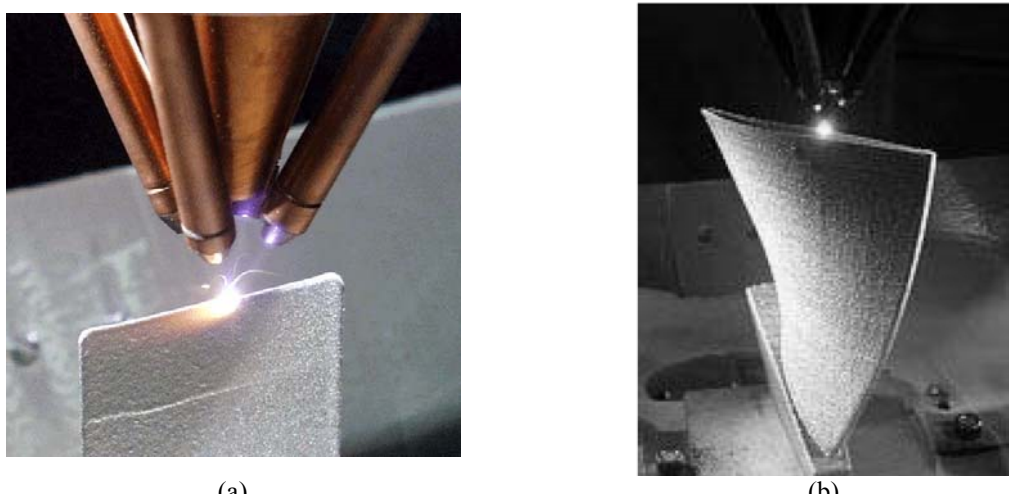


**Fig. 1.7:** (a) The LENS process performing a single-line build (Hofmeister et al., 1999) and (b) fabrication of a blade by Laser Engineering Net Shaping (LENS) (Toyserkani et al., 2005).

#### Selective laser sintering (SLS)

SLS is an additive manufacturing technique that laser selectively fuses powder, from plastic (e.g. nylon and polystyrene), metal (e.g. steel, titanium, alloy mixtures, and composites), or ceramic powders, layer by layer to fabricate solid objects. The physical processes associated to this technology are the heat transfer and the sintering phenomena.

The basic concept, common to all rapid prototyping techniques, is that any complex shape can be sintered and produced by the superposition of small thickness layers described by CAD software. After a layer is sintered, the powder bed is lowered by one layer thickness, a new layer of material is applied on top, and the process is repeated until the part is completed. The process has been shown schematically in Fig. 1.8 (Dong et al., 2009, Franco et al., 2010).

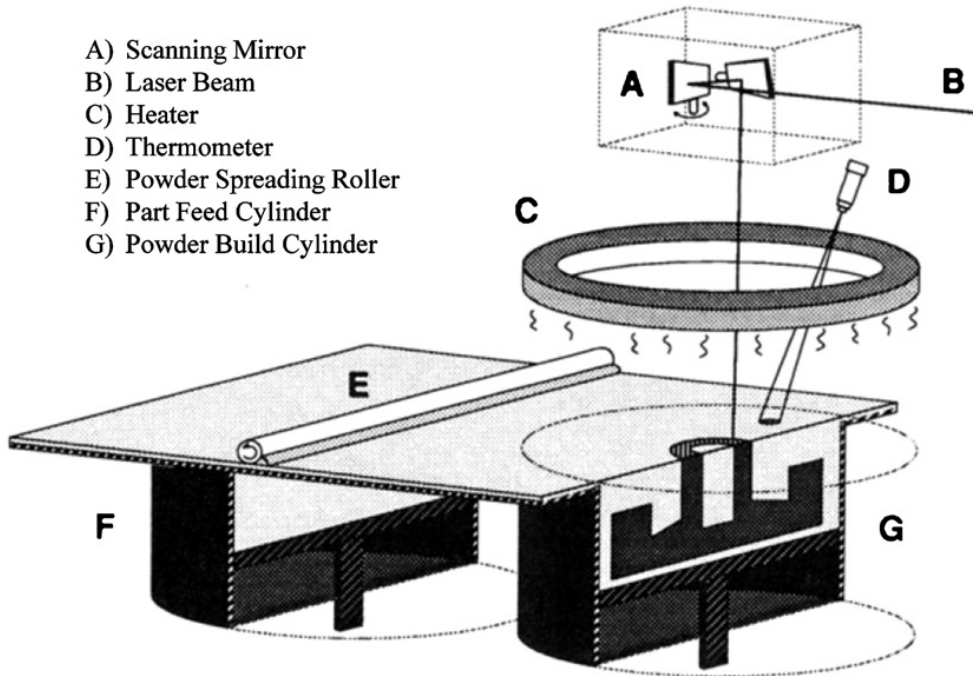


**Fig. 1.8:** A schematic of selective laser sintering (SLS) process (Nelson et al., 1993).

### 1.3. Selective Laser Melting (SLM) and Applications

#### 1.3.1. Principles of SLM

Selective laser melting (SLM) is an ALM process and emerged as a new manufacturing technique to directly fabricate metal alloys and metal matrix composites (MMCs) products. SLM, also termed Direct Metal Laser Sintering as similar to selective laser sintering (SLS), is one of the most versatile ALM processes to generate complex 3D parts by solidifying successive layers of powder material on top of each other. The selective laser melting process which is very close to selective laser sintering (SLS) is described in US Patent 6,215,093 (Meiners et al., 2001) as follows:

"The method is characterised in that the metallic material in powder form is applied in the form of a metallic powder free of binders and fluxing agents, that it is heated by the laser beam to melting temperature, that the energy of the laser beam is chosen in such a way that the layer of metallic powder is fully molten throughout at the point of impact of said laser beam". It should be noted that while SLS uses sintering mechanism to partially melt and then fuse powder materials, SLM typically melts metal powders to fabricate parts for functional end-use applications. In SLM, a bed of metallic powders or metallic composite powders is melted by a beam spot laser projected from the above and solidifies the powder layer. The powder-bed then drops down by a measure of one cross-section layer thickness. It is followed by an automated levelling system that distributes a new layer of powder over the top of the previous layer. The laser then melts a new cross-section and the process repeats to form a solid metal or MMC part (comprised of hundreds or possibly thousands of thin layers) with relatively good densities. The schematic pattern of procedure and relevant scanning strategy is shown in Fig. 1.9 (Abe et al., 2001, Kruth et al., 2007, Levy et al., 2003, Li et al., 2009, Meiners et al., 2001, Osakada and Shiomi, 2006).

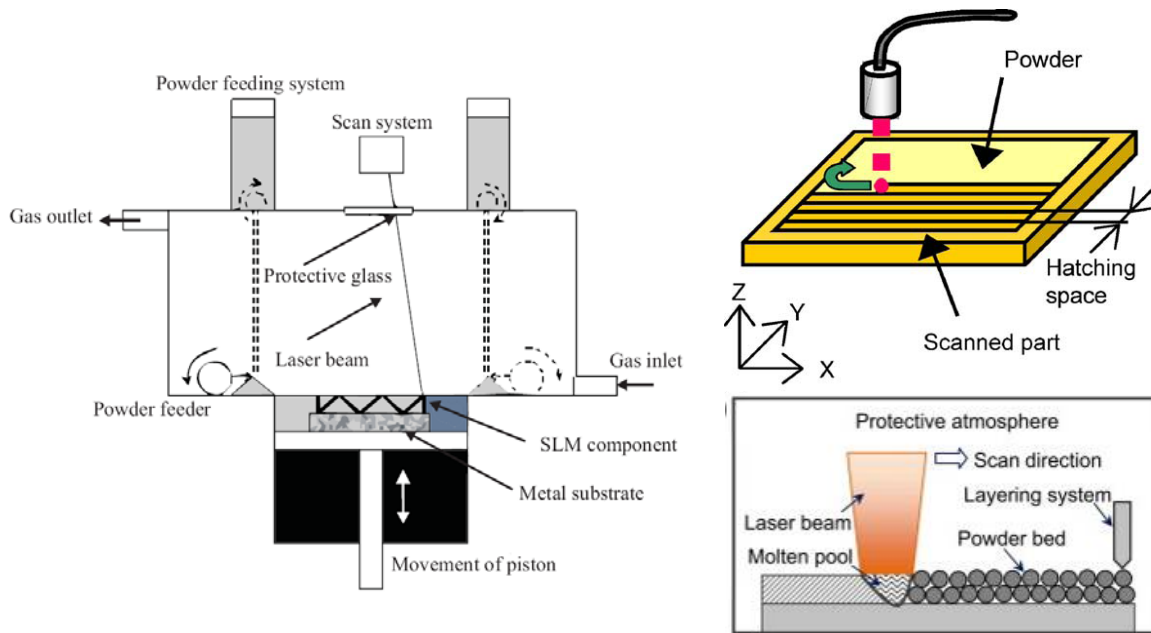


**Fig. 1.9:** Diagram showing (a) how the SLM system works (Li et al., 2009) and (b) laser scanning and corresponding melting of powders (Gu et al., 2011a, Osakada and Shiomi, 2006).

### **1.3.2. Benefits and disadvantages of SLM process**

The benefits of SLM can be given as:

- 1) The capability to produce parts with high density and strength.
- 2) The negligible wastage of material; unused powders can be recycled.
- 3) The ability to produce complicated shapes, e.g. a one-piece steel mould with a looped internal cooling channel can be produced via SLM.
- 4) SLM can produce parts from a relatively wide range of commercially available powder metals including steel, titanium, super alloys, alloy mixtures, and composites.
- 5) No distinct binder and melt phases is required; hence, the process can produce “single material” parts (e.g. Steel, Ti or Al alloys), rather than producing a composite green parts which might not be desired (Kruth et al., 2007, Levy et al., 2003).

Some of the current drawbacks of SLM can be introduced as:

- 1) SLM suffers from melt pool instabilities leading to imperfections such as low quality of down facing surfaces, higher upper surface roughness and the risk of internal pores. Thus, SLM parts have a coarse and grainy surface finish, and often require a secondary machining or polishing process.
- 2) Higher temperature gradients in SLM lead to high residual stresses. Therefore, it is commonly required to build and anchor the part on a solid base plate. This increases the risk of delamination and distortion in removing the base plate.
- 3) The laser melting processing needs higher energy source. This means more expensive lasers to provide a high laser power and good beam quality. On the other hand, it commonly takes too long to complete, making it unsuitable for mass production.

### **1.4. Application of Additive Layer Manufacturing, Especially SLM**

ALM including SLM is currently used to manufacture parts and medical implants from some metallic and mostly non metallic materials systems. The geometrical independence and greater liberty seems to be the most attractive feature of ALM processes: undercuts, overhangs, free forms, as well as elementary shapes can be easily produced (Levy et al., 2003). Steel and Titanium have been used as the most common metallic materials in SLM processes. Some examples of SLM parts and applications are shown in Figs. 1.10 and 1.11.

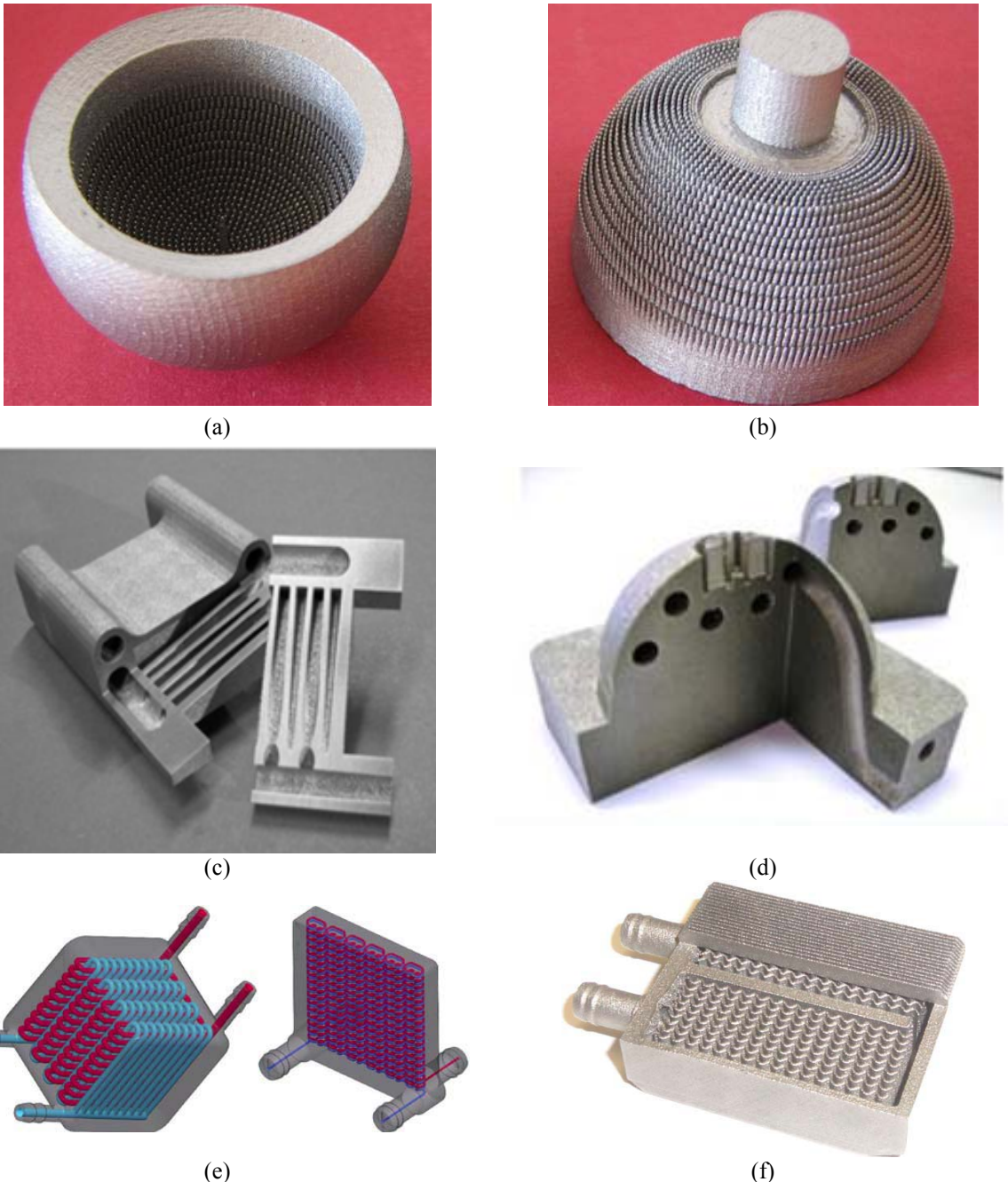


**Fig. 1.10:** Some parts manufactured by SLM process; (a),(b) Ti alloy prototype of the resurfacing hip arthroplasty (RHA) endoprosthesis with the original multi-spiked connecting scaffold taken directly from the SLM machine (Uklejewski et al., 2011), (c),(d) 316L stainless steel and Ti6Al4V parts with internal structures (Yasa et al., 2011) and (e),(f) heat exchanger designs and the miniature cooler part with extremely intricate inner geometry (Neugebauer et al., 2011).



(a)



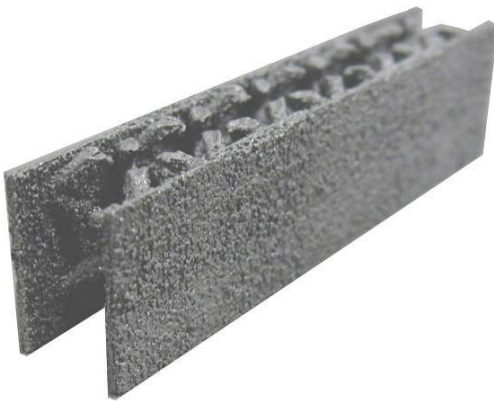
(b)



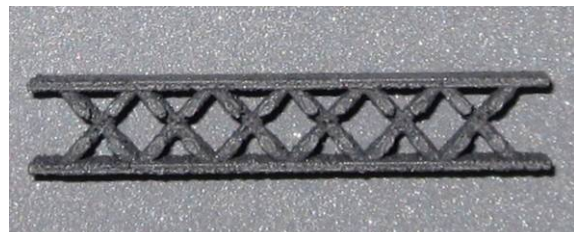
(c)



(d)



(e)



(f)

**Fig. 1.11:** Some parts manufactured by SLM process; (a),(b) synthetic and porous bone structures made from 316L stainless steel available at Centre for Additive Layer Manufacturing (CALM) - University of Exeter, (c),(d) Al alloy aerospace part made by EADS UK, and (e),(f) Al composite sandwich panel part manufactured by the author (designed by Nunzio Palumbo, University of Exeter).

---

# Chapter 2: SLM Processing Aspects

---

This project mainly concentrates on selective laser melting (SLM) as an ALM technique to fabricate parts from powders. The SLM is a multifaceted process, magnifying many physical phenomena (Verhaeghe et al., 2009). Particular issues may occur during the process as well, affecting the final properties. Accordingly, an understanding about the powder consolidation mechanisms, the SLM processing aspects, the influence of various SLM parameters, and the issues associated with the SLM is vital. Here, a literature review is presented, mainly focusing on layer by layer processes which work based on melting/sintering of fine powders using a laser or electron beam, followed by subsequent consolidation.

## 2.1. Powder Consolidation Mechanisms

Various mechanisms can be considered for classification of consolidation in laser-based powder processes, including solid state sintering, liquid phase sintering, full melting, and chemical induced binding (Fig. 2.1). These mechanisms are enlightened below:

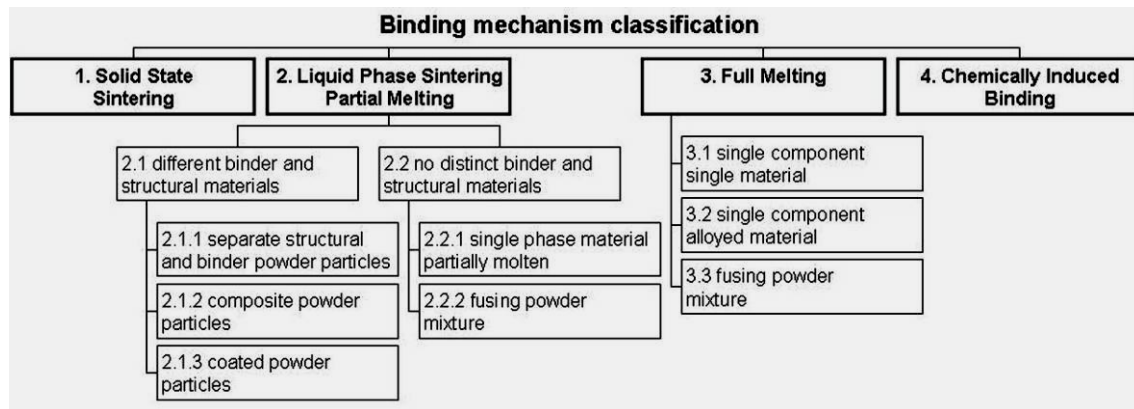


Fig. 2.1: Laser-based powder consolidation mechanisms (Kruth et al., 2007).

**Solid State Sintering (SSS)** is a consolidation process occurring below the material's melting temperature on the basis of diffusion of atoms in solid state, creating necks between adjacent powder particles that will grow with time. This binding mechanism is rarely applied in layer manufacturing since diffusion of atoms in solid state is slow and can not fulfil the desired high laser scan speed to achieve economic process productivity (Kruth et al., 2007).

**Liquid Phase Sintering (LPS)** and **partial melting** include a number of binding mechanisms in which part of the powder material is melted while other parts remain solid. The melted material will spread between the solid particles almost instantaneously as it is driven by intense capillary forces. This allows much higher laser scan velocities than for SSS (Kruth et al., 2007).

**Full melting** is a third major consolidation mechanism, which can lead to densities over 99% by applying modern laser sources and optics yielding high energy densities in the spot (Vandenbroucke and Kruth, 2007).

**Chemical induced binding** is still not commonly employed in commercial ALM equipment, but it turns out to be a feasible consolidation mechanism for polymers, metals and ceramics (Kruth et al., 2007). Chemical induced binding of metals can be applied for sintering of powders e.g. Al powder by controlling the reaction with the N<sub>2</sub> atmosphere used commonly in SLS machines. This creates an AlN binder phase holding the Al particles together.

## 2.2. Process Parameters

SLM is a complex thermo-physical process. An understanding of suitable materials, processing parameters and environmental conditions is very important to manipulate the interactions of lasers and materials and ensure good quality and properties of the SLM parts. This section briefly illustrates the roles of powder materials, SLM process parameters, and environmental conditions on the SLM.

### 2.2.1. Material parameters

#### 2.2.1.1. Composition

Characteristics of the material, especially those that control the thermal response of materials, such as melting temperature, transformation temperatures, thermal conductivity, specific heat capacity, thermal diffusivity, coefficient of thermal expansion, flow properties, laser absorption, latent heat of vaporisation, and etc, originate from chemical composition and are the major parameters to select the appropriate method and parameters of powder bed laser processing. These properties affect crack sensitivity, porosity, heat affected zone (HAZ) embrittlement, poor absorption of the radiation, etc (Steen, 1991).

### 2.2.1.2. Powder density and particle shape and size

The apparent density of powders, related to the powder size, shape and size distribution, directly influences the final density of the SLM parts. Generally, packing of spheres leads to a higher density than other shapes. Moreover, finer powders result in a higher apparent density, meaning a higher final density and mechanical properties. For example, Fig. 2.2 shows that decreasing the particle size is accompanied with increasing the fractional density of laser-sintered iron parts. However, the final density seems to have an upper limit for a given metal powder system (Kruth et al., 1996, Simchi, 2006, Zhu et al., 2007). Simchi (2006) has also reported that finer particles provide larger surface area to absorb more laser energy, assisting the SLM/SLS processes.

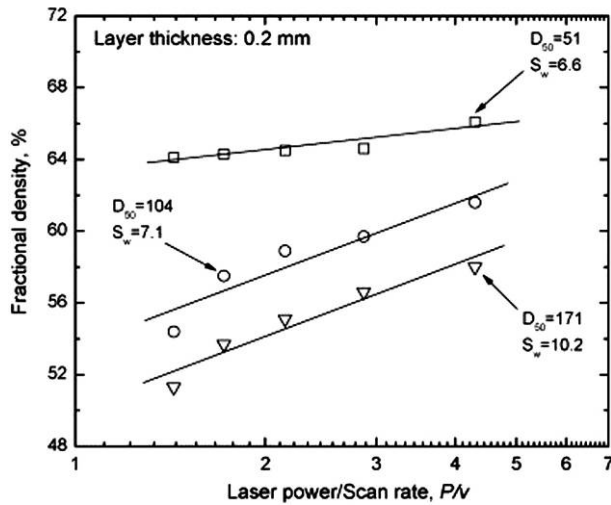


**Fig. 2.2:** Effect of powder particle size on the fractional density of laser-sintered iron at the scan line spacing of 0.2 mm.  $D_{50}$  is particle size at 50% of the cumulative particle size distribution ( $\mu\text{m}$ ) and  $S_w$  is particle size distribution slope (Simchi, 2006).

For mono-sized spheres the best packing density obtainable is 74% theoretically. However, the apparent powder density can be enhanced by mixing different size powders. The principle involves using finer particles to fill the voids formed by the larger powders (see Fig. 2.3 where the higher apparent density (Fig. 4(b)) is schematically observed through mixture of powder with various sizes) (Zhu et al., 2007).

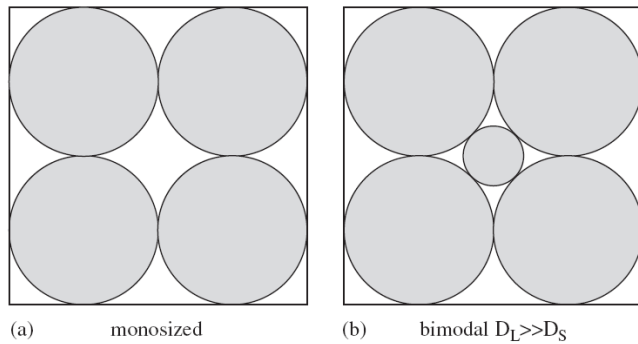


**Fig. 2.3:** The schematic of the effects from combinations of different sizes (Zhu et al., 2007).

It is worth mentioning that reduction in size of particles facilitates the cooling, accelerating the solidification rate and resulting in finer microstructural features (Rajabi et al., 2008). These finer microstructural features (due to smaller particles) commonly produce higher mechanical properties (Dieter, 1986), as reported by Rajabi et al. (2008).

### 2.2.1.3. Microstructure

The heat treatment history of powder and its microstructure may influence the phases after rapid melting and solidification due to laser melting. For example, in the case of stainless steels, fine structures are produced in both martensitic and austenitic stainless steels in high cooling rates. However, different thermal expansions associated with martensitic and austenitic steels lead to various residual tensile stresses, e.g. single tracks of martensitic steel are usually under compression, which becomes tensile when overlapped zones are heated. These residual tensions adversely affect the stress corrosion properties and the pitting potential (Steen, 1991).

### 2.2.1.4. Flow properties

Low viscosity is generally desirable for ALM since this means that the material will flow easily. This is particularly important for SLM where powder binding is critical for successful processing (Bourell, 2006). In addition to lower fluidity of liquid due to higher viscosity, larger droplets and more balling appear in the melt with increasing the viscosity, negatively influencing the SLM process (Rombouts et al., 2006).

## 2.2.2. Laser and scan parameters

### 2.2.2.1. Energy density input: laser power, scan speed, scan line spacing, and layer thickness

An optimal scanning strategy and appropriate energy density can minimise the harmful effects of phenomena such as distortions (as curling or delamination appearing due to the contraction of molten material after solidification under high thermal gradients during SLM processes (Matsumoto et al., 2002)) and provide a proper melting. The energy density is an absolute process parameter representing the energy delivered to a unit volume of powder material and combining some important laser and scan parameters such as laser power, scan speed, scan line spacing, and layer thickness:

$$E_\rho = \frac{P}{\pi r^2} \frac{2r}{v} \frac{2r}{s} \quad (\text{Eq. 2.1})$$

where  $E_\rho$  = energy density ( $\text{J/mm}^2$ ),  $P$  = laser power (W),  $v$  = scanning speed ( $\text{mm/s}$ ),  $s$  = scan line spacing (mm), and  $r$  = beam radius (mm) (Morgan et al., 2004, Xie et al., 2005). Some other researchers (Gu et al., 2006, Gu and Shen, 2009a) have used energy density as the energy delivered to a unit volume and described using the following equation:

$$\eta = \frac{P}{vst} \quad (\text{Eq. 2.2})$$

where again  $\eta$  = energy density per volume ( $\text{J/mm}^3$ ) and  $t$  = layer thickness. According to Eqs. 2.1-2.2, increasing in laser power as well as decreasing in scanning speed, scan line spacing, or layer thickness enhance the energy density of laser which is necessary for melting of materials. The greater the energy imparted to the powder, the greater is the particle fusion contributing to full melting (Hao et al., 2009, Hao et al., 2006). As mentioned, full melting has the main advantage of fabrication of a mostly dense product in one step, but it has also some disadvantages such as the high temperature gradients during the process involving internal stresses or part distortion (Mercelis and Kruth, 2006), and the risk of balling and dross formation in the melt pool resulting in a bad surface finish (Kruth et al., 2007), requiring further process control.

In general, higher energy density results in a denser material processed by SLM, as shown in Fig. 2.4 (Morgan et al., 2004). This is in such a manner that part densities even up to 99.9% may be reached in the case of titanium (Fig. 2.5) (Vandenbroucke and Kruth, 2007, Vandenbroucke and Kruth, 2008). However, at high laser energy may intensify delamination of layers and formation of large cracks (as seen in Fig. 2.6) leading to a

reduction in density. This phenomenon can be attributed to high thermal gradients in the materials accompanied by thermal stresses (Simchi, 2006).

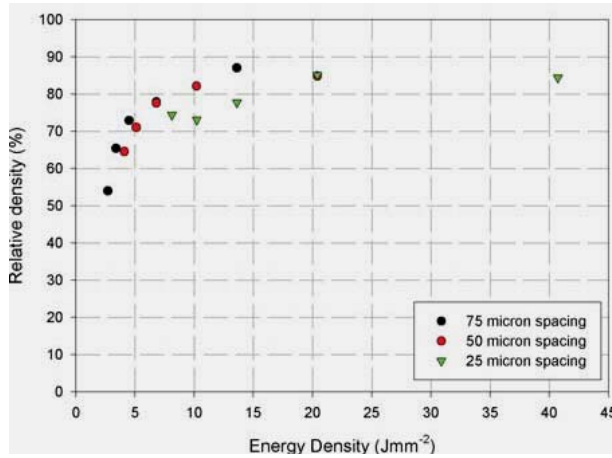


**Fig. 2.4:** Density of 316L stainless steel cubic parts made by direct metal laser re-melting (DMLR) as a function of energy density (when  $v = 100$  mm/s) for variation in scan spacing (Morgan et al., 2004).

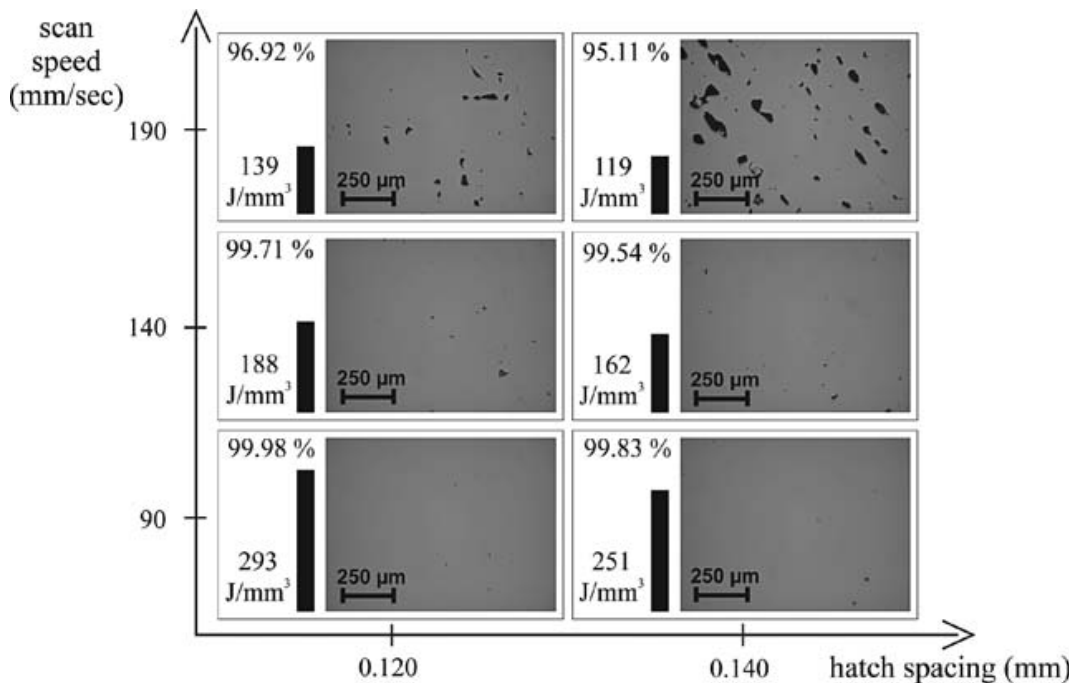


**Fig. 2.5:** SLM process parameter study for Ti-6Al-4V. Used energy density, measured part density and one micrograph are shown for six parameter sets (Vandenbroucke and Kruth, 2007).

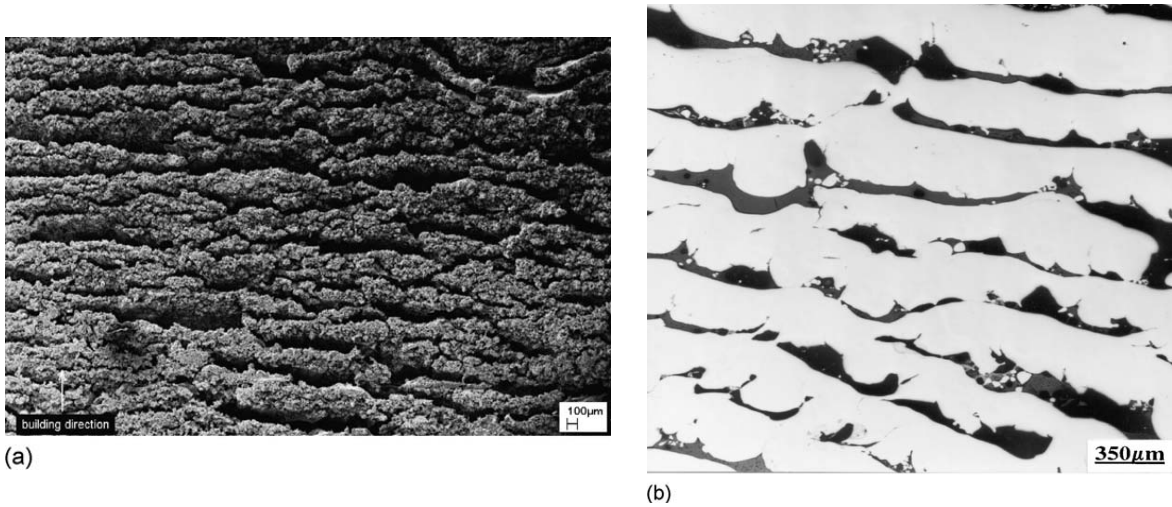


**Fig. 2.6:** (a) Delamination of the sintered iron layers and (b) formation of large horizontal cracks in laser sintered iron ( $D_{50} = 51 \mu\text{m}$ ) due to applying a high value of laser energy ( $P = 215 \text{ W}$ ,  $v = 50 \text{ mm/s}$ ,  $s = 0.1 \text{ mm}$ ,  $t = 0.05 \text{ mm}$ ) (Simchi, 2006).

The layer scanning flow and solidification behaviour of the melt is strongly influenced by scan line spacing, in such a manner that a progressive transition from a highly rippled surface to a smooth surface occurs with decreasing in scan line spacing (as seen from Fig. 2.7). The formation of these continuous rows of agglomerated metals is related to the solidification tracks in the format of molten cylinder, while the formation of large inter-agglomerated pores can be attributed to tension effect and solidification shrinkage. Note that formation of metal balls due to instability of the molten cylinder according to Marangoni effect is likely to occur (Simchi, 2006, Simchi and Pohl, 2003).

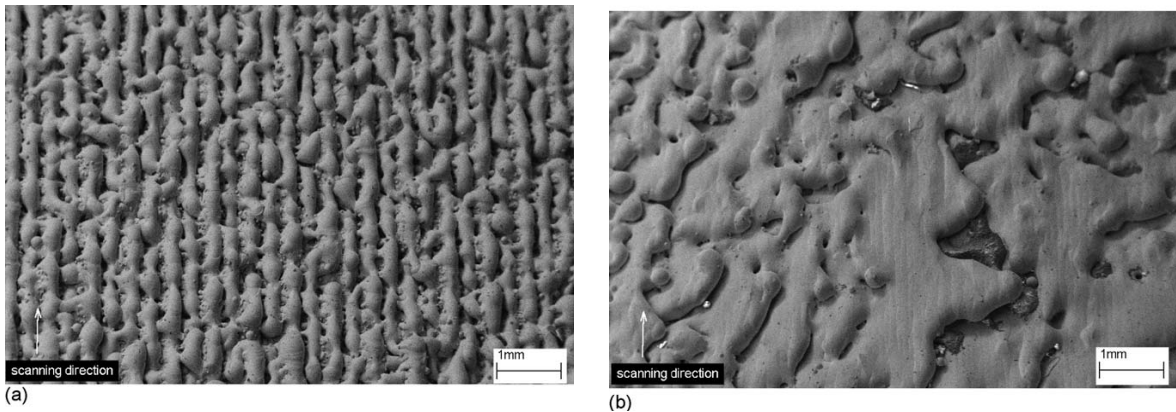


**Fig. 2.7:** SEM micrographs show the surface morphology of laser sintered iron.  $P = 215\text{W}$ ,  $v = 50 \text{ mm/s}$ ,  $t = 0.1 \text{ mm}$ , and (a)  $s = 0.3 \text{ mm}$  and (b)  $s = 0.1 \text{ mm}$  (Simchi, 2006).

The amount, shape, and connectivity of pores are strongly affected by scan line spacing. Narrowing the scan line spacing makes the scan tracks close to each other and increases the overlap. The overlapping is the scanning over the previously scanned track leading to

remelting of processed material. Therefore, the overlapping could result in the flowing and spreading of liquid between adjacent scan tracks and escaping of some previously trapped air, and, hence, enhancement of the intertrack binding and reduction in the porosity, as seen in Fig. 2.8 (Gu et al., 2006). However, Aiyiti et al. (2006), worked on a rapid prototyping system based on micro-plasma arc welding (MPAW), emphasised that there might be an optimum overlap to form a smooth surface, as observed in Fig. 2.9. This is in confirmation with the results reported by Xie et al. (2005).

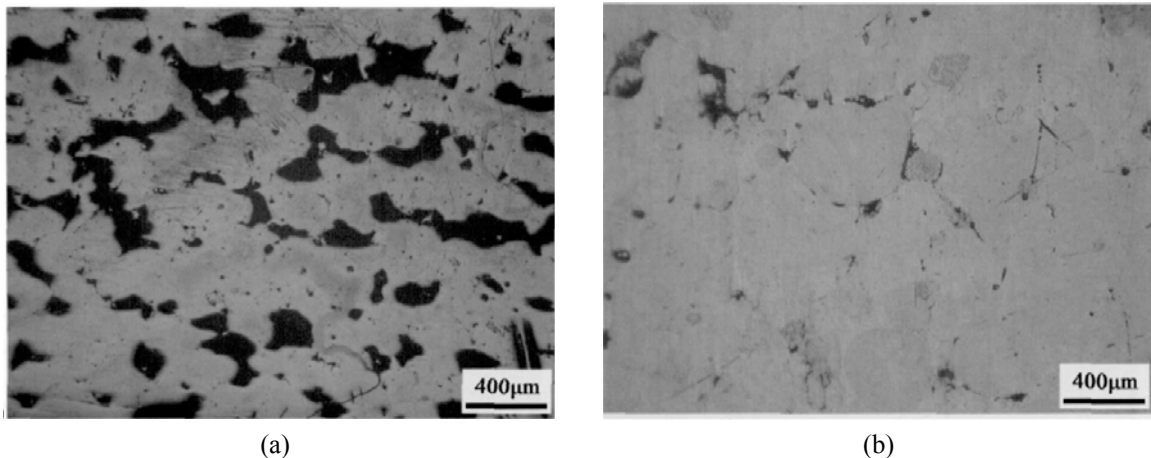


**Fig. 2.8:** Polished but non-etched microstructure of CuSn/Cu/CuP composite samples, laser sintered with laser power of 375 W, scan speed of 0.05 m/s, layer thickness of 0.30 mm, and varied scan line spacing of (a) 0.30 mm (showing much porosity) and (b) 0.15 mm (showing a reduced porosity) (Gu et al., 2006).

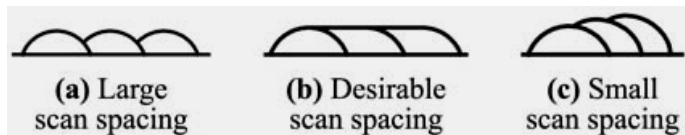


**Fig. 2.9:** Schematic pattern of different scan spacing (Aiyiti et al., 2006).

It is worth mentioning that in laser sintering process, the duration of the laser beam at any powder particles is very short ( $\leq 4$  ms) depending on scan rate and beam radius. Obviously, under this short heating cycle the mechanism of particle bonding must be rapid and solid state mechanisms are not feasible. Furthermore, with metals the viscous flow cannot result in powder densification since the viscosity is high, even at temperatures approaching the melting point. Thus, melting/solidification approach is the dominant mechanism for rapid bonding of metal powders in laser sintering (Niu and Chang, 1998, Simchi, 2006, Simchi and Pohl, 2003), being similar to laser melting. This can be the

explanation for the same behaviour of density with laser energy of metallic parts manufactured by SLM or SLS.

### 2.2.2.2. Spot size

A laser beam is capable of being focused to a small spot size (Ready and Farson, 2001). The spot size acts in two ways; a decrease in spot size firstly, increases the power density and influences the temperature of molten pool and secondly, decreases the affected area (Steen, 1991).

### 2.2.2.3. Scanning strategy

Simchi and Pohl (2003) carried out a series of experiments to assess the effect of three different scanning patterns (see Fig. 2.10) on the density of rectangular specimens of iron powder. The results demonstrate that the densification of the iron powder depends on the scanning pattern and the effect is less pronounced for specimens with high dimensional ratio Y/X. Furthermore, higher sintered density was obtained when “Sorted” scanning pattern in X-direction (short scan vector) was used. In fact, the scan vector length strongly influences the thermal history of the part in such a manner that, the sintered density was higher using short vector length (X-direction) (Simchi and Pohl, 2003). It should be noted that the scan vector length influences the development of thermal stresses as well. These residual internal stresses reduce part performance. They also produce warp, loss of edge tolerance and delamination in parts (Li et al., 2000). Therefore, in laser sintering it is always preferred to use short vector length (X-direction).

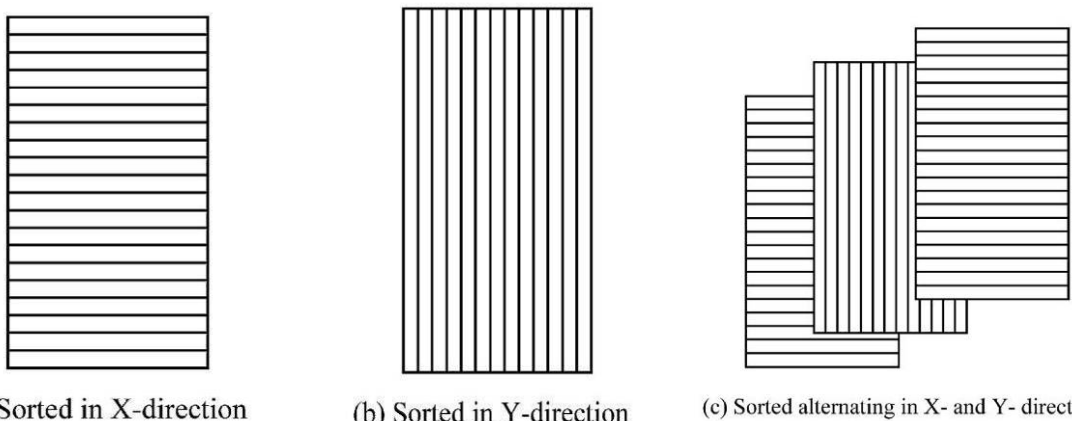


**Fig. 2.10:** Schematic of scanning patterns used in the mentioned study for direct laser sintering of iron powder (the scan line distance in X- and Y- direction is equal): (a) short raster pattern in X- direction; (b) long raster pattern in Y-direction; (c) alternating from layer to layer, starting with a short raster pattern for the first layer (Simchi and Pohl, 2003).

### 2.2.3. Environment

Dust and smoke, vibration, and extreme temperatures can adversely affect laser operation. A careful assessment of the operating environment must be made. Suitably designed lasers should be used, and steps need to be taken to isolate sensitive lasers from unfavourable conditions (Ready and Farson, 2001). The influence of sintering atmosphere on the densification of iron powder is shown in Fig. 2.11. It appears that sintering in an argon atmosphere leads to a slightly better densification than nitrogen (though the effect of sintering atmosphere is not very significant especially when compared to the other parameters). In fact, the absorption of nitrogen in the iron liquid during the laser processing may serve some influence (Simchi, 2006).

The impact of sintering atmosphere on the densification could also be related to the amount of available oxygen during sintering. It is known that the presence of oxygen allows the formation of surface oxides and slag when the powder particles are heated and melted by the scanning laser beam. The formation of oxide layer on the surface of powder particles significantly increases the absorption rate of CO<sub>2</sub> laser radiation (Simchi, 2006, Simchi and Pohl, 2003). This changes the temperature-time history of sintering and increases the melt volume, allowing surface tension become more dominant. Another concern is the liquid metal surface tension, which influences the wetting angle between the solid and the liquid phases that can disrupt bonding between raster lines and individual layers (Nickel et al., 2001).

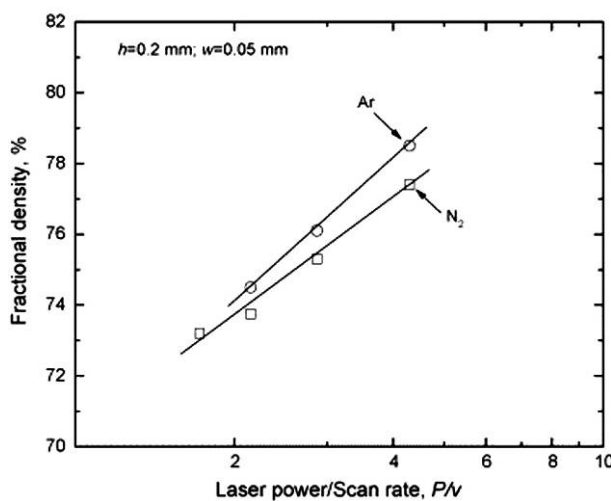


**Fig. 2.11:** Effect of scan vector length on the fractional density of laser sintered iron ( $D_{50} = 41 \mu\text{m}$ ) (Simchi, 2006).

## 2.3. Effects of Laser-Material Interaction

### 2.3.1. Laser induced compression and vaporisation

The power densities exerted by short laser pulses are high enough to cause even reflective materials to rapidly reach the vaporisation temperature. This vaporisation may induce such immense pressures which result in a shock wave as illustrated in Fig. 2.12 (O'Neill et al., 1999) and Fig. 2.13 as well (Chang and Na, 2002). The shock wave is responsible for the recoil forces which act in the opposite direction. Thus, this recoil pressure is considered as laser induced compression. When the energy intensity is high, such as is the case with a small beam diameter, the recoil pressure is greater resulting in blast removal of the powder (O'Neill et al., 1999).

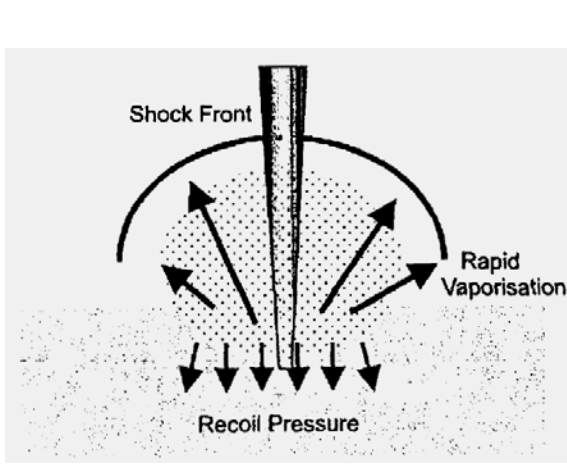


**Fig. 2.12:** Laser induced shock waves using Q-switched laser light (O'Neill et al., 1999).

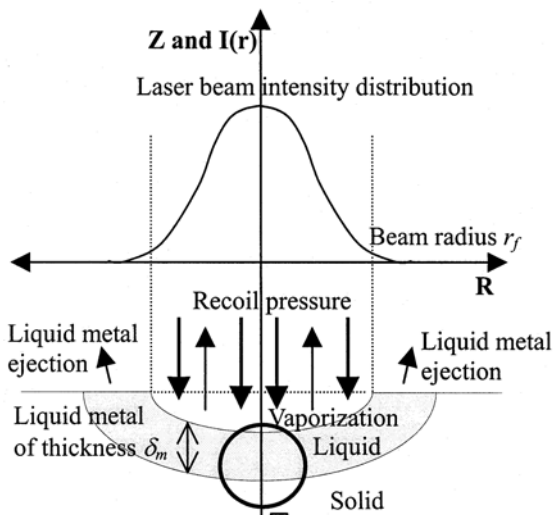


**Fig. 2.13:** Physical model of melt removal from the interaction zone (Chang and Na, 2002).

### 2.3.2. Laser absorption

Understanding of the absorption mechanisms plays an important role to determine the optimum processing parameters and conditions in laser processing of metals. The absorptance, the fraction of the incident laser light which is absorbed, depends on a number of different variables related to laser source and material. These variables include laser properties (such as wavelength, polarisation, angle of incidence, and intensity), material properties (such as chemical composition, temperature, roughness/topography, oxide layers), and contaminations (e.g. dust, dirt, bulk defects, etc) (Bergström et al., 2007, Silva et al., 2000).

Fig. 2.14 demonstrates some of the complexities of photon absorption by an engineering grade metal surface. The part surfaces have roughness characteristic, covered by an oxide layer. The surface roughness can result in multiple reflections, which involve multiple absorption events (Fig. 2.14b). Surface roughness can also affect the incoming radiation in absorption events at high angles of incidence. This can result in very high local absorptions. The oxide layer may absorb the beam in its own right or may be responsible for multiple reflections or wave guiding (Fig. 2.14c). In addition to these effects, the surface may be contaminated by materials having a higher absorptance than the underlying metal (Bergström et al., 2007).

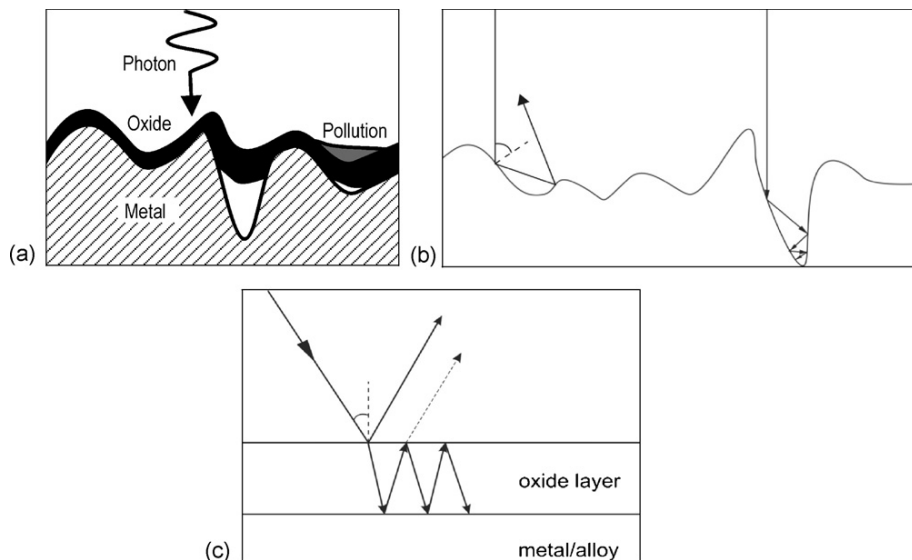


**Fig. 2.14:** Some of the mechanisms which increase the absorptivity of real engineering surfaces: (a) typical cross section of an engineering surface; (b) high angle absorptance and multiple reflections due to surface roughness and (c) multiple reflections within an oxide layer (Bergström et al., 2007).

## 2.4. Powder Consolidation

### 2.4.1. Sintering

Rapid manufacturing of metals can be carried out using processes involving powder spray and direct SLS providing high energy for melting and flow of liquid metal rather than solid-state sintering (which is too long to complete). For pressureless sintering, a reduction in total surface area is the only driving force for the densification of the powder mass. Sintering is, in fact, described by neck growth in a two-particle system (Bourell, 2006). Fig. 2.15 illustrates the characteristic of laser sintered tracks of stainless steel powder with various laser powers. As seen, increasing laser power (in Fig. 2.15b) forms a sintering necks between the neighbouring spherical-shaped sintered agglomerates, and establishes an inter-agglomerate bonding (Gu and Shen, 2009b).

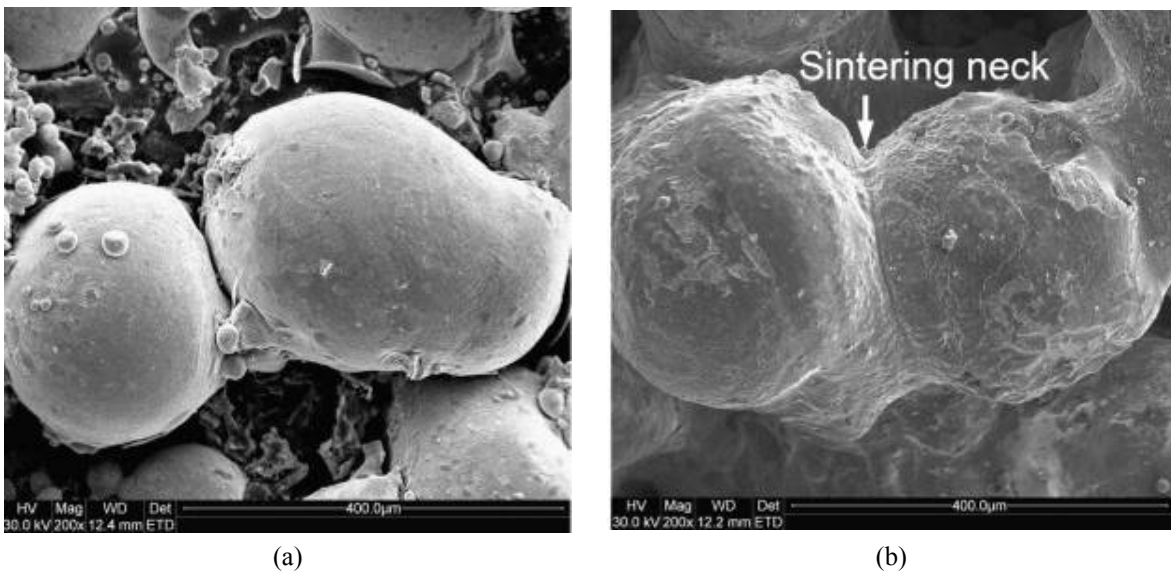


**Fig. 2.15:** SEM images showing typical microstructures of laser sintered tracks at different laser powers: (a)  $P = 350$  W; (b)  $P = 400$  W. Fixed parameters are  $v = 0.04$  m/s and  $t = 0.25$  mm (Gu and Shen, 2009b).

#### Mechanism of sintering: coalescence of spheres

The amount of liquid formation depends on the operating temperature of the sintering system, which is controlled by two main parameters, i.e., laser power and scan speed, during a single line scanning. The molten materials tend to aggregate into an individual sphere with a size of about the diameter of laser beam. The stage of sintering is schematically depicted in Fig. 2.16 (Gu and Shen, 2009b).

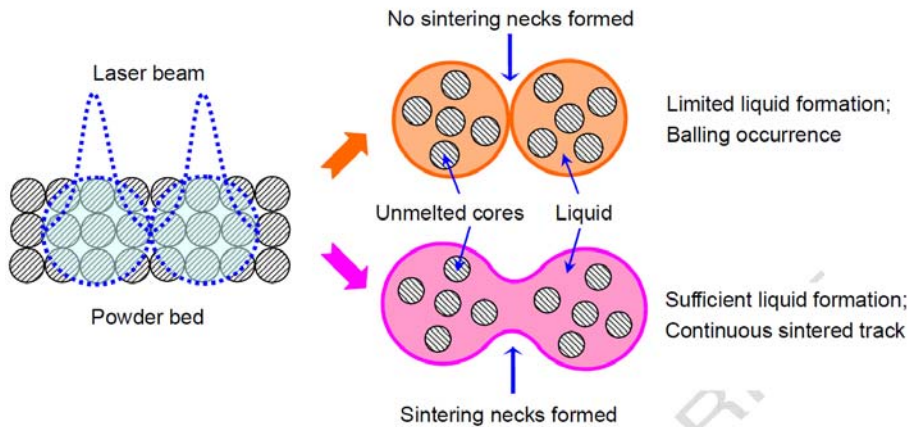
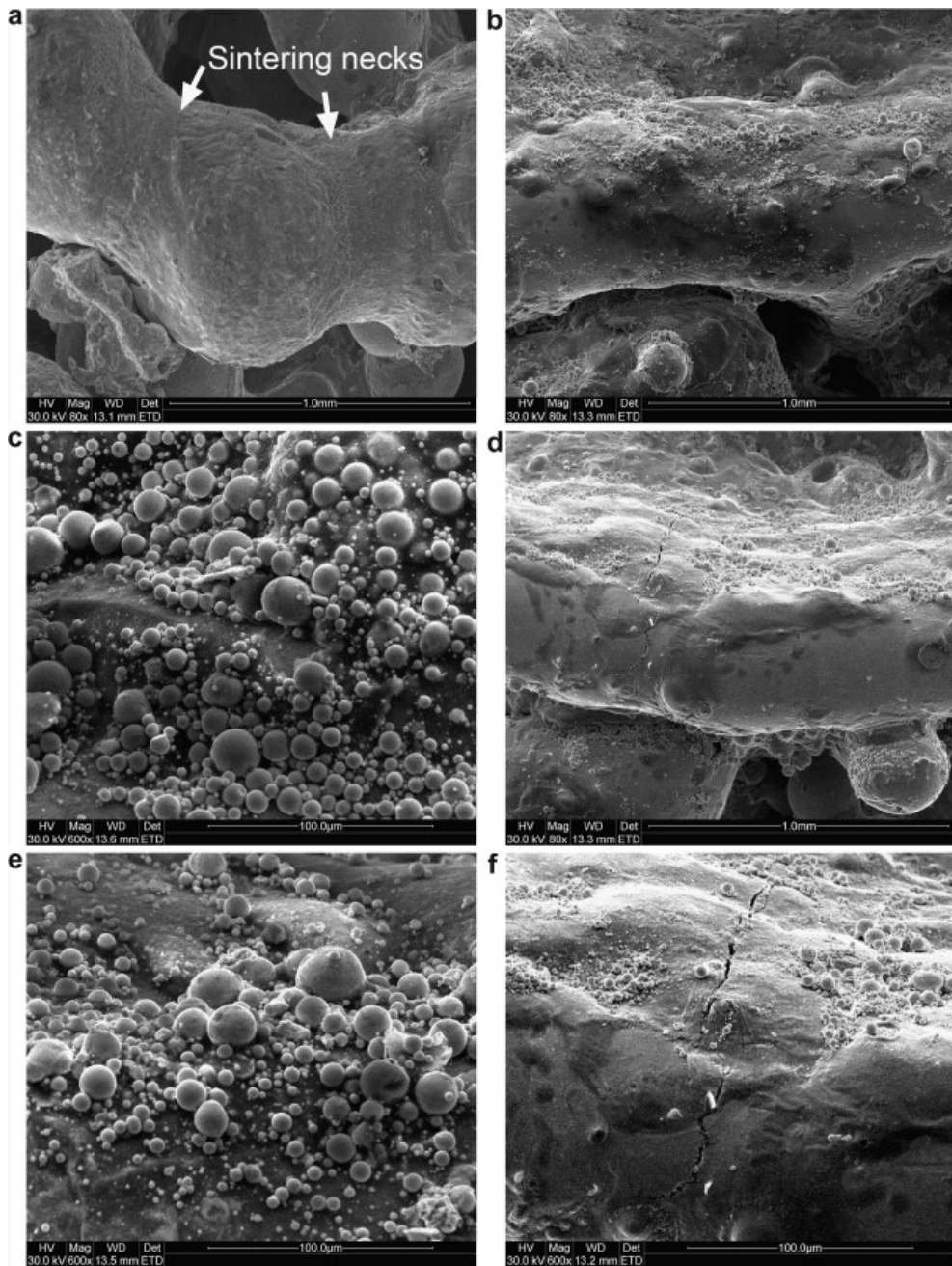


Fig. 2.16: Schematic of sintering by coalescence phenomenon caused by limited liquid formation (Gu and Shen, 2009b).

When a sufficient amount of liquid phase (in relatively high laser powers and speeds) is generated, the melt instability may increase. Under this condition, some small droplets may splash from the surface of the molten track, due to a reduction in the surface energy of liquid at a very short time. After solidification, a large amount of micrometer-scaled spherical splashes are formed around the sintered surface (Fig. 2.17b-e). At higher scan speeds, a significantly bigger instability of the liquid cylinder tends to alter its shape to reduce the surface energy. This causes the breaking up of the molten cylinder and producing longitudinal cracks after solidification (Fig. 2.17d and f) (Gu and Shen, 2009b).



**Fig. 2.17:** SEM characterisation of laser sintered tracks at different scan speeds: (a)  $v = 0.05 \text{ m/s}$ ; (b)  $v = 0.07 \text{ m/s}$ ; (d)  $v = 0.10 \text{ m/s}$ . (c) is local magnification of (b). (e) and (f) are local magnifications of (d).  $P = 400 \text{ W}$  and  $t = 0.25 \text{ mm}$  are constant (Gu and Shen, 2009b).

#### 2.4.2. Melting pool, rapid solidification, and potential defects

The final phases and consequently final properties of laser processed materials are affected by rapid cooling due to SLM, when metal powders are melted and consolidated from high temperature at a very short interval of time. This can lead to various issues for metal materials to densify properly and bond smoothly in the layer-by-layer building

process. The typical defects such as porosity, hot tear, balling and residual stress can be potentially generated and associated with SLM process. Thus, this section briefly reviews melting pool characteristics, effects of rapid solidification on material microstructure and properties, and defects appearing in laser melting solidifications.

#### 2.4.2.1. Formation of the melting pool

Radial temperature gradients on the order of  $10^2\text{-}10^4$  K/mm develop between the centre of the melt pool and the cooler solid/melt interface. In most materials, the coefficient of surface tension increases with a decrease in temperature, driving fluid flow from the centre of the melt towards the edges (Marangoni flow: Certain elements invert the relationship between surface tension and temperature leading to a reversal of the fluid flow geometry). Marangoni flow is the dominant convection mechanism in a laser melted pool (Ion, 2005b). Fig. 2.18 is a schematic drawing of the molten pool and the laser trace, showing the geometrical relationship between the beam travel velocity and the local solidification rate. In the surface-melting processes, the local solidification rate can be assessed quantitatively from the shape of the molten pool (Takeshita and Matsunawa, 2001). The laser melting cooling rates can be estimated over  $10^4$  K/s (Lavernia and Srivatsan, 2010). Fig. 2.19 schematically demonstrates a severe convection existing in the melt pool and influencing the solidification behaviour significantly. The shape of the keyhole dictates the flow field and, in turn, may alter the microstructural characteristics. The motion of the solid/liquid interface occurs unsteadily, leading to fluctuating growth rates, although the scanning velocity is steady (Mohanty and Mazumder, 1998).

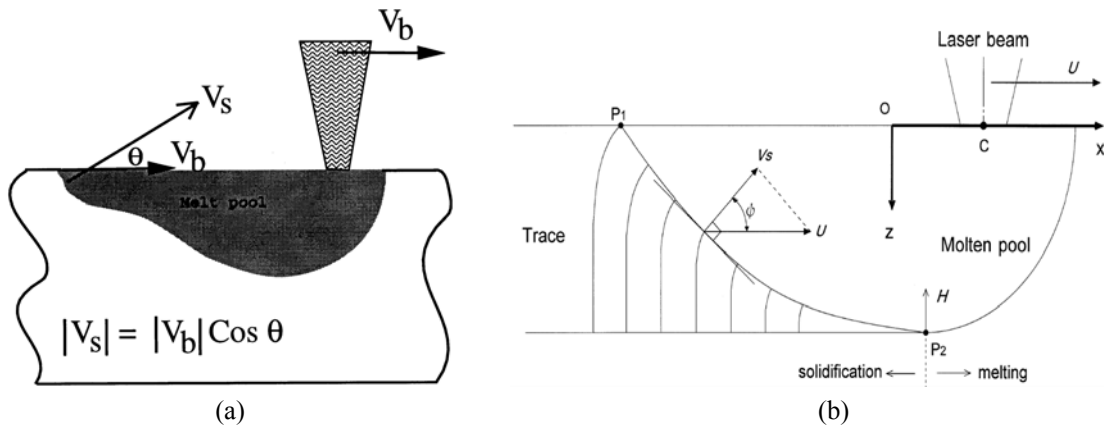


**Fig. 2.18:** Schematic drawing of (a) laser surface melting (Mohanty and Mazumder, 1998) and (b) the central longitudinal section of the molten pool and resultant laser trace (Takeshita and Matsunawa, 2001).

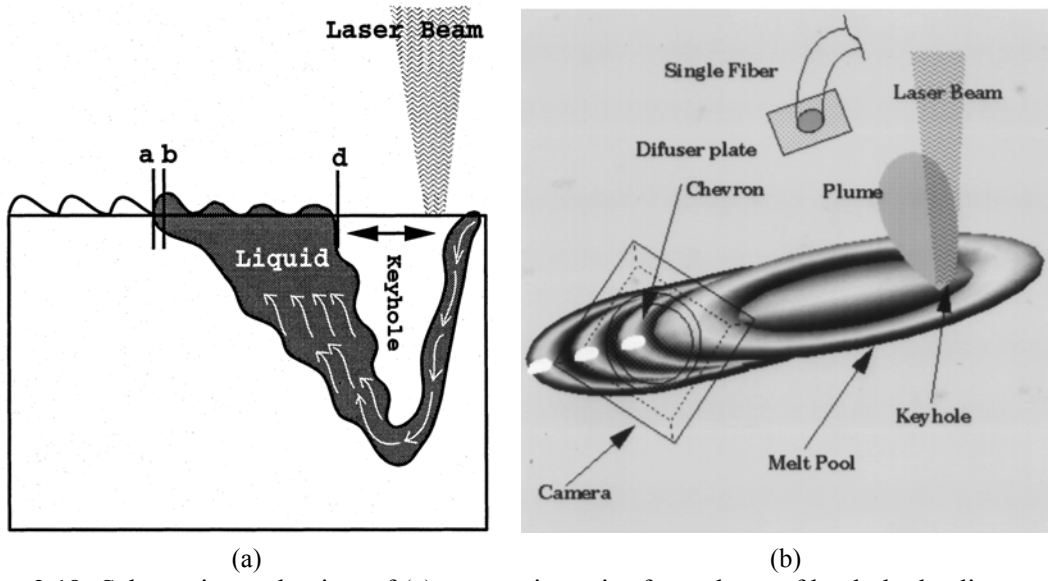


**Fig. 2.19:** Schematic mechanism of (a) convection arise from shape of keyhole, leading to (b) unsteady and discrete solidification conditions (Mohanty and Mazumder, 1998)

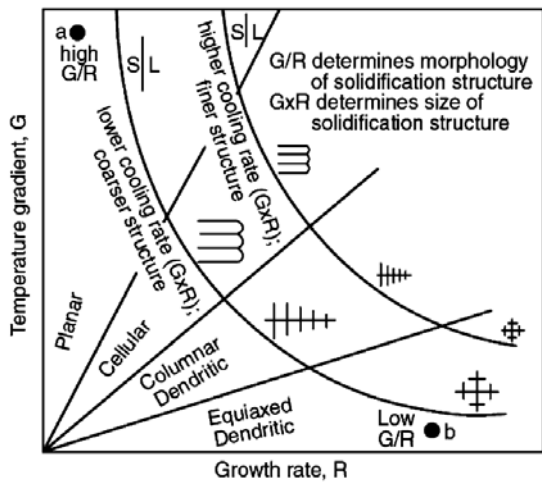
#### 2.4.2.2. Effect of rapid cooling and solidification on microstructure

Temperature gradient within the molten pool controls cooling rates and influences solidification microstructures. With relatively low cooling and solidification rates, primary solidification products may be estimated from equilibrium phase diagrams. However, cooling rates during laser surface treatment are significantly higher.

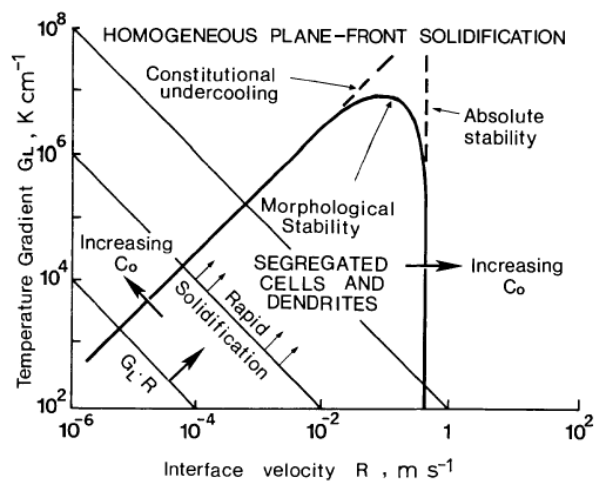
The rapid extraction of thermal energy that occurs during rapid solidification causes a large deviations from equilibrium, and offers some important advantages including: (i) a refined microstructure (very small grain size and fine precipitates), (ii) extension of solid solubility, even by orders of magnitude, (iii) increased chemical homogeneity (reduced segregation, uniform distribution of secondary phase particles), and (iv) formation of metastable (crystalline, quasicrystalline, amorphous) phases (Birol, 1996, Lavernia and Srivatsan, 2010).

Four different types of reaction can occur during rapid solidification associated with laser surface melting: amorphous glass formation; primary crystallisation; massive or polymorphous crystallisation; and eutectic crystallisation. Conditions for the formation of amorphous structures have been calculated; these are material dependent but indicate that a cooling rate on the order of  $10^6$  K/s is required in alloys of iron and boron (Ion, 2005b).

Planar, cellular, dendritic or eutectic solidification fronts may form (Fig. 2.20a); depending on the temperature gradient ( $G$ ), the rate of growth (or solidification) ( $R$ ), and solute concentration gradients. The ratio ( $G/R$ ) should be large for a stable planar front solidification mechanism. Fig. 2.20b introduces the concept of "absolute stability" when the solidification rate,  $R$ , is so large that there is insufficient time for diffusion (Ion, 2005b, Steen, 1991).



(a)



(b)

**Fig. 2.20:** Effect of temperature gradient  $G$  and growth (solidification) rate  $R$  on (a) the formation of various solidification microstructures (Chowdhury et al., 2011), and (b) absolute stability in change from planar to unstable growth: at low growth (interface velocity) rates, the solute destabilises the planar front growth, whereas, at higher growth rates, surface energy has a stabilising effect (Lavernia et al., 1992).

Higher undercooling due to laser processing leads either to partitionless solidification of one or the other phase (and even may lead to a featureless microstructure) or to the formation of a crystalline phase that is not one of the equilibrium phases in the system (Birol, 1996, Ready and Farson, 2001). It would, therefore, be extremely useful to predict what microstructures would develop under certain processing conditions so that the optimum microstructure could be selected by the appropriate choice of laser processing parameters. Several researchers have developed microstructural maps with the aim of providing this type of information. An example of such a map is given in Fig. 2.21 for an Al rich binary Al-Fe alloy. The solid lines in the figure indicate results of experimental observations, whereas the dashed lines indicate calculated values from solidification models (Toyserkani et al., 2005).

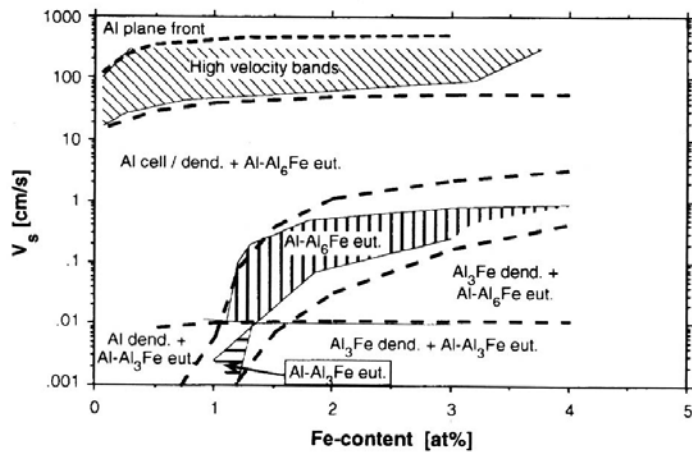


Fig. 2.21: The type of microstructure observed (solid lines) and predicted (dashed lines) in an Al-Fe binary alloy as a function of solidification rate and Fe content (Gilgien et al., 1995, Toyserkani et al., 2005).

### 2.4.2.3. Potential defects in the SLM parts

#### 2.4.2.3.1. Porosity formation

Even when the particles are completely melted in the SLM process, porosity can be found due to trapped gas, shrinkage, and etc, harming mechanical properties. Adjustments of the laser processing parameters can improve the densification above 90% of the theoretical full density values. Porosity as a major problem in consolidation originates from the short material heating times caused by the scanning laser beam, relative to the time required for consolidation and the fact that there is no mechanical pressure (as in moulding processes). Post-processing is then required if a pore-free material is needed (Kruth et al., 2007).

Shrinkage microporosity in alloys is a result of a lack of feeding of the mushy zone, i.e. the density increase associated with solidification cannot be fully compensated by an interdendritic fluid flow (Fig. 2.22) (Campbell, 2003). Gas is another common source of porosity. If porosity is found in any atomised powder, the first suspicion can be gas solution in the melt, normally hydrogen, but possibly oxygen or steam. This defect usually occurs due to a reduction in solubility limit of gases such as hydrogen or nitrogen with decrease in temperature. In other words, with decrease in temperature, gas actual composition in the liquid increases and might exceed their solubility limit at some point, leading to pore nucleation (ASM International Handbook Committee, 1998).

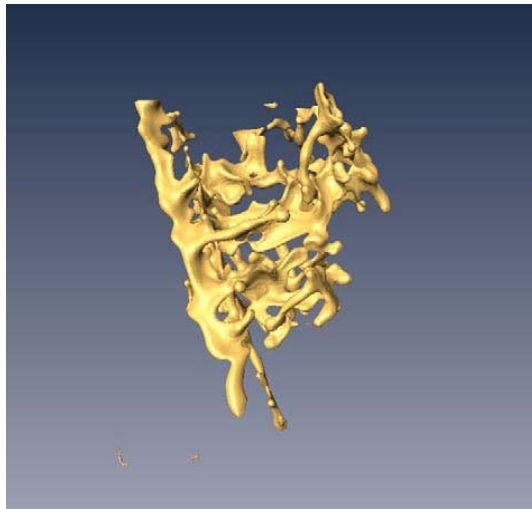


**Fig. 2.22:** Three-dimensional high-resolution X-ray tomography of a shrinkage porosity formed in an Al–4.5 wt% Cu alloy (Asta et al., 2009).

#### 2.4.2.3.2. Hot tearing

If microporosity is the major defect in shape casting, hot tearing is certainly the major defect of continuous or semi-continuous casting processes and of welding. In fact, hot tear is a tensile creep-fracture, created when the solid cools and shrinks, and develops due to the thermal stresses originating from the differences in thermal expansion (Asta et al., 2009, Ashby, 2005, Fox et al., 2008). The hot tear most likely occurs where a narrow cross-section is joined to a large cross-section.

#### 2.4.2.3.3. Balling

Balling can be a particular issue associated with the SLM process. The balling occurs when the molten material does not wet the underlying substrate due to the surface tension, which tends to spheroidise the liquid. This results in a rough and bead-shaped surface (Fig. 2.23c). The pool of molten metal must wet the previously processed metal below it. And when it solidifies, its upper surface must be flat enough to enable a next layer of powder to be spread over it (Abe et al., 2001). For example, Fig. 2.23a shows an ideal wetting angle to reach a good result from laser melting (Toyserkani et al., 2005). Accordingly, the low wettability leads to not solid parts exhibiting a tendency of the melted powder to ‘ball up’ (Abe et al., 2001).

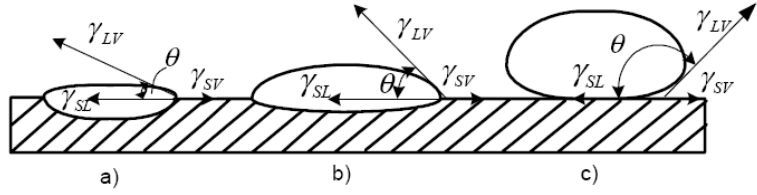


**Fig. 2.23:** Associated wetting angle and interfacial free energies: a) high dilution, well wetting, and ideal for full melting b) ideal clad, c) no dilution, and non-wetting (Toyserkani et al., 2005).

During SLM process, a temperature gradient in the molten pool will be formed. The temperature gradients in the molten pool can increase surface tension as well as Marangoni convection. This results in balling to minimise surface free energy. This means formation of spheres to reduce the surface area, as shown in Fig. 2.24 (Simchi and Pohl, 2003). In addition to huge temperature gradient between the melting powder and the adjacent powder, the low viscosity of the material can lead to balling effects (Klocke and Wagner, 2003).

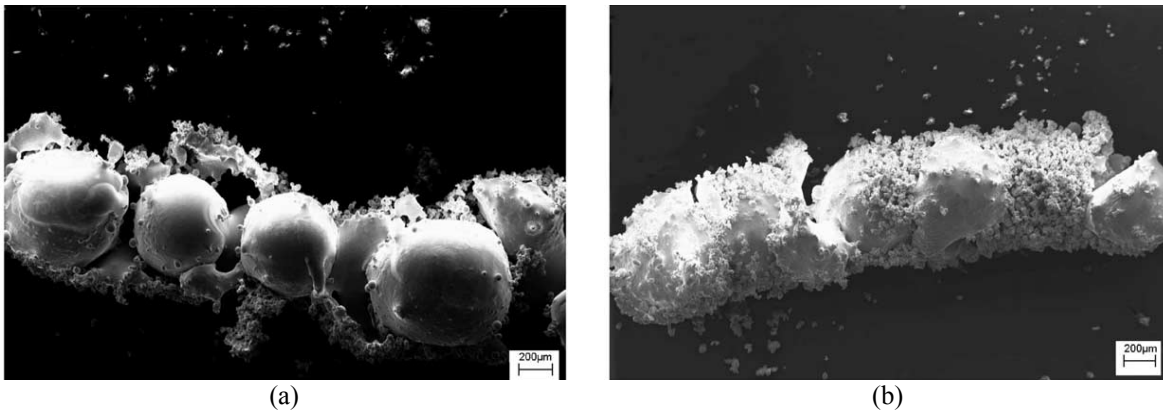
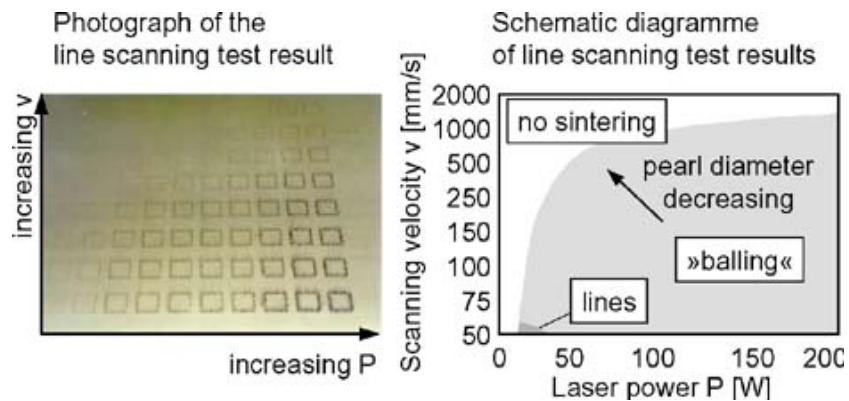


Fig. 2.24: SEM micrographs of iron powder after single line laser scanning ( $P = 215 \text{ W}$ ,  $v = 50 \text{ mm/s}$ ,  $N_2$  atmosphere, ambient powder bed temperature): (a) top view and (b) side view of metallic balls (Simchi and Pohl, 2003).

Generally, both materials properties and processing variables can influence wettability and consequently balling (Kruth et al., 2007). Also, as liquid metals do not wet surface oxide films in the absence of a chemical reaction, it is very important to avoid oxidation. Therefore sufficient remelting of the previous layer is necessary to remove surface contaminants, to break down oxide films, and to provide a clean solid–liquid interface at the atomic level. Another possibility to improve wetting is addition of certain alloying elements, like phosphor in selective laser melting of iron-based powder (Kruth et al., 2004). Finally a last method to suppress balling is applying very high pulse energies.

Figs. 2.25 and 2.26 exhibit the results of laser sintering experiments on stainless steel. Three different process behaviours can be observed: no sintering, balling (unconnected welding pearls) and closed lines (connected material). Zoomed areas of the photograph from Fig. 2.25 are shown in Fig. 2.26. It can be seen that low scanning velocity and low laser power promote the development and formation of semisolid conditions in the process zone, improving the bonding of stainless steel powders. That means the slow scanning velocities in combination with low laser powers are suitable to reduce balling effects, due to the moderate heating and uniform temperature distribution. These conditions lead to semi solid metal with high viscosity allowing viscous sintering instead of balling (Klocke and Wagner, 2003).



**Fig. 2.25:** Result of line scanning test (Klocke and Wagner, 2003).

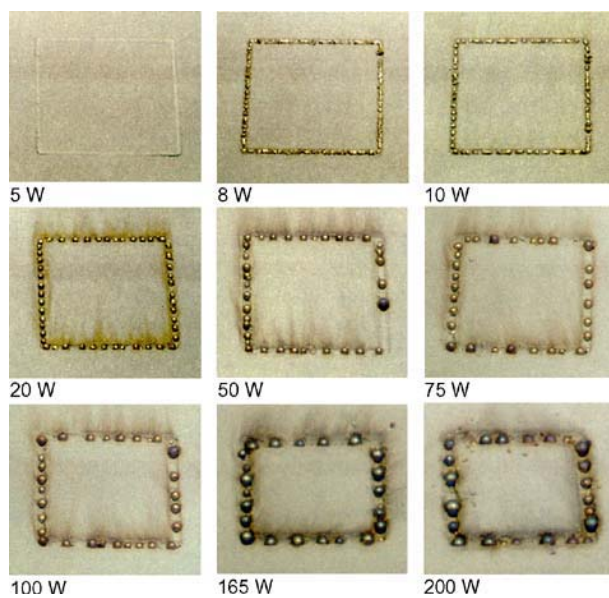


**Fig. 2.26:** Effect of laser power on balling mechanism ( $v = 50 \text{ mm/s}$ , square dimension:  $10 \times 10 \text{ mm}^2$ ) (Klocke and Wagner, 2003).

Kruth et al. (2004) have sketched a process window for selective laser melting of iron powder shown in Fig. 2.27. This process window illustrates that high scan speeds combined with high laser powers result in less balling attributed to the melt pool which rapidly solidifies behind the laser spot, while the length of the molten track remains in an appropriate degree.

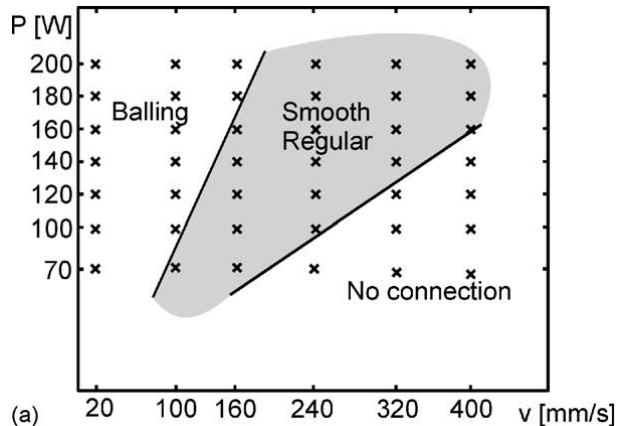


Fig. 2.27: Process window for selective laser melting of iron-based powder in continuous wave operation (Kruth et al., 2004).

#### 2.4.3.2.3. Residual stress

One major issue associated with the SLM is the residual stress remaining inside the parts and causing delaminations, cracks and deformation and also reduction of fatigue strength when tensile stress remains in the part. Laser based processes (laser welding, SLM, etc) are known to introduce large amounts of residual stresses, due to the large thermal gradients which inherently exist in the processes. Two mechanisms can be distinguished which cause residual stresses. The first mechanism is called the temperature gradient mechanism (TGM, Fig. 2.28a). Due to the rapid heating of the upper surface by the laser beam and the rather slow heat conduction, a steep temperature gradient develops. Since the expansion of the heated top layer is restricted by the underlying material, a compressive strain will be created. So, in the absence of mechanical constraints, a counter bending away from the laser beam may occur. The second mechanism, creating residual stresses in SLM, is due to the shrinkage of the molten layer(s) during cooling. With regards to this shrinkage, the newly deposited layer will be subjected to tensile stresses, creating compressive stresses at the bottom (Kruth et al., 2004, Mercelis and Kruth, 2006).

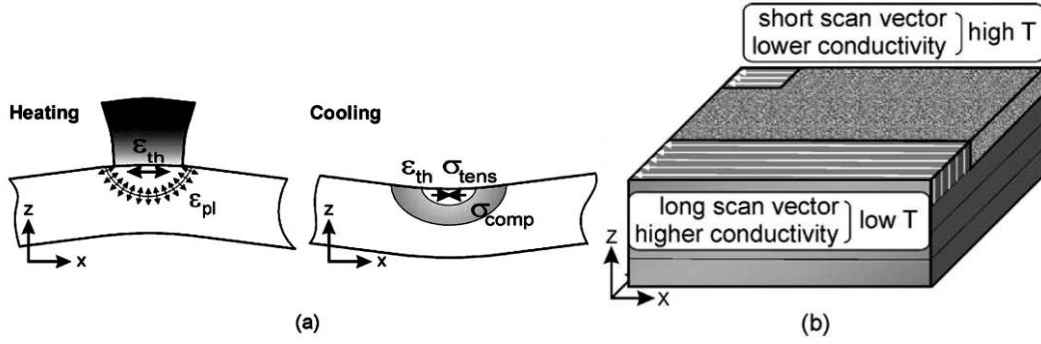


Fig. 2.28: (a) Temperature gradient mechanism, (b) different temperatures through different scan vector lengths (Kruth et al., 2004).

In general, a small scanning area leads to high temperatures (see Fig. 2.28b). For larger areas the laser beam travel much longer distances, resulting to a lower temperature of the scanned area. Consequently lower wetting may happen, leading to a lower density of the material (Kruth et al., 2004). Accordingly, different scanning strategies and part sizes can lead to various residual stresses. For example, different scanning strategies and applied parameters, shown in Fig. 2.29, lead to various residual stresses and consequently part curvature. It has been reported that scanning along the  $X$ -direction-(1) resulted in the smallest curvature in that direction, but the largest curvature in the  $Y$ -direction (vice versa for the  $Y$  scanned part (2)). Applying the sector wise scanning (3)–(6) resulted to less deformation, though there are relatively small curvatures along  $X$ - and  $Y$ -directions. No significant difference of curvature between the 3 to 6 sector strategies can be found. Nevertheless, because of the shorter scan length (higher temperatures) a less laser energy input can be applied to obtain the same melting behaviour and the same temperature. This would further reduce the deformations caused by the TGM, which increase the benefits of smaller sectors. In fact, the exposure strategy to fuse the powder layers influences the residual stress significantly (Kruth et al., 2004, Mercelis and Kruth, 2006).

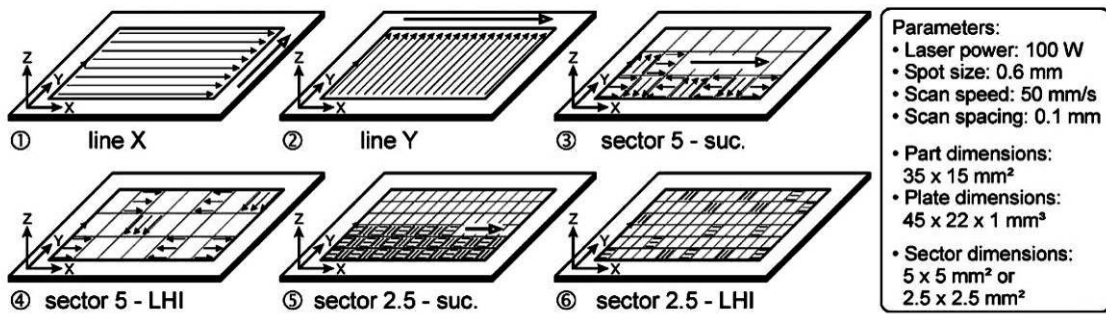


Fig. 2.29: The six different scanning strategies used in the comparison (Kruth et al., 2004).

With regards to commonly unfavourable influences of residual stress on final quality of the parts, reduction of the residual stress arise from laser processes is usually desirable. The following instructions can be helpful to reduce residual stress (Kruth et al., 2004, Mercelis and Kruth, 2006, Shiomi et al., 2004):

- 1- Part removal drastically relieves the residual stresses which are present in the part. The residual stress after removal consists of a zone of tensile stress at the upper and lower zone of the part and a compressive stress zone in between. The stresses after part removal are much smaller than before part removal.
- 2- In general, the stresses are larger perpendicular to the scan direction than along the scan direction. A subdivision of the surface to smaller parts reduces the residual stress level.
- 3- Increasing of additive layers increases the residual stress.
- 4- It is possible to reduce the stress level by applying a post heat-treatment.
- 5- Heating of the substrate plate results in a reduction of the residual stress level. This can be attributed to a reduction in temperature gradients due to heating of subsurface plate.
- 6- Some post processing such as hot isostatic pressing (HIP), shot pinning, and etc can assist to reduce tensile residual stress.

## 2.5. Characterisation of Density and Porosity

Final density (the ratio of the density of a powder metallurgy (P/M) material to that of its wrought counterpart) has the greatest effect on mechanical properties of P/M materials. Powder metallurgy parts with theoretical densities less than 75% are considered to be low density, those above 90% are high density, and those in between are classified as medium density. As shown in Fig. 2.30, illustrating the effects of density on the mechanical properties of as-sintered nickel steels, mechanical properties generally improve with increase in density (higher density in sintered steels resulted in higher tensile strength, elongation, and impact resistance values). In other words, any residual porosity will have a harmful influence on both the elastic properties and strength (ASM International Handbook Committee, 1998). Moreover, physical properties of material can be affected significantly with the degree of porosity. For example, thermal conductivity decreases with porosity rate in P/M materials (Kurt and Ates, 2007, Sastry et al., 2004).

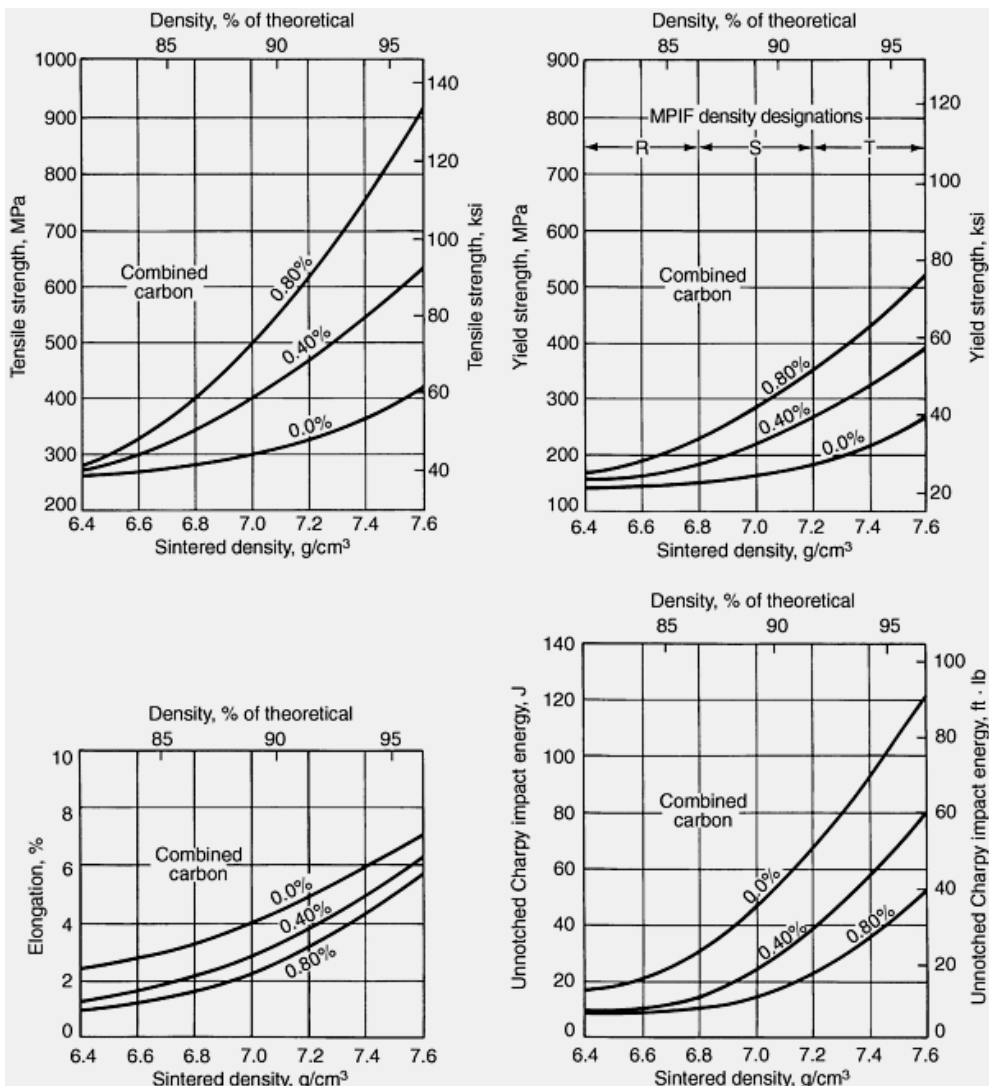


**Fig. 2.30:** Effects of density on mechanical properties of as-sintered 4% nickel steel. The processing includes pre-sintering and re-pressing of material above  $6.6 \text{ g/cm}^3$  (ASM International Handbook Committee, 1998).

On the other hand, porosity is a very common defect in laser processed materials due to short consolidation time and no mechanical pressure (Kruth et al., 2007). Thus, porosity measurement plays an important role to qualify the parts fabricated by laser melting. This section briefly explains some methods to evaluate the porosity. It should be noted that the calculation of porosity can be carried out on the base of density ( $\rho$ ) regarding Eq. 2.3 (ASM International Handbook Committee, 1998):

$$\text{Porosity (\%)} = \frac{\rho_{\text{pore-free}} - \rho_{\text{measured}}}{\rho_{\text{pore-free}}} \times 100 \quad (\text{Eq. 2.3})$$

### 2.5.1. Calculating the density from dimension and mass

Density is the ratio of mass to volume ( $\rho = m/v$ ). The volume could be calculated easily using simple geometrical shapes such as cubes (Fig. 2.31) or right cylinders (the dimensions can be measured after machining process). From volume, density can be easily evaluated with regards to the weight of a part. This yields a value that, under ideal conditions, differs by 0.04 g/cm<sup>3</sup> (0.5%) with the actual density (ASM International Handbook Committee, 1998).

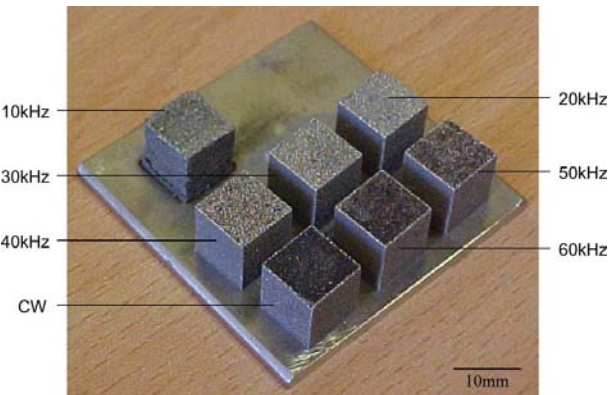
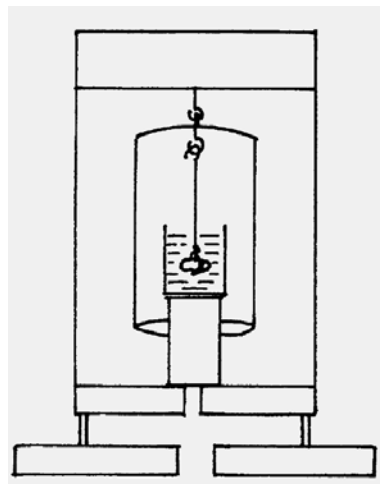


Fig. 2.31: Array of cubes produced in an experimental run. Cubes are produced at varying laser pulse repetition frequencies to study density of material (Morgan et al., 2004).

### 2.5.2. Methods based on Archimedes' principle to measure density.

There are methods of measuring density on the basis of Archimedes' principle, in which hydrostatic forces in liquids exert buoyant forces proportional to the part volume. This measurement is standardised in ASTM B 311 (2005), as illustrated in Fig. 2.32. When an object is immersed in a liquid, the liquid exerts an upward buoyant force that is equal to the product of the object volume and the density of the liquid. The difference in weight between an object weighed in air and its weight when suspended in water is equal to the object volume in cubic centimeters times the density of water. The drawback of this method is that it has only been developed for low amount of porosity, since not sealed pores will absorb some of the water. This will decrease its buoyancy and exhibit an erroneously high density.



**Fig. 2.32:** Method for weighing in water (ASTM Standard B311, 2005).

### 2.5.3. Porosity measurement on the basis of metallographic examinations

The amount of porosity can be revealed by using metallographic techniques. Careful metallographic preparation is significant in the analysis of sintered structures because the shape of the porosity is as important as its amount. Proper polishing should open the smeared pores revealing their true shapes and area fractions. The image analysis on metallographic images can significantly assist the density measurements. The area fraction of porosity is equal the volume fraction of porosity, and must be equal to the porosity calculated from Eq. 2.3 relating the actual measured density and pore-free density of a uniformly dense part (ASM International Handbook Committee, 1998).

### 2.5.4. Non-destructive testing (NDT) to measure porosity

Non-destructive testing (NDT) experiments are a wide group of analysis techniques and can be employed to evaluate porosity of components without damaging them. The common NDT methods to evaluate porosity include methods such as ultrasonic, magnetic-particle, liquid penetration, radiographic, etc.

For example, Fig. 2.33 schematically shows the basic elements of radiography include a radiation source, the test piece or object being evaluated, and a sensing material. The test piece is a plate of uniform thickness containing an internal flaw that has absorption characteristics different from those of the surrounding material. Radiation from the source is absorbed by the test piece as the radiation passes through it; the flaw and surrounding

material absorb different amounts of radiation. This produces an image, or shadow, of the flaw on the sensing material. A typical example of voids detected by radiographic technique has been shown in Fig. 2.34 (ASM Handbook, 1992).

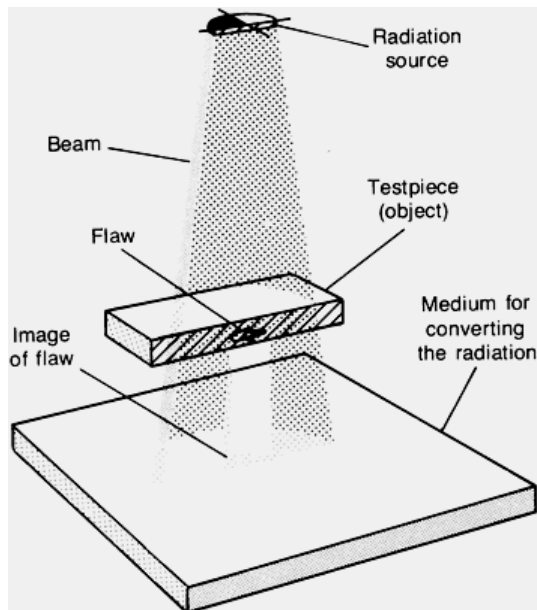


**Fig. 2.33:** Schematic of the basic elements of a radiographic system showing the method of sensing the image of an internal flaw in a plate of uniform thickness.

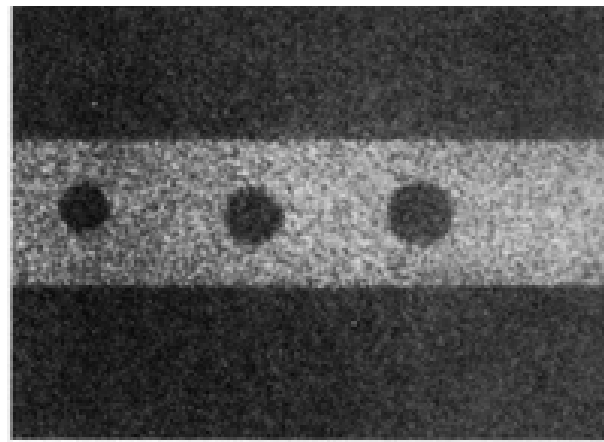


**Fig. 2.34:** A typical radiographic picture.

---

# **Chapter 3: Developments of SLM of Metal Alloys and MMCs**

---

The development of SLM has been driven by the need to produce near dense components with comparable mechanical properties to those of bulk materials, and by the desire to avoid lengthy and costly post processing cycles. All metals may be considered as candidate materials, however, different processing behaviour (e.g. laser absorption, surface tension and viscosity of the liquid metal, etc) influences their applications. For each new material, a processing window (e.g. Fig. 2.27) needs to be assessed with various experiments, in order to ovoid scan track instabilities (sphereodisation of the liquid melt pool, also known as “balling”) as well as porosity (Kruth et al., 2005). Research on the SLM of metal powders such as iron, tool steels, titanium alloys, nickel based alloys, cobalt based alloys, and aluminium have been reported.

Moreover, as a powder based process, SLM provides an outstanding opportunity to consolidate second or multiple material particles with metal powders to form novel metal matrix composites and their products. The additional material elements influence the SLM process and relevant consolidation behaviour, as well as the microstructure and the properties of the resulting MMCs. Hence, there are increasing research attempts to develop SLM process for the fabrication of MMCs.

## **3.1. SLM of Advanced Metal Alloys**

During the last decade, there has been an increasing research work to develop SLM process of advanced metallic alloys including steel, cobalt, nickel, titanium and aluminium based alloys. This has also been driven by the broad industrial applications of advanced metallic parts made by SLM process.

SLM of steel alloys have been subjected to an extensive research. A fundamental study have illustrated that the alloying elements (e.g. oxygen, carbon, silicon, titanium and copper) can affect the binding and melting pool stability in SLM of steel powders, attributed to their influence on physical phenomena of the process such as laser absorption, heat transfer, wetting and spreading of the melted material, oxidation, Rayleigh instability

and Marangoni convection (Rombouts et al., 2006). Experimental studies on M2 high speed steel, 316L and 314S-HC stainless steels have confirmed that variations of layer mass with scan speed are not consistent with what is expected from the delivered energy to the powder bed. In fact, the thermal history of processing is influential in determining the amount of melted material under a laser beam irradiation (Badrossamay and Childs, 2007).

Some research has dedicated to improve density of steel parts, e.g. it has been reported that the higher laser power, lower scan speed, narrower hatch spacing and thinner layer thickness could enable a much smoother melting surface and consequently a higher densification in SLM of 316L stainless steel (Li et al., 2010). There are also some efforts to improve functionality through the SLM of steel powder mixtures. For instance, an experimental study on the SLM of austenitic and martensitic stainless steel powder mixtures with varying composition ratios has shown that various powder mixtures influence the laser consolidation mechanisms. The microstructural studies, shown in Fig. 3.1, demonstrate that a new stainless steel grade can be produced via the SLM process to have tailored mechanical and magnetic properties (Jerrard et al., 2009b).

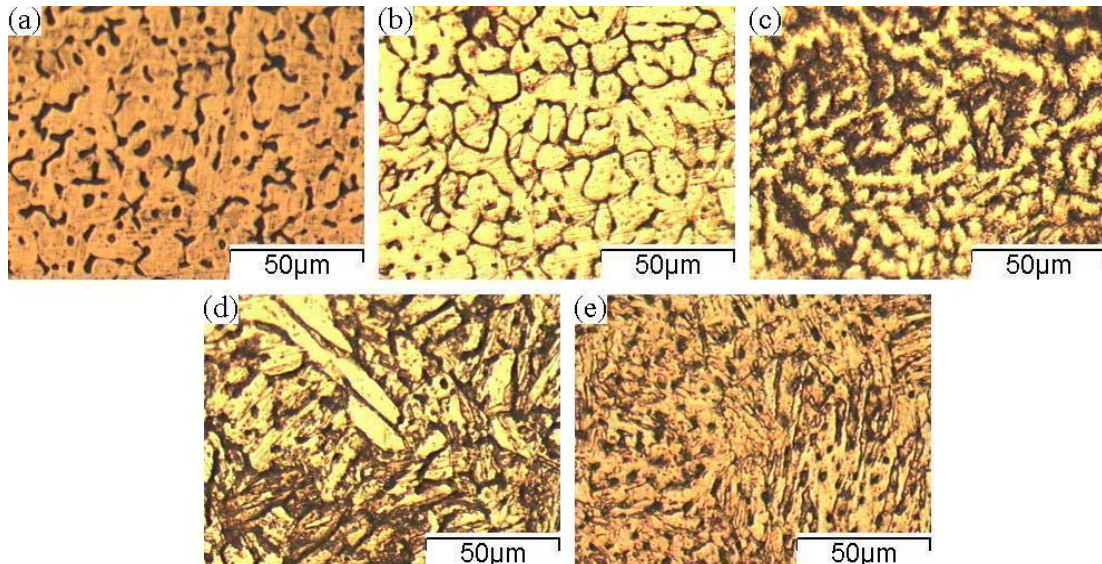


**Fig. 3.1:** Optical etched microstructures taken from below the lased surface of the 316L steel samples with: (a) 0wt% 17-4PH, (b) 25wt-% 17-4PH, (c) 50wt-% 17-4PH, (d) 75wt-% 17-4PH, (e) 100wt-% 17-4PH (Jerrard et al., 2009b).

SLM of cobalt-chromium (Co-Cr-Mo) has been investigated for medical application. The cobalt-chromium alloys have been key materials in dentistry for a long time, and now they are also used for high-strength hip replacements and cardiovascular devices due to their high corrosion and fatigue resistance. It has been reported that 99.9% dense Co-Cr-Mo

parts can be fabricated using optimal SLM processing parameters having high hardness, strength, stiffness and favourable corrosion behaviour (Vandenbroucke and Kruth, 2007). This illustrates the capability of SLM as an efficient production method for medical and dental parts with great economical potential.

SLM of nickel alloys is also a subject for research works. Nickel-based alloy powders containing of 83% Ni and 9.4% Cr are found to be suitable candidate for SLM process to directly make metallic parts such as die (Osakada and Shiomi, 2006). SLM has also been applied to manufacture cantilever beams of NiTi shape memory alloys for MEMS applications and induces a mixture of the martensitic and rhombohedral R-phase in the alloy (Clare et al., 2008). An experimental study has demonstrated the capability of SLM to fabricate high dense supernickel alloy Waspaloy® up to 99.7% density using appropriate parameters (e.g. pulse width, pulse energy, repetition rate and scan speed) of a Nd:YAG laser (Mumtaz et al., 2008).

SLM of titanium and titanium alloys is investigated intensively due to its promising application in aerospace and medical sectors. The titanium specimens made by SLM using a Nd:YAG pulsed laser demonstrate approximately 240 HV hardness, higher than that of wrought material, and can have a comparable fatigue strength if the small hatching distance and post-treatment of hot isostatic pressing (HIP) are used (Santos et al., 2004). The microstructural analysis on Ti6Al4V parts shows a significant influence of SLM conditions (i.e. fast cooling from high temperature and etc) on microstructural characteristics such as morphology of phases, orientation of grains, and secondary phases (Thijs et al., 2010).

SLM of aluminium alloys has raised increasing research interest most recently due to its lightweight property and relative low expense comparing to titanium alloys (Bartkowiak et al., 2011, Brandl et al., 2012, Buchbinder et al., 2011, Louvis et al., 2011). There are a number of difficulties in the SLM processing of aluminium powders; I) SLM needs to spread a thin powder layer, but this procedure is difficult in the case of aluminium powders (being light and having poor flowability, especially in the presence of moisture). This can suppress the deposition of powder and makes aluminium alloy powders unsuitable for many existing powder deposition mechanisms. II) The high reflectivity of aluminium (91%) increases the laser power required for melting. III) The major difficulty in processing of aluminium and its alloys is reported to be oxidation and thin oxide films on both the

solid and molten materials. The oxide layers act as a barrier for diffusion and melting development, and also reduce the wettability (Louvis et al., 2011).

A preliminary study showed that the pure aluminium powder can be fully melted in the SLM process, but the molten aluminium tends to agglomerate into globules due to the balling effect and possibly the existing oxide layer (Jerrard et al., 2009a). However, despite difficulties to manufacture parts from SLM, most recent efforts has led to some promising results, e.g. the cubic parts produced by Louvis et al. (2011) as seen in Fig. 3.2, though the difficulties for SLM of Al still exists. In fact, the SLM parts contained defects such as delamination (Fig. 3.2b), porosity (Fig. 3.3a), or oxide layers between the laser hatches (Fig. 3.3b). The role of Marangoni convection in producing these defects by striation the oxides (which disrupt solidification and the melt pool) is schematically shown in Fig. 3.4.

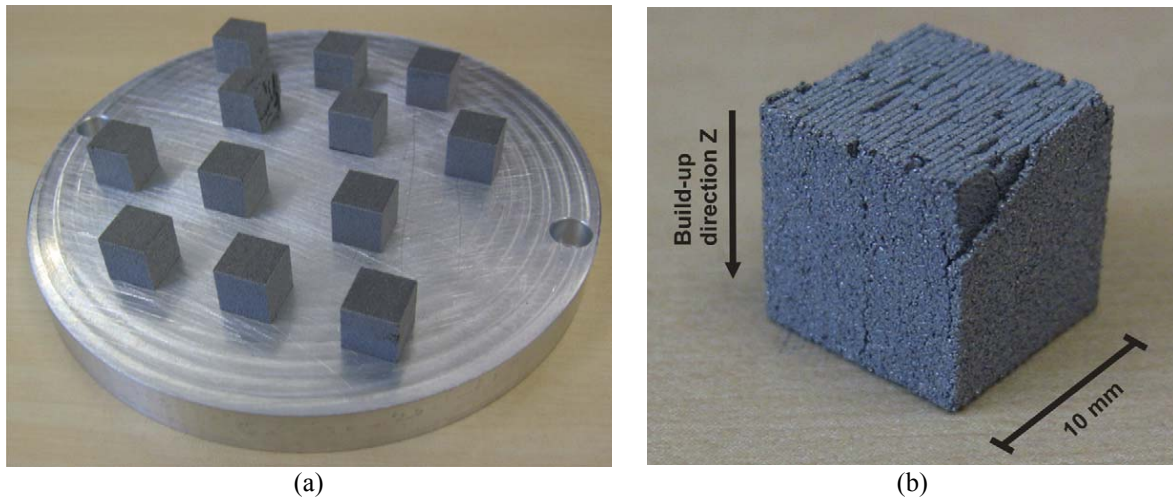


**Fig. 3.2:** (a) SLM cubic aluminium specimens on aluminium SLM build substrate, and (b) wall delamination of Al6061 SLM specimen (Louvis et al., 2011).

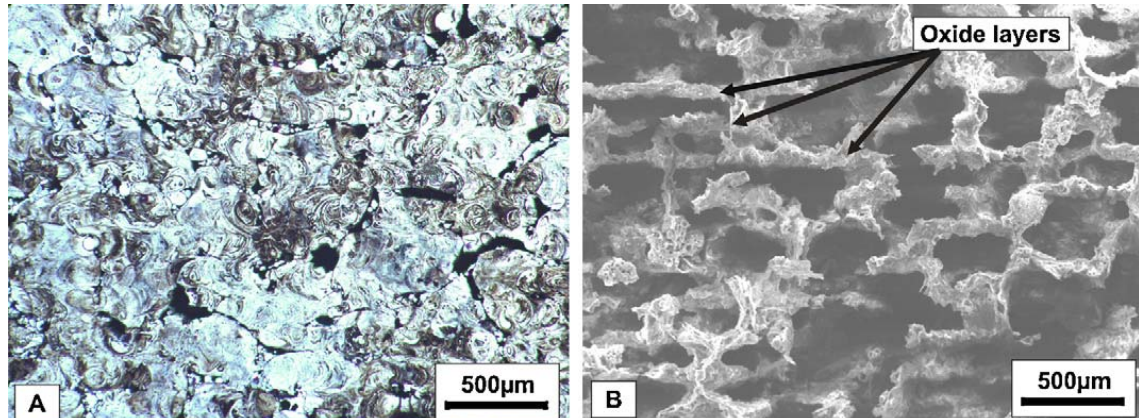


**Fig. 3.3:** Optical and SEM micrographs of an Al6061 sample; (A) sample after polishing and etching with Keller's reagent; (B) deep etched with NaOH solution (Louvis et al., 2011).

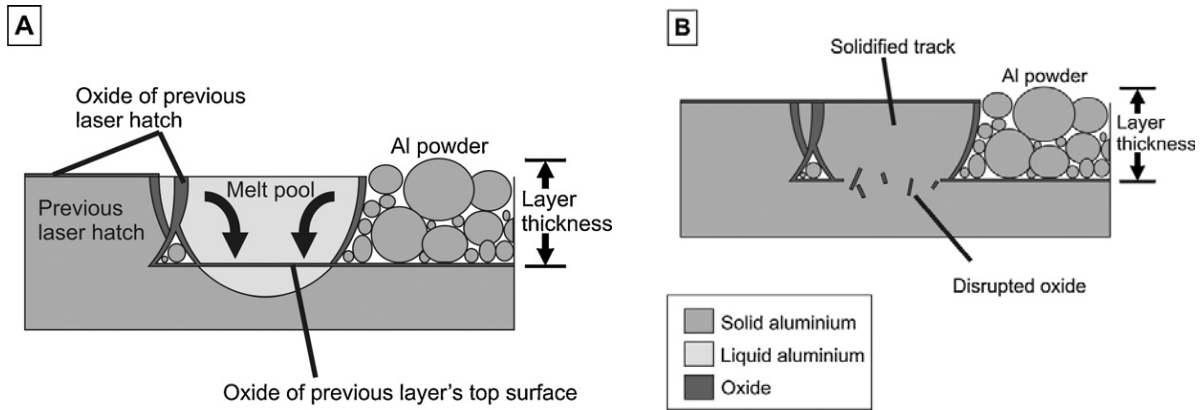


**Fig. 3.4:** (A) Marangoni convection in the melt pool. (B) Oxide disruption and solidification of the melt pool (Louvis et al., 2011).

Regarding the mentioned difficulties in SLM production of Al, the SLM needs to be developed to break the oxide films in order to achieve a dense Al component. This advancement has been very recently practiced by using very high laser powers and advanced SLM machines, as seen from Figs. 3.5 and 3.6 (Buchbinder et al., 2011).

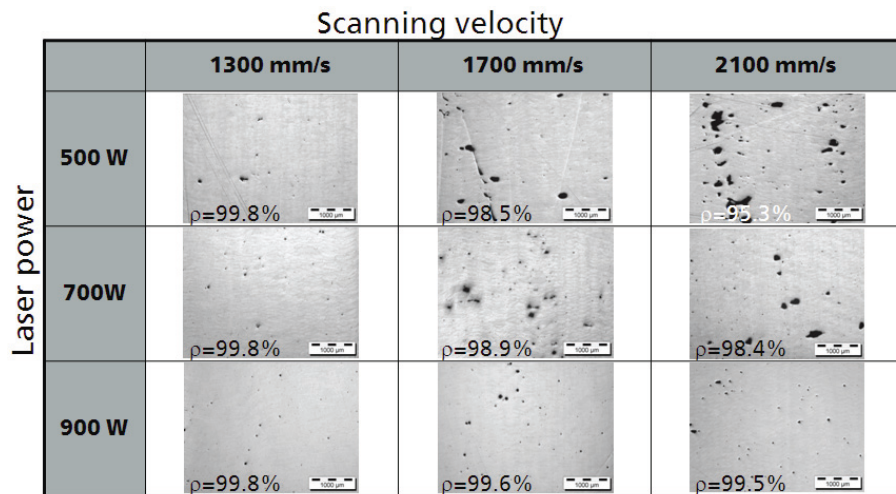


**Fig. 3.5:** Densities by means of cross sections of SLM samples depending on scanning velocity and laser power (Buchbinder et al., 2011).

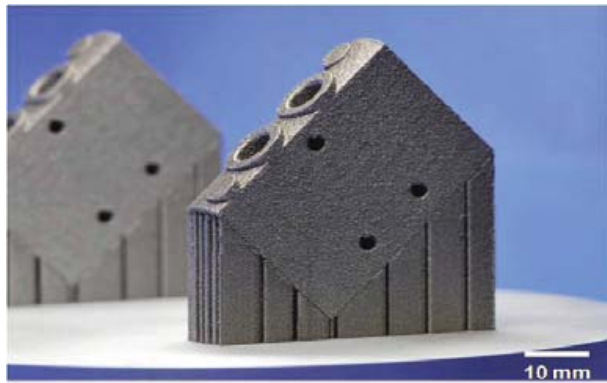


**Fig. 3.6:** Produced Al-part with 1 kW laser power, Courtesy of Festo AG & Co. KG (Buchbinder et al., 2011).

### 3.2. SLM of MMCs

MMCs are one of the main categories of composites, combining metallic properties of matrix (ductility and toughness) with ceramic characteristics of reinforcements (high strength and modulus), and leading to greater strength in shear and compression and to higher service temperature capabilities. The attractive physical and mechanical properties that can be obtained with MMCs, such as high specific modulus, strength, and thermal stability, have been documented extensively (Surappa, 2003, Tjong and Ma, 2000). The attractive properties of MMCs combined with the valuable SLM capability to consolidate second or multiple material particles have motivated the researchers to develop MMCs via SLM process. The researches in this area can be categorised into two main approaches. The first approach is ex-situ particle and powder blending (being manufacturing of composites using various mixtures of powders). The second approach is in-situ particle and powder interaction. In this method, SLM is used to ignite a chemical reaction between additive particles and metallic powders to create in-situ MMCs. Here, a review on the researches carried out on the SLM of MMCs is presented.

#### 3.2.1. SLM of MMCs through ex-situ techniques

The study on SLM of iron with graphite shows that homogeneous powder blends of 0.4, 0.8, 1.2, and 1.6 wt% graphite and iron can be processed by EOS SLM system to produce 3D specimens. The graphite addition can increase the sintering kinetics of iron powder. This significantly affects the resulting microstructure which includes austenite and

martensite structure, while it is very heterogeneous due to the very short laser interaction time (Simchi and Pohl, 2004).

With an objective to develop load-bearing implants, the SLM has applied to fabricate hydroxyapatite and stainless steel composites. It has been found that hydroxyapatite particles affect the melting and fusion of the stainless steel powder and dual scanning strategy needs to be applied in order to control the balling effects. As shown in Fig. 3.7, the stainless steel/hydroxyapatite part has a finer grain size than that of the stainless steel attributed to the hydroxyapatite particles as nuclei to assist heterogeneous nucleation. These finer grains enhance the hardness of the stainless steel/hydroxyapatite part (Hao et al., 2009).

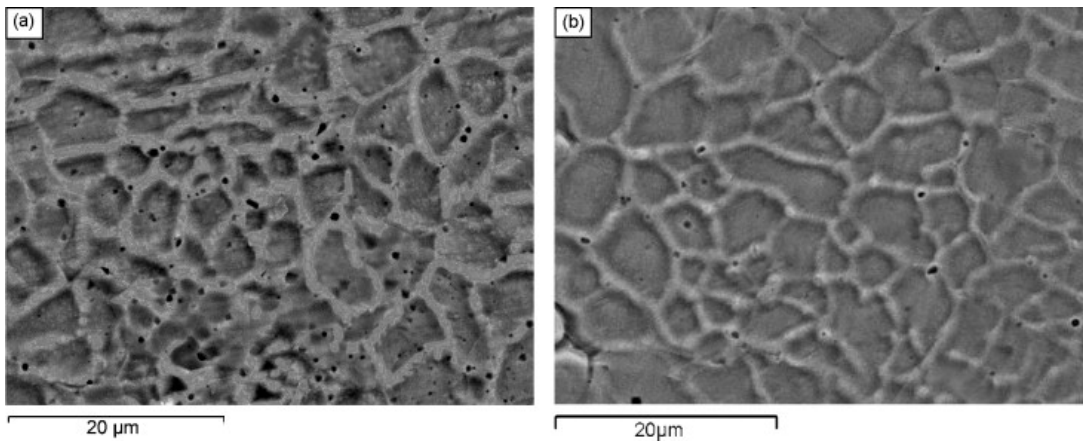


**Fig. 3.7:** Typical SEM view of (a) stainless steel/hydroxyapatite and (b) 316L stainless steel microstructure (Hao et al., 2009).

The study on SLM of submicron WC-Co particulate reinforced Cu MMCs shows that the sintering activity and densification response of the laser processed MMCs generally become worse with a high weight fraction of reinforcement. This is due to a severe particulate aggregation and the resultant crack formation between the reinforcement and the matrix (Gu and Shen, 2006). An addition of 1 wt% rare earth (RE) oxide ( $\text{La}_2\text{O}_3$ ) into this WC-Co-Cu material system results in the improvement of densification, microstructure refinement, particulate dispersion homogeneity and particulate/matrix interfacial coherence (Gu et al., 2007).

The study of SLM of  $(\text{Fe},\text{Ni})-\text{TiC}$  MMC shows that TiC particles can be homogeneously distributed in the Invar metal matrix, however, the dissolution of Ti and C in the liquid of invar alloy leads to spherical particles formation and cracking of the

specimens. The low 30 wt% TiC content leads to crack free parts, but this can result in the relatively low bending rupture strength and hardness (Gåård et al., 2006).

The study on silicon carbide particulates (SiCp) reinforced aluminium based metal matrix composite produced by direct metal laser sintering process shows the influences of SiCp size on density, porosity and microhardness. The larger SiCp particles provide higher density and lower porosity because of lower clustering effect, but higher microhardness was achieved in smaller size of reinforcement due to lower grain size. Cracks can also develop within interfacial zones due to difference between co-efficient of thermal expansion of matrix alloy and SiCp (Ghosh et al., 2010).

The main drawbacks of ex-situ methods are incorporating the homogeneous reinforcements into the matrix, the interfacial reaction between the reinforcement and the matrix, and the agglomeration and poor wettability between the ex-situ reinforcement and the matrix (Fan et al., 2003, Lu et al., 1997). In contrast, the in-situ techniques to fabricate Al MMCs have been developed to mitigate the mentioned difficulties. These methods involves chemical reactions producing in-situ formed reinforcement particles within the melted material and provides more stable reinforcements, cleaner particle–matrix interface and stronger interfacial bonding, and better distribution of fine reinforcements inside matrix (Fan et al., 2003, Tjong et al., 2004, Tong and Fang, 1998b, Yu et al., 2003).

### **3.2.2. SLM of MMCs through in-situ techniques**

SLM can be used to induce chemical reactions between reinforcement particles and metallic powders to create in-situ MMCs. The laser energy not only is able to trigger the chemical reaction of the composites to form chemical compound, but also can generate additional thermal energy to propagate melting and binding of particle powders. SLM of in-situ MMCs have significant benefits in terms of fine and uniform distribution of compounds, inherent interface between reinforcement material and matrix and exothermic energy to facilitate melting and densification.

SLM is used to synthesise Cu-based MMCs reinforced with in-situ  $\text{TiB}_2$  particles through the reaction between Cu, Ti and  $\text{B}_4\text{C}$  using a 3-kW  $\text{CO}_2$  laser. The in-situ reaction resulted in the formation of  $\text{TiB}_2$  and non-stoichiometric  $\text{TiC}_{1-x}$  particles in a Cu matrix. Some porosity was observed in the Cu–Ti– $\text{B}_4\text{C}$  system. However, with addition of Ni in the

Cu–Ti–B<sub>4</sub>C system, almost fully dense parts could be obtained due to improvement of wetting (Leong et al., 2002, Lu et al., 2000).

SLM of TiO<sub>2</sub>, Al and C using a Q-switched Nd:YAG laser source can result in the combustion wave propagation of the self-propagating high-temperature synthesis (SHS) to form in-situ TiC-Al<sub>2</sub>O<sub>3</sub> composites. Further work is needed to identify a proper operating window to control the reaction and produce a complex part. It is also required to increase the scanning speed since a threshold for the in-situ formation exists at scan speed 2 mm/s and power 60 W. This is not a practical speed to build parts with a reasonable size (Slocombe and Li, 2001).

SLM production of in-situ TiN/TiC/Ti<sub>5</sub>Si<sub>3</sub> reinforcements is possible in Ti powder systems by using SLM process (Gu et al., 2009c, Gu et al., 2009d, Gu et al., 2011b). For example, SLM of SiC/Ti powder system was performed to produce bulk-form TiC/Ti<sub>5</sub>Si<sub>3</sub> in-situ composites (Fig. 3.8a). A fibre laser with a considerably high energy was used to ensure the completion of melting of both the Ti constituent and the high melting point SiC component. The uniformly dispersed TiC reinforcing phase with a unique network distribution and a submicron-scale dendritic morphology appeared around laser energy density of 0.4 kJ/m (Fig. 3.8b). The 96.9% dense SLM-processed TiC/Ti<sub>5</sub>Si<sub>3</sub> composites showed a high microhardness of 980.3 HV, being 3 times more than that of the unreinforced Ti part (Gu et al., 2011b). In such systems, the microstructural refinement usually occurs due to rapid cooling rates of SLM and grain nucleation from reinforcing phases (Gu et al., 2009c).

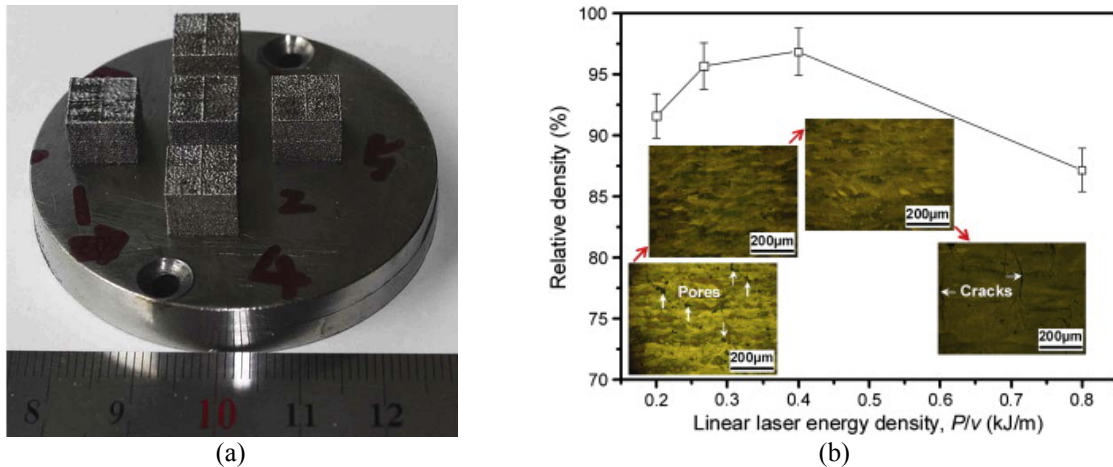


**Fig. 3.8:** (a) Photograph of SLM parts made by various processing parameters from SiC/Ti powder system. (b) Influence of laser energy density on density and microstructure of SLM-processed composite parts (Gu et al., 2011b).

### **3.3. Research Hypothesis: SLM of Al MMCs from Powder Mixture of Al/Fe<sub>2</sub>O<sub>3</sub>**

Aluminium-alumina (Al<sub>2</sub>O<sub>3</sub>) particle composites are important since Al<sub>2</sub>O<sub>3</sub> particles serve as an effective reinforcement for Al leading to improved mechanical properties. There have been attempts to fabricate these composites by in-situ techniques, using the traditional methods. The traditional manufacturing methods commonly involve casting, powder metallurgy, mechanical alloying, etc. The in-situ method uses the reaction between Al and metal oxide, such as CuO, NiO, TiO<sub>2</sub>, or Fe<sub>2</sub>O<sub>3</sub>, in order to produce Al<sub>2</sub>O<sub>3</sub> particle or whisker reinforcements. After the reaction, the reduced metal usually further reacts with Al to form intermetallic phases (Hsu et al., 2006, Maity et al., 1997, Wu and Li, 2000, Yu et al., 2004, Yu et al., 2003).

The Fe<sub>2</sub>O<sub>3</sub>/Al mixture is a well known thermite system producing an exothermic reaction regarding the following stoichiometric reaction:



The final phases, Al<sub>2</sub>O<sub>3</sub> and Fe<sub>3</sub>Al intermetallics, are formed by an in-situ chemical reaction in which Al reduces the iron oxide (Fan et al., 2006, Yang et al., 2004). This stoichiometric reaction is proposed for thermite mixture when powder mixture of 8Al-3Fe<sub>2</sub>O<sub>3</sub> (given in mol%) is prepared (mass ratio of Fe<sub>2</sub>O<sub>3</sub>/Al ~ 2.2), though non-stoichiometric compositions may manipulate the final products (Durães et al., 2007). The in-situ formed Al<sub>2</sub>O<sub>3</sub> and Al-Fe intermetallic products are of high strength and can contribute to strengthening, when they act as fine reinforcements with homogenous structure containing very fine particles with a rough appearance.

The proposed research work aims to investigate the feasibility of the SLM process to activate the in-situ reaction in the mixture of Al/Fe<sub>2</sub>O<sub>3</sub> and directly produce net-shape Al matrix composite parts. It is envisaged that the SLM process has great potential of manufacturing Al composite parts with complicated geometries as well as good particulate reinforcement distributions, while other techniques are not (or hardly) able to do so. In addition, the SLM is associated with the rapid solidification phenomena, due to the short laser-material interaction time and quick movement of laser after melting, modifying the microstructure through microstructural refinement, solid solubility extension and increasing chemical homogeneity. This can be particularly interesting for Al alloys where the

equilibrium solid solubility of many elements is very limited (Lavernia and Srivatsan, 2010, Rajabi et al., 2008).

Hence, the new technique could provide new opportunity for producing novel in-situ Al matrix composites reinforced by ultrafine alumina and iron combination particles to deliver high mechanical performance, whereas conventional techniques usually lead to large reinforcement particles making the material very brittle. The success of this new development could extend the capability of SLM process to produce high performance Al matrix composite components for commercial applications in various industrial sectors.

This is the first time that this new SLM technique is applied in Al alloys. In addition to unexpected challenges due to novelty of the technique, the issues such as material compositions for desired properties, health and safety requirements, controlling the exothermic reaction to initiate and stop the process, and suitable manufacturing parameters to produce Al matrix composite products should be considered. To overcome these challenges, the compositions of powder mixtures as well as manufacturing parameters are closely controlled. Some modification to overcome technical issues such as powder deposition might be necessary as well.

## **Part Two: Materials, Experimental Procedures, and Preliminary Experiments**

---

# Chapter 4: Materials and Experimental Procedures

---

## 4.1. Materials and SLM Experimental Setup

This chapter describes the material powders used in the SLM experiments as well as the SLM machinery setup that produces samples. It also explains the setup of tests which are used to measure and characterise the products.

### 4.1.1. SLM powders

#### 4.1.1.1. 316L stainless steel

Stainless steels are currently one of the most commonly used materials in SLM processes. The as-received 316L stainless steel (Sandvik Osprey Ltd, UK) was supplied in the form of powders. The diameter of 316L stainless steel powder was determined in a range of approximately 30  $\mu\text{m}$  to 80  $\mu\text{m}$  with an average particle size of approximately 50  $\mu\text{m}$ , as seen from Fig. 4.1. The composition of the alloy in wt% was 17 Cr, 11 Ni, 0.03 C, 1.8 Mn, 2.6 Mo, 0.8 Si, and Fe balance. This powder was used in preliminary SLM studies to calibrate the machine and illustrate its performance.

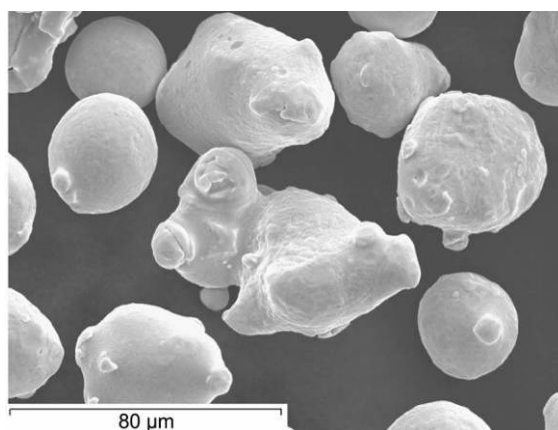


**Fig. 4.1:** The typical SEM images of 316L stainless steel powder.

#### 4.1.1.2. Pure aluminium and iron oxide

The main scope of this PhD research is to investigate the in-situ formation of Al matrix composite through the SLM of Al and Fe<sub>2</sub>O<sub>3</sub> powder mixture. The pure Al (Aluminium Powder Co. Ltd, UK) was supplied in the form of powders with an average particle size of 40 µm and 99.7 wt% purity. Iron (III) oxide (Fe<sub>2</sub>O<sub>3</sub>) particles (Inoxia Ltd, UK) with a dark red colour (Fig. 4.2a) were sieved below 53 µm and used as the filler material. To produce the powder mixtures, 5, 10, and 15 wt% Fe<sub>2</sub>O<sub>3</sub> powder were added to Al powder. Then, the mixture was shaken at least 25 minutes using a test sieve shaker. Since the Fe<sub>2</sub>O<sub>3</sub> powder is dark red, it changes the colour of powder mixture from silver (being Al colour) to red (e.g. Fig. 4.2b) in such a manner that higher Fe<sub>2</sub>O<sub>3</sub> percentage makes the mixture more reddish. This change in colour can enhance the laser absorption by powder mixture resulting in better consolidation during SLM. Moreover, the reddish colour can assist to evaluate the homogeneity in powder mixture distribution. In other words, when the powders are uniformly mixed and distributed, the colour of mixture is consistent (Fig. 4.2b).

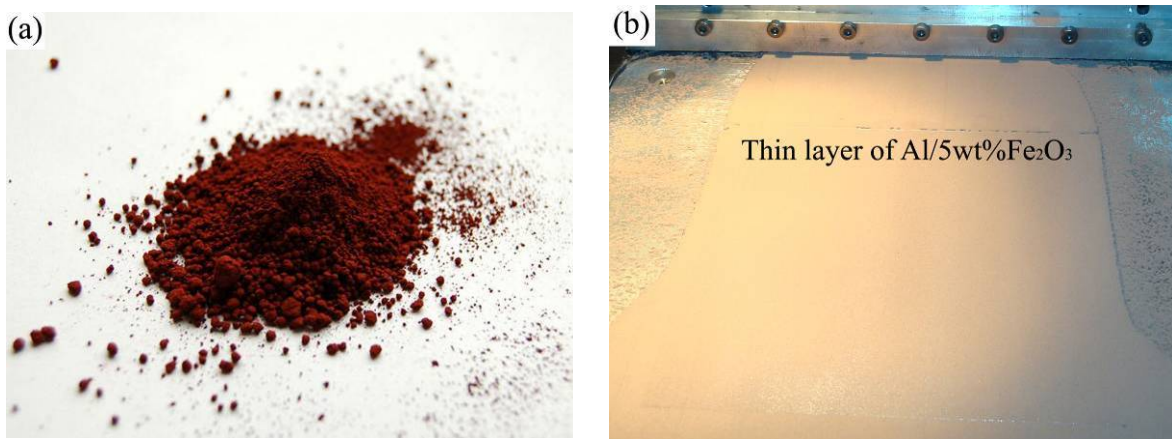


**Fig. 4.2:** (a) Iron (III) oxide powder sample with a dark red colour. (b) The uniform and reddish colour of Al/5wt%Fe<sub>2</sub>O<sub>3</sub>.

In addition to visual colour appearance of powder mixtures, the uniform distribution of Al and Fe<sub>2</sub>O<sub>3</sub> was confirmed by SEM results. Fig. 4.3 shows examples of the mixed powders (Al/(5-10)wt%Fe<sub>2</sub>O<sub>3</sub>) demonstrating a random distribution of powders within each other in such a manner that, one may not distinguish them easily. In addition, an attraction and adherence can be observed between the two powders, making them better distributed (Fig. 4.3b). Fig. 4.3c suggests that Al and Fe<sub>2</sub>O<sub>3</sub> particles correspond to spectrums 1 and 2 respectively, on the basis of their chemical compositions. Oxygen naturally exists in all

spectrums attributed to two different sources; (i) Al oxide formed on Al particles surface and (ii) iron oxide.

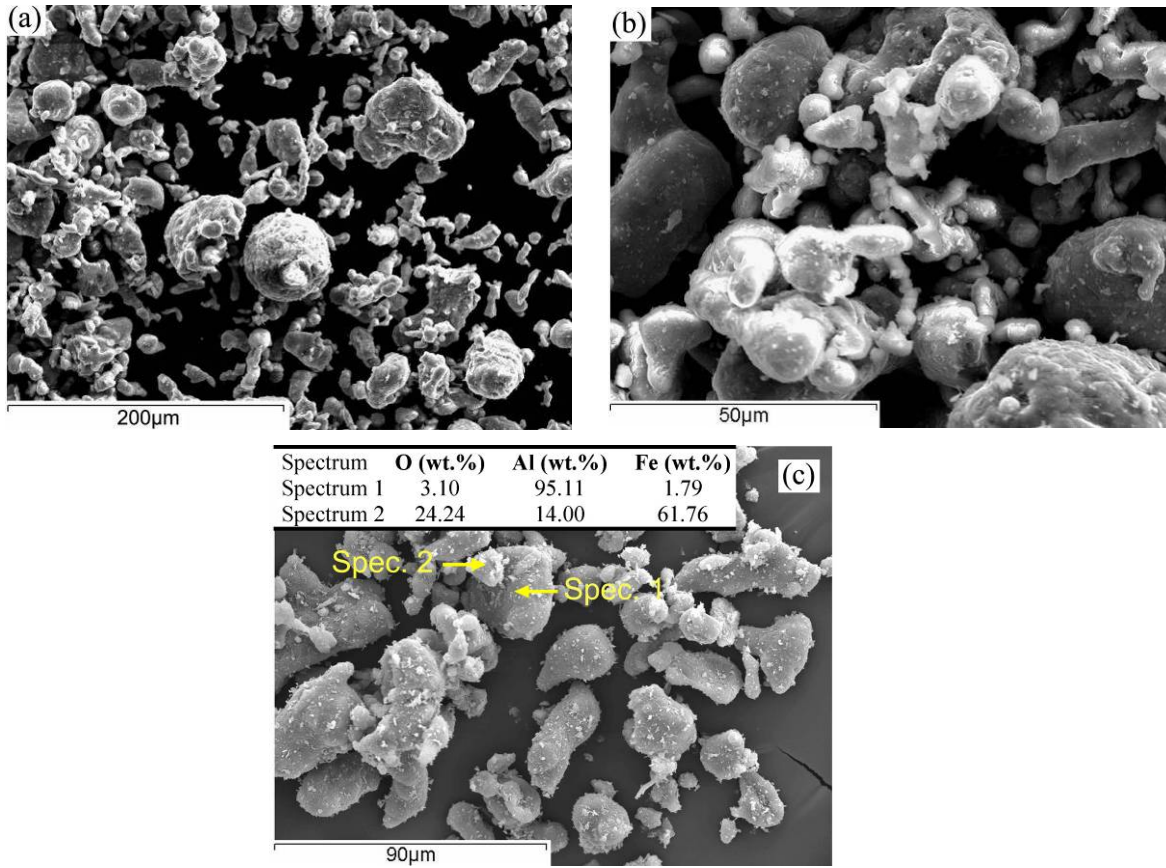


**Fig. 4.3:** The pure Al/Fe<sub>2</sub>O<sub>3</sub> particle interaction; (a) Al/5wt%Fe<sub>2</sub>O<sub>3</sub> powder mixture, (b) the previous picture with higher magnification, and (c) Al/10wt%Fe<sub>2</sub>O<sub>3</sub> powder mixture (the chemical composition was acquired by EDS).

#### 4.1.1.3. Al6061 and AlSi10Mg and Iron Oxide

In addition to the pure Al (99.7 wt% purity), Al6061 (mean particle size ~ 40 μm), and AlSi10Mg (mean particle size ~ 40 μm) was mixed with 15 wt% Fe<sub>2</sub>O<sub>3</sub> powder (sieved below 53 μm). The chemical compositions of these Al alloys are shown in Table 4.1.

**Table 4.1:** Chemical composition (in weight %) of the standard alloys used in this work

Element	Si	Fe	Cu	Mn	Mg	Other	Al
<b>Al6061</b> (provided from Alpoco)	0.40-0.80*	≤ 0.70	0.15-0.40*	0.15	0.80-1.20	≤ 0.6	Balance
<b>AlSi10Mg</b> (Provided from EOS)	9.0-11.0	≤ 0.55	≤ 0.05	≤ 0.45	0.2-0.45	≤ 0.40	Balance

\* The content was slightly higher than the standard.

#### 4.1.2. SLM machinery setup and processing apparatus

Experiments investigating the SLM of metals and metal matrix composites were carried out using a commercial SLM machine (MCP Realizer 250, MTT Technologies Group) with a fibre laser. This machine is shown in Fig. 4.4 with descriptions for various apparatus. Fig. 4.5 shows a close up image of the open processing chamber, where the laser is located at the top and motion of devices distribute powders. The Realizer has a  $250 \times 250$  mm build area with filleted corners (approximate radii of 50 mm) and can build to a height of 300 mm. The visual progress of the build process can be seen in Fig. 4.6.



**Fig. 4.4:** The SLM Realizer installed at the University of Exeter: 1) argon cylinder, 2) interface PC, 3) interim PC and motor controller, 4) laser unit, 5) storage cabinet, 6) status monitor, 7) build chamber, and 8) gas regulator.



**Fig. 4.5:** Close up view of the build chamber.

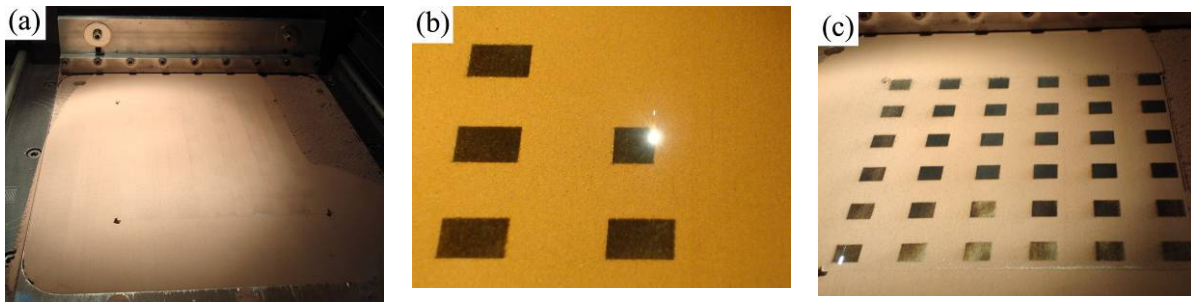


**Fig. 4.6:** Example of the SLM process in action on Al/5wt%Fe<sub>2</sub>O<sub>3</sub> powder mixture: (a) a deposited powder layer, ready for laser scanning, (b) laser melting of rectangular parts, and (c) end of the first scanning and starting the second scanning.

### Laser

The laser is an IR fibre laser, operating continuously at a wavelength of 1064 nm (no pulsed modes are available): the beam is unpolarised. The minimum lasing power was measured to be approximately 5 W and the maximum possible was 120 W, though this was over the laser's rated capacity of 100 W and therefore only used in experiments with a short running time. The minimum spot diameter was about 160 µm, achieved using a focus length of 60 mm.

### Laser scanning

An analogue mirror galvanometer is installed in the Realizer, allowing the laser spot to be moved and positioned by the control software. Due to the nature of the galvanometer, a single value for laser scan speed isn't given: instead, two parameters control the scan speed: *point distance* and *dwell time*. The machine manufacturer (MTT Ltd) defines scanning speed as:

$$\text{Scan Speed (m/s)} = \frac{\text{Point Distance (\mu m)}}{\text{Exposure Time (\mu s)}} \quad (\text{Eq. 4.1})$$

Eq 4.1 defines the theoretical scan speed, while in reality the scan speed may differ slightly due to the workings of the galvanometer. The reported scanning speeds are the theoretical numbers and are calculated regarding this equation.

The MCP Realizer SLM machine had a scanning strategy for each layer that begins in the front-left corner of the part and builds vertically towards the back. The scanning routine was alternating i.e. in x direction for the first layer and subsequently in y direction for the next layer, and so on. The schematic pattern of the mentioned scanning strategy has been

shown in Fig. 4.7. The double scanning (scanning each layer twice for ensuring melting) was carried out for most of samples. Scan line spacing (hatching distance), like point distance, is another laser parameter (Fig. 4.7 visually exhibits it), having various optimum value regarding the used material.

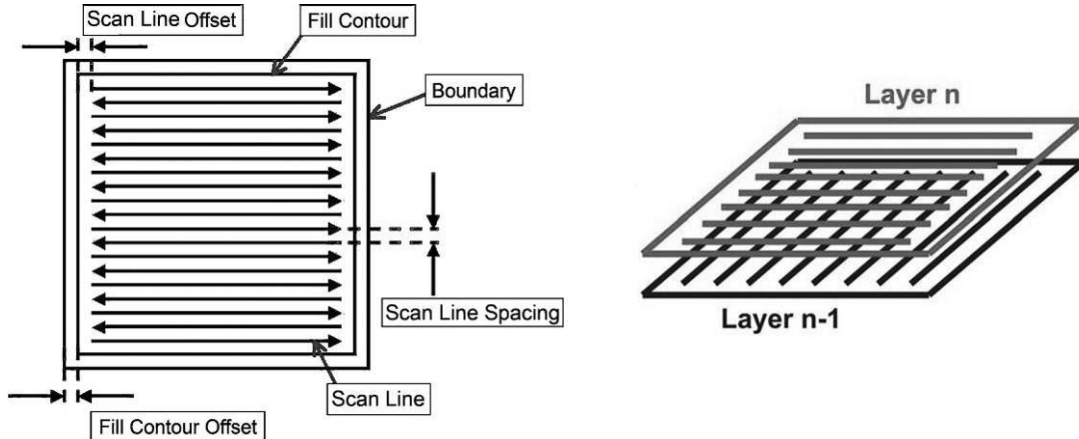


**Fig. 4.7:** Schematic pattern of scanning strategy for single and additive layers.

Optionally, the boundary of the cross section can be additionally scanned to improve surface quality. The software can also allow a fill contour to be employed between the boundary scan and the internal hatching (Fig. 4.7). However, for samples produced in following chapters, the boundary scan and fill counter were not used to eliminate variables in investigations.

### Powder deposition

Powder deposition is controlled by software by using two devices, referred to as 'loader 1' and 'loader 2'. Loader 1 is simply a large tank on the back of the machine that feeds loader 2 with powder, allowing large builds to be processed without the need for refilling. This is achieved by moving loader 2 to the back of the machine (under Loader 1) and depositing powder into the top of Loader 2 enabled by a turning slotted shaft. Loader 2 is able to move both forward and backward, allowing deposition of powders after building each layer and leveling it by using a device called 'wiper' in the way back (Fig. 4.8a). Fig. 4.8b demonstrates the mechanism of powder deposition at the bottom of loaders due to rotation of a slotted shaft.

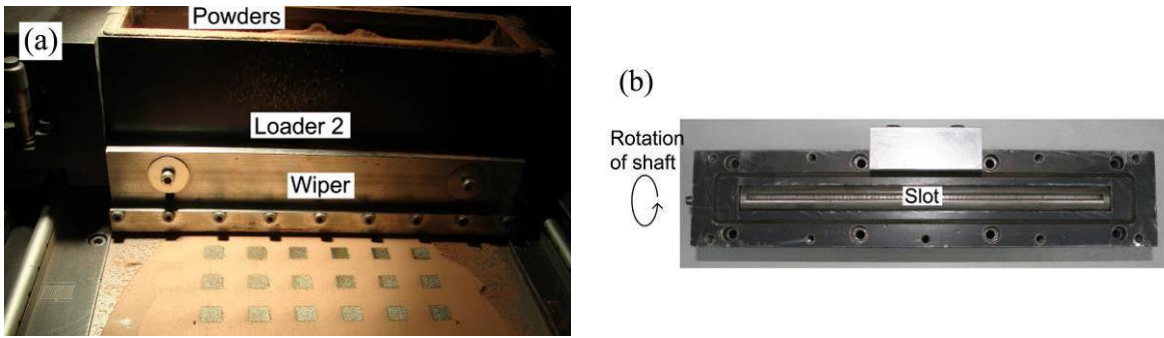


**Fig. 4.8:** (a) The forward movement of loader 2 to start powder deposition. (b) Demonstration of a shaft with slots, used to deposit powder in loader 1 and 2.

### Inert environment inside chamber

An inert gas such as argon is pumped into processing chamber of SLM machine to reduce the pressure of air. Pressure (and oxygen) is read by an internal sensor plus an analogue gauge attached to the outside of the build chamber. The internal gas is also filtered constantly to remove floating powder particles. It should be noted that the O<sub>2</sub> level was kept below 0.9% in all cases.

### Computer interface

The laser selectively melts powders by scanning cross sections generated from a CAD file, which is converted to an STL file, on the surface of a powder bed. To do so, the Realizer uses custom software to process STL files (if support is needed, it should be added which can be generated by specialist software called 'Magics'). The software 'slices' the inputted CAD model(s) and generates a file for each layer that contains coordinates for scanning as well as other key parameters such as laser power, dwell time and point distance.

In addition, Dr Neil Sewell in University of Exeter developed software that generated grids of rectangular samples to be made with varying parameters. This was greatly helpful to save time and effort to produce samples built by various parameters.

## **4.2. Hot Isostatic Pressing (HIP) Post-Treatment**

With regards to presence of porosity within products, the effect of HIP, as an effective process to densify various materials, was investigated on Al SLM composite parts. The HIP post-treatment was carried out on selected samples through a commercial service provided by one experienced company (*Bodycote H.I.P Ltd*). They informed us that they first wrapped the samples in foil and then processed them under pressure of ~ 98 MPa at ~ 485-525 °C for ~ 2 hrs, through a widely used cycle for the HIP of Al casting parts. This was in the common range for the HIP of Al alloys (Bocanegra-Bernal, 2004).

## **4.3. Experimental Measurements and Characterisations**

### **4.3.1. Density and porosity measurements**

The density and porosity of the samples were calculated by determining their dimensions and weight (mass/volume measurements). However, other methods such as Archimedes' principle or metallographic examinations were employed in some cases (see section 2.5).

### **4.3.2. Hardness**

The Vickers hardness was achieved by measuring the length of the effect of indenter on the test piece and converting it to hardness. The hardness was measured using Vickers hardness test (5 kg load was applied for 30 s) from the average of at least 4 hardness readings in conjunction with an Aleco Hardness Tester. The microhardness (100 g load was applied for 30 s) was measured from the average of at least 5 hardness readings using a Future-Tech Microhardness Tester FM testing machine.

### **4.3.3. Tensile, compression, and shear-punch testing**

Lloyd Instruments mechanical testing machine was used to stretch or compress specimens for tensile, compression and shear-punch testing. The tensile specimens were prepared and tested according to E8 ASTM standard (ASTM, 2004). The compression testing was carried out according to E9 ASTM standard (ASTM, 2004) with a length/diameter ratio of 2. Molybdenum disulfide ( $\text{MoS}_2$ ) was used as a lubricant to reduce

bearing surface friction in compression test (Fig. 4.9a). For shear-punch testing, a hole was made in a steel die for the passage of a hard punch. The diameters of punch and die were 5 mm and 5.2 mm, respectively (Fig. 4.9b). The punch was used to make a hole in 1 mm thick specimens to draw curves of load versus displacement in shear-punch testing. The crosshead speed of 0.5 mm/min was used for all test methods.

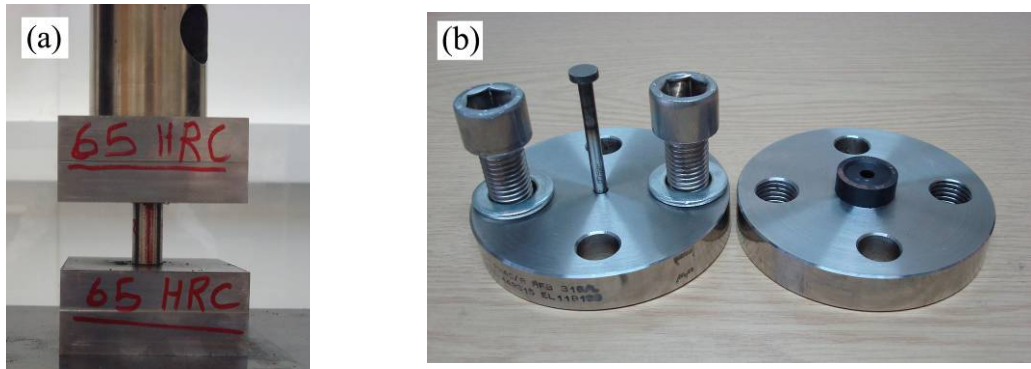


**Fig. 4.9:** (a) Compression testing setup and (b) shear-punch testing die.

#### 4.3.4. Surface roughness measurements

The surface roughness in this work was measured by using a Talyscan-150 (Taylor Hobson Precision Ltd.) with a non-contact laser probe to measure any vertical displacement (Fig. 4.10). The tests could measure the roughness in both 2D and 3D mode. The 2D measurements could be performed in a 5 mm line in X-direction (perpendicular to the deposition tracks) or Y-direction (along the tracks). The 2D roughness parameter of  $R_a$  was reported from the average of at least 4 measurements for each sample. On the other hand, the 3D measurements were carried out on an area of 5 mm × 5 mm, providing a 3D profile and surface roughness parameter of  $S_a$ .  $R_a$  and  $S_a$  are, in fact, the arithmetic average of the 2D and 3D roughness profiles, respectively, demonstrating the magnitude of surface roughness.



**Fig. 4.10:** The surface roughness tester at the University of Exeter; (a) surface roughness machine and (b) close up of the machine when a part is being scanned by laser probe apparatus.

#### 4.3.5. Metallographic analysis

The Microstructural analyses were carried out on samples by using both optical and electron microscopy. The optical investigations were mainly conducted by a Zeiss Axioplan 2 optical microscope, while the scanning electron microscopy (SEM) was performed by using a Hitachi S-3200N scanning electron microscope (SEM) equipped with an energy dispersive spectrometry (EDS) microprobe system (Fig. 4.11).

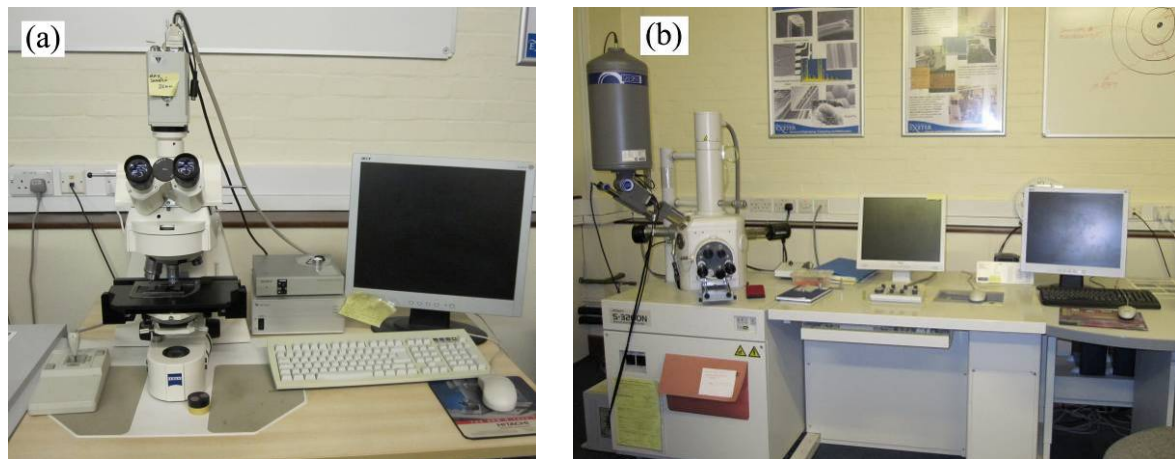


**Fig. 4.11:** (a) Optical and (b) SEM microscopy equipments at the University of Exeter.

For microstructural analysis, the cross section of samples were polished and viewed before and after chemical etching. A solvent composed of 95 ml water, 2.5 ml HNO<sub>3</sub>, 1.5 ml HCl and 1.0 ml HF were used to chemically etch the SLM parts made from Al/Fe<sub>2</sub>O<sub>3</sub> powder mixtures at the room temperature. However, in the case of single layer SLM tests

on Al and Al/Fe<sub>2</sub>O<sub>3</sub> powder mixtures, a solvent composed of 25 mL H<sub>2</sub>SO<sub>4</sub>, 70 mL H<sub>3</sub>PO<sub>4</sub>, and 5 mL HNO<sub>3</sub> at 85°C were successfully utilised as well.

#### **4.3.6. X-ray diffraction (XRD) and CT scanning**

X-ray diffraction (XRD) analyses using CuKa1 radiation was carried out to identify material phases in conjunction with a Bruker D8 Advance X-ray diffractometer. The phases were identified using the machine software.

A µCT scanning system (X-Tek Benchtop CT 160Xi) was used to reveal the porosity formation in three dimensions. The relative density could be calculated on the basis of the CT scanning images.

---

# **Chapter 5: Preliminary Experiments on SLM of 316L Stainless Steel**

---

## **5.1. Introduction**

The initial step of the PhD study is set to investigate the capabilities of the SLM machine and build a practical understanding of its working principal. This is also aimed to provide a knowledge of the issues, challenges, and final properties that can be expected from this process. This is done through preliminary experiments on SLM of 316L stainless steel. The stainless steel is used since it has been commonly reported in published researches. They also show a good SLM processability, making them a common material within relevant industries. The preliminary experiments build a detailed knowledge of the process, being necessary for processing of more advanced materials.

During SLM process, injection of an inert gas like argon into the chamber is very commonplace. This inert gas can prevent oxidation during the melting and solidification stages. Despite this benefit, the movement of gas in the SLM chamber can influence the mechanical properties of manufactured parts leading to inhomogeneous properties. Part layout is another factor which may contribute to variable temperature distribution and affect the products. However, there is no report of the effects of layout and its relation with the gas flow condition on the quality and mechanical properties of the parts produced by SLM.

As mentioned, SLM involves many issues (such as balling, porosity, lack of intra-laminar fusion, and delamination within the layers (Kruth et al., 2007, Morgan et al., 2004)) necessitating a variety of investigations regarding consolidation between the particles and porosity as well as the relevant effects on mechanical properties. The investigations should ensure the reliability and repeatability of properties, which means quality assurance. Quality assurance can lead to a control of the SLM process to identify the appropriate parameters in order to minimise the issues associated with the process and to set up appropriate standards for successful application. Therefore, various mechanical tests are normally involved in SLM processes (Scaravetti et al., 2008). Accordingly, design of a convenient, easy-to-use and practical mechanical test procedure to evaluate SLM parts

would be valuable for the research development for industrial application of the SLM process.

This preliminary study investigates the effects of process conditions including part layout and inert gas flow during SLM process on the quality and mechanical properties of consolidated 316L stainless steel specimens. A straightforward mechanical qualification procedure involving tensile, compressive and shear-punch mechanical tests is used to assess the effects of consolidation and porosity on the mechanical performance of the cylindrical samples made by SLM. The parts were manufactured with different layouts, i.e. perpendicular and parallel to gas flow. Visual inspection, temperature distribution imaging, density measurements, and optical microscopy were used to illustrate the effects of part layout on the consolidation and mechanical performance of the specimens made by SLM. The procedure introduced here can be applied to other machines individually depending on manufacturers' demand.

## 5.2. Experimental Procedures

Two sets of cylindrical 316L stainless steel specimens (with a diameter of 14 mm and a length of 120 mm) were produced using SLM, parallel and perpendicular to the gas flow. The gas (argon) flowed from the right hand side of the chamber to the left hand side at a height just above the bed surface. In each set, 4 specimens were placed on the bed, as shown in Fig. 5.1. These sets were designed in order to investigate the outcome of different layouts of the SLM bed.

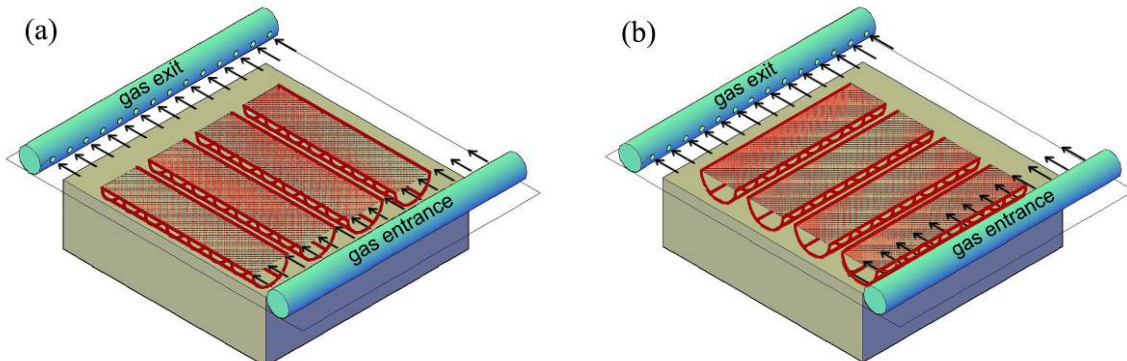


**Fig. 5.1:** Schematic layouts of parts regarding the gas direction; (a) parallel and (b) perpendicular to gas flow.

A laser power of 87 W, scan speed of 0.15 m/s, scan line spacing of 130  $\mu\text{m}$ , and layer thickness of 75  $\mu\text{m}$  was used to produce both sets of parts. These parameters were in the range of parameters suggested by machine manufacturer. The temperature distribution at the end of SLM process was revealed using a Fluke Ti40FT thermal imager infrared camera. The manufactured cylindrical parts were cross-sectioned to be prepared as tensile, compression, and shear-punch specimens, as seen from Fig. 5.2. The pieces were milled to form mechanical test specimens. The tensile specimens were machined from front positions of bars (in the case of perpendicular to gas flow) and from left side (in the case of parallel to gas flow). The compression samples were taken from back (in the case of perpendicular to gas flow) and from right side (in the case of parallel to gas flow) of bars. The shear-punch test specimens were taken from both ends of each bar and their average was reported. The compression test samples were machined accurately to form a cylinder (Fig. 5.2). The densities of these samples were calculated by determining their dimensions and weight (mass/volume measurements) and converted to porosity utilising Eq. 2.3.

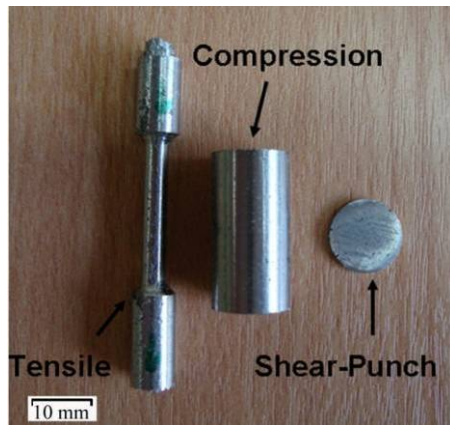


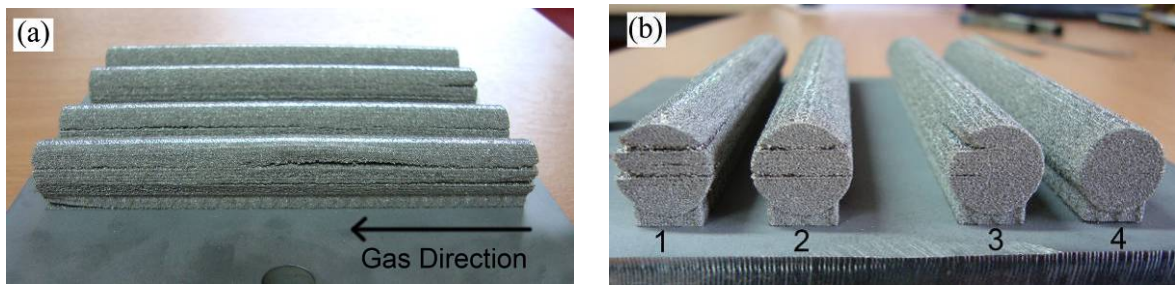
**Fig. 5.2:** Different samples for different testing methods.

### 5.3. Results and Discussion

This study aims to depict part qualification and layout calibration using a straightforward mechanical tests procedure and does not seek to produce a successful series of parts with establishment of appropriate parameters. Thus, it does not concentrate on improvement of part quality and instead simply explains the mechanical outcome of the defects and the relevant influence by part layout.

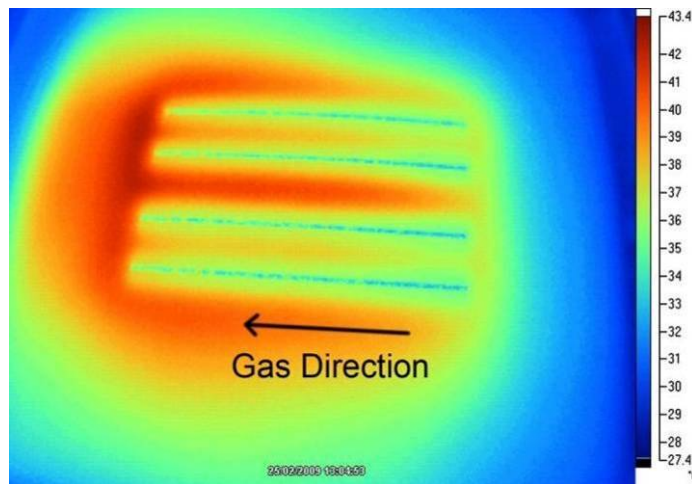
### 5.3.1. Primary inspections on quality of SLM process

Fig. 5.3 shows the visual appearance of the parts fabricated parallel to gas flow. As seen from Fig. 5.3a, delamination is more pronounced at locations close to the entrance of argon gas. The material located in these areas (close to entrance of gas) is subjected to gas with lowest temperature which, therefore, cools fastest. In fact, the gas entrance and exit positions (located at both sides of the chamber) develop a cooling direction along specimens. The large length of specimens collaborates with the gas and cooling direction leading to sharper temperature gradient over the specimens. The outcome of this temperature gradient is thermal stresses, and subsequently deformations and delaminations (Nickel et al., 2001, Zaeh and Branner, 2010), as observed in Fig. 5.3a. Another view of the part delaminations is shown in Fig. 5.3b. The first part (No. 1) shows more delamination than the last part (No. 4) which was produced on a hotter powder bed environment. This is likely due to the temperature distribution and its gradient affected by gas direction and fabrication sequence. In other words, less temperature gradient at the location where the part is cooled slower or fabrication on a pre-heated bed will lead to less thermal stresses and subsequently fewer delaminations. Similar concepts were reported in previous studies in which temperature gradient has been introduced as the first source of thermal stress (Mercelis and Kruth, 2006, Shiomi et al., 2004).



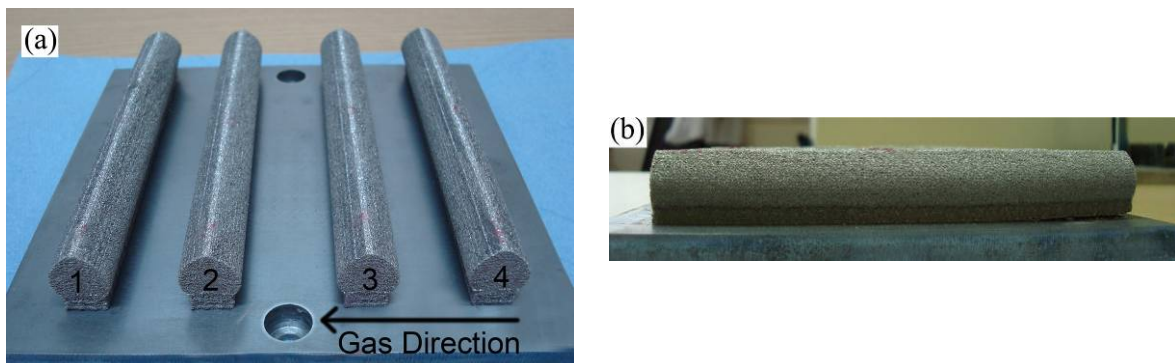
**Fig. 5.3:** A set of cylindrical parts fabricated parallel to gas flow showing the decrease of delamination with the gas direction as well as fabrication sequence; (a) front and (b) right view.

The temperature profile of the powder bed at the end of SLM process, shown in Fig. 5.4, confirms the inhomogeneous temperature distribution. This shows that the right side of the bed (where argon enters) has a lower temperature than that of the left side. It should be noted that although this image has been taken at the end of the process, it still indicates temperature differences between the two sides, implying higher temperature variations existed during the SLM process.



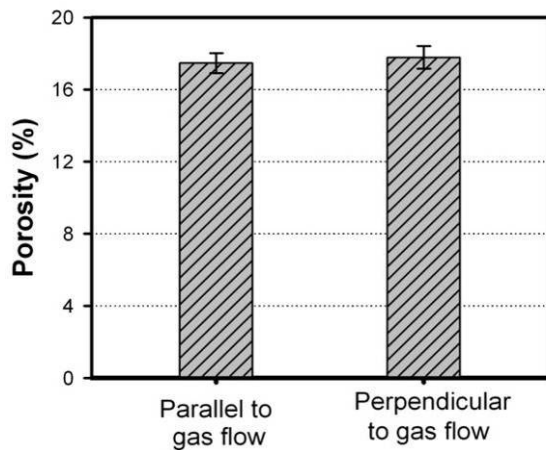
**Fig. 5.4:** The thermal image of the bed showing temperature distribution at the end of process.

Fig. 5.5 indicates that laying the parts perpendicular to gas flow leads to an obvious reduction in deformations, i.e. this figure shows almost no delaminations for the parts. This result can be attributed to a lower temperature gradient produced in each part due to the laying direction. Thus, one may conclude that to produce less thermal stress (and subsequently less delamination) the parts should be laid on the bed with a view of producing a less temperature gradient, which here appears to be perpendicular to gas flow. It is interesting to note that the scanning strategy influences delaminations as well. This is why the same scanning strategy was applied to all specimens in order to isolate the effect of the scanning strategy and carry a comparison study on the influence of the processing gas. A better scanning strategy might help to achieve relatively more homogenous temperature distribution in the SLM process which can be combined with a better laying direction of the parts.



**Fig. 5.5:** A set of cylindrical parts fabricated perpendicular to gas flow showing no delamination; (a) front and (b) right view.

In addition to delamination, porosity is another common defect observed in SLM parts (Li et al., 2010, Rombouts et al., 2006, Thijs et al., 2010, Yadroitsev et al., 2007). Fig. 5.6 exhibits the porosity of the parts produced parallel and perpendicular to gas flow and can be seen to be around 18%. This indicates that the layout of parts has a negligible influence on porosity formation and powder consolidation conditions. In fact, this suggests that the porosity is almost independent of part layout, while these parameters strongly affect part deformations.



**Fig. 5.6:** Material porosity of the samples fabricated parallel and perpendicular to gas flow.

### 5.3.2. Mechanical properties investigations

After identification of part defects introduced by the SLM process, the part response to various testing methods or strain paths must be clarified. This is to evaluate the properties and defects of the parts produced parallel and perpendicular to gas flow. To do so, the focus is on the response of material to tension, compression, and shear load, comparatively. It should be noted that although the porosity content is very high, it is almost the same in all the parts; therefore this does not harm the comparison study as is common in powder metallurgy investigations. In addition, the influence of location on mechanical properties of individual parts seemed to be arbitrary within a normal range of variation. Thus, the average data are presented with relevant error bars.

Fig. 5.7 shows the material behaviour under tensile stress demonstrating much lower tensile strength (less than 100 MPa) and ductility (less than 3% for fracture strain) compared to that of bulk material. These very low tensile properties can be attributed to a high percentage of porosity (Fig. 5.6) existing in the parts. In fact, voids and pores are the

basic sources of fracture (Dieter, 1986). Such pores may concentrate stress during mechanical loading. Moreover, these pores as volume defects can grow or coalesce due to applied tensile stresses. The growth of three-dimensional defects may lead to catastrophic failure in engineering parts and structures (Soboyejo, 2003).

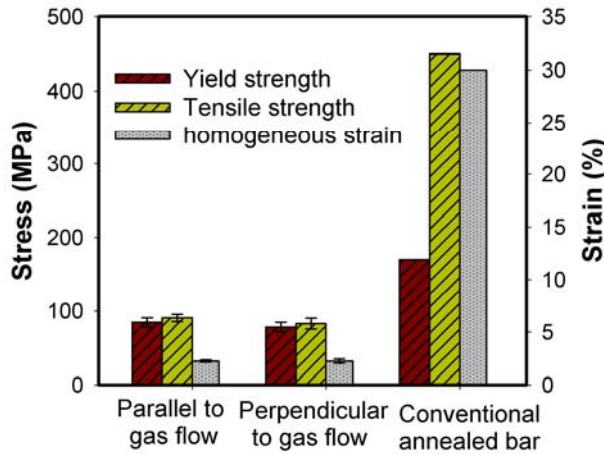


**Fig. 5.7:** Tensile properties of the SLM parts produced parallel and perpendicular to gas flow. For comparison, tensile properties of a conventionally manufactured annealed bar is given from references (ASM International Handbook Committee, 1990).

Fig. 5.7 also implies that the layout did not have a remarkable effect on tensile properties, in such a manner that tensile properties of the parts for both layouts appear in a similar range. This can be attributed to low influence of part layout on amount of porosity (Fig. 5.6) which leads to almost similar tensile properties. However, the parts fabricated parallel to gas flow seem to have slightly higher tensile strength. This might be due to a slightly lower level of porosity assessed in samples fabricated parallel to gas flow in comparison with those fabricated perpendicular to it (see Fig. 5.6).

The shear-punch testing is a small-specimen testing technique which measures the necessary load to punch a specimen vs. the displacement. Then, the punching load can be converted to shear stress ( $\tau$ ) using the following equation to characterise the flow behaviour of material:

$$\tau = \frac{P}{2\pi r_{ave} t} \quad (\text{Eq. 5.1})$$

where  $r_{avg} = (r_{punch} + r_{die})/2$ ,  $P$  is applied load and  $t$  is specimen thickness (Guduru et al., 2005). The outcome, shear stress–displacement curves, can be considered as a factor to assess bonding strength between the particles according to physical behaviour of the test

(Rider, 1977). In fact, shear-punch testing is less sensitive to material microstructure and specimen preparation procedure (Prabhakaran et al., 2008) and can be considered as a proper technique to evaluate melting degree by demonstrating the bonding strength. Fig. 5.8 shows the shear strength of samples produced parallel and perpendicular to gas flow respectively. The average shear strength is about 225 MPa for the specimens produced parallel to gas flow, while the specimens produced perpendicular to gas flow are slightly stronger with an average shear strength of about 240 MPa. This implies that the shear strength is generally higher for the parts produced perpendicular to gas flow which can be attributed to slightly higher bonding strength between particles perhaps due to slower solidification rates. However, the general strengths of the parts seem to be in a small range showing an almost repeatable melting behaviour during SLM of different parts.

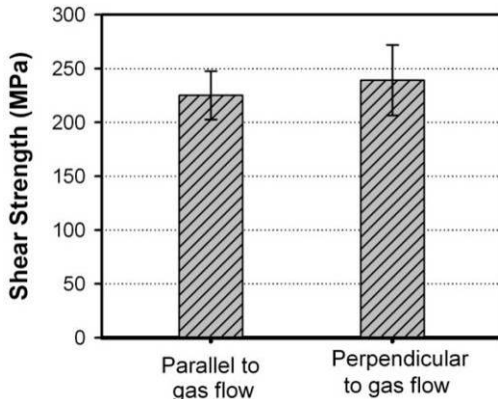


**Fig. 5.8:** Shear strength of the specimens produced parallel and perpendicular to gas flow (for comparison, the estimated shear strength of a conventionally manufactured annealed bar is  $\sim 250$  MPa).

It has been reported that the tensile strength is 1.8 times the shear stress (Guduru et al., 2005). With regards to tensile strength of 450 MPa reported for annealed stainless steel bar, the shear stress can be predicted about 250 MPa. On the other hand, regarding 18% porosity, one may ascertain that shear stress should be enhanced due to the reduction in the area that load is applied. Thus, the shear stress to pull apart the particles can be estimated in a range of about 250-330 MPa. Accordingly, one can conclude that the parameters of fabrication used in this work may lead to a fair level of melting and particles bonding for most of the part, while high porosity in the parts has strongly harmed the tensile properties (Figs. 5.7). However, the material behaviour under compression is still unknown. Compression testing can assist to clarify this aspect of part performance.

A metal which is brittle in tension may be ductile under compression. This is due to no stress amplification associated with any existent flaws. That means pores do not harm compressive strength of material. For this reason, brittle ceramics display much higher strengths in compression rather than in tension, and they are generally utilised when load conditions are compressive (Callister, 2007). Accordingly, compression testing was carried out on the specimens produced by the SLM process. The results were then compared to the results from tensile and shear-punch tests. It should be noted that the porous structure affects the volume constancy and consequently the engineering strain. However, with the early assumption of constant porosity for all the specimens, the strain axis in compression stress-strain curves was just considered for comparison between the samples.

Fig. 5.9a shows the material behaviour of the parts produced parallel and perpendicular to gas flow under compressive stress. Parts produced parallel to gas flow demonstrate a yield stress and strength close to those of annealed 316L stainless steel bar. This confirms that pores do not affect compressive strength, while they reduce the tensile strength more than 5 times (see Fig. 5.7). This result is also another confirmation for reasonable melting and particle bonding achieved from the parameters used in this work. Fig. 5.9b shows the typical shape of the rupture that occurred in compression specimens. As seen, the rupture has propagated in the layers oriented at 40-60 degrees with the compressive axis, which is not a common appearance of compression fracture. Commonly during deformation, as the metal spreads due to the compression in order to increase its diameter, the flow of metal will be restricted where it contacts with the ends by frictional forces. This leads to a cone-shaped region of dead metal (nondeforming material) at each end, with the result that the specimen becomes barrel shaped. As these cone-shaped zones develop, they cause an increase in force for a given increment of deformation. Accordingly, the rupture usually develops along these cone shape zones (Dieter, 1986, Hosford, 2005). However, this unusual appearance of compression fracture in Fig 5.9b perhaps arises from consolidation issues existing between additive layers. Thus, the rupture develops between additive layers with greater SLM defects between them. Accordingly, one may conclude that the compressive tests fairly demonstrate the consolidation issues between the layers.

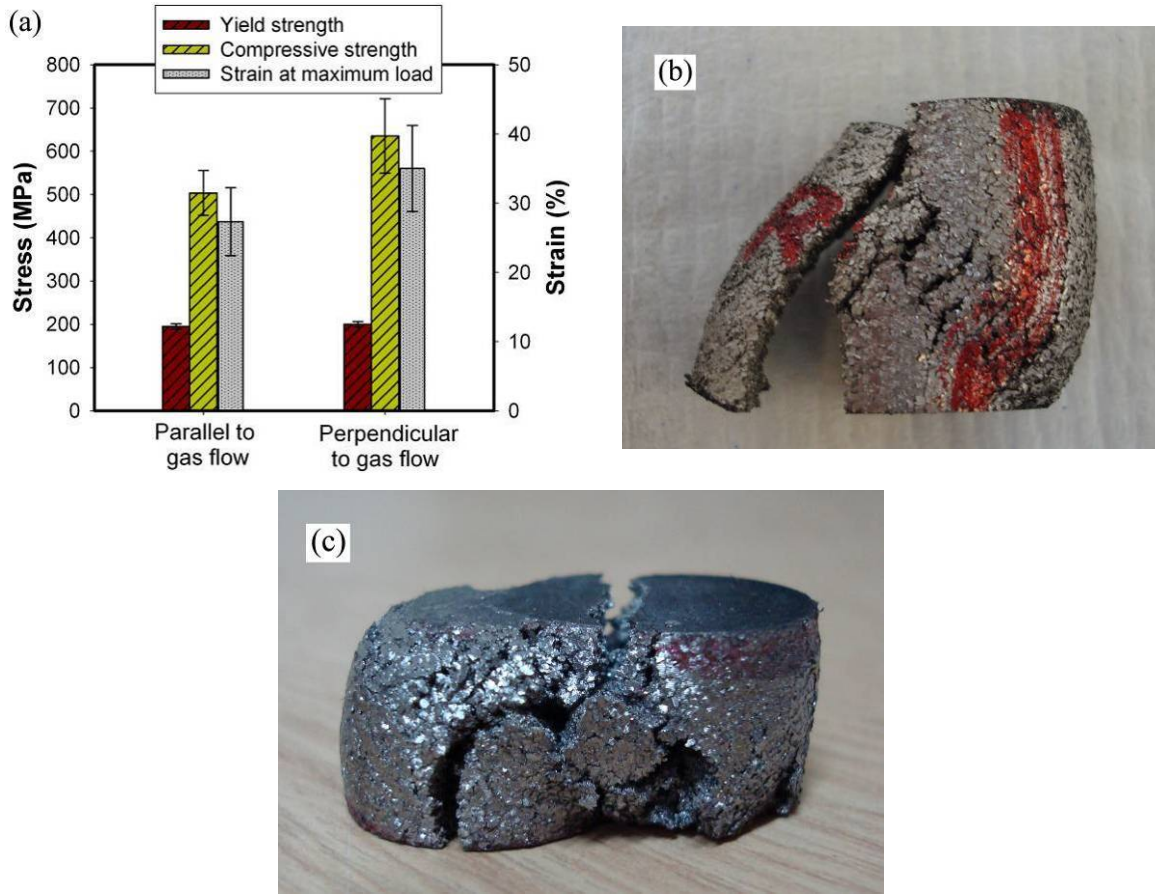


**Fig. 5.9:** (a) Compression properties of the parts produced parallel and perpendicular to gas flow; and typical apparent rupture of a compression specimen produced (b) parallel and (c) perpendicular to gas flow.

Fig. 5.9a also shows the strength and strain at maximum load of the parts produced perpendicular to gas flow under compressive stress demonstrating a relatively higher strength than those parallel to gas flow. This is while the apparent rupture, Fig. 5.9c, shows more characteristics of a common compression fracture (the rupture has developed along cone shape zones), though some irregularities still can be observed. These, higher compression strength and more common shaped ruptures, are perhaps because of a better bonding between additive layers in this case. In other words, laying the parts perpendicular to the gas flow (shorter length of part in direction of cooling) leads to a slower cooling and consequently less thermal stress and better bonding of additive layers in comparison with that parallel to gas flow. This hypothesis fits with lower delaminations observed in the parts fabricated perpendicular to gas flow in comparison with those laid parallel to gas flow (see Figs. 5.3 and 5.5).

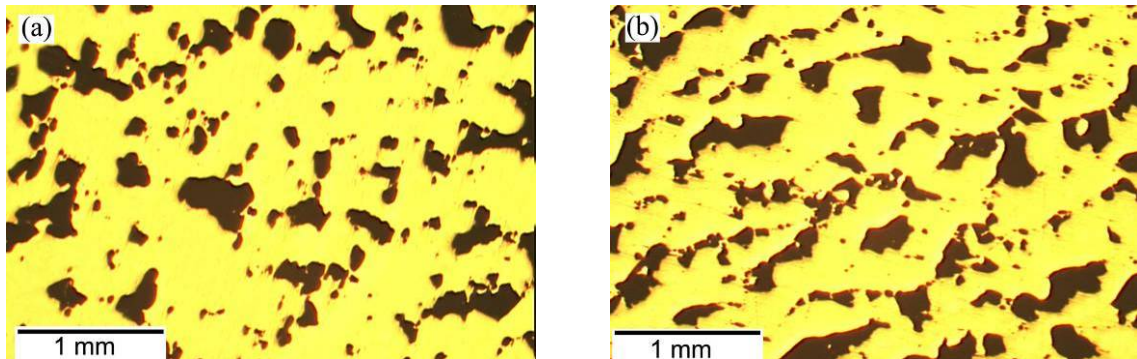
Generally, manufacturing of parts perpendicular to gas flow seems to lead to less thermal stresses, higher bonding strength, and better consolidation between layers rather than that of parallel to the gas flow. Moreover, it seems that the mechanical properties of individual parts were in a normal range of variation implying a less significant effect of part position compared to its direction. However, it has been observed that the relation between mechanical properties of SLM materials (such as their tensile, compression and shear strength) can be far from those that have been developed for traditionally fabricated metals (e.g. tensile and compression strength are usually considered the same or tensile strength is usually estimated 1.8 times the shear stress for metallic materials (Dieter, 1986, Guduru et al., 2005)).

### 5.3.3. Cross sectional analyses

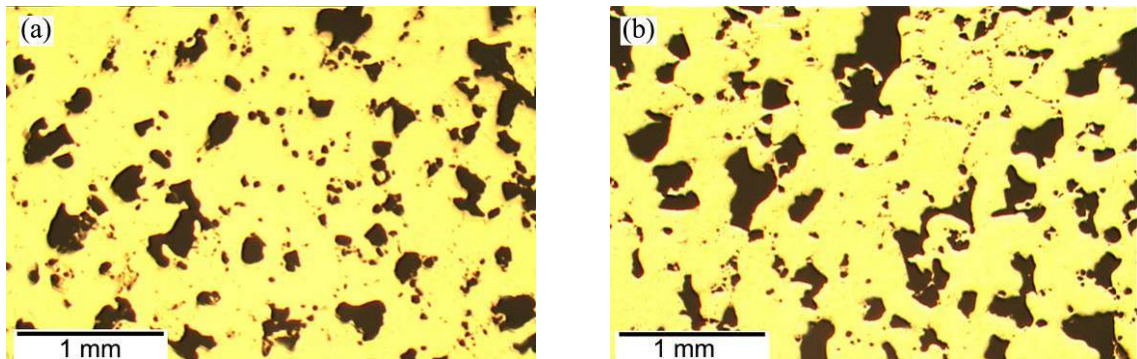
Cross sectional analyses were performed on polished samples to gain a better understanding of the material response under tension, shear and compression. Figs. 5.10 and 5.11 show the typical cross sectional micrographs of the samples produced parallel and perpendicular to gas flow respectively. These optical pictures demonstrate a variety of porous structures across the scanned area, but the parts still seem to be integrated where no porosity exists. In other words, the melting seems to be in a fair level despite the high porosity content. This confirms previous findings where very low tensile properties (attributed to high porosity content) and a fair shear strength (attributed to a fair bonding strength between particles) were observed.

Fig. 5.10a demonstrates large areas of porosity randomly distributed in XY cross section (across layers), while Fig. 5.10b shows a more regular porosity features developed in an angular format across build up direction (transversal section). This porosity format across many layers may lead to preferable progress of cracks under load application, which fits the results presented in Fig. 5.9b. In fact, this interconnected porosity across additive layers can join together under compression load, leading to layered rupture appearance and consequently lower compression strength of the part produced parallel to the gas flow (see Fig. 5.9). In contrast, Fig. 5.11 shows an irregular and random distribution of porosity in both XY and transversal section of the part produced perpendicular to gas flow. The corresponding outcome, shown in Fig. 5.9c, is higher compression strength and a more common shape of rupture as described before. In fact, the production of the parts

perpendicular to the gas flow may lead to a slower solidification. Thus, molten zones may find more time to penetrate the beneath layers compared to that of laying the parts parallel to the gas flow.



**Fig. 5.10:** Typical cross sectional micrograph of samples produced parallel to gas flow; (a) XY section and (b) transversal section.



**Fig. 5.11:** Typical cross sectional micrograph of samples produced perpendicular to gas flow; (a) XY section and (b) transversal section.

Overall, the above results were in confirmation with previous findings which showed tensile tests properly demonstrate the harmful influence of porosity, shear-punch tests illustrate the degree of melting and bonding strength, and compression testing implies layer consolidation issues. Accordingly, comparison of these tests can assist researchers to develop standards for qualification of the parts produced by SLM processes.

#### 5.4. Conclusions

The study has proved that the processing condition such as part layout and gas flow direction can significantly influence the quality and mechanical properties of stainless steel parts produced by the SLM technique. It was found that the temperature distribution and cooling rate caused by part layout and gas flow influences deformations appearing in final

parts. In fact, the gas has its lowest temperature at the entrance and then it is heated until exits from the opposite side. This develops a cooling direction along specimens. The larger the length of specimen in direction of gas flow, the bigger is the temperature difference. Therefore, the more homogeneous temperature distribution from laying the parts perpendicular to gas flow (smaller length of the parts in direction of cooling) results in the fewer delaminations. The porosity, another indication of quality of SLM parts, was exhibited to a high percentage, but it was not affected significantly by part layout.

Mechanical testing procedures consisting of tensile, compression and shear-punch tests are able to clarify the mechanical quality of the SLM parts. It was shown that an almost equal content of part porosity led to the fact that the part layout did not affect the tensile properties significantly. The bonding strength between the particles was investigated using the shear-punch test, demonstrating a reasonable melting degree. The compression tests showed that pores do not affect compressive strength leading to properties close to those of bulk material. The compressive results also clarified a stronger bonding between different layers of parts produced perpendicular to the gas flow than those produced parallel to the gas flow. The cross sectional analysis confirmed the observed behaviour of parts under tension, shear and compression load. Overall, this study suggests that process conditions need to be carefully selected in order to develop standards for SLM to fabricate reliable parts with a proper quality.

As seen, this chapter provides a valuable understanding of the performance of SLM machine and the effect of various parameters including part layout and gas flow. It also produces useful information about the SLM experimental equipment and the products that should be expected from this equipment, e.g. a high content of porosity is anticipated within the parts fabricated using the current machine (regardless of the location of the parts). This understanding provides experimental guidance on the following PhD research, especially where the small cubic parts are designed to provide a more consistent and comparable results.

---

# **Chapter 6: Preliminary Experiments to Fabricate In-Situ Al Matrix Composite through SLM of Al/Fe<sub>2</sub>O<sub>3</sub>**

---

## **6.1. Single Layer SLM Preliminary Experiments on an In-Situ Al Composite**

### **6.1.1. Introduction**

Particles reinforced aluminium alloy matrix composites which possess high-specific elastic modulus and strength are being widely used in the aerospace and automobile industries to satisfy applications such as pistons, drive shafts, suspension components, brake discs and structural components. As pointed out before (chapter 3), uniform distribution of the reinforcement particulates inside the matrix, good wettability between the particulate and matrix and suitable bonding strength of the reinforcement/matrix interface are considered as the major factors controlling the properties of this kind of material. To improve these factors, an in-situ technique are proposed to fabricate MMCs (Fu et al., 2006b, Fu et al., 2006a).

The SLM process has been used to manufacture net shape parts from various materials such as steels and titanium alloys, while there is little literature for SLM of Al parts and Al-matrix composites. Furthermore, the in-situ production of Al/Al<sub>2</sub>O<sub>3</sub> composite has not been carried out using SLM process. The objective of this preliminary study is to investigate the feasibility of the SLM process to fabricate Al/Al<sub>2</sub>O<sub>3</sub> composite with a view to inducing intermetallics and alumina properties to Al matrix through thermite reaction in the mixture of Al/Fe<sub>2</sub>O<sub>3</sub>. The addition of Fe<sub>2</sub>O<sub>3</sub> particles to Al powder to produce a composite could be significantly affected by processing parameters such as laser power, scanning speed and scanning strategy. This preliminary research studies the effects of SLM parameters on apparent conditions and microstructure of the single layer parts produced from the mixture of Al/Fe<sub>2</sub>O<sub>3</sub> and compares it to those from pure Al. It also identifies the appropriate SLM process parameters for generating suitable specimens for characterisation and testing, while

the successful ranges of parameters and overall performance of this process using this new material are unclear before the experiments.

### 6.1.2. Experimental procedure

Both pure Al powder and Al powder mixture with 5 wt% Fe<sub>2</sub>O<sub>3</sub> were used in SLM experiments for comparison investigation. A set of specimens from Al and Al/Fe<sub>2</sub>O<sub>3</sub> mixture were produced with 12 mm length and 12 mm width in an array format on a thick powder bed (~ 2-4 mm). The scan line spacing of 100 μm, while the scanning was carried out in y and y-x direction. The laser power of 17 W to 82 W and the scanning speed of 80 mm/s to 921 mm/s were used in subsequent steps, as shown in Table 6.1. The sample surfaces, to be investigated, were chemically etched at 85°C using a solvent composed of 25 mL H<sub>2</sub>SO<sub>4</sub>, 70 mL H<sub>3</sub>PO<sub>4</sub>, and 5 mL HNO<sub>3</sub>. Moreover, X-ray diffraction (XRD) was carried out to investigate the presence phases in material matrix structure.

**Table 6.1:** Summary of different steps to improve parameters

Step	Material	Laser power (W)	Scanning speed (mm/s)	Scan (direction)
1	Al/5wt%Fe <sub>2</sub> O <sub>3</sub> , Al	39, 52, 61, 70, and 82	80, 106, 125, 143, and 168	Once (y)
2	Al/5wt%Fe <sub>2</sub> O <sub>3</sub> , Al	17, 23, 28, 34, and 39	72, 97, 122, 144, and 168	Once (y)
3	Al/5wt%Fe <sub>2</sub> O <sub>3</sub> , Al	17, 23, 28, 34, and 39	168, 227, 284, 337, and 394	Once (y)
4	Al/5wt%Fe <sub>2</sub> O <sub>3</sub> , Al	17, 23, 28, 34, and 39	394, 530, 665, 787, and 921	Once (y)
5*	Al/5wt%Fe <sub>2</sub> O <sub>3</sub> , Al	17, 23, 28, 33, and 39	394, 530, 665, 787, and 921	Twice (y-x)

\*The parameters belong to the second laser scanning pass. The first pass parameters were laser power and scanning speed of 17 W and 921 mm/s respectively.

### 6.1.3. Results and discussion

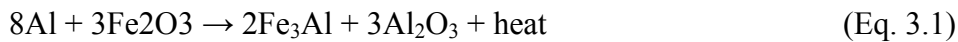
#### 6.1.3.1. SLM processing

The quality of SLM fabricated parts can be affected by many factors such as materials properties, powder bed characteristics and process parameters. Of the process parameters, laser power and scanning speed have been found as the most influential parameters (Hao et al., 2006). The relationship of these parameters with energy density, as the energy delivered to scanned area, can be described using the Eq. 2.1. According to this equation, increasing laser power and decreasing scanning speed or/and scan line spacing enhance the energy

density of laser which is necessary to melt the material. In fact, the greater the energy imparted to the powder, the greater the particle fusion (Hao et al., 2006) contributing to full melting. Although full melting has the main advantage of fabrication of a mostly dense product in one step, there are some disadvantages requiring further process control. These disadvantages are 1) the high temperature gradients during the process involving internal stresses or part distortion (Mercelis and Kruth, 2006), and 2) the risk of balling and dross formation in the melt pool resulting in bad surface finish (Kruth et al., 2007). Accordingly, to determine optimum parameters of SLM including laser power and scanning speed, various experiments were carried out as summarised in Table 6.1.

#### **6.1.3.2. Visual inspection during SLM process**

The apparent melting pool can be considered as an important phenomenon governing the quality of SLM process. So, to investigate appropriate process parameters, visual inspections on melting pool and laser spark were carried out during SLM process. Fig. 6.1 shows the spark irradiated during the SLM of Al and Al/Fe<sub>2</sub>O<sub>3</sub> mixture using laser power of 39 W and scanning speed of 72 mm/s. As seen from Fig. 6.1a, the energy induced by the laser generates a focused spot-shaped spark to produce pure Al parts, causing the Al particles melt together over a short distance area. In contrast, in Fig. 6.1b, the same parameters for SLM of Al/Fe<sub>2</sub>O<sub>3</sub> powder mixture lead to an expanded spark and melting pool. This spark and melting expansion can be attributed to thermite interaction between the mixture components which produce extra heat as well as new components with regards to following stoichiometric reaction (explained in literature review as Eq. 3.1):



The final phases, Al<sub>2</sub>O<sub>3</sub> and Fe<sub>3</sub>Al intermetallics, are formed by an in-situ chemical reaction in which Al reduces the iron oxide (Fan et al., 2006). The extra heat shows itself as an eruptive spark and extended melting pool. Furthermore, the extra heat causes a showering of particles (i.e. spreading the particles around). It might be assumed that sudden increase in volume and pressure of air trapped within the particles due to sudden increase in temperature lead to a force on particles which pushes them nearby.

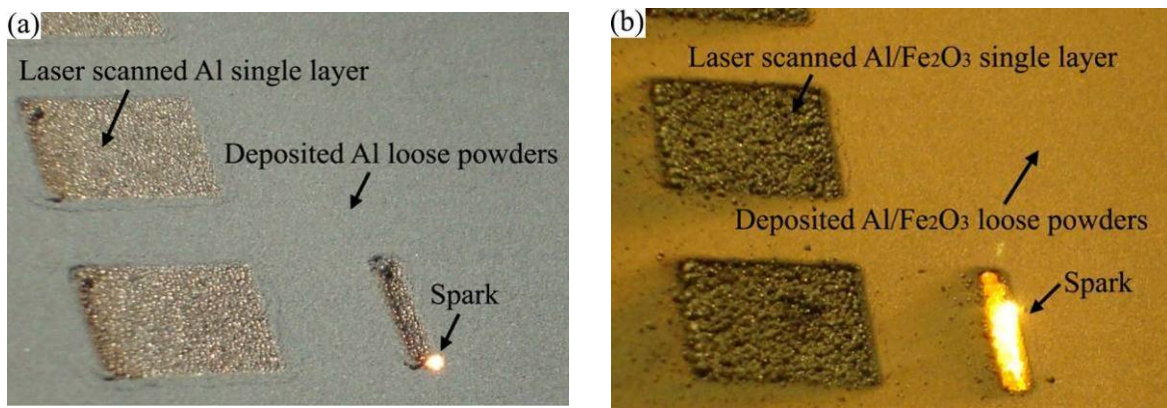


**Fig. 6.1:** The visual process development to fabricate single layer parts from (a) Al and (b) Al/5wt%Fe<sub>2</sub>O<sub>3</sub> mixture using laser power of 39 W and scanning speed of 72 mm/s within the second step. Reddish colour of Al/5wt%Fe<sub>2</sub>O<sub>3</sub> powder mixture in comparison with silver colour of Al powder is evident in the background.

Fig. 6.2 shows the laser beam fabricating parts from Al and Al/5wt%Fe<sub>2</sub>O<sub>3</sub> mixture with low laser energy from a laser power of 17 W and a scanning speed of 921 mm/s. This very low laser energy creates a barely enough heat to form a melting pool and melt Al powders (Fig. 6.2a), while a small and narrow spark is still observed from SLM process on the mixture of Al/5wt%Fe<sub>2</sub>O<sub>3</sub> (Fig. 6.2b). In fact, one may ascertain that this low energy can still activate a partial thermite reaction leading to a narrow melting pool. At this condition, the gradient temperature is low enough to prevent some drawbacks such as showering or formation of particles as drops.

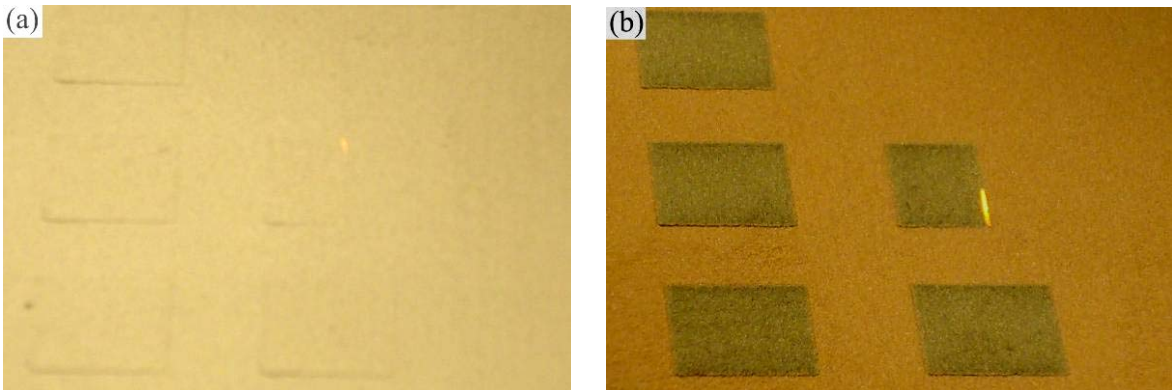


**Fig. 6.2:** The visual process development to fabricate single layer parts from (a) Al and (b) Al/5wt%Fe<sub>2</sub>O<sub>3</sub> mixture using laser power of 17 W and scanning speed of 921 mm/s.

### 6.1.3.3. Visual inspection after SLM process

A series of specimens were made from Al and Al/5wt%Fe<sub>2</sub>O<sub>3</sub> mixture using laser power of 39, 52, 61, 70, and 82 W and scanning speed of 80, 106, 125, 143, and 168 mm/s. The specimens shown in Fig. 6.3 indicate that addition of Fe<sub>2</sub>O<sub>3</sub> to Al influences the SLM

performance and manipulates the influence of processing parameters. As seen from Fig. 6.3a, the Al particles seem reasonably joined together leading to some acceptable parts. Alteration in parameters has significantly affected the quality of the parts. For example, increasing of laser power enlarges the melting area, but too large laser powers can lead to over melting. On the other hand, increasing scanning speed has improved the surface quality, but reduced degree of material melting. In the case of Al/Fe<sub>2</sub>O<sub>3</sub> mixture (Fig. 6.3b), the particles are placed together with a darker colour than that of pure Al material. These dark coloured particles are formed as spherical balls next to each other, referred to balling as a common instability in the first line scan of SLM process (Qi et al., 2007). As mentioned before, this can be due to the huge temperature difference between the melting powder and the adjacent powder or the high temperature gradients during the process, which form the melted particles as large drops (Mercelis and Kruth, 2006). Accordingly, it can be expected that the addition of Fe<sub>2</sub>O<sub>3</sub> to Al powder increases the gradient temperature and consequently the chance of balling phenomenon. The Fe<sub>2</sub>O<sub>3</sub> particles could increase the temperature gradient by both reducing heat conductivity (due to low heat conductivity of Fe<sub>2</sub>O<sub>3</sub> and/or introducing new non-metallic components to the system) and generating an extra local heat through exothermic in-situ interaction with Al particles.

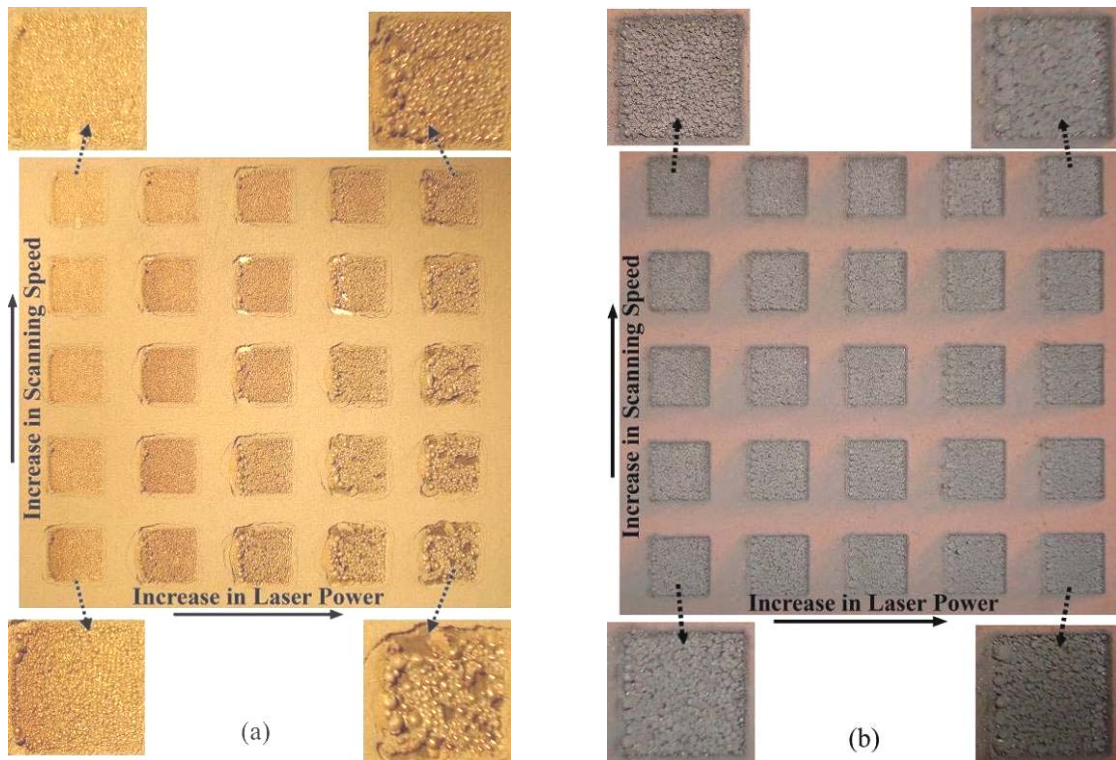


**Fig. 6.3:** The visual appearance of the parts fabricated from (a) Al and (b) Al/5wt%Fe<sub>2</sub>O<sub>3</sub> mixture using first set of parameters. Balling is evident especially in the parts made from Al/5wt%Fe<sub>2</sub>O<sub>3</sub>.

As seen from Fig. 6.3, various defects such as over melting (especially in Al) and balling (especially in Al/Fe<sub>2</sub>O<sub>3</sub> mixture) exist in the surface of the parts as a result of the high laser energy and high temperature gradient. To reduce high energy of laser as well as temperature gradient, it was decided to reduce the laser power through second set of parameters. So, the second set of experiment was designed to fabricate parts from Al and Al/Fe<sub>2</sub>O<sub>3</sub> mixture using laser powers of 17, 23, 28, 34, and 39 W and scanning speeds of 72, 97, 122, 144, and 168 mm/s. The results were positive for Al material and showed acceptable surface finish as well as melting degree. In contrast, the parts fabricated from Al/Fe<sub>2</sub>O<sub>3</sub> mixture were unsuccessful because of ball-shape materials forming within the SLM process (see Fig. 6.1b). However, it should be noted that reduction in laser power decreased the size of ball-shape particles in comparison with those from the first set of experiment.

Further studies were carried out through the third set of experiment, keeping the laser power constant and enhancing the scanning speed to 168, 227, 284, 337, and 394 mm/s. The results indicated that although higher scanning speed and lower laser power improved the appearance and consistency of the specimens from Al/Fe<sub>2</sub>O<sub>3</sub> mixture, the corresponding low laser energy led to an inadequate melting of Al particles. In fact, the extra energy arising from thermite reaction could compensate the low energy of the laser and contribute to providing sufficient heat to melt the Al/Fe<sub>2</sub>O<sub>3</sub> mixture. Therefore, this set of parameters can lead to an appropriate melting in the mixture of Al/Fe<sub>2</sub>O<sub>3</sub>, but a less effective melting in Al powders.

The fourth set of experiment was designed for a further increase of scanning speeds to 394, 530, 665, 787, and 921 mm/s. The results demonstrated the corresponding laser energy are inadequate to develop melting in Al powders leading to partially sintered parts, in contrast, the laser could develop a fine and narrow melting pool on Al/Fe<sub>2</sub>O<sub>3</sub> mixture resulting in parts with acceptable visual condition (see Fig. 6.2). However, the specimens made from Al/Fe<sub>2</sub>O<sub>3</sub> mixture were not composed of firmly joined particles, indicating a need for further improvement. It should be addressed that very high scanning speed for manufacturing parts from Al/Fe<sub>2</sub>O<sub>3</sub> mixture not only has a positive influence on surface quality and visual condition but also reduce cost through enhancing manufacturing rate.

In the fifth set of experiment, the single layer specimens were scanned twice. The laser beam was first fired and traversed in y direction with laser power and scanning speed of 17 W and 921 mm/s. Then, the laser scanned the same layer twice with various laser powers of 17, 23, 28, 34, and 39 W and scanning speeds of 394, 530, 665, 787, and 921 mm/s. This double scanning strategy was chosen to enhance the melting of powders due to inadequate melting and partial sintering in the fourth set of experiment. For pure Al powders, the single layer specimens were not fully melted despite repeated scanning strategy providing more energy to reach a higher degree of melting. In contrast, for Al/Fe<sub>2</sub>O<sub>3</sub> powder mixture the range of a laser power of 17-23 W and a scanning speed of 394-921 mm/s led to single layer specimens with an acceptable appearance. However, further increase in laser power resulted in a strong spark during SLM process and, subsequently, the formation of ball-shape particles on specimen surfaces (Fig. 6.4). The results of fifth set of experiment imply that repeated scanning strategy (with different parameters for first and second scanning) could potentially provide an optimal condition to satisfy good surface finish as well as high degree of melting.

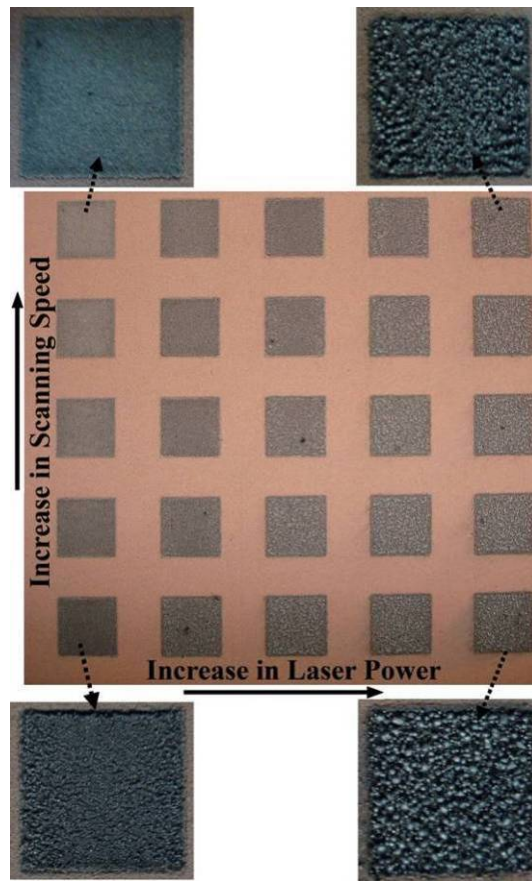


**Fig. 6.4:** The visual appearance of the parts fabricated from Al/Fe<sub>2</sub>O<sub>3</sub> mixture using fifth set of parameters.

#### **6.1.3.4. Microstructural investigations**

Fig. 6.5 shows optical microscopic graphs of the single layer specimens fabricated from Al using laser power of 82 W and scanning speed of 80 mm/s. As seen, the Al matrix has a fine dendritic structure with dendrite arm spacing of about 5-20  $\mu\text{m}$ . The interdendritic regions are common locations for placing defects such as pores. For example, during solidification, excess hydrogen is rejected from solution and it recombines as molecular gas which may be entrapped in the solid structure leading to porosity, notably in interdendritic regions (Polmear, 2005). Dendritic matrix is a common structure obtained from Al casting. In casting, there are attempts to increase the rate of solidification which has a desirable influence to produce finer dendrite arm spacings, which in turn reduces microsegregation in interdendritic regions (Polmear, 2005). Fortunately, in this work, rapid solidification in the SLM process led to an acceptable microstructure (fine dendrite arm spacing), as observed in Fig. 6.5.

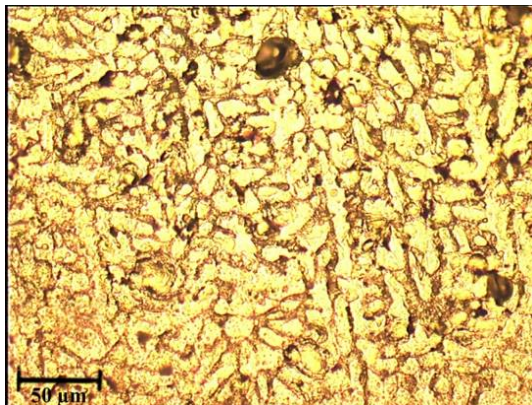


**Fig. 6.5:** Typical optical microstructural view of the Al part fabricated using laser power of 82 W and scanning speed of 80 mm/s.

Fig. 6.6 exhibits a very fine granular matrix with a grain size of about 5-20  $\mu\text{m}$  from the single layer specimens made from Al/5wt% $\text{Fe}_2\text{O}_3$  mixture using laser power of 82 W and scanning speed of 168 mm/s. This fine grain structure is highly desirable, being different from that of dendritic Al matrix shown in Fig. 6.5. This new structure could be attributed to the in-situ consolidated compositions originating from the thermite reaction between Al and  $\text{Fe}_2\text{O}_3$ . These new compositions (perhaps  $\text{Al}_2\text{O}_3$  and Al-Fe intermetallics according to Eq. 3.1) could act as nucleation sites to facilitate heterogeneous nucleation (Smallman and Bishop, 1999) of melted Al powders resulting in a fine and granular grain structure. It should be noted that although the specimen was fabricated from Al/ $\text{Fe}_2\text{O}_3$  mixture, only one phase is apparent in the matrix microstructure. In other words, there is no evidence of

secondary phases including new components. To explain this phenomenon, it can be postulated that i) the new components were too small to be detected by the applied technique or ii) the observed phase is a super saturated solid solution which has resolved secondary phases. However, more sophisticated and accurate material characterisations are required to fully elucidate this phenomenon.

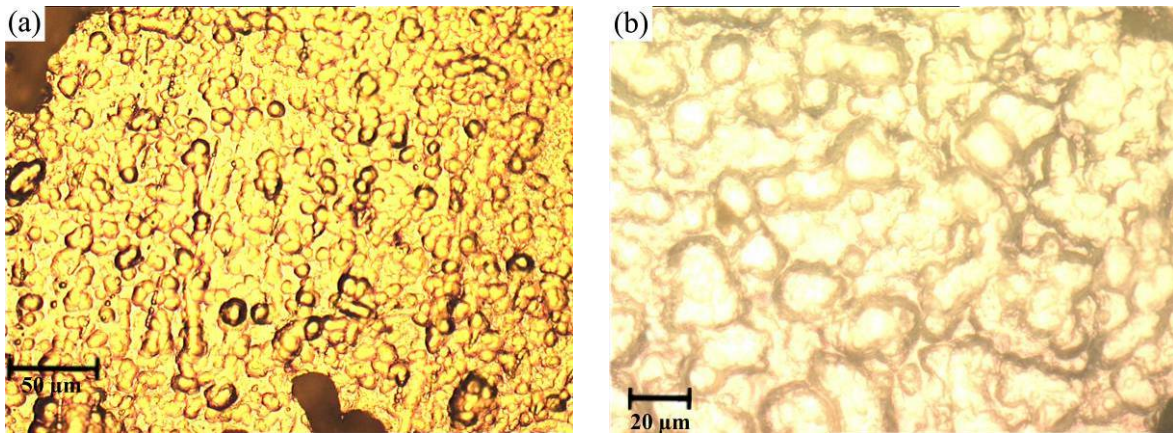


**Fig. 6.6:** (a) Typical optical microstructural views of the part fabricated from Al/5wt% $\text{Fe}_2\text{O}_3$  mixture using laser power of 82 W and scanning speed of 168 mm/s and (b) an image of higher magnification.

#### 6.1.3.5. Phase analysis using X-ray diffraction (XRD)

The phases of a specimen made from the SLM of Al/ $\text{Fe}_2\text{O}_3$  mixture with a laser power of 82 W and a scanning speed of 168 mm/s were analysed by XRD. The result, shown in Fig. 6.7, only exhibits diffraction peaks of Al. This is in confirmation with Fig. 6.6 showing one phase material structure. It can be postulated that too low concentration of new components prevented detection by XRD and masked their peaks by the peaks of background, or the observed phase is a super saturated solid solution and no secondary phases exist.

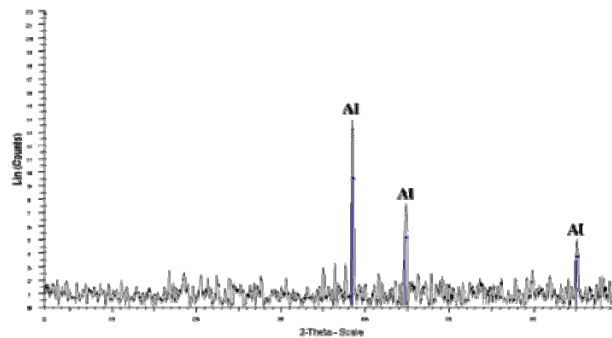


**Fig. 6.7:** XRD diffraction pattern of the of the part fabricated from Al/5wt% $\text{Fe}_2\text{O}_3$  mixture using laser power of 82 W and scanning speed of 168 mm/s.

#### **6.1.4. Conclusions**

This preliminary single-layer study investigated the feasibility of selective laser melting (SLM) to directly fabricate an Al matrix composite by an in-situ technique from the Al/5wt%Fe<sub>2</sub>O<sub>3</sub> mixture and compared it to SLM of pure Al powders. The visual inspection revealed that the Al/Fe<sub>2</sub>O<sub>3</sub> powder mixture performed exothermic reaction in the SLM process and released the extra heat to cause eruptive spark and extend melting pool compared to pure Al in the SLM process.

It was found that the addition of Fe<sub>2</sub>O<sub>3</sub> in the Al powder significantly influences the SLM process parameters. The appropriate parameters for SLM of Al/Fe<sub>2</sub>O<sub>3</sub> mixture are different from those of Al. This could be attributed to the extra heat originating from thermite reaction and alternation in heat conductivity within Al/Fe<sub>2</sub>O<sub>3</sub> mixture. Furthermore, the material processing phenomena for the SLM of Al and Al/Fe<sub>2</sub>O<sub>3</sub> mixture were pronounced differently, i.e., more balling and showering was shown for SLM of Al/Fe<sub>2</sub>O<sub>3</sub> mixture in comparison with that from Al. It was found that a repeated scanning strategy might manipulate the melting and fusion of the particles to produce acceptable net-shape specimens.

Different microstructural structures were observed for the single layer specimens fabricated from Al and Al/5wt%Fe<sub>2</sub>O<sub>3</sub> mixture. The Al specimens showed a dendritic structure while, in contrast, the part from Al/5wt%Fe<sub>2</sub>O<sub>3</sub> mixture exhibited a granular structure that could lead to more desirable mechanical properties. This could be attributed to the in-situ formed compositions originating from the thermite reaction between Al and Fe<sub>2</sub>O<sub>3</sub> and acting as nuclei to facilitate heterogeneous nucleation. It was unexpected that the optical microscopy and XRD examinations showed no secondary phases in the part fabricated from Al/Fe<sub>2</sub>O<sub>3</sub> mixture. This is most likely because of low contents and small sizes of secondary phases or formation of a super saturated solid solution with no secondary phases.

## **6.2. Preliminary Multilayer SLM Experiments on In-Situ Formation of Particle Reinforced Al Matrix Composite**

### **6.2.1. Introduction**

The single layer preliminary studies on SLM of Al/5wt%Fe<sub>2</sub>O<sub>3</sub> powder mixture (presented in previous section) demonstrated the capability of the SLM process as a new manufacturing technique to activate the in-situ reaction in the mixture of Al/Fe<sub>2</sub>O<sub>3</sub>. In continuation, this section is dedicated to preliminary studies on the fabrication of multi-layer net-shape Al matrix composite parts. The SLM process should enable the manufacturing Al composite parts with complicated geometries as well as good reinforcement distributions, while other techniques are not (or hardly) able to do so. Moreover, the new technique could produce a novel in-situ Al matrix composite reinforced by very fine oxides and intermetallics to deliver high mechanical performance, whereas conventional techniques usually lead to large reinforcement particles making the material very brittle. The success of this development could provide new means of making high performance Al matrix composite components, extending the commercial applications of the Al matrix composite in various industrial sectors.

### **6.2.2. Experimental procedure**

The multilayer three-dimensional specimens with cubic shapes (10 mm × 10 mm × 6 mm dimensions) were fabricated by the SLM of Al/5wt%Fe<sub>2</sub>O<sub>3</sub> powder mixture. Scan line spacing was set 0.05 mm and powder layer thickness ( $t$ ) was 0.05 mm. Each layer scanned twice. A multilayer sample produced with laser power ( $P$ ) of 91 W and scanning speed ( $v$ ) of 0.14 m/s was selected for material characterisation. After polishing and chemical etching (95 ml water, 2.5 ml HNO<sub>3</sub>, 1.5 ml HCl and 1.0 ml HF) of the sample XY cross-section (i.e. in the plane of one layer), the microstructure was viewed using optical and SEM microscope. Phase identification of product was carried out using XRD system.

## 6.2.3. Results and discussion

### 6.2.3.1. Multilayer part processing

A series of multilayer three-dimensional cubic parts were produced from the Al/5wt%Fe<sub>2</sub>O<sub>3</sub> mixture using SLM process, as seen in Fig. 6.8. This demonstrates that SLM process can be used as a novel in-situ technique to produce Al net-shape matrix composite parts.

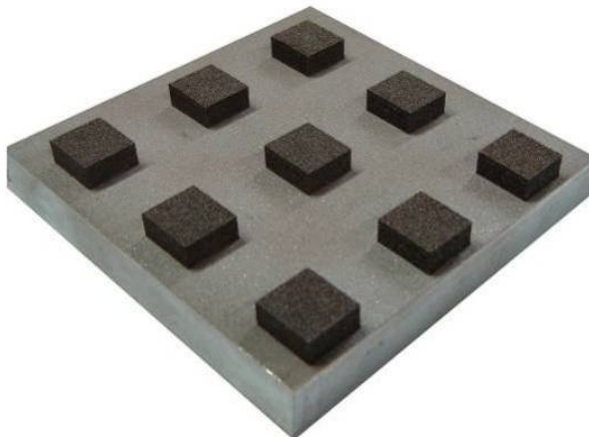


**Fig. 6.8:** The typical multilayer cubic parts (10 mm × 10 mm × 6 mm) produced by SLM of Al/5wt%Fe<sub>2</sub>O<sub>3</sub> powder mixture.

### 6.2.3.2. Microstructural characterisation and phase identification

Fig. 6.9a shows optical microstructural images of a three-dimensional part fabricated from Al/5wt%Fe<sub>2</sub>O<sub>3</sub> mixture ( $P \sim 91$  W,  $v \sim 0.14$  m/s). The images exhibit a random grain structure, leading to uniform properties. Moreover, grains and relevant grain boundaries contain a series of very fine particles, but magnification of optical microscopy is not enough to characterise them. Further SEM analysis has been carried out (on previous sample) to characterise very fine phases in the microstructure. Fig. 6.9b-c shows the typical structural appearance of the sample, demonstrating the presence of very fine particles inside grains and in boundaries. The particles should be in the form of aluminium oxides and Al-Fe(-O) combinations (Al, O, and Fe are the main elements). The particles are very fine (perhaps 50-2000 nm) in size, have a strong bonding in their interface with the matrix, and are distributed uniformly. These particles act as reinforcement phases, with very high strength of ceramics and intermetallics. This is highly desirable in Al matrix composites leading to desirable mechanical properties. Overall, the results indicate that the particle

reinforced Al matrix composite has been produced through SLM activated in-situ reaction process.

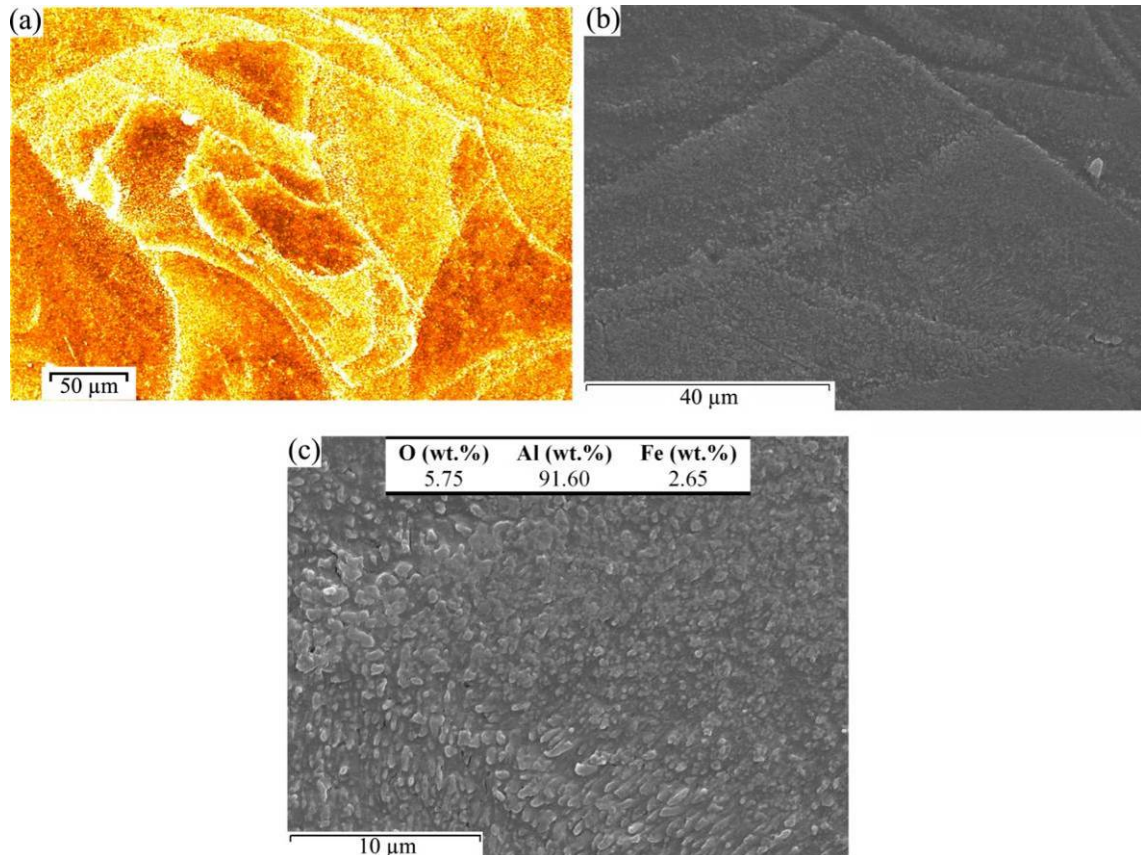


**Fig. 6.9:** Typical microstructural views of the SLM part fabricated from Al/5wt% $\text{Fe}_2\text{O}_3$  mixture; a) optical microscopy image showing random grain structure, b) SEM overall view of grain structure and c) previous image with higher magnification showing fine particles formed inside grains and boundaries (overall chemical composition was acquired by EDS).

The XRD pattern of the in-situ Al matrix composite part is shown in Fig. 6.10. It shows that the peaks correspond to those of Al and  $\text{Fe}^{2+}\text{Al}_2\text{O}_4$  (iron aluminium oxide). The diffraction peaks for  $\alpha\text{-Al}_2\text{O}_3$  (alumina) are also well detected, though the intensity is comparatively weak. The results indicate that the SLM of Al/5wt% $\text{Fe}_2\text{O}_3$  mixture powder generates combinations such as  $\text{Al}_2\text{O}_3$  and  $\text{Fe}^{2+}\text{Al}_2\text{O}_4$  which could reinforce the Al matrix (Figs. 6.9 and 6.10). The Al matrix is most likely saturated by Fe due to rapid solidification from a high temperature during SLM process. Previous research showed that rapid solidification assists saturation of Al by other elements (Rajabi et al., 2008, Wong and Liang, 1997). In the case of resolving Fe in Al matrix, it contributes to strengthening by solution hardening. The unresolved Fe can appear in XRD spectrum in the form of  $\text{Fe}^{2+}\text{Al}_2\text{O}_4$  or other Al-Fe intermetallics.

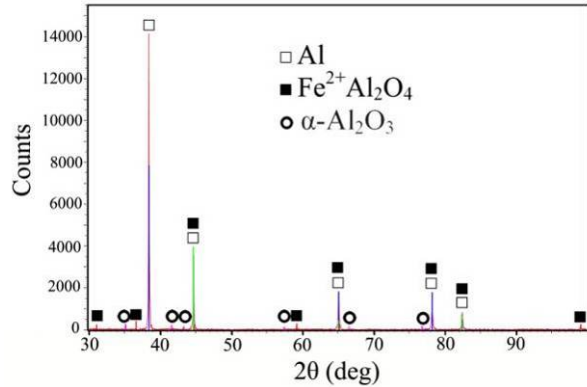


**Fig. 6.10:** The XRD pattern of the SLM sample shown in previous figure (in addition to present phases, the weak peaks of  $\text{Al}_{13}\text{Fe}_4$  may be observed in the sample spectrum).

#### 6.2.4. Conclusions

In summary, selective laser melting (SLM) was used to process Al/5wt% $\text{Fe}_2\text{O}_3$  powder mixture to make multilayer three dimensional (3D) net-shape parts. It was found that SLM can directly produce in-situ formed Al matrix composite parts from the Al/ $\text{Fe}_2\text{O}_3$  mixture using appropriate parameters. The SEM images showed very fine particles uniformly distributed in the Al matrix, establishing a good interface with the matrix. The particles (as reinforcements) mainly appeared to be minerals and ceramics such as  $\text{Fe}^{2+}\text{Al}_2\text{O}_4$  and  $\text{Al}_2\text{O}_3$  (revealed by XRD). These well-distributed reinforcing particles are expected to provide enhanced mechanical properties.

This preliminary study proved the feasibility and potential of fabricating Al composites using the SLM process. This assured a very promising prospective for future studies, investigating the SLM behaviour of this new material and the influence of various parameters such as layer thickness, laser power and scanning speed, proportion of  $\text{Fe}_2\text{O}_3$ , Al alloy composition, and hot isostatic pressing (HIP) post-treatment. The results of these investigations will be presented in part III (including 5 chapters), which comprehensively explore various aspects of in-situ fabrication of Al matrix composites by using SLM of Al/ $\text{Fe}_2\text{O}_3$  powder mixture.

# **Part Three: In-situ Fabrication of Al Matrix Composites by Using Selective Laser Melting of Al/Fe<sub>2</sub>O<sub>3</sub> Powder Mixture**

---

# **Chapter 7: Experimental Investigation on Selective Laser Melting Behaviour and Processing Windows of In-Situ Reacted Al/Fe<sub>2</sub>O<sub>3</sub> Powder Mixture**

---

## **7.1. Introduction**

As demonstrated in previous chapter, the preliminary studies have proved the feasibility and potential of SLM as a novel production method to manufacture high performance *in-situ* formed Al metal matrix composite via an exothermic reaction in the mixture of Al/Fe<sub>2</sub>O<sub>3</sub>. However, there is still a lack of understanding on the melting and consolidation behaviour of this family of materials and consequently it has not yet fully exploited the potential of the SLM of Al alloy and composites for industrial application. To address this issue, this work has investigated the processing windows to execute SLM of the mixture of Al with 5, 10, and 15 wt% Fe<sub>2</sub>O<sub>3</sub>. It analyses the materials behaviours and the resulting material properties including surface roughness, density and hardness over a wide range of laser powers and scanning speeds. The influence of additional Fe<sub>2</sub>O<sub>3</sub> on the processing windows (sketched on the basis of surface roughness, density and hardness) is discussed in conjunction with a brief microstructural analysis. The microstructural characteristics of these SLM processed materials are comprehensively reported in upcoming chapters.

## **7.2. Materials and Experiments**

Multilayer SLM samples were fabricated from Al/5wt%Fe<sub>2</sub>O<sub>3</sub>, Al/10wt%Fe<sub>2</sub>O<sub>3</sub> and Al/15wt%Fe<sub>2</sub>O<sub>3</sub>, as explained in section 6.2.2, using  $P \sim 39\text{-}91$  W and  $v \sim 0.5\text{-}0.14$  m/s. After fabrication, the surface roughness, hardness and density were measured. Optical microscopy investigations were carried out after chemical etching at room temperature using a solvent composed of 95 ml water, 2.5 ml HNO<sub>3</sub>, 1.5 ml HCl and 1.0 ml HF.

## 7.3. Results

### 7.3.1. Visual inspections

As mentioned, the apparent melting pool can be considered as an important parameter for process control and optimisation. So, the visual inspections on melting pool and laser spark were recorded during SLM process. Fig. 7.1a-b shows the spark to fabricate parts from Al/5wt%Fe<sub>2</sub>O<sub>3</sub> and Al/15wt%Fe<sub>2</sub>O<sub>3</sub> powder mixture using the same laser power and scanning speed. As seen from Fig. 7.1a, the energy produced by the laser creates a focused spot-shaped spark to produce Al/5wt%Fe<sub>2</sub>O<sub>3</sub> parts, causing the material melting within a relatively small area. In contrast, in Fig. 7.1b, the same parameters used to fabricate parts from Al/15wt%Fe<sub>2</sub>O<sub>3</sub> powder mixture lead to a clearly larger spark and larger melting area. Moreover, the showering of powders (pushing powders around and vaporising melted material) is more evident in the presence of higher Fe<sub>2</sub>O<sub>3</sub> content (15 wt% - Fig. 7.1b). This may affect the surface morphology of melted layer and overall surface finish of SLM parts. The top surface of parts made from Al/5wt%Fe<sub>2</sub>O<sub>3</sub> powder mixture is composed of small individual sphere-shaped particles (like balls), as seen from Fig. 7.1c. In contrast, the top surface of parts made from Al/15wt%Fe<sub>2</sub>O<sub>3</sub> powder mixture is fused and seems as interconnected valley-type spheres (Fig. 7.1d). It is likely that the extra heat released from higher thermite mixture (i.e. 15wt% Fe<sub>2</sub>O<sub>3</sub> in this case) enlarges the laser melting pool leading to connections between melted spheres. It is interesting to note that Fe<sub>2</sub>O<sub>3</sub> powder is dark red, and causes a more reddish colour for Al/15wt%Fe<sub>2</sub>O<sub>3</sub> powder mixture (Fig. 7.1b) than that of Al/5wt%Fe<sub>2</sub>O<sub>3</sub> (Fig. 7.1a).

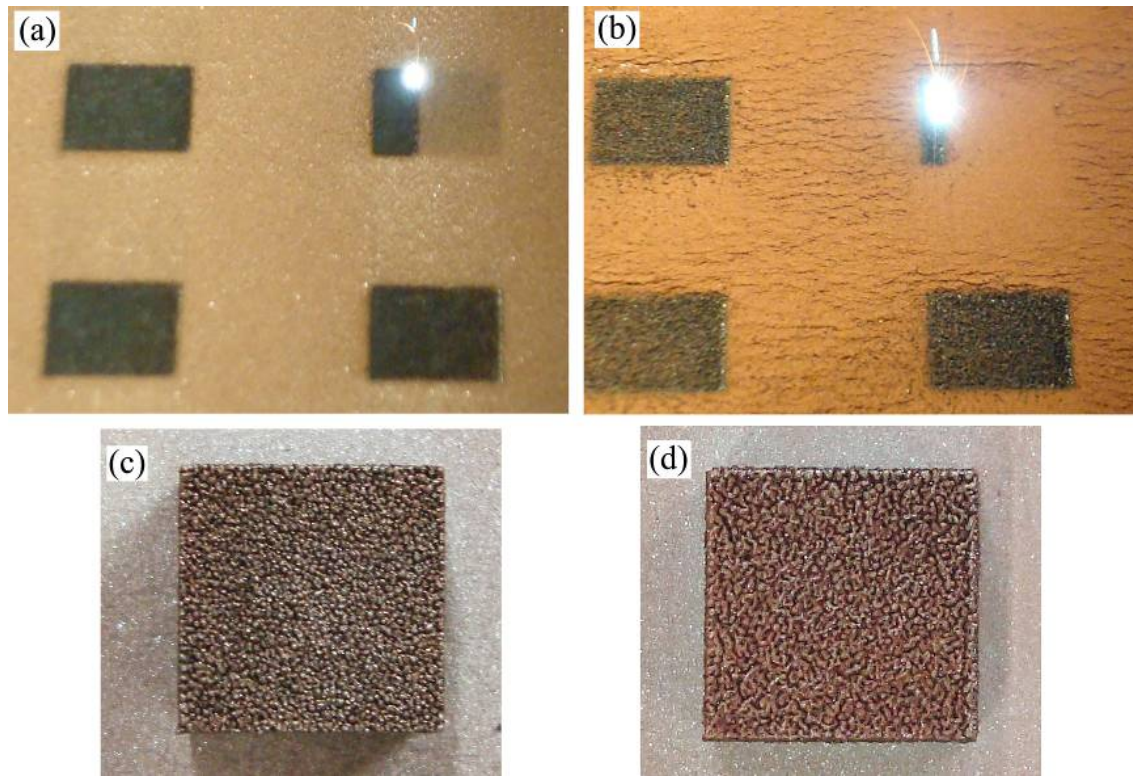


**Fig. 7.1:** The visual appearance of parts being fabricated from (a) Al/5wt%Fe<sub>2</sub>O<sub>3</sub> and (b) Al/15wt%Fe<sub>2</sub>O<sub>3</sub> powder mixture using  $P = 82$  W and  $v = 0.33$  m/s. The surface appearance of final parts manufactured from (c) Al/5wt%Fe<sub>2</sub>O<sub>3</sub> and (d) Al/15wt%Fe<sub>2</sub>O<sub>3</sub> powder mixture.

An example of the resulting array of final cubic-shaped parts is shown for Al/5wt%Fe<sub>2</sub>O<sub>3</sub>, Al/10wt%Fe<sub>2</sub>O<sub>3</sub> and Al/15wt%Fe<sub>2</sub>O<sub>3</sub> in Fig. 7.2a-c illustrating that parts have been successfully manufactured almost all over the wide range of parameters ( $P = 39$ -91 W and  $v = 0.5$ -0.14 m/s), leading to an array of solid parts.

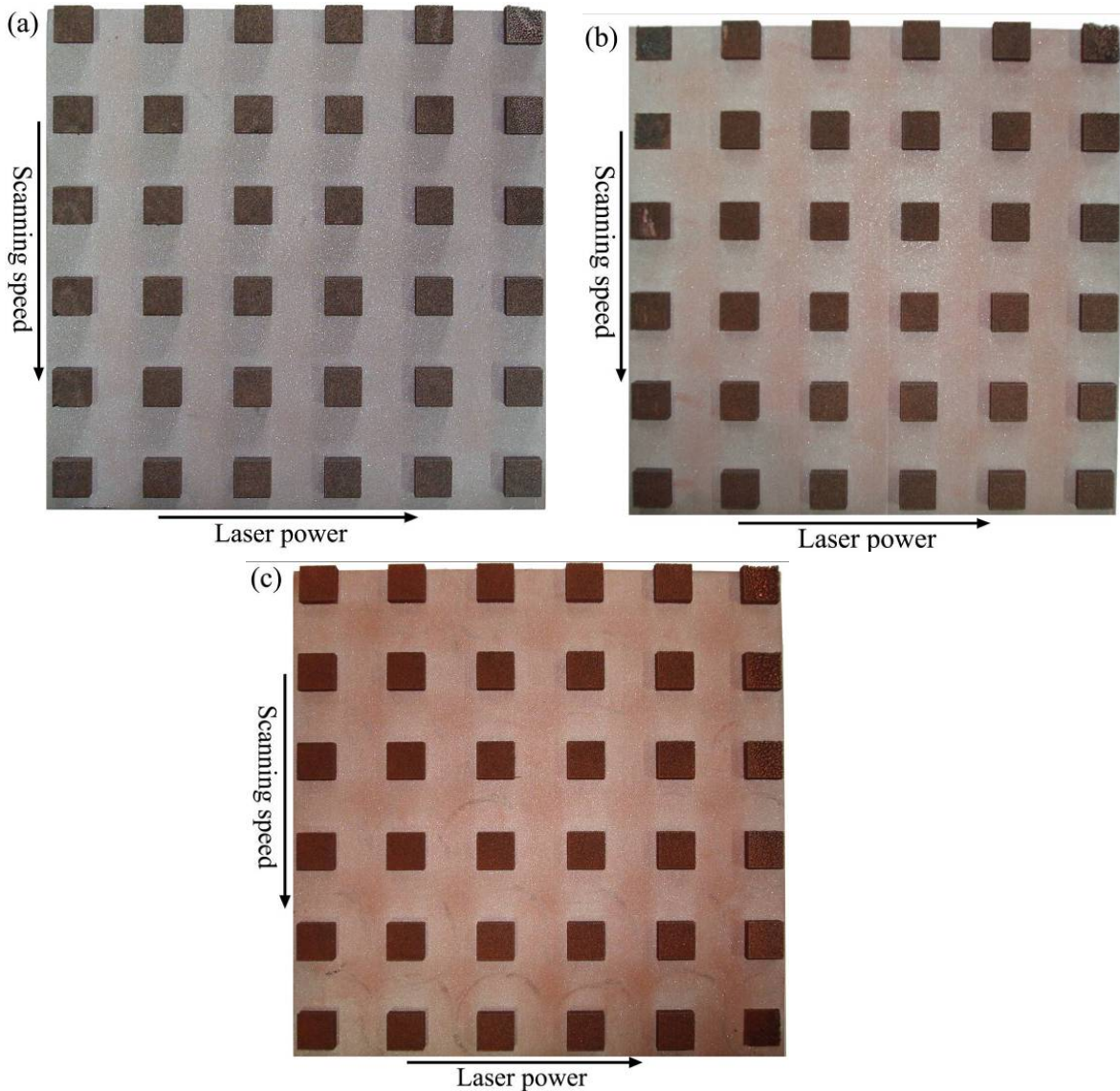


**Fig. 7.2:** The visual appearance of parts fabricated from (a) Al/5wt% $\text{Fe}_2\text{O}_3$ , (b) Al/10wt% $\text{Fe}_2\text{O}_3$ , and (c) Al/15wt% $\text{Fe}_2\text{O}_3$  powder mixture ( $P = 39\text{--}91 \text{ W}$  and  $v = 0.5\text{--}0.14 \text{ m/s}$ ).

### 7.3.2. Surface roughness

According to the surface roughness measurements, presented in Fig. 7.3, the highest speed of 0.5 m/s generally leads to relatively low surface roughness ( $R_a$ ) at the range of 25–29  $\mu\text{m}$  for Al/5wt% $\text{Fe}_2\text{O}_3$  (Fig. 7.3a) and 22–27  $\mu\text{m}$  for Al/10wt% $\text{Fe}_2\text{O}_3$  (Fig. 7.3b), while the highest speed of 0.5 m/s does not result in the lowest relative surface roughness for the Al/15wt% $\text{Fe}_2\text{O}_3$  which has a  $R_a$  at the range of 23–32  $\mu\text{m}$  (e.g. one may consider 51 W and 0.14 m/s as an optimum laser power and scanning speed for Al/15wt% $\text{Fe}_2\text{O}_3$ ). Fig. 7.3 also shows that increasing in laser power has been accompanied with increasing in the surface roughness as a general trend in all diagrams, though there might appear a maximum value

in the increasing  $R_a$  curve. The increase of  $\text{Fe}_2\text{O}_3$  content has also affected the value of surface roughness of parts. The data suggests that higher  $\text{Fe}_2\text{O}_3$  content first decreases the surface roughness, though this influence may be weakened in high proportions of  $\text{Fe}_2\text{O}_3$  contents (e.g. 10-15 wt%).

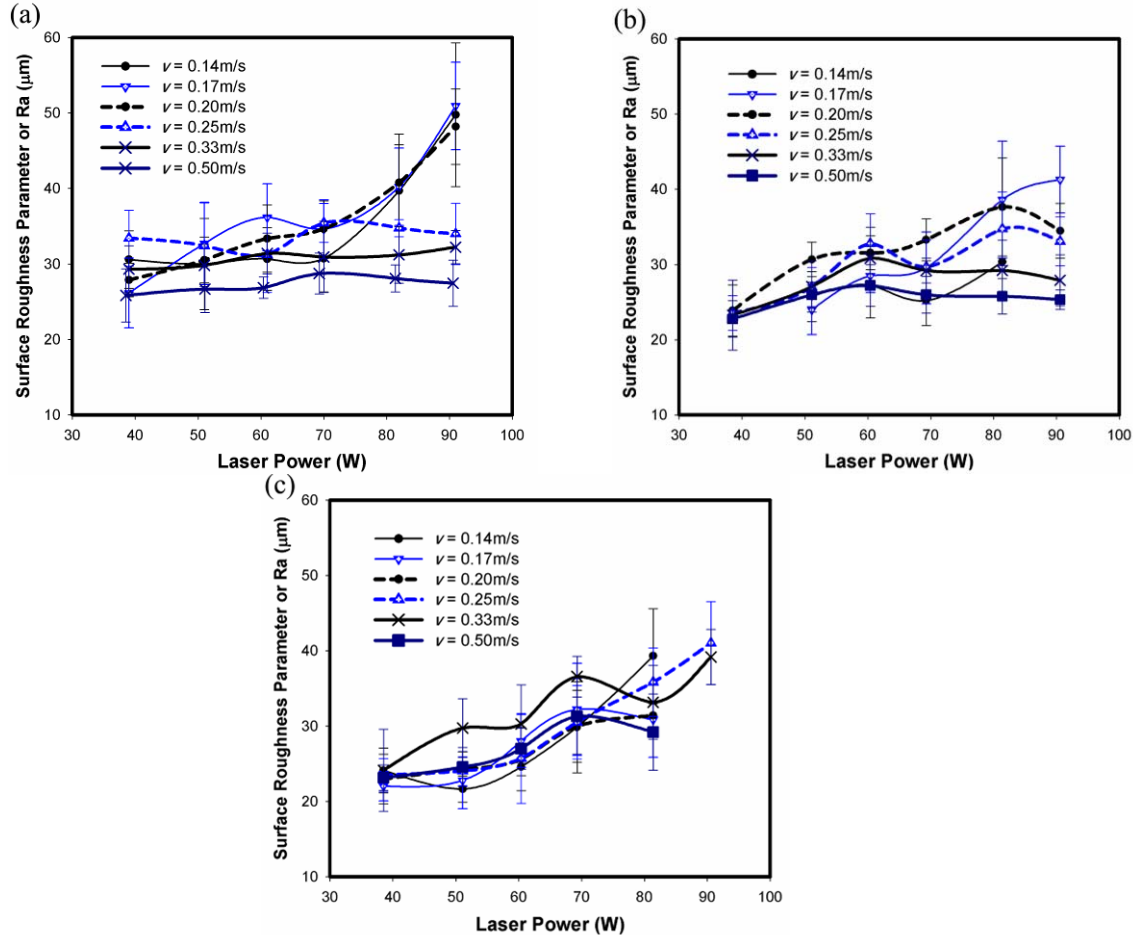


**Fig. 7.3:** Surface roughness properties of the SLM parts made from Al powder mixed with (a) 5 wt%, (b) 10 wt% and (c) 15 wt%  $\text{Fe}_2\text{O}_3$  powder in different laser powers and scanning speeds.

### 7.3.3. Density

The results of density vs. laser power and scanning speed are plotted in Fig. 7.4. Fig. 7.4a shows the general trend of density vs. laser power for Al/5wt%Fe<sub>2</sub>O<sub>3</sub> where density increases with laser power until it reaches a peak and then it falls with further increase of laser power. There is also an optimum laser power and speed to achieve the highest density which is 82 W and 0.25 m/s in this case. In the case of Al/10wt%Fe<sub>2</sub>O<sub>3</sub> (see Fig. 7.4b) the highest density has appeared in relatively lower laser power of about 50 W when the laser speed is low (0.14-0.20 m/s), while in the cases of higher scanning speeds (0.25-0.5 m/s)

the highest density can be observed in higher laser powers ( $\sim 70$ - $91$  W). As seen from Fig. 7.4c, an increase in  $\text{Fe}_2\text{O}_3$  content to 15 wt% further affects the density, i.e. density generally increases with decrease in laser power, which is different from what observed for 5 wt%  $\text{Fe}_2\text{O}_3$  content. A comparison between Fig. 7.4a-c illustrates that increase of  $\text{Fe}_2\text{O}_3$  content to 10 wt% (Fig. 5b) has led to a general drop in density in the range of 1.78– $2.10 \text{ g/cm}^3$  compared to parts made from  $\text{Al}/5\text{wt\%}\text{Fe}_2\text{O}_3$  in the range of 1.90– $2.30 \text{ g/cm}^3$  (Fig. 7.4a). Whereas a further increase in  $\text{Fe}_2\text{O}_3$  may change this trend and increase the density (Fig. 7.4c) to a range of 1.90– $2.20 \text{ g/cm}^3$ .

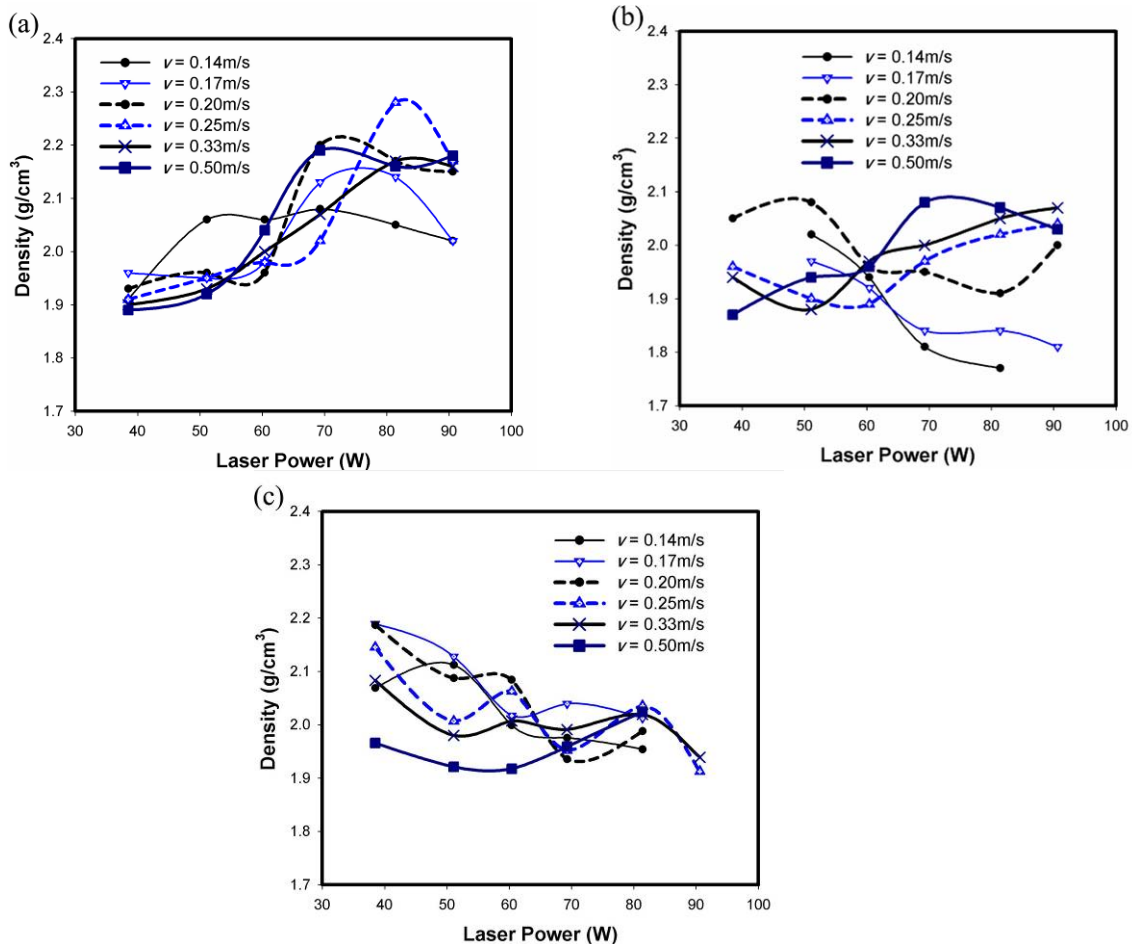
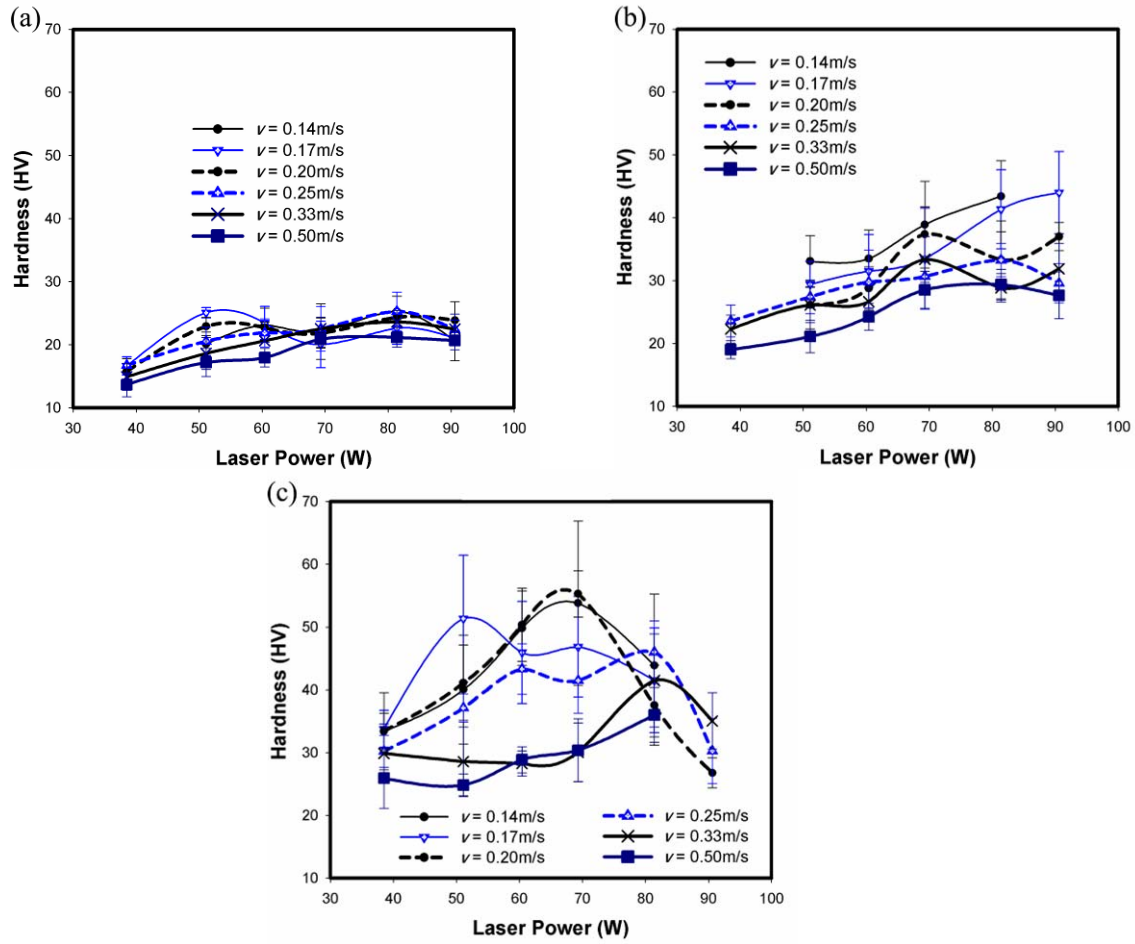


**Fig. 7.4:** Density of the SLM parts fabricated from (a)  $\text{Al}/5\text{wt\%}\text{Fe}_2\text{O}_3$ , (b)  $\text{Al}/10\text{wt\%}\text{Fe}_2\text{O}_3$  and (c)  $\text{Al}/15\text{wt\%}\text{Fe}_2\text{O}_3$  powder mixture vs. laser power in various scanning speeds.

### 7.3.4. Hardness

As seen from hardness results in Fig. 7.5, the hardness of  $\text{Al}/5\text{wt\%}\text{Fe}_2\text{O}_3$  first increases with laser power until it reaches a maximum value and then it decreases, forming a peak in the curve of hardness vs. laser power (Fig. 7.5a). The parameters of  $P = 82$  W and  $v = 0.25$

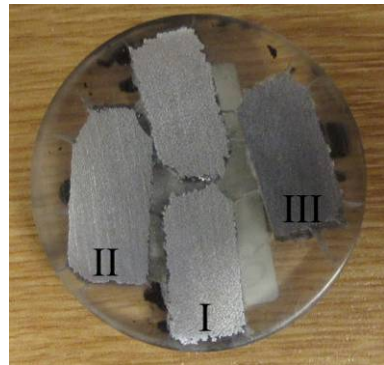
m/s can be considered as an optimum to achieve the best hardness in this case. This suggests that there is also an optimum scanning speed to achieve highest hardness. This trend of hardness vs. laser power, i.e. increasing the hardness with laser power to reach a maximum value, has been repeated more or less in higher  $\text{Fe}_2\text{O}_3$  contents of 10-15 wt% (Fig. 7.5b-c). The positive influence of  $\text{Fe}_2\text{O}_3$  content to improve hardness is evident, e.g. maximum hardness in Fig. 7.5c (15 wt%  $\text{Fe}_2\text{O}_3$ ) is about 56 HV while the maximum in Fig. 7.5a (5 wt%  $\text{Fe}_2\text{O}_3$ ) is about 26 HV (i.e. 115% increase in hardness). This implies the significant effect of  $\text{Fe}_2\text{O}_3$  to modify the microstructure and subsequently improve the hardness. Some optical microscopy examinations are reported (in the next section) to illustrate this effect.



**Fig. 7.5:** Hardness of the SLM parts fabricated from (a) Al/5wt% $\text{Fe}_2\text{O}_3$ , (b) Al/10wt% $\text{Fe}_2\text{O}_3$  and (c) Al/15wt% $\text{Fe}_2\text{O}_3$  powder mixture vs. laser power in various scanning speeds.

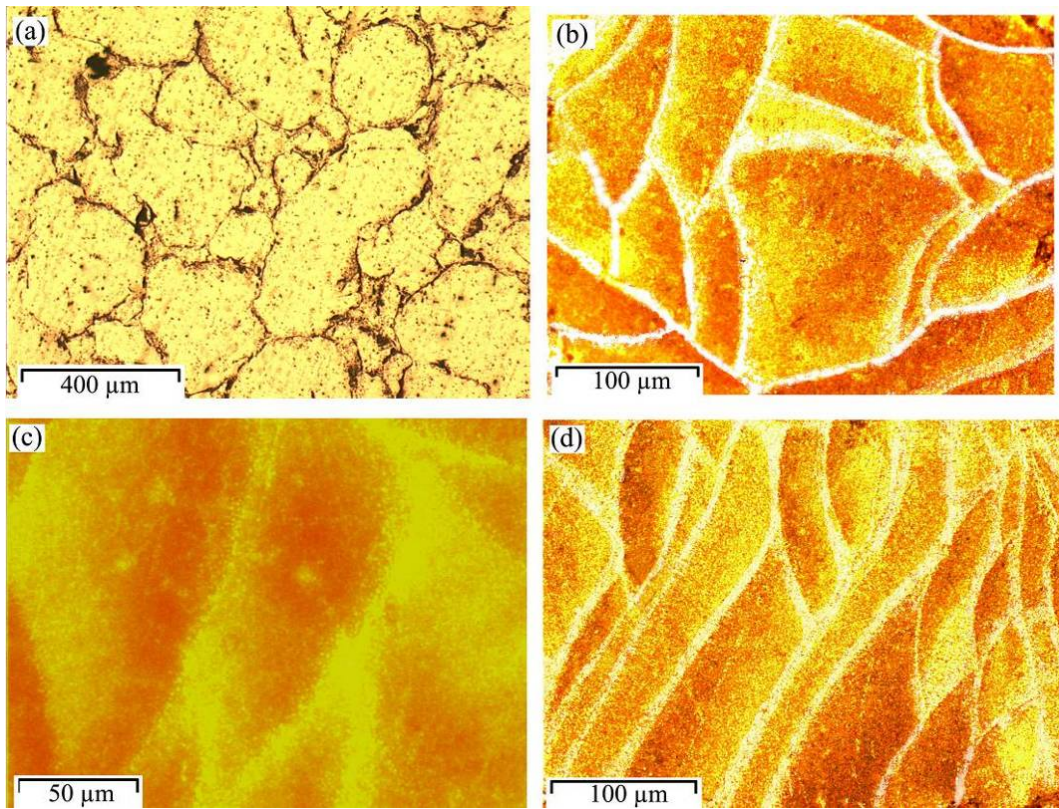
### 7.3.5. Optical microscopy results

Based on the hardness results, the laser parameters producing the highest hardness were used to fabricate samples from Al/5-15wt%Fe<sub>2</sub>O<sub>3</sub> for optical microscopy examinations. The samples were cross sectioned and polished for taking optical photography. The cross sections after polishing are shown in Fig. 7.6, illustrating the dense appearance of the samples.



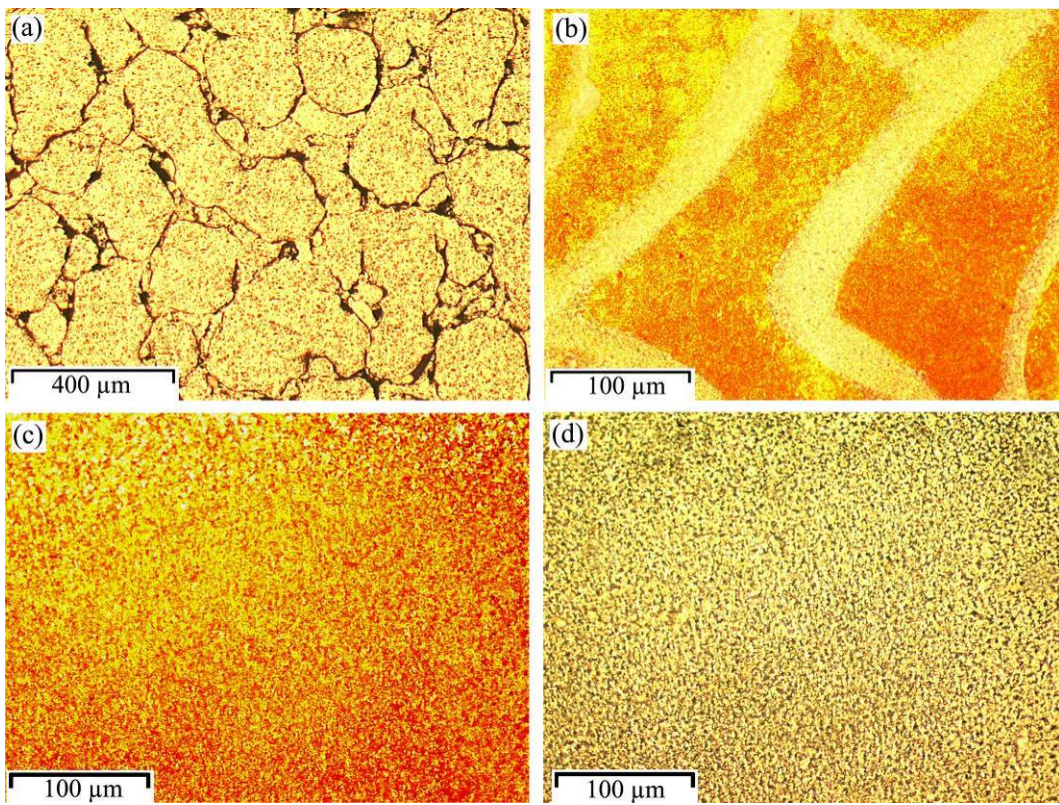
**Fig. 7.6:** Visual appearance of the cross section in SLM samples made from I) Al/5wt%Fe<sub>2</sub>O<sub>3</sub> ( $P = 82$  W,  $v = 0.25$  m/s), II) Al/10wt%Fe<sub>2</sub>O<sub>3</sub> ( $P = 82$  W,  $v = 0.2$  m/s), and III) Al/15wt%Fe<sub>2</sub>O<sub>3</sub> ( $P = 70$  W,  $v = 0.14$  m/s).

Fig. 7.7 shows optical microscopic graphs of parts fabricated from Al/5wt%Fe<sub>2</sub>O<sub>3</sub> using  $P = 82$  W and  $v = 0.25$  m/s. As seen, solid areas with a size of 300-500  $\mu\text{m}$  has been formed in the matrix side by side, while a clear interconnected gap appears between them (Fig. 7.7a). These solid zones contain a grain microstructure after etching (Fig. 7.7b-c), randomly formed with clear boundaries (Fig. 7.7b). They show polygon morphology with curved sides with about 50-100  $\mu\text{m}$  in length. The boundaries of these grains seem to embed very fine particles (Fig. 7.7c). Fig. 7.7d shows the microstructure of the same specimen, but cut through transverse direction. As seen, SLM orients the grains curvature from the bottom to top during building, within a distance of about 30-60  $\mu\text{m}$  which is about the layer thickness of 50  $\mu\text{m}$ .



**Fig. 7.7:** The micrographs of the SLM sample fabricated from Al/5wt% $\text{Fe}_2\text{O}_3$  mixture ( $P = 82$  W,  $v = 0.25$  m/s); (a) polished surface (along XY section), (b) random grain structure (along XY section), (c) higher magnification of boundaries composed of fine particulate phases, and (d) grain structure along SLM building direction.

The Al/10wt% $\text{Fe}_2\text{O}_3$  part is also composed of relatively large solid zones separated by an interconnected gap (Fig. 7.8a). The microstructure within the solid zones seems to be different in various positions. For example, grains with thick boundaries embedding very fine particles can be seen in Fig. 7.8b. In contrast, Fig. 7.8c-d shows a uniform distribution of very fine particles inside matrix in such a manner that no clear boundaries are recognisable.



**Fig. 7.8:** The micrographs of the Al/10wt% $\text{Fe}_2\text{O}_3$  SLM sample (cut along XY section - fabricated by  $P = 82$  W and  $v = 0.20$  m/s); (a) polished surface, (b) random grain structure with thick boundaries, (c) particulate phases spread in microstructure, and (d) dark-field of image (c).

The Al/15wt% $\text{Fe}_2\text{O}_3$  part contains porous solid zones (Fig. 7.9a), while reduced inter-solid gaps are evident in comparison with the figures for Al/5-10wt% $\text{Fe}_2\text{O}_3$ . This implies that increasing the iron oxide to 15 wt% (in this case) has intensified the fusion of solid zones. The microstructure is formed from very fine particulate features, while grain boundaries are not evident (Fig. 7.9b).

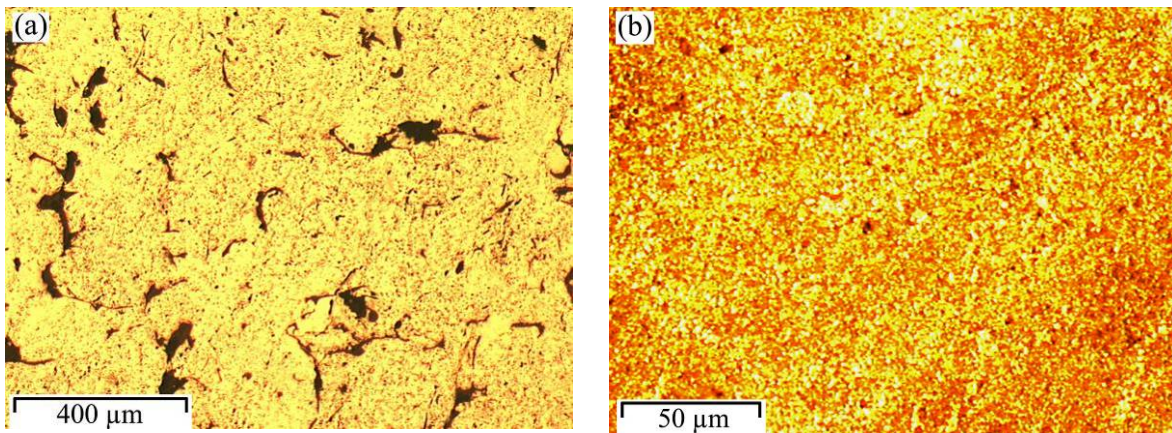


**Fig. 7.9:** (a) Polished surface and (b) particulate phases spread in microstructure appearing in Al/15wt% $\text{Fe}_2\text{O}_3$  part (cut along XY section - fabricated by  $P = 70$  W and  $v = 0.14$  m/s).

## 7.4. Discussion

### 7.4.1. Visual condition, surface roughness, density, hardness and microstructure

The powder analysis shown in material section illustrates that pure aluminium (Al) and iron oxide ( $\text{Fe}_2\text{O}_3$ ) particles are uniformly distributed and fully mixed together, whilst these different particles tend to adhere to each other. This adherence could be very helpful, particularly in the powder deposition step and *in-situ* material reaction, when SLM process activates the thermite reaction in the mixture of Al and  $\text{Fe}_2\text{O}_3$  powders. The thermite reaction progresses with a highly exothermic *in-situ* chemical reaction in which Al reduces the iron oxide, leading to new products such as Al oxide and Al-Fe combinations (Fan et al., 2006). Accordingly, the proposed Al/ $\text{Fe}_2\text{O}_3$  material system releases a significant degree of energy within the SLM process (depending on the mixture composition), assisting powder melting and consolidation, as clearly observed in Fig. 7.1a-b. This also reduces the SLM energy consumption and enables either lower laser powers ( $P$ ) or higher laser scanning speeds ( $v$ ). The extra heat released from the *in-situ* Al/ $\text{Fe}_2\text{O}_3$  reaction can also offer a possibility to minimise or eliminate the pre-heating of the powder bed before and during SLM process of Al alloys. According to these benefits, a series of 3D SLM parts were produced from Al/ $\text{Fe}_2\text{O}_3$  powder mixture over a wide range of parameters (see Fig. 7.2), despite difficulties (such as high reflectivity of Al and formation of thin oxide films on both the solid and molten materials reducing wettability) to produce non *in-situ* Al SLM parts (Louvis et al., 2011).

The melting development due to higher  $\text{Fe}_2\text{O}_3$  content can even manipulate the surface of parts, e.g. it might changes the surface profile from individual small ball-shape particles (Fig. 7.1c) to fused semi-spherical solid features (Fig. 7.1d). The extra heat also intensifies the showering of particles nearby. Perhaps, the sudden increase in volume and pressure of air trapped within particles due to sudden increase in temperature pushes the particles nearby. This showering phenomenon might have a negative effect on final surface finish, increasing the surface roughness.

Various SLM parameters including laser parameters (such as laser power and scanning speed) and material parameters (such as  $\text{Fe}_2\text{O}_3$  content in Al) affect the part properties including surface roughness, density and hardness, as seen in Fig. 7.3 to Fig. 7.5. These

variations are linked to combined effects of various phenomena such as melting, balling and showering. For example, surface roughness and laser power generally form some maximum peaks (Fig. 7.3) attributed to simultaneous influence of laser power to enhance good melting and wetting (smoothing the surface) and on the other hand ball sizes and showering (roughening the surface). Moreover, the highest scanning speed of 0.5 m/s leads to smaller balls formed on surface (see Fig. 7.1c) which makes the surface smoother in the case of Al/5-10wt%Fe<sub>2</sub>O<sub>3</sub>. Higher Fe<sub>2</sub>O<sub>3</sub> content (15 wt%) increases the showering of powders to a critical level, while lower scanning speed may reduce it and, therefore, leads to occurrence of best surface finish (lowest surface roughness) in lower laser speeds. Moreover, increase in Fe<sub>2</sub>O<sub>3</sub> content slightly improves the surface quality until the surface finish reaches its best (where fused semi-spheres appear on surface (see Fig. 7.1d)).

The melting development with laser power also increases the density until mixture reaches full melting. After that, the density starts to decrease due to the formation of bigger spheres (balls) during SLM process creating larger vacant positions in between. This leads to a maximum in the curve of density vs. laser power (see Fig. 7.4a), being generally shifted to lower laser powers with increased proportion of Fe<sub>2</sub>O<sub>3</sub> added to the powder mixture (Fig. 7.4) due to extra *in-situ* energy assisting the process to achieve full melting condition. This is more evident especially in the case of Al/15wt%Fe<sub>2</sub>O<sub>3</sub>, where the highest densities occur in low laser powers (Fig. 7.4c). In fact, smoother surface in low laser powers (with less cavities) helps density improvement while high Fe<sub>2</sub>O<sub>3</sub> content provides necessary energy for melting development which means lower necessary laser powers. The Fe<sub>2</sub>O<sub>3</sub> content also manipulates the magnitude of maximum density by influencing fluidity of material. Fluidity is affected by two inverse influences of Fe<sub>2</sub>O<sub>3</sub> content; i) inclusions (which reduce fluidity) and ii) released heat (which increases fluidity). Accordingly, 10 wt% Fe<sub>2</sub>O<sub>3</sub> has most likely led to lowest fluidity when effect of inclusion (new combinations in melting zone) has dominated the effect of extra heat (decreasing the density). The higher Fe<sub>2</sub>O<sub>3</sub> (15 wt%) may mitigate the negative influence of such additional inclusions (in some extent), by further incorporation of extra energy into the process (increases again the density). In some cases, this extra energy might be even sufficient to fuse solids together, fading the interconnected format of porosity (see Fig. 7.9a). Moreover, the optimum scanning speed to achieve highest density (Fig. 7.4) can be explained by the fact that higher laser speed decreases the fluidity of molten material (decreases the density),

but at the same time leads to smaller spheres (increases the density). However, the peak of density might occur in lower scanning speeds when lower laser power is used because of increased melting (increased energy input) when the scanning speed decreases.

The hardness of SLM parts is mainly a function of density, but does not exactly follow the density variations in all cases, e.g. maximum densities are not always compatible to hardness or even 2 peaks can be observed in some cases in Fig. 7.5. This indicates the significant role of SLM formed material microstructure (Figs. 7.7-7.9) in hardness, considerably affected by  $\text{Fe}_2\text{O}_3$  content. The grains and relevant boundaries (filled by fine particles) are dominant microstructure feature in presence of low  $\text{Fe}_2\text{O}_3$  content of 5 wt% (Fig. 7.7), while an increase in  $\text{Fe}_2\text{O}_3$  to 10 wt% thickens the particulate boundaries (Fig. 7.8b) and in some cases develops a fine, homogeneous and well-bounded particulate feature all over the solid zones (Fig. 7.8c-d). This well-bounded and homogeneous particulate feature becomes the dominant microstructure in higher  $\text{Fe}_2\text{O}_3$  of 15 wt% (Fig. 7.9b). This microstructural evolution due to increasing the  $\text{Fe}_2\text{O}_3$  contents may activate dispersion hardening mechanisms (Lu et al., 1997, Tong and Fang, 1998b) and diminish large boundaries acting as defects and weakening the material, being in confirmation with consistent increasing of hardness due to higher  $\text{Fe}_2\text{O}_3$  in Fig. 7.5 despite general reduction in density.

Despite the dense appearance of the samples (Fig. 7.6), they have a high porosity content appearing in an interconnected gap feature and surrounding the solid zones, as shown in Figs. 7.7a and 7.8a. The same has been observed in some earlier reports where interconnected gaps filled by oxides have been shown between solids (Louvis et al., 2011, Sercombe and Schaffer, 2004). Since this interconnected format of porosity can drastically damage the overall strength of material, enhanced fusion of solids in high  $\text{Fe}_2\text{O}_3$  contents (Fig. 7.9a) may improve the hardness as well (in addition to modifying the microstructure).

#### 7.4.2. Material properties in relation to laser energy and processing window

As seen, the laser parameters such as laser power and scanning speed had a significant influence on the material melting behaviour and final properties of parts. Their combined effects can be illustrated by the influence of laser energy density, as mentioned in literature review by Eq. 2.1:

$$E_\rho = \frac{P}{\pi r^2} \frac{2r}{v} \frac{2r}{s} \quad (\text{Eq. 2.1})$$

where  $E_\rho$  = energy density ( $\text{J/mm}^2$ ),  $P$  = laser power (W),  $v$  = scanning speed ( $\text{mm/s}$ ),  $s$  = scan line spacing (mm), and  $r$  = beam radius (mm). According to this equation, increasing in laser power and decreasing in scanning speed or/and scan line spacing enhance the energy density delivered in SLM process. The greater the energy imparted to the powder, the greater is the material melting (Hao et al., 2009). The laser energy density vs. surface roughness, density, and hardness of materials were respectively plotted in Figs. 7.10 to 7.12. The results did not follow a precise trend like some previous research works (Hao et al., 2009), and therefore approximated trend bands were sketched using a specialist software, assisting to follow the relatively wide scatter of data. Fig. 7.10 illustrates the influence of laser energy input on top surface roughness showing an upward roughness with increased input energy. The higher energy input (despite its importance to increasing melting) increases the risk of balling and dross formation in the molten pool (Kruth et al., 2007) and may damage the surface finish. Increasing the  $\text{Fe}_2\text{O}_3$  content and the *in-situ* reaction assist the fusion of spheres (balls) (see Fig. 7.1d), having a positive influence on surface finish (Fig. 7.10a-b). It also reduces the rate of roughness increase (the slope of roughness vs. laser energy in Fig. 7.10b is lower than Fig. 7.10a), perhaps once again due to enhanced fusion of surface. The larger scatter of data in  $\text{Al}/15\text{wt\%}\text{Fe}_2\text{O}_3$  than those of  $\text{Al}/5\text{wt\%}\text{Fe}_2\text{O}_3$  may be attributed to larger showering phenomenon in higher iron oxide contents which makes the data more alternated.

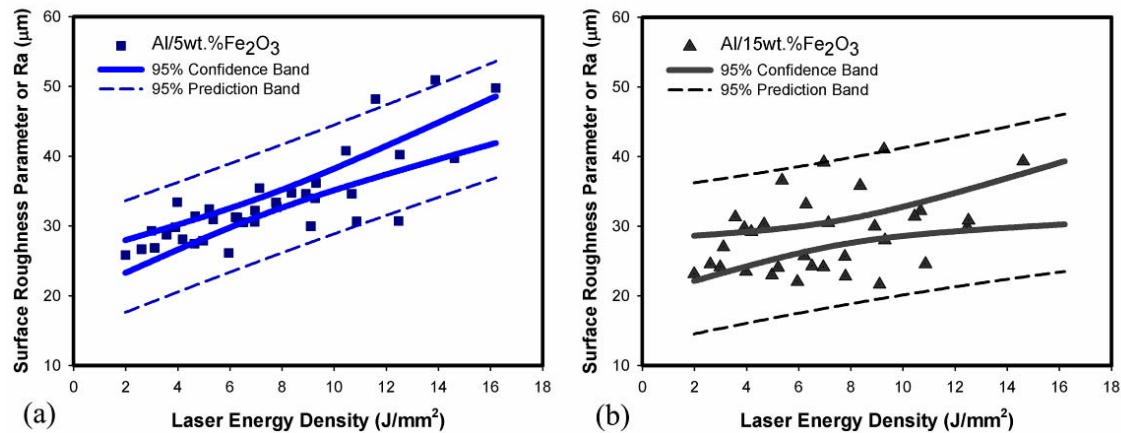


**Fig. 7.10:** Material surface roughness parameter as a function of laser energy density for (a)  $\text{Al}/5\text{wt\%}\text{Fe}_2\text{O}_3$  and (b)  $\text{Al}/15\text{wt\%}\text{Fe}_2\text{O}_3$ . The confidence and prediction bands are uncertainty in estimated data occurrence with no and with observational error respectively.

The variation of density of Al/5wt%Fe<sub>2</sub>O<sub>3</sub> and Al/15wt%Fe<sub>2</sub>O<sub>3</sub> vs. laser energy density is shown in Fig. 7.11a and 7.11b respectively, which takes the form of a curve with a maximum. The maximum happens where material experiences full melting while the balls (spheres on the surface) are not too big to leave much cavity in between. This peak may shift slightly to lower energy densities as a result of using higher percentage of Fe<sub>2</sub>O<sub>3</sub>, due to *in-situ* released heat. The higher percentage of Fe<sub>2</sub>O<sub>3</sub> may also slightly reduce the density as a result of the suppressed fluidity by new combinations and inclusions.

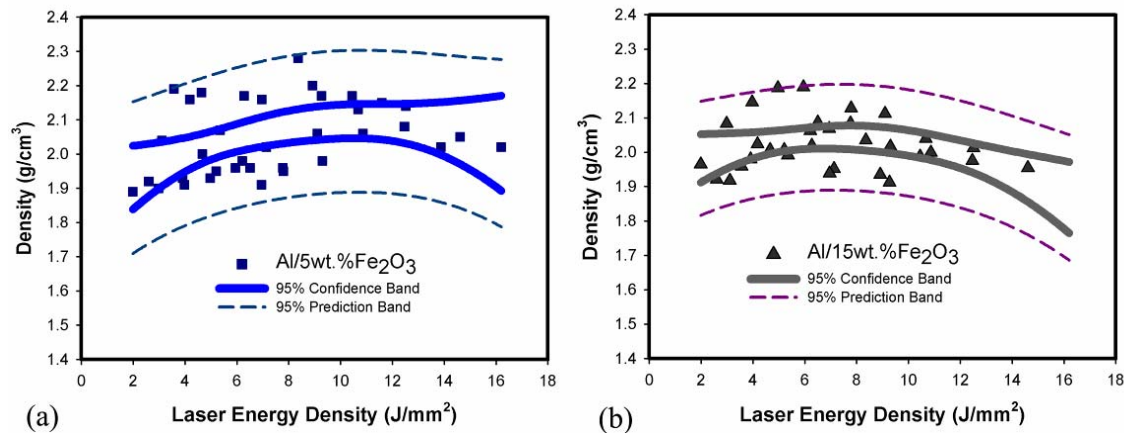


**Fig. 7.11:** Material density as a function of laser energy for (a) Al/5wt%Fe<sub>2</sub>O<sub>3</sub> and (b) Al/15wt%Fe<sub>2</sub>O<sub>3</sub>.

As seen from relation of energy density and hardness in Fig. 7.12 (for Al/5wt%Fe<sub>2</sub>O<sub>3</sub> and Al/15wt%Fe<sub>2</sub>O<sub>3</sub>), increasing the energy density first enhances the hardness, until the hardness reaches a maximum and after that it seems to become more or less consistent. The higher Al/15wt%Fe<sub>2</sub>O<sub>3</sub> hardness than that of Al/5wt%Fe<sub>2</sub>O<sub>3</sub> (despite the decrease in density) is associated with the development of well dispersed fine particles throughout Al matrix at higher Fe<sub>2</sub>O<sub>3</sub> content. The large data band is likely due to the influence of individual processing variables (such as laser power and scanning speed) on the resulting microstructure as well as part density.

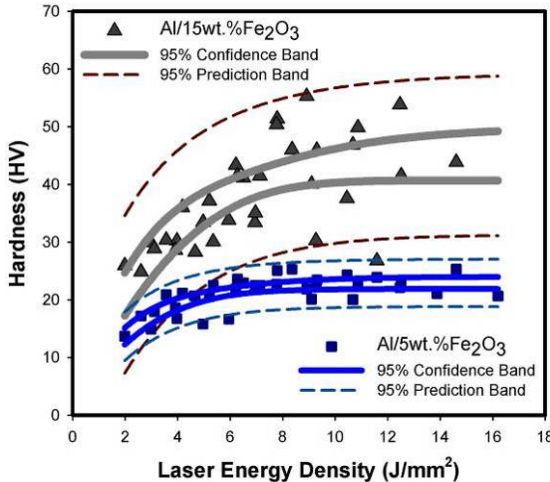


**Fig. 7.12:** Material hardness as a function of laser energy density for Al mixed with 5 and 15 wt%  $\text{Fe}_2\text{O}_3$ .

In summary, the processing windows for Al/5-15wt% $\text{Fe}_2\text{O}_3$  have been sketched in Fig. 7.13 on the basis of surface roughness, density and hardness data. As seen, there is no surface finish below  $R_a = 25 \mu\text{m}$  for Al/5wt% $\text{Fe}_2\text{O}_3$  (Fig. 7.13a), while the window of better surface finish appears with increasing the  $\text{Fe}_2\text{O}_3$  to 10 wt% where  $R_a < 25 \mu\text{m}$  (Fig. 7.13b), existing in low laser powers (leads to less balling phenomenon). This window will be further extended when  $\text{Fe}_2\text{O}_3$  increases to 15 wt% content (to higher laser powers but in low scanning speeds) (Fig. 7.13c).

Regarding Fig. 7.13a, high laser powers (providing a better melting degree) lead to a better density for Al/5wt% $\text{Fe}_2\text{O}_3$ . The increase in  $\text{Fe}_2\text{O}_3$  content damages the density, e.g. no window of density  $> 2.1 \text{ g/cm}^3$  for Al/10wt% $\text{Fe}_2\text{O}_3$  (Fig. 7.13b) and a small window of density  $> 2.1 \text{ g/cm}^3$  for Al/15wt% $\text{Fe}_2\text{O}_3$  (left-bottom in Fig. 7.13c) can be observed. In other words, the increase in  $\text{Fe}_2\text{O}_3$  content has restricted the operational window for achieving better density, attributed to the influence of inclusions on reducing fluidity compared to extra heat on increasing it. In addition to density, the overall hardness is another key factor for adopting SLM process for Al matrix composite materials. The acceptable hardness might be compared to hardness of annealed pure aluminium which is about 15-20 HV. The hardness of Al/5wt% $\text{Fe}_2\text{O}_3$  seems to be acceptable in a relatively large window covering relatively high energy inputs (i.e. higher laser powers in conjunction with lower laser speeds in Fig. 7.13a). In the case of Al/10-15wt% $\text{Fe}_2\text{O}_3$  acceptable hardness window has extended all over the processing window (though density decreases),

and even a new window with better hardness ( $HV > 40$ ) opens up (Fig. 7.13b-c). As seen, the increase in  $Fe_2O_3$  content has shifted the better hardness zone to left side (which means decreasing energy input), as a result of larger heat released by *in-situ* reaction in higher  $Fe_2O_3$  content. However, this window is formed in lower scanning speeds perhaps due to better dispersion of the particulate features (e.g. see Fig. 7.9b) in these speeds.

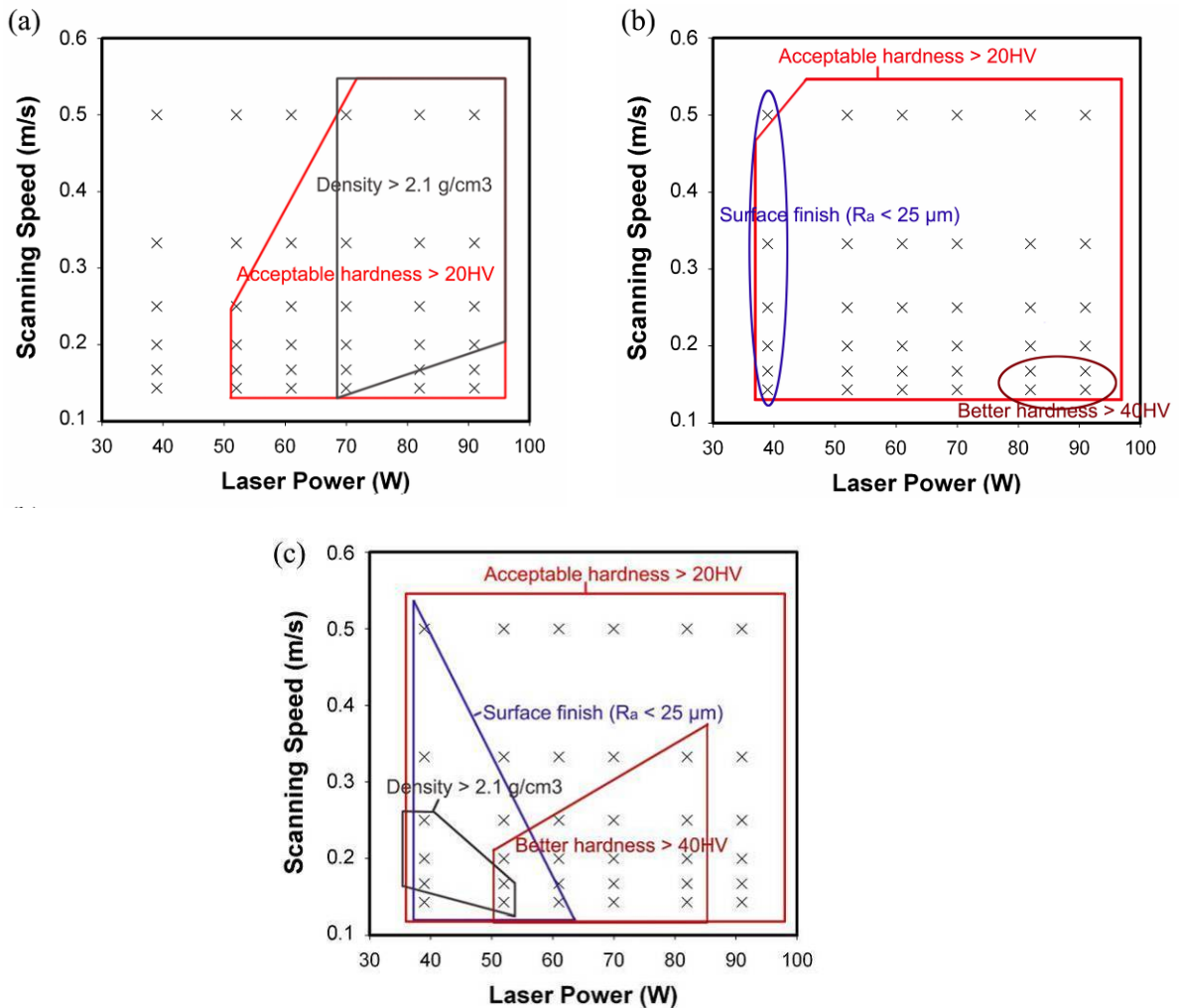


**Fig. 7.13:** SLM processing window for the SLM parts fabricated from (a) Al/5wt% $Fe_2O_3$ , (b) Al/10wt% $Fe_2O_3$  and (c) Al/15wt% $Fe_2O_3$  powder mixture.

The inexpensive  $Fe_2O_3$  additives provide new opportunities to expand processing windows, enhance the laser speeds, and save energy inputs for the SLM of Al matrix composites. As a production approach, it is reasonable to first select higher scanning speeds for achieving higher production rate and then lower laser energies (after making sure of having enough SLM energy) for enhanced sustainability, leading to the lower production time and cost for individual part.

## 7.5. Conclusions

This chapter, for the first time, investigated the material behaviour and processing window of Al powders with Fe<sub>2</sub>O<sub>3</sub> additives for selective laser melting process. The *in-situ* material reaction between Al and powder releases extra heat and energy to assist melting development and improve the SLM processability and production over a wide range of SLM parameters. The released energy (proportional to Fe<sub>2</sub>O<sub>3</sub> content) is capable of manipulating the visual surface profile and roughness. The higher amount of Fe<sub>2</sub>O<sub>3</sub> additive may not provide a positive effect on the part density as inclusions suppress fluidity, which presumably is more powerful than that of extra heat to increase fluidity. Despite a negative influence on density, hardness significantly increases with higher Fe<sub>2</sub>O<sub>3</sub> content because of superior microstructural features of the particle reinforced matrix.

The processing windows, plotted on the basis of part quality data such as surface roughness, density and hardness, show different range of laser powers and scanning speeds for fabricating Al/5wt%Fe<sub>2</sub>O<sub>3</sub>, Al/10wt%Fe<sub>2</sub>O<sub>3</sub>, and Al/15wt%Fe<sub>2</sub>O<sub>3</sub>. This also reveals the critical role of Fe<sub>2</sub>O<sub>3</sub> additive as an excellent opportunity to expand the processing windows to deliver higher production rate (i.e. enhancing the laser speeds) and reduce energy consumption for SLM production of Al metal matrix composite parts.

In the following chapters, further analysis and discussion will be presented to illustrate the microstructural characteristics of the parts made at various processing conditions such as SLM layer thickness, laser power, scanning speed, and percentage of Fe<sub>2</sub>O<sub>3</sub>.

---

# **Chapter 8: Effect of Layer Thickness on Microstructural Evolution of Al/5wt%Fe<sub>2</sub>O<sub>3</sub> Powder Consolidated Parts Made by Selective Laser Melting at Different Laser Powers and Scanning Speeds**

---

## **8.1. Introduction**

As discussed, the SLM process not only activates exothermic in-situ reaction to form new constituents, but also achieves rapid solidification to manipulate the microstructural characteristics. Therefore, a large difference is expected between the microstructural characteristics of Al MMC parts (with a wide range of non-equilibrium phenomena) made by SLM and those produced by conventional casting methods. These specific microstructural characteristics could lead to advanced material properties for novel net shape MMCs components made by SLM.

The SLM process parameters can play an important role on microstructural evolution as well. For example, the powder layer thickness can affect the heat released from in-situ reaction and the solidification (due to change in heat transfer condition), and subsequently the microstructure. Also, laser power and scanning speed can influence the material melting and consolidation phenomena. This chapter is dedicated to illustrate the microstructural outcome of in-situ reaction in Al/5wt%Fe<sub>2</sub>O<sub>3</sub> powder mixture activated by SLM. Effect of laser power ( $P$ ) and scanning speed ( $v$ ), and also layer thickness ( $t$ ) on the microstructural evolution, phase changes and material microhardness is presented and discussed in this chapter.

## **8.2. Materials and Experiments**

Al/5wt%Fe<sub>2</sub>O<sub>3</sub> powder mixture was processed by SLM. Single layer samples were made on a thick powder bed in the preliminary study with a laser power of 17-51 (W). Multilayer SLM samples were fabricated using powder layer thicknesses of 75  $\mu\text{m}$  and 50  $\mu\text{m}$ . The samples were examined using techniques such as SEM, XRD, and microhardness.

## 8.3. Results

### 8.3.1. Hardness properties

Microhardness tests were carried out to investigate the evolution of microstructural hardness with various laser powers when the multilayer parts were manufactured with layer thicknesses of 50  $\mu\text{m}$  and 75  $\mu\text{m}$  at two different scanning speeds ( $v \sim 0.14 \text{ m/s}$  and  $0.5 \text{ m/s}$ ). The results, shown in Fig. 8.1, appear as a similar trend of hardness with laser power for all curves treated at the different scanning speeds and layer thicknesses in such a manner that the hardness usually increases with laser power, but it may reach a maximum value. For example, the hardness in the curve of  $v = 0.5 \text{ m/s}$  and  $t = 75 \mu\text{m}$  increases up to about 82 W reaching a maximum value of about 53 HV and then it starts to slightly decrease with further increase of laser power. Scanning speed also affects the hardness, i.e. lower scanning speed leads to higher hardness (compare hardness curves with different scanning speeds). This demonstrates that microstructural phases of the parts have been varied by applying different laser powers and scanning speeds. Effect of layer thickness on hardness can be studied through comparison of curves belonging to  $t = 50 \mu\text{m}$  and  $t = 75 \mu\text{m}$ . The comparison shows that thinner layer thickness of 50  $\mu\text{m}$  has a slight positive effect to enhance hardness, e.g. maximum hardness of the curve of 0.14 m/s with  $t = 50 \mu\text{m}$  is 63 HV while the maximum in  $t = 75 \mu\text{m}$  is 60 HV. The highest hardness belongs to part manufactured with  $P = 91 \text{ W}$ ,  $v = 0.14 \text{ m/s}$  and  $t = 50 \mu\text{m}$  and provides approximately three times hardness value as that of pure aluminium (no conventionally manufactured Al composite with the same reinforcement characteristics were found in the literature to be used as a basis of the comparison) reported in a previous research work (ASM International Handbook Committee, 1992). The lowest hardness result of SLM parts is 40 HV and still as twice as the pure annealed aluminium, indicating the SLM of Al/5wt%Fe<sub>2</sub>O<sub>3</sub> introduced new microstructural characteristics and reinforcement particles to Al matrix and enhanced its mechanical performance.

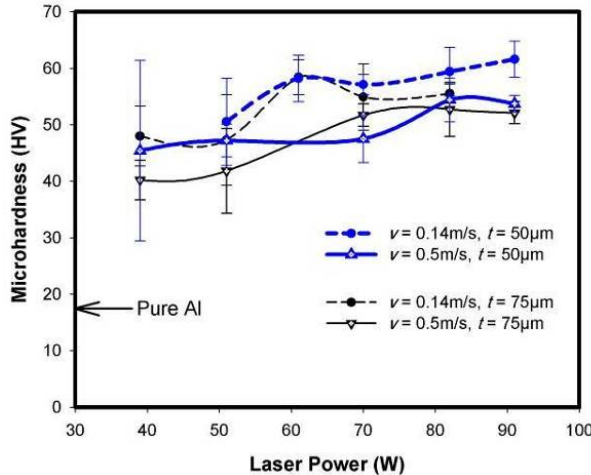


**Fig. 8.1:** Microhardness of the multilayer parts fabricated with layer thicknesses of 50  $\mu\text{m}$  and 75  $\mu\text{m}$  and scanning speeds of 0.14 m/s and 0.5 m/s vs. laser power.

### 8.3.2. Microstructural characterisation and phase identification using XRD

#### 8.3.2.1. Single layer specimens made by SLM on a thick powder bed

The building of single layer specimens on a thick powder bed can be used as very large layer thickness in comparison study for the effect of various SLM layer thicknesses. Fig. 8.2a exhibits a very fine granular matrix with a grain size of about 5-15  $\mu\text{m}$  in a single layer specimen made at low laser power of 17 W. The sintering lines (the boundaries separating fully melted areas) between consolidated solids are recognisable. Increasing the laser power to 51 W has diminished the sintering lines to produce more integrated matrix, though small pores (originating from entrapped gas) exist in matrix, as shown in Fig. 8.2b. The EDS analysis implies the effect of high laser power to remove the oxygen from the Al matrix (about 4 wt% oxygen in Fig. 8.2a has been disappeared in higher SLM power in Fig. 8.2b). Fig. 8.2c shows the XRD pattern of the part corresponding with Fig. 8.2b, demonstrating the matrix is a single Al phase.

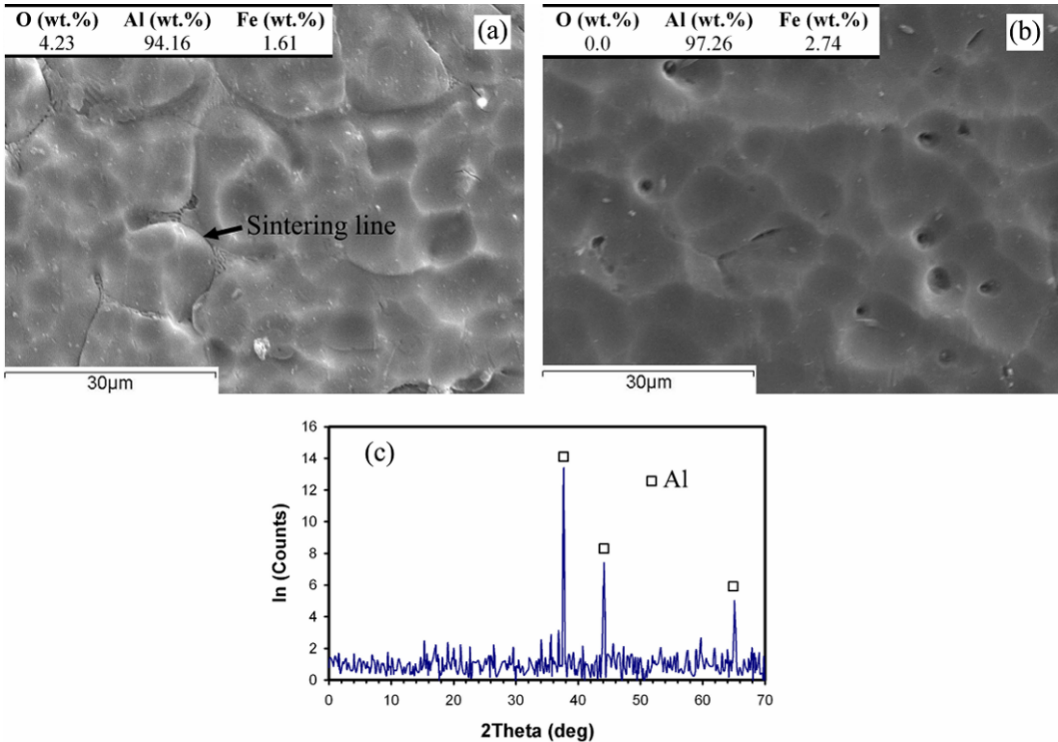
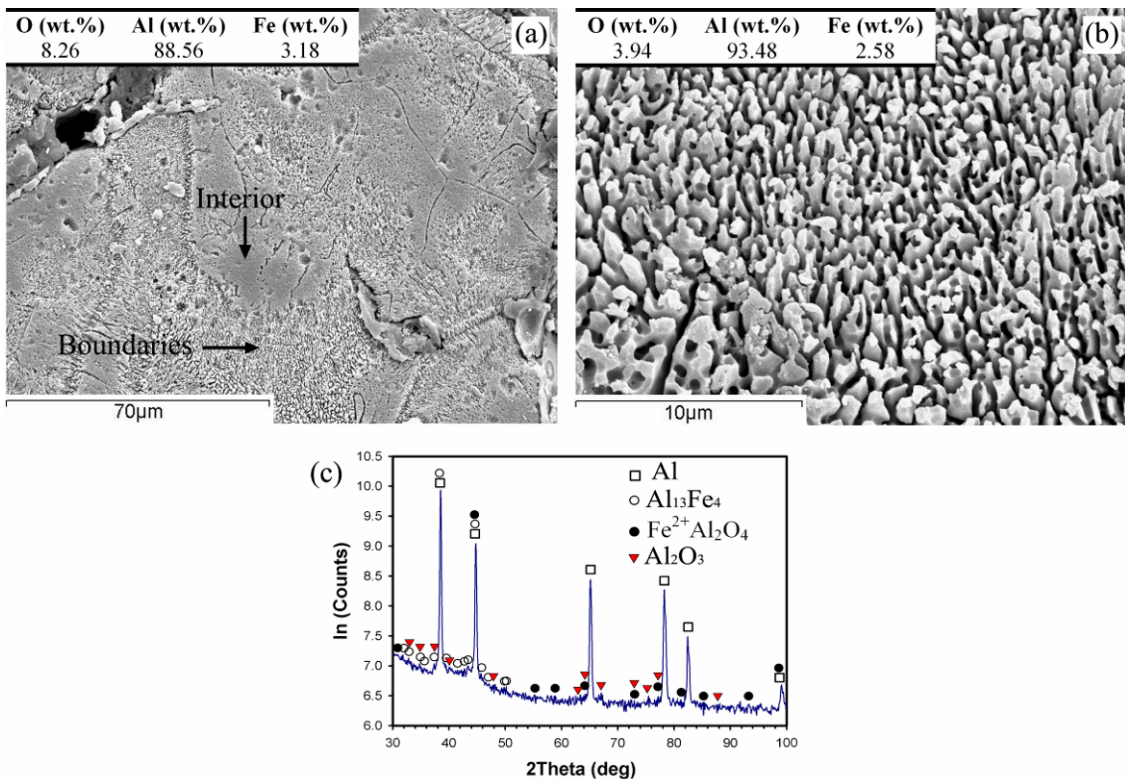


Fig. 8.2: The typical SEM microstructural views of the part fabricated on a thick powder bed using (a)  $P = 17$  W and  $v = 0.14$  m/s (showing granular structure including sintered lines), and (b)  $P = 51$  W and  $v = 0.14$  m/s (showing a granular structure). The overall chemical composition was acquired by EDS. (c) X-ray diffraction pattern of the part shown in image (b).

### 8.3.2.2. Multilayer parts with layer thickness of 75 µm

Figs. 8.3 and 8.4 show the SEM microscopic graphs of the multilayer parts (built with  $t = 75$  µm and  $P = 39$  W) under different laser speeds of  $v = 0.5$  m/s and  $v = 0.14$  m/s, respectively. Fig. 8.3a exhibits grains (smooth, with a size of about 30-50 µm) surrounded by thick boundaries (appearing with a fuzzy appearance). The fuzzy appearance of boundaries may look like a coralline-like feature (the coralline tips are  $\sim 0.5$  µm), as shown in Fig. 8.3b. The XRD results (Fig. 8.3c) suggest that the part is composed of combinations such as Al,  $\text{Al}_{13}\text{Fe}_4$ ,  $\text{Fe}^{2+}\text{Al}_2\text{O}_4$ , and  $\text{Al}_2\text{O}_3$  (weak peaks of some metastable  $\text{Al}_2\text{O}_3$  were identified, indicating low content of this oxide). The lower scanning speed ( $v = 0.14$  m/s) leads to almost the same overall microstructure (Fig. 8.4a), though the thick boundaries appear coarser (the coralline tips are widen  $\sim 1$ - $2$  µm), as better demonstrated in Fig. 8.4b, containing Al, Fe and lower oxygen content. The X-ray pattern (Fig. 8.4c) showed Al and Al-Fe intermetallics such as  $\text{Fe}_3\text{Al}$  and  $\text{Al}_{13}\text{Fe}_4$  intermetallics, and Al-Fe(-O) combinations such as  $\text{Fe}^{2+}\text{Al}_2\text{O}_4$  (iron aluminium oxide), while apparent presence of  $\text{Al}_2\text{O}_3$  was not identified.



**Fig. 8.3:** (a) Overall view of microstructure, (b) higher magnification of coralline-like and fuzzy appearance of boundaries in previous image, and (c) XRD pattern of the SLM part fabricated when  $P = 39$  W,  $v = 0.5$  m/s, and  $t = 75$  μm.

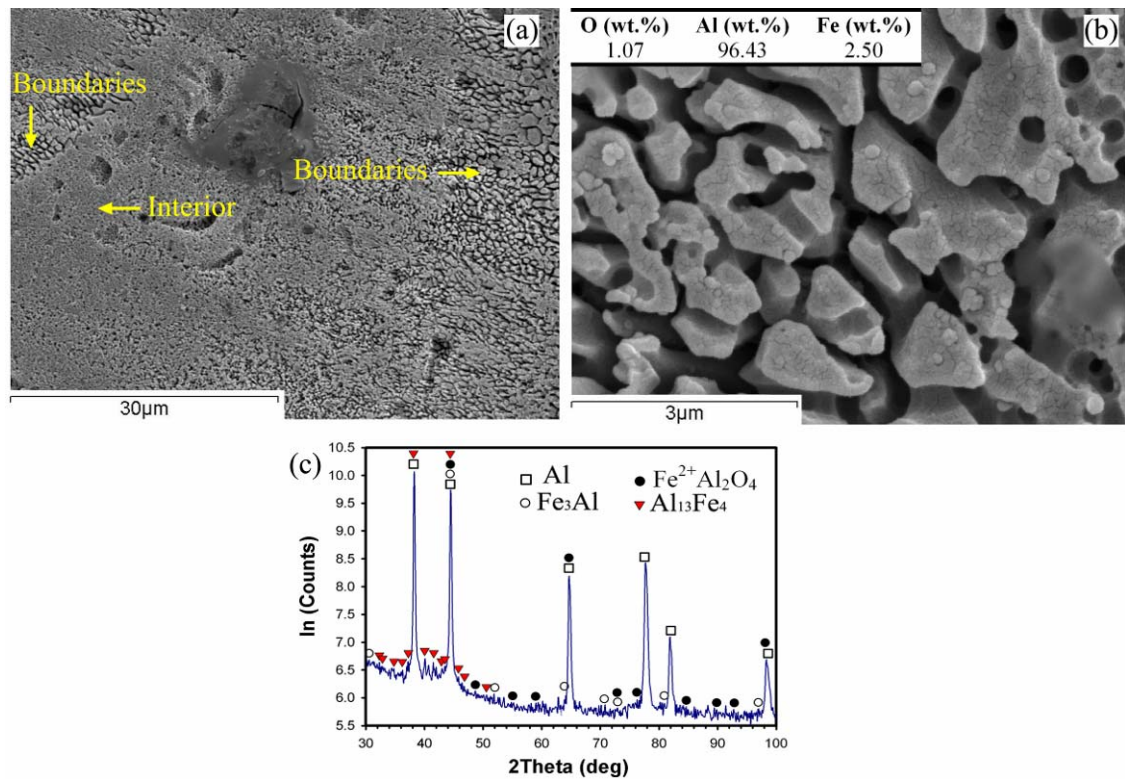


**Fig. 8.4:** (a) Overall view of microstructure, (b) higher magnification of boundaries seen in previous image, and (c) XRD pattern of the part fabricated when  $P = 39$  W,  $v = 0.14$  m/s, and  $t = 75$  μm.

The part fabricated by  $P = 61$  W,  $v = 0.14$  m/s, and  $t = 75$   $\mu\text{m}$  contains a porous and coralline-like feature propagated throughout the sample, while primary boundaries in narrow lines are recognisable with darker colour (Fig. 8.5a). Fig. 8.5b shows an example of this coralline-like porous phase spreading in matrix, mainly composing of Al and Fe with negligible content of oxygen. The chemical composition is in confirmation with the XRD results demonstrating Al,  $\text{Al}_{82}\text{Fe}_{18}$  and  $\text{Al}_{13}\text{Fe}_4$  as the main combinations of these coralline-like features (Fig. 8.5c). It should be noted that  $\text{Al}_{82}\text{Fe}_{18}$  and  $\text{Al}_{13}\text{Fe}_4$  propose almost the same elemental ratio and they can be considered as the same constituents. However, higher scanning speed ( $v = 0.5$  m/s) even in higher laser power ( $P = 82$  W) and scanning speed ( $v = 0.5$  m/s) leads to the finer coralline-like features (in submicron sizes), as shown in Fig. 8.6a-b, containing Al and Fe element with negligible amount of oxygen (Fig. 8.6b). These Al and Fe elements form Al-Fe intermetallics such as  $\text{Al}_{13}\text{Fe}_4$  and  $\text{Fe}_3\text{Al}$  (Fig. 8.6c) spreading over Al matrix with coralline-like appearance.

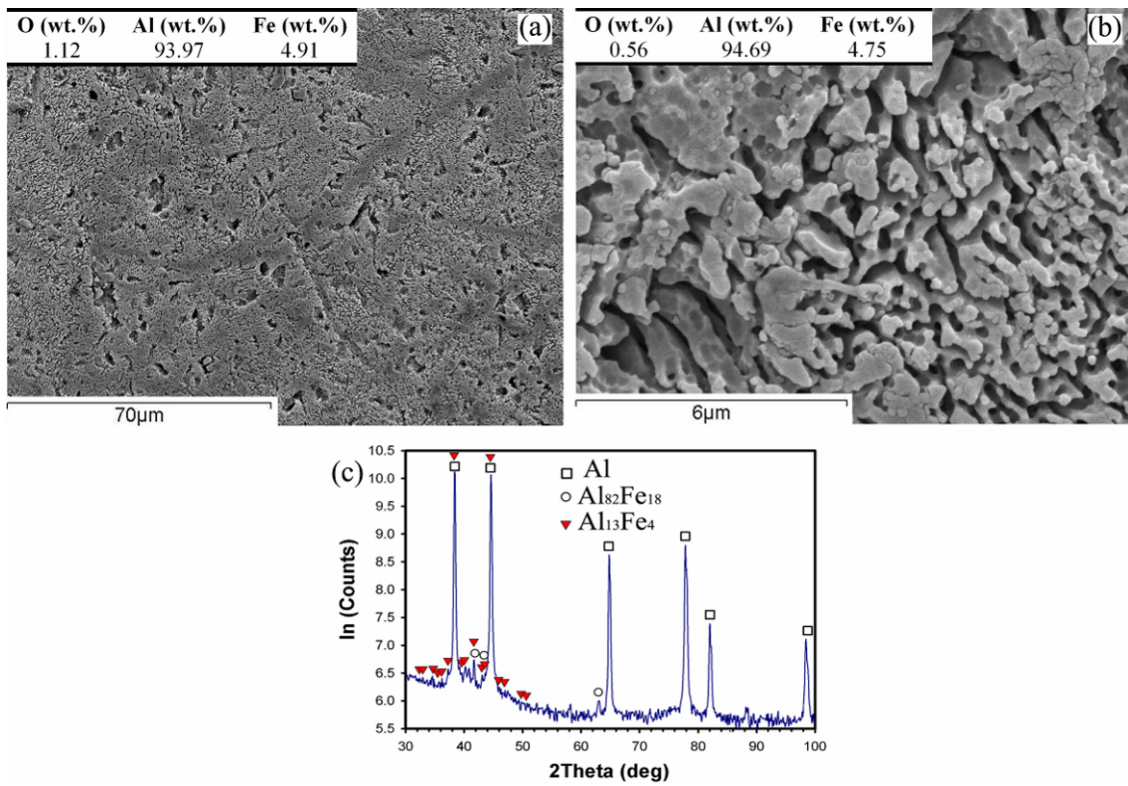


**Fig. 8.5:** (a) Overall appearance of microstructure, (b) the interior seen in previous image, and (c) XRD pattern of the part fabricated when  $P = 61$  W,  $v = 0.14$  m/s, and  $t = 75$   $\mu\text{m}$ .

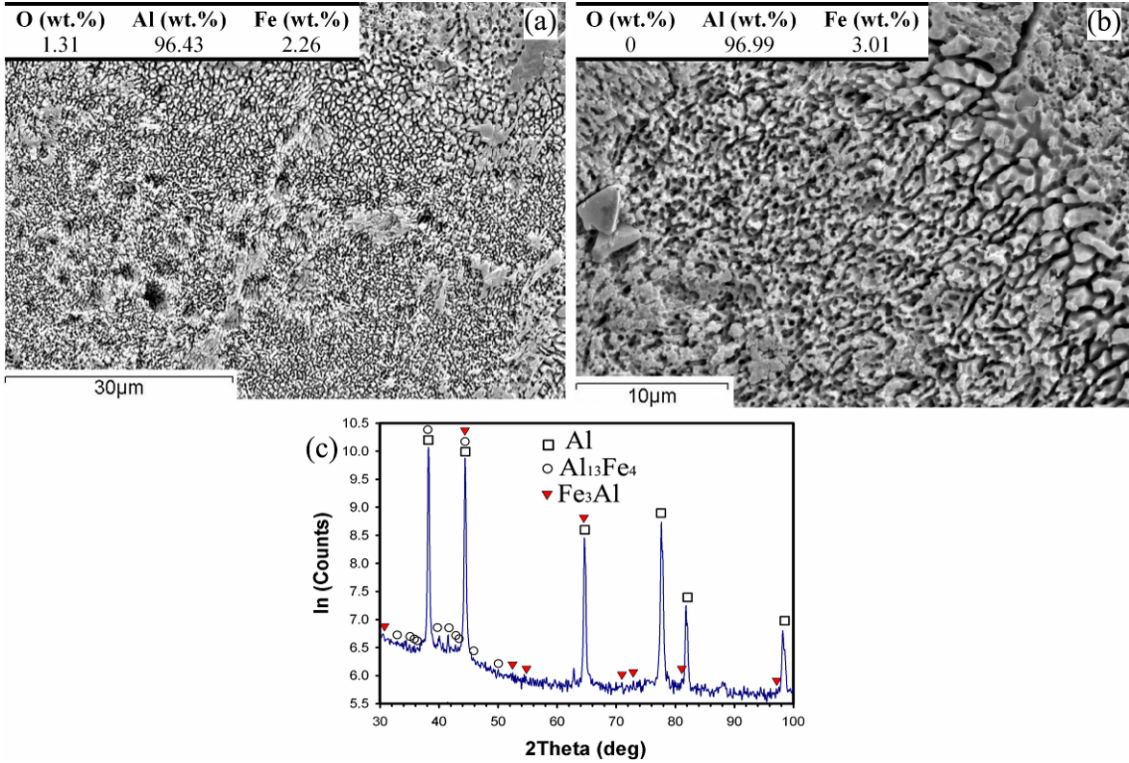


**Fig. 8.6:** (a) Overall appearance of the grain structure, (b) higher magnification of coralline-like and fuzzy appearance in previous image, and (c) XRD pattern of the part fabricated when  $P = 82$  W,  $v = 0.5$  m/s, and  $t = 75$   $\mu\text{m}$ .

### 8.3.2.3. Multilayer parts with layer thickness of 50 $\mu\text{m}$

As shown in Fig. 8.7a-b, the microstructure of the parts fabricated at  $P = 91$  W,  $v = 0.5$  m/s, and  $t = 50$   $\mu\text{m}$  contains grain with a porous and random feature being finer around interiors ( $\sim 0.5\text{-}2$   $\mu\text{m}$  length). The XRD pattern (Fig. 8.7c) shows Al, iron aluminium oxides like  $\text{AlFeO}_3$ , and Al oxides like  $\alpha\text{-Al}_2\text{O}_3$  (alumina), as the main combinations existing in the matrix. At low scanning speed ( $v = 0.14$  m/s), the homogeneous distribution of very fine particles (in nano-sizes and submicron scales) within polygon grains is observed (Fig. 8.8a-b). The coarser particles ( $\sim 0.6\text{-}0.8$   $\mu\text{m}$ ) form boundaries while finer particles ( $\sim 0.2\text{-}0.3$   $\mu\text{m}$ ) are embedded inside grains (Fig. 8.8b). The XRD pattern (Fig. 8.8c) exhibits the peaks corresponding to those of Al,  $\text{Fe}^{2+}\text{Al}_2\text{O}_4$  (iron aluminium oxide) and  $\alpha\text{-Al}_2\text{O}_3$  (alumina), formed from addition of Fe and O to Al matrix. The diffraction peaks for  $\text{Al}_{13}\text{Fe}_4$  are also detected, though the intensity is comparatively weak.

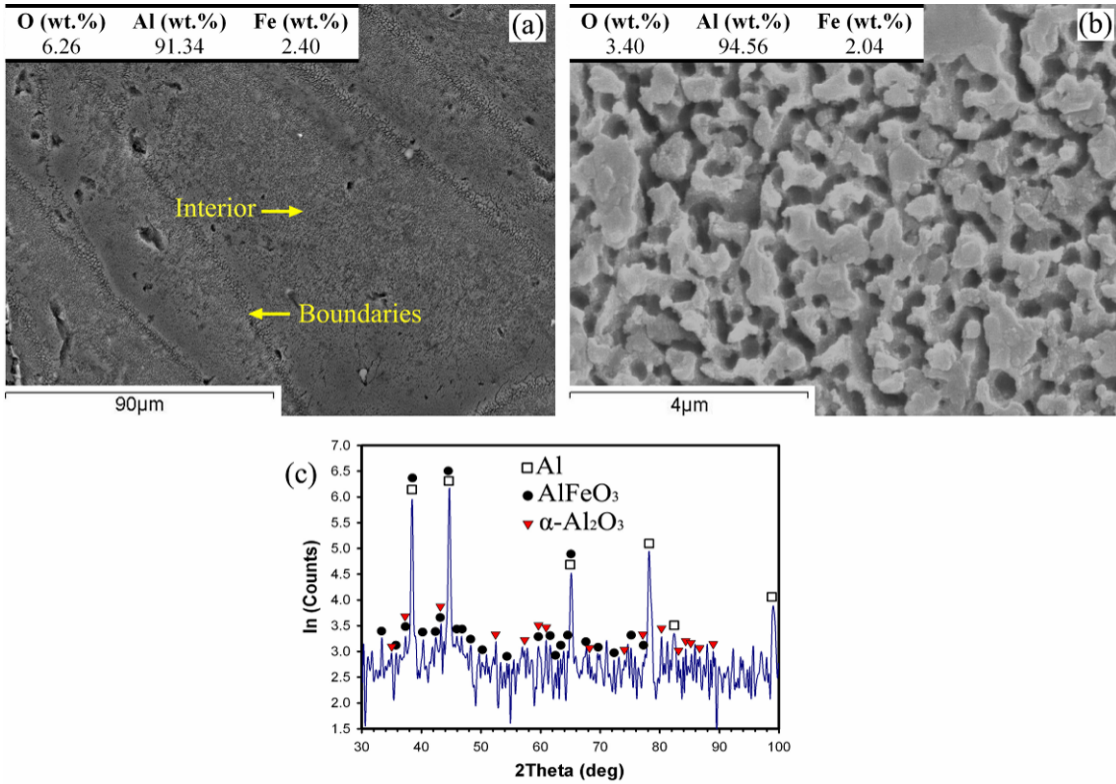


**Fig. 8.7:** (a) Microstructure containing (b) porous feature around interior, and (c) XRD pattern of the part made by  $P = 91$  W,  $v = 0.5$  m/s, and  $t = 50$   $\mu\text{m}$ .

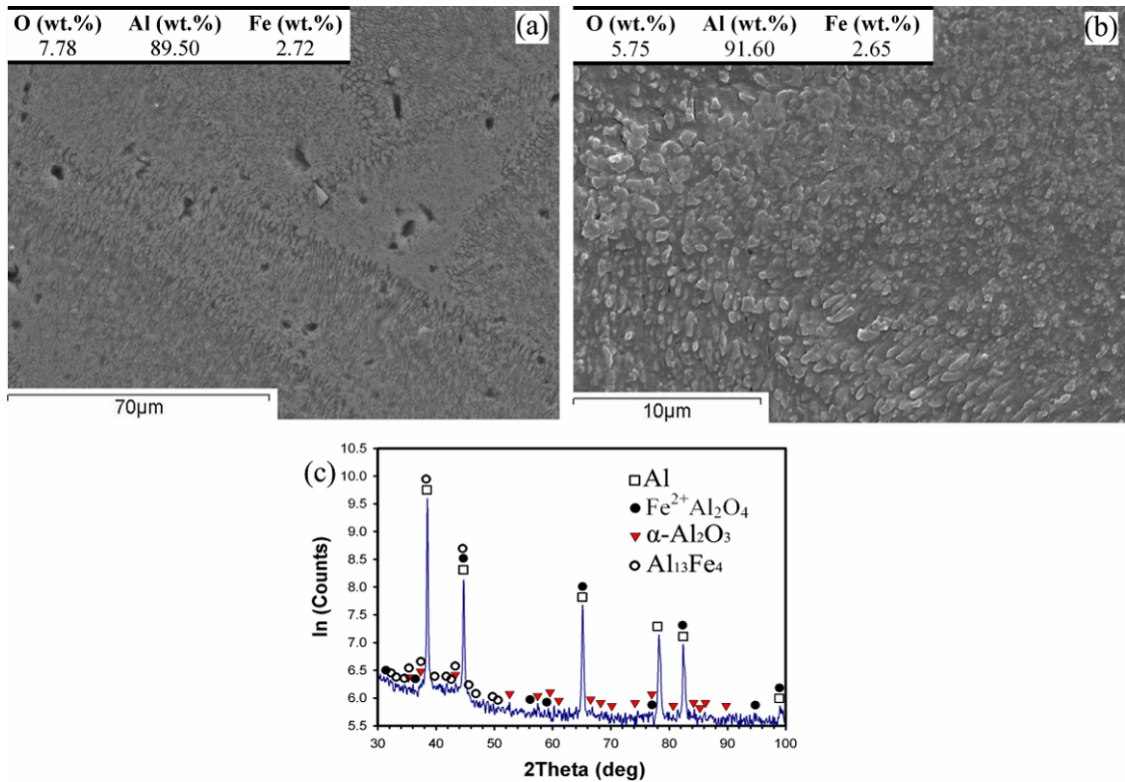


**Fig. 8.8:** a) View of grain structure, b) fine particles formed inside grains and boundaries (close-up of previous image), and (c) XRD pattern of the part made by  $P = 91$  W,  $v = 0.14$  m/s, and  $t = 50$   $\mu\text{m}$ .

## **8.4. Discussion**

### **8.4.1. In-situ interaction initiation**

In an initial stage of laser-material interaction, the energy is absorbed in a narrow layer of individual powder particles, leading to a high temperature of the surface of particles during the interaction (Fischer et al., 2003, Gu et al., 2009d). The melting/exothermic reaction starts from these interfaces between Al and iron oxide interface and the thermite reaction progresses, as mentioned in literature review by Eq. 3.1:



The final phases,  $\text{Al}_2\text{O}_3$  and  $\text{Fe}_3\text{Al}$  intermetallics, are formed by an in-situ chemical reaction in which Al reduces the iron oxide (Fan et al., 2006, Yang et al., 2004). The extra heat from in-situ reaction facilitates melting during SLM process. The mechanism of reaction involves reducing  $\text{Fe}_2\text{O}_3$  to  $\text{Fe}_3\text{O}_4$  and  $\text{FeO}$  by releasing the oxygen and Al oxidation, interaction of Al with iron oxides, and formation of phases such as iron–aluminium-oxide, alumina, iron, and Al-Fe intermetallics, depending on reaction temperature and  $\text{Fe}_2\text{O}_3/\text{Al}$  ratios (Durães et al., 2007, Hofmeister et al., 1999).

### **8.4.2. Effect of layer thickness, laser power, and scanning speed on oxide formation**

The oxygen content as the main factor for quantity of oxides can be reduced due to the increased laser power, e.g. oxygen appears in low laser power in Fig. 8.2a (oxides should be mainly piled up along sintering lines) but not in Fig. 8.2b with higher laser power. This can be attributed to relation of oxide formation with temperature. The increased reaction temperature (due to higher laser power) and inert atmosphere leads to the decomposition of  $\text{Fe}_2\text{O}_3$  into  $\text{FeO}$  and  $\text{Fe}$ , and oxygen which escapes from the specimen (Hofmeister et al., 1999). In a parallel manner, the vaporisation of thin oxide films to fume can occur on the top of the Al molten pool at high temperatures of laser/material interaction (Louvis et al., 2011). The released oxygen and oxide film fume can be carried away by the inert gas flowing over the bed (Verhaeghe et al., 2009). The Marangoni forces can contribute to this oxygen removal by stirring and breaking oxides (Louvis et al., 2011). Likewise, low scanning speed of 0.14 m/s facilitates the removal of the oxygen (e.g. oxygen content is

comparatively much lower in Fig. 8.4 than that of Fig. 8.3 ( $v = 0.5$  m/s) by intensifying the melting flow, decomposition and evaporation (Hofmeister et al., 1999, Louvis et al., 2011).

The general effect of layer thickness on oxygen content can be recognised through a comparison between Figs. 8.7-8.8 ( $t = 50$   $\mu\text{m}$ ) to Figs. 8.3-8.6 ( $t = 75$   $\mu\text{m}$ ) and Fig. 8.2 (thick powder bed). As observed, the thicker layer thickness enhances the oxygen removal mechanisms by enhancing temperature and stirring (since a thicker layer reduces the cooling rate, activates more exothermic reaction and produces a larger melting pool). This higher oxygen in lower layer thicknesses contributes to the formation of hard oxides in the form of aluminium oxide ( $\text{Al}_2\text{O}_3$ ) or iron aluminium oxides (like  $\text{Fe}^{2+}\text{Al}_2\text{O}_4$  and  $\text{AlFeO}_3$ ), reinforcing the matrix.

#### 8.4.3. Microstructures, phases, and microhardness

The microstructural outcome of in-situ reaction is affected from interaction of constituents during SLM of Al and  $\text{Fe}_2\text{O}_3$  powder mixture. In fact, the available constituents (see Eq. 3.1) can act as nucleation sites to facilitate heterogeneous nucleation (Smallman and Bishop, 1999) in molten Al powders. It is well established that active heterogeneities assist rapid solidification to achieve refined microstructure by heterogeneous nucleation mechanisms (Rieker and Morris, 1990). For instance, a fine and granular grain feature from single Al phase (regarding XRD pattern shown in Fig. 8.2c) was formed in the SLM specimen built on a thick Al/ $\text{Fe}_2\text{O}_3$  powder bed (Fig. 8.2), with no evidence of secondary phases including new components. Perhaps, the new components are below the minimum range of detection by the applied techniques, though they still contribute to facilitate heterogeneous nucleation refining the microstructure. It can also be postulated that the observed phase is a super saturated solid solution. In fact, the oxygen has been efficiently removed from the surface of thick powder bed and remained iron has been resolved inside the matrix. This leads to an Al matrix saturated by Fe due to rapid solidification from a high temperature during SLM process (rapid solidification assists saturation of Al by other elements (Rajabi et al., 2008, Wong et al., 1997)). This contributes to strengthening by solution hardening. However, the microstructure can also be influenced by laser parameter, e.g. increasing the laser power improves melting degree and fusion of the grain boundaries (sintering lines in Fig. 8.2a have been diminished in Fig. 8.2b).

As shown in the Fig. 8.1, all the SLM multilayer parts exhibit higher microhardness than that of the conventional pure aluminium and their hardness generally increases with the laser power. Among the SLM parts, the lowest hardness belongs to the part made by  $P = 39$  W,  $v = 0.5$  m/s and  $t = 75$   $\mu\text{m}$ . The microstructure of this sample has been shown in Fig. 8.3, where fuzzy and coralline-like boundaries seem to develop into interior. These fuzzy phases are mainly composed of Al and Al-Fe(-O) combinations such as  $\text{Al}_{13}\text{Fe}_4$  (the  $\text{Fe}_3\text{Al}$  is the ordinary production of Eq. 3.1, but excessive Al leads to the formation of equilibrium  $\text{Al}_{13}\text{Fe}_4$  instead (Griger and Stefániay, 1996)) and  $\text{Fe}^{2+}\text{Al}_2\text{O}_4$  ( $\text{Fe}^{2+}\text{Al}_2\text{O}_4$  formation requires a lower activation energy than that of  $\text{Al}_2\text{O}_3$  (Fan et al., 2006), and therefore is a main product of thermite reaction, though it tends to transform into  $\text{Al}_2\text{O}_3$  and Al-Fe intermetallics (Hofmeister et al., 1999)) plus  $\text{Al}_2\text{O}_3$ , according to the XRD pattern (Fig. 8.3b-c). These phases are intermetallics and oxides, commonly have a high hardness, and are demanded for hardening/strengthening purposes (e.g.  $\text{Al}_2\text{O}_3$  has been used as reinforcement in Al alloys (Dirras et al., 2011) or  $\text{Al}_{13}\text{Fe}_4$  been recognised as major hardening phase in surface hardening of Al by Fe-ion implantation (Gao and Liu, 1997)). Therefore, they enhance the hardness of Al matrix compared to pure Al. However, since the low laser power was used, the energy input has not been adequate to fully melt the mixture and spread the in-situ reaction all over the Al powder particles, and hence the part hardness is still low.

The boundaries in Fig. 8.3a (with coralline-like appearance) are composed of Fe-rich intermetallics and Al oxides (forming during in-situ reaction), while interior mostly contains Al. This is in confirmation with average particle size of Al powders (about 40  $\mu\text{m}$ ) which leads to a similar range size of grain structure. In contrast, coralline-like feature develops throughout the part fabricated by higher laser power of 82 W, when other parameters were kept the same (see Fig. 8.6). The higher laser power in the same scanning speed assist the reaction to be further developed, producing ultra fine Al-Fe coralline-like intermetallics such as  $\text{Al}_{13}\text{Fe}_4$  and  $\text{Fe}_3\text{Al}$  (see XRD pattern in Fig. 8.6c). It seems that large amount of available Al interacts with released Fe and forms  $\text{Fe}_3\text{Al}$  (as a product of Eq. 3.1) and/or  $\text{Al}_{13}\text{Fe}_4$  as an equilibrium intermetallic (Griger and Stefániay, 1996). Obviously, this transformation lasts as much as possible (depending on time and temperature). However, this is accompanied with removing oxides from matrix and lowering the oxygen content, in such a manner that  $\text{Al}_2\text{O}_3$  and  $\text{Fe}^{2+}\text{Al}_2\text{O}_4$  disappeared (Fig. 8.6b-c). Instead, the fine and

hard Al-Fe intermetallics are placed in matrix enhancing the microstructural hardness (see the corresponding microhardness curve in Fig. 8.1).

Similar to Fig. 8.3, Fig. 8.4 ( $P = 39$  W,  $v = 0.14$  m/s and  $t = 75$   $\mu\text{m}$ ) contains coralline-like features in boundaries, belonging to  $\text{Fe}_3\text{Al}$  and  $\text{Al}_{13}\text{Fe}_4$  intermetallics and  $\text{Fe}^{2+}\text{Al}_2\text{O}_4$  (iron aluminium oxide), though the corallines are slightly further developed due to lower scanning speed. In fact, lower laser speed enhances the laser input and decreases the cooling rate leading to coarsening of corallines and further spreading them. As a result, the corallines due to lower scanning speed seem to be coarser (the coralline tips are  $\sim 1\text{-}2$   $\mu\text{m}$  in Fig. 8.4, but  $\sim 0.5$   $\mu\text{m}$  in Fig. 8.3). Also, enhancing the melting (by increasing laser input) results in further propagation of these Al-Fe intermetallics into interior, a more uniform microstructure, and a higher hardness. This continues with higher laser powers in low scanning speed of 0.14 m/s (leading to efficient oxygen removal) where Fig. 8.5 shows coralline-like phases (mainly from  $\text{Al}_{13}\text{Fe}_4/\text{Al}_{82}\text{Fe}_{18}$  intermetallics) all over the sample in the absence of  $\text{Al}_2\text{O}_3$  in XRD results. This leads to the highest hardness in the relevant curve of this specimen treated at  $P = 61$  W,  $v = 0.14$  m/s and  $t = 75$   $\mu\text{m}$  (see Fig. 8.1). After this, the hardness may fall despite bonding improvement in higher laser powers. Perhaps, further laser energies might lead to excessive coarsening effects or other softer in-situ products which might decrease the hardness of the parts.

Decreasing the layer thickness of the parts to 50  $\mu\text{m}$  also affects the microstructural characteristics. For instance, lowering the layer thickness changes the sharp-pointed coralline-like appearance of microstructure (Fig. 8.6) into round-headed porous features in Fig. 8.7b ( $P = 91$  W,  $v = 0.5$  m/s, and  $t = 50$   $\mu\text{m}$ ). The oxygen content is considerably higher than what observed in higher layer thickness (for example compare Fig. 8.7 to Fig. 8.6), leading to  $\text{Al}$ ,  $\text{AlFeO}_3$ , and  $\alpha\text{-Al}_2\text{O}_3$  (alumina) as the main combinations (Fig. 8.7c) which clearly indicates a greater influence of oxygen. Alumina can originate from both fragmented surface oxides and in-situ products, while  $\text{AlFeO}_3$  is another ternary compound (existing in Fe-Al-O system) and is only stable at certain temperatures e.g. between 1318 and 1500 °C, and at oxygen partial pressures greater than 0.5 atm (Subramanian et al., 1998). It seems that rapid solidification (due to high laser speed of 0.5 m/s) at high temperature (due to high laser power of 91 W) accidentally provides such conditions producing the  $\text{AlFeO}_3$  followed by quenching via rapid solidification. This new phase may appear with such round-headed porous features (like piles of particles or rough corallines)

and perhaps wetted by Al liquid, instead of Al-Fe intermetallics (such as  $\text{Al}_{13}\text{Fe}_4$ ) which comes into view mostly as fine coralline-like features.

Reducing the laser speed in conjunction with lower layer thickness of 50  $\mu\text{m}$  leads to very promising results in the term of microstructure. The lower layer thickness intensifies the remelting of ex-layers leading to breaking and separating the corallines. It also increases the cooling rate which refines the microstructure. Moreover, it decreases the oxygen removal which increases the oxides. On the other hand, the lower laser speed assists the fragmentation of oxide layers. The result, as seen from Fig. 8.8a-b, is very fine particles (in nano-size and submicron scale), being homogeneously distributed and seeming to establish a strong bonding at the interface with the matrix. These particles act as reinforcements and mainly are from hard materials such as  $\text{Fe}^{2+}\text{Al}_2\text{O}_4$ ,  $\text{Al}_2\text{O}_3$ , and  $\text{Al}_{13}\text{Fe}_4$  (Fig. 8.8c). These fine, hard, stable, well-bonded and well-distributed reinforcing particles result in the highest hardness for this sample (shown in Fig. 8.1), and in fact are bright characteristics of an advanced metal matrix composite part. A summary of the effect of layer thickness and laser parameters on microstructural evolution is gathered in Table 8.1.

**Table 8.1:** Summary of microstructural evolution in dependence of layer thickness, laser power and scanning speed

	Thick powder bed	$t = 75 \mu\text{m}$	$t = 50 \mu\text{m}$
Morphology (appearance)	Single Al phase – granular structure	Predominantly coralline-like	Coralline-like/porous feature/particulate
Oxygen/oxides content	Least oxygen/oxide	medium oxygen/oxide	Highest oxygen/oxide
Predominant phases	Al	Al , Al-Fe intermetallics such as $\text{Al}_{13}\text{Fe}_4$ and $\text{Fe}_3\text{Al}$ , some oxides (like $\text{Fe}^{2+}\text{Al}_2\text{O}_4$ and $\text{Al}_2\text{O}_3$ ) may also be detected	Al , aluminium oxide ( $\text{Al}_2\text{O}_3$ ) plus iron aluminium oxides (e.g. $\text{Fe}^{2+}\text{Al}_2\text{O}_4$ and $\text{AlFeO}_3$ ) , Al-Fe intermetallics such as $\text{Al}_{13}\text{Fe}_4$
Increasing laser power	Development of melting and diminishing the sintering lines – enhanced oxygen removal	Development of corallines (mainly Al-Fe intermetallics) and oxide particles from primary Al/ $\text{Fe}_2\text{O}_3$ interface – enhanced oxygen removal	N/A
Lowering scanning speed	N/A	Coarsening of corallines – enhanced oxygen removal	Improved dispersion of secondary phases leading to well-placement of fine particles inside grains and boundaries

#### 8.4.4. In-situ combined SLM phenomena

The Al-Fe equilibrium binary diagram shows a eutectic point around 1.8 wt% iron which is composed of Al and Al<sub>3</sub>Fe (Al<sub>13</sub>Fe<sub>4</sub>) (Allen et al., 2001, Griger and Stefániay, 1996). The eutectics usually tend to form with a lath-like morphology, but, here, the rapid solidification restricts their growth. Thus, these incomplete Al-Fe lath-like eutectics appear with a coralline-like morphology. As seen, the fine coralline-like phases demonstrate a low oxygen content denoting the Al and Al-Fe intermetallics as the main constituents (e.g. Fig. 8.6b). Although the existence of coralline-like phases is unusual, it was reported by other researchers as well. For example, Wong et al. (Wong et al., 1997) was observed that the eutectic silicon in Al-Si alloys was strongly modified during laser treatment, in such a manner that silicon crystal in eutectic was changed morphologically from lath-like into coralline-like.

As summarised in Table 8.1, lowering layer thickness alters the microstructure and phases by intensifying the remelting of ex-layers (breaking and separating the corallines), increasing the cooling rate (refining the microstructure), and decreasing the oxygen removal (increasing the oxides). The SLM of single layer specimens on a thick powder bed (especially at higher laser powers) forms an Al granular feature saturated by Fe and diminishes the oxygen content. When the 75 µm layer thickness is used, low laser energies form the coralline-like phases (being in fact rapidly solidified Al-Fe eutectics), though Al oxide (mainly in the form of particles) may also be found from surface oxide fragmentations or in-situ products. Higher laser power develops the in-situ reaction leading to incorporation of Al into Fe<sup>2+</sup>Al<sub>2</sub>O<sub>4</sub> and transforming it into Fe<sub>3</sub>Al and then equilibrium Al<sub>13</sub>Fe<sub>4</sub> (as much as possible depending on the condition). Simultaneously, oxygen removal is highly efficient in the high energy inputs and mitigates the oxides, leaving mainly Al and Al-Fe intermetallics in the microstructure. Thus, coralline-like features propagate all over the samples in these conditions. A decrease in layer thickness into 50 µm suppresses the oxygen removal and increases the stable and particulate Al<sub>2</sub>O<sub>3</sub>. It also increases the solidification rate which decreases the transformation of iron aluminium oxides (like Fe<sup>2+</sup>Al<sub>2</sub>O<sub>4</sub> and AlFeO<sub>3</sub>) into intermetallics. The lower scanning speed may increase the fragmentation of oxide layers. This collaborates with the ex-layer remelting which breaks the corallines formed in previous layers. Consequently, coralline-like appearance may disappear and particulate reinforced Al matrix may be revealed.

## 8.5. Conclusions

In-situ reaction was successfully activated by using SLM process in a powder mixture of Al/5wt%Fe<sub>2</sub>O<sub>3</sub>. The microstructural evolution of SLM parts was investigated in dependence of various parameters such as powder layer thickness, laser power and scanning speed. The main results can be summarised as:

- Various powder layer thicknesses led to various microstructures. The microstructure after SLM of a thick powder bed, 75 µm layer thickness, and 50 µm layer thickness appeared with dominantly granular, coralline-like (being in fact rapidly laser solidified Al-Fe eutectics), and round-headed coralline-like/particulate features, respectively. These microstructures represent mainly pure Al, Al-Fe intermetallics (such as Fe<sub>3</sub>Al, Al<sub>13</sub>Fe<sub>4</sub>, Al<sub>82</sub>Fe<sub>18</sub>), and Al(-Fe)-O oxides (such as Al<sub>2</sub>O<sub>3</sub>, Fe<sup>2+</sup>Al<sub>2</sub>O<sub>4</sub> and AlFeO<sub>3</sub>) after rapid solidification.
- The primary in-situ products are phases such as Fe<sub>3</sub>Al and Al(-Fe)-O oxides (e.g. Fe<sup>2+</sup>Al<sub>2</sub>O<sub>4</sub>), but they tend to transform into more stable combinations such as Al<sub>13</sub>Fe<sub>4</sub> and α-Al<sub>2</sub>O<sub>3</sub>.
- Thicker layers lead to more efficient oxygen removal during SLM. This can be considered as the main reason for the large microstructural and phase differences due to changing in layer thickness.
- Higher laser power also contributes to more efficient oxygen removal during SLM. Higher scanning speed leads to finer Al-Fe coralline-like features, though it may restrict the in-situ progress and transformation of products.
- A very promising result (useful to manufacture Al matrix composites) was achieved by using low layer thickness, high laser power, and low scanning speed. This led to well-bonded and uniform distribution of fine, hard and stable particles in Al matrix, and consequently resulted in the highest comparative microhardness.

---

# **Chapter 9: Effect of Fe<sub>2</sub>O<sub>3</sub> Content on Microstructural Evolution of Al/Fe<sub>2</sub>O<sub>3</sub> Powder Consolidated Parts Made by Selective Laser Melting at Different Laser Powers and Scanning Speeds**

---

## **9.1. Introduction**

The in-situ formed combinations in the mixture of Al with less expensive Fe<sub>2</sub>O<sub>3</sub> powders can reinforce or modify the matrix, in such a manner that the mechanical properties of MMCs are controlled by the size and volume fraction of the reinforcements, matrix–reinforcement interface, and matrix nature. On the other hand, the microstructure is influenced by rapid solidification and heating conditions during SLM processing (Tong and Fang, 1998a). Accordingly, understanding the outcome of all these aspects is critical to combine the advantageous of both in-situ Al MMCs and rapid solidification. Chapter 7 of this study explained the SLM behaviour and processing windows of in-situ reacted Al/Fe<sub>2</sub>O<sub>3</sub> powder mixture. After that, chapter 8 illustrated the effect of layer thickness in conjunction with various laser parameters on the microstructural evolution of Al/5wt%Fe<sub>2</sub>O<sub>3</sub>. However, the effect of Fe<sub>2</sub>O<sub>3</sub> content on the microstructure remained unknown. This chapter fills this gap and investigates the effect of different Fe<sub>2</sub>O<sub>3</sub> contents (5, 10 and 15 wt%) on microstructural evolution of Al matrix in-situ composites. For this purpose, the samples are manufactured as described in section 7.2 page 114. The outcome microstructures (affected by in-situ formed particles and laser rapid solidification) are characterised and its relationship with microhardness is discussed. The findings of this study provide an in-depth scientific understanding to develop novel Al MMCs by using SLM assisted in-situ processes.

## 9.2. Results

### 9.2.1. Hardness measurements

Fig. 9.1 shows the results of microhardness vs. laser power in dependence of  $\text{Fe}_2\text{O}_3$  contents and scanning speeds ( $v \sim 0.14 \text{ m/s}$  and  $0.5 \text{ m/s}$ ), that appear as a trend in which the hardness usually increases with laser power, but it may reach a maximum value. For example, the hardness in the curve of  $\text{Al}/10\text{wt}\%\text{Fe}_2\text{O}_3$  and  $v = 0.5 \text{ m/s}$  increases up to about 82 W reaching a maximum value of about 89 HV and then it decreases with further increase of laser power. On the other hand, scanning speed also affects the hardness, i.e. lower scanning speed usually leads to higher hardness. The significant influence of  $\text{Fe}_2\text{O}_3$  content to improve the hardness is also evident. For example, highest hardness in the curve of  $\text{Al}/5\text{wt}\%\text{Fe}_2\text{O}_3$  ( $P = 91 \text{ W}$ ,  $v = 0.14 \text{ m/s}$ ) is about 60 HV, while increasing the  $\text{Fe}_2\text{O}_3$  to 15 wt% enhances the highest hardness to about 100 HV. The positive effect of  $\text{Fe}_2\text{O}_3$  becomes more clearly in comparison with hardness of pure aluminium (ASM International Handbook Committee, 1992), when the highest hardness in Fig. 9.1 belongs to  $\text{Al}/15\text{wt}\%\text{Fe}_2\text{O}_3$  and is about 5 times higher than pure Al hardness. It also seems that the  $\text{Fe}_2\text{O}_3$  have a stronger impact on hardness than that of the laser power and scanning speed. For instance, the hardness of  $\text{Al}/15\text{wt}\%\text{Fe}_2\text{O}_3$  treated at low laser power (39 W) and high scanning speed (0.5 m/s) is higher than those of  $\text{Al}/5\text{wt}\%\text{Fe}_2\text{O}_3$  and  $\text{Al}/10\text{wt}\%\text{Fe}_2\text{O}_3$  treated at relative high laser powers (e.g. 80-90 W) and low scanning speeds (e.g. 0.14 m/s).

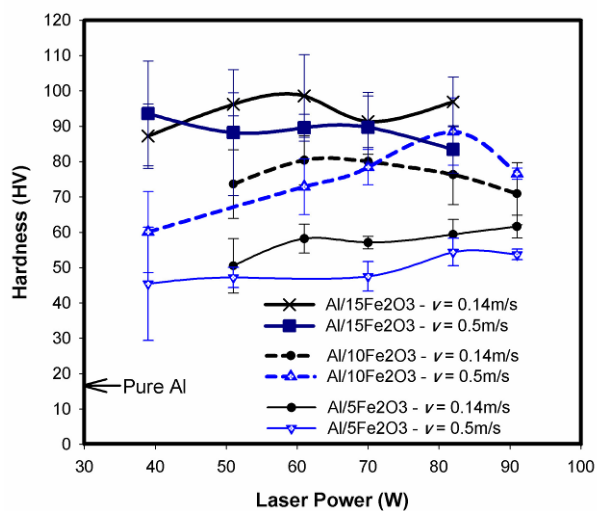
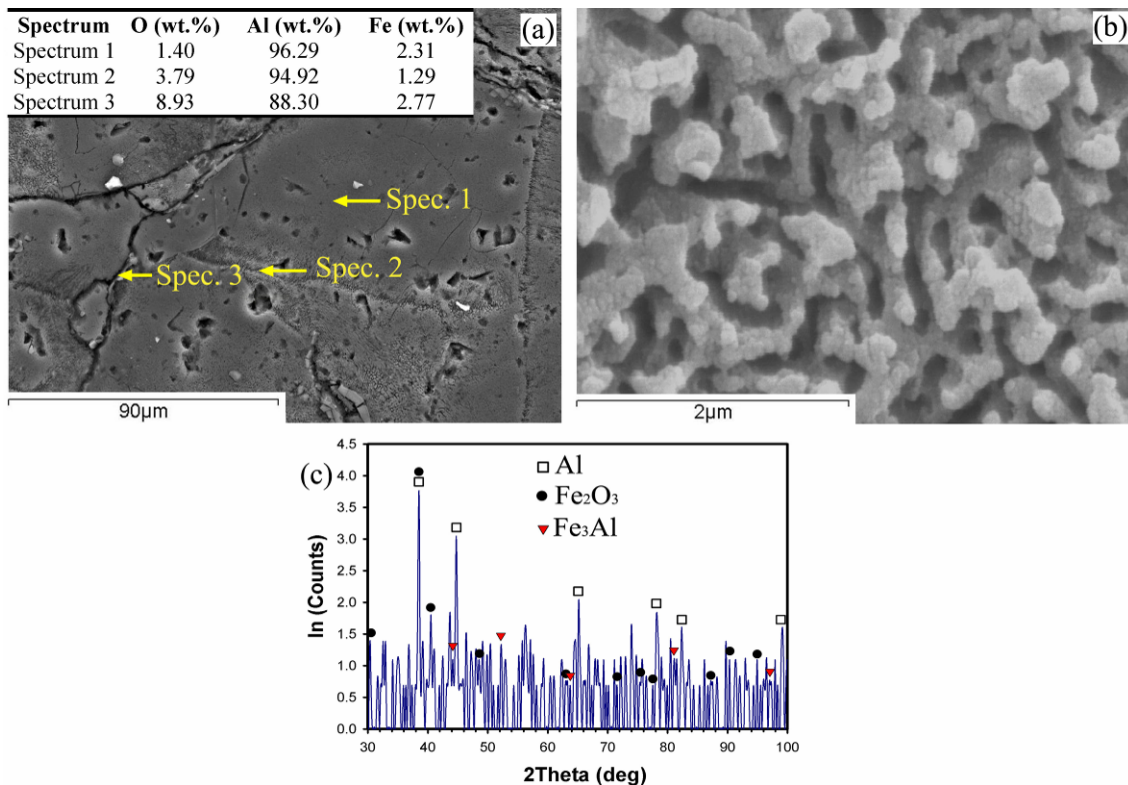


**Fig. 9.1:** Microhardness of the parts fabricated from  $\text{Al}/5\text{-}15\text{wt}\%\text{Fe}_2\text{O}_3$  powder mixtures as a function of laser power in conjunction with various scanning speeds.

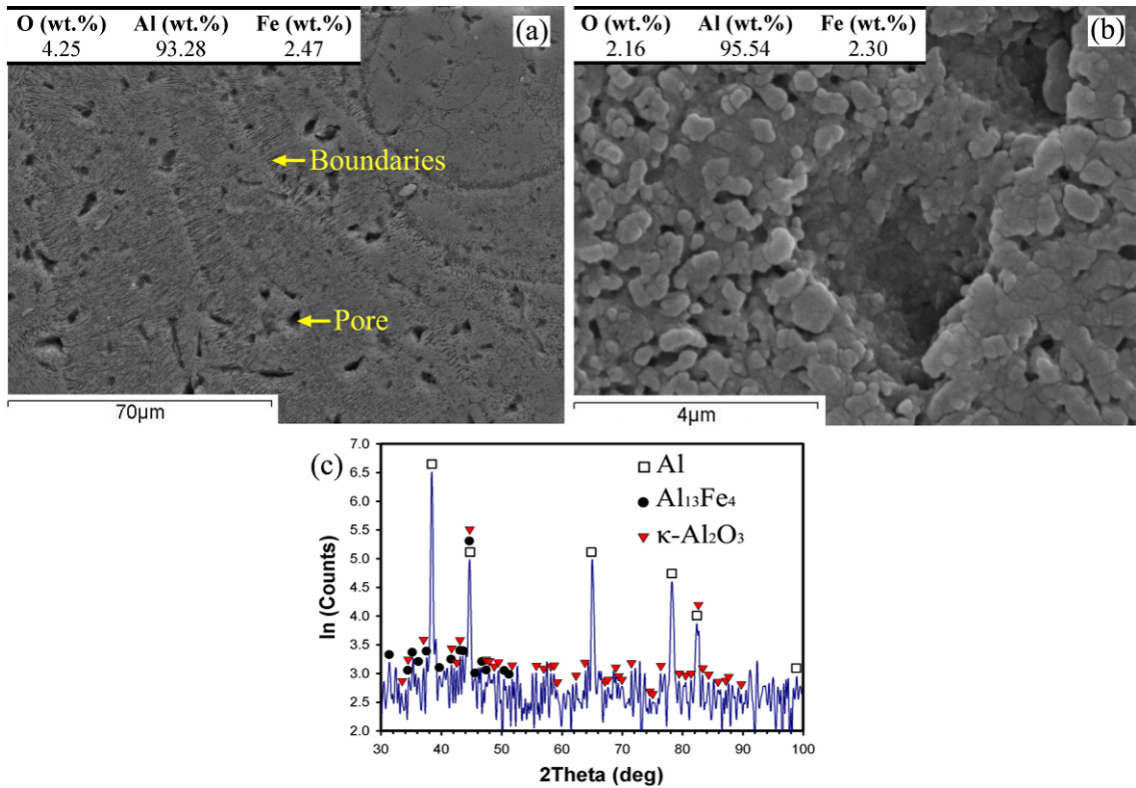
## 9.2.2. Microstructural characterisation and phase identification using XRD

### 9.2.2.1. Al/5wt%Fe<sub>2</sub>O<sub>3</sub>

Fig. 9.2a-b is SEM microscopic graphs of the part fabricated from Al/5wt%Fe<sub>2</sub>O<sub>3</sub> using  $P = 39$  W and  $v = 0.5$  m/s. Fig. 9.2a exhibit grains and corresponding boundaries. The gap between solid areas (around spectrum 3) is due to insufficient melting and contains the highest oxygen. The grain boundaries (around spectrum 2) demonstrate a very fine (submicron) coralline-like appearance (Fig. 9.2b), and contain higher oxygen than interior (compare spectrum 2 to 1). The XRD results in Fig. 9.2c shows Al, Fe<sub>3</sub>Al and Fe<sub>2</sub>O<sub>3</sub> as the main phases forming the matrix. However, a decrease in the scanning speed to  $v = 0.14$  m/s when  $P = 51$  W further develops the boundaries into the interior (Fig. 9.3a), and the microstructure contains porosity formed in particulate matrix (Fig. 9.3a-b). The XRD spectrum (Fig. 9.3c) indicates that the part is mainly composed of phases such as Al, Al<sub>13</sub>Fe<sub>4</sub>, and  $\kappa$ -Al<sub>2</sub>O<sub>3</sub>.

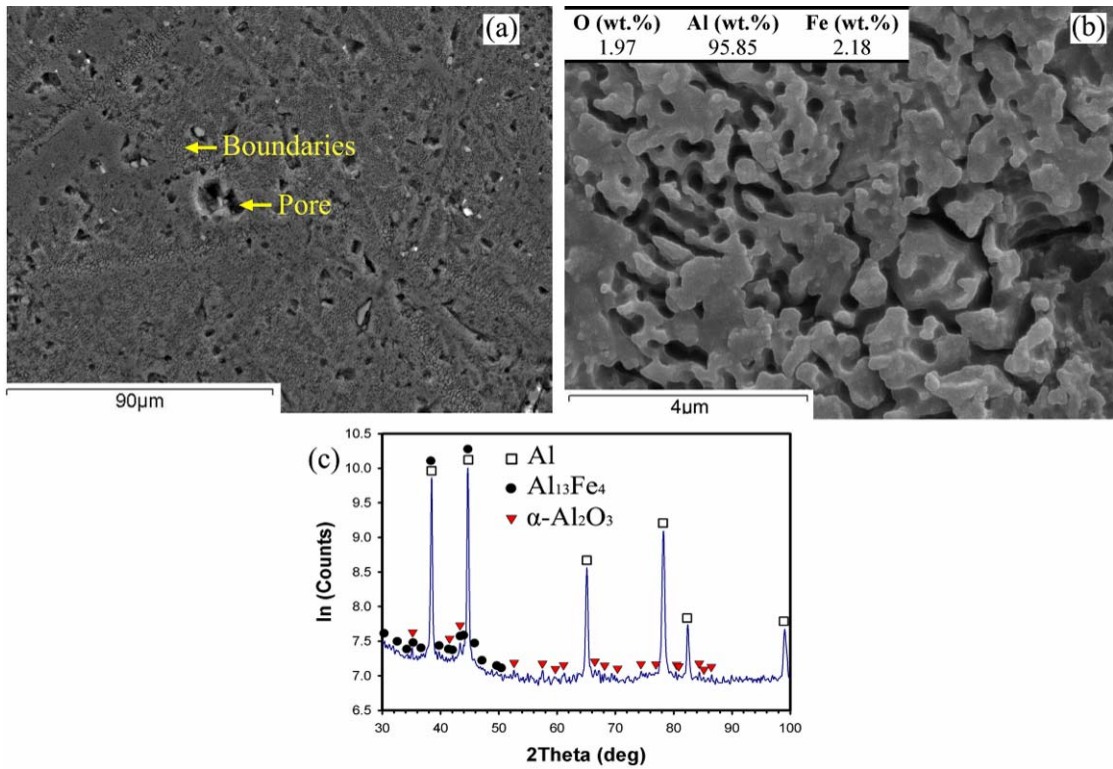


**Fig. 9.2:** SEM micrographs of Al/5wt%Fe<sub>2</sub>O<sub>3</sub> when  $P = 39$  W and  $v = 0.5$  m/s; (a) overall view of solid formations and microstructure, and (b) high magnification of coralline-like appearance of boundaries (around spectrum 2). (c) X-ray diffraction pattern of the corresponding part.

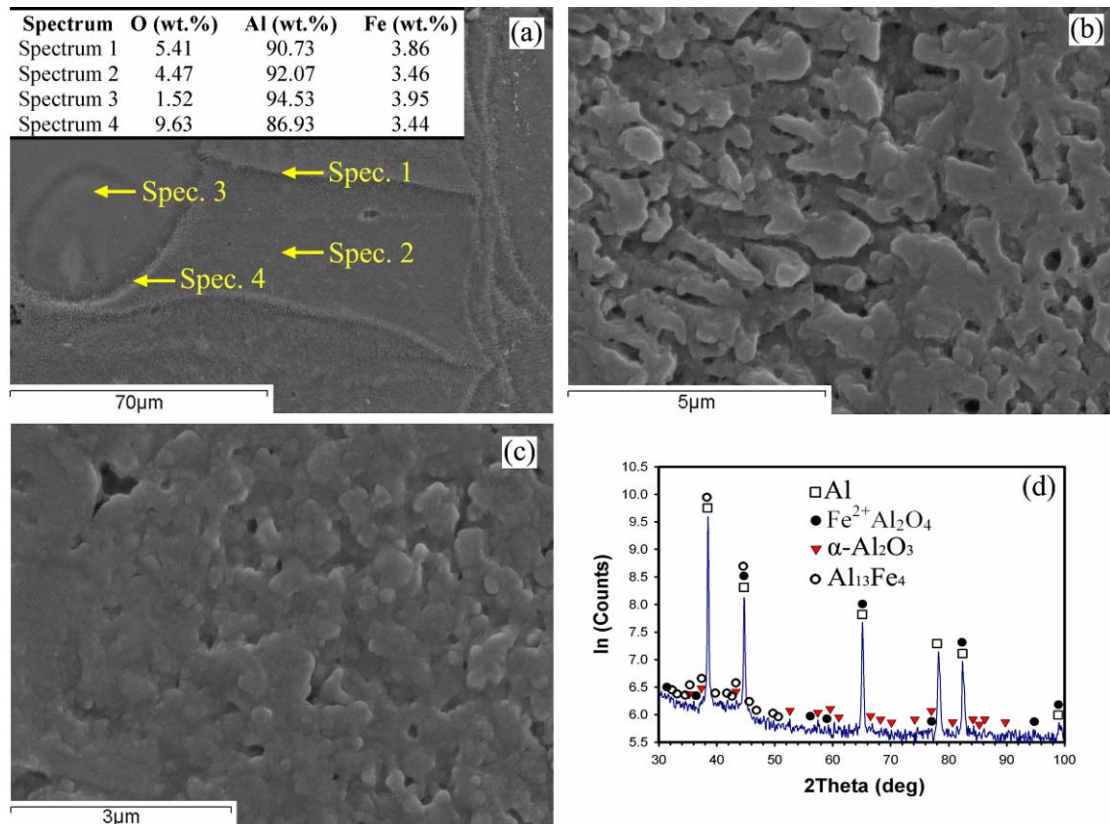


**Fig. 9.3:** (a) Overall view of microstructure, (b) details around a pore and particulate format of phases inside matrix, and (c) XRD pattern of the Al/5wt%Fe<sub>2</sub>O<sub>3</sub> part when  $P = 51$  W and  $v = 0.14$  m/s.

The overall view of microstructure of the part fabricated from Al/5wt%Fe<sub>2</sub>O<sub>3</sub> using  $P = 82$  W and  $v = 0.5$  m/s contains a porous coralline-like structure in boundaries, relatively smoother interior, in the presence of certain porosity, as seen from Fig. 9.4a). The porous coralline-like boundaries (formed from Al, Fe, and O) may include very fine (sub-micro or even nano-scale) particles (Fig. 9.4b). Fig. 9.4c shows Al, Al<sub>13</sub>Fe<sub>4</sub>, and  $\alpha$ -Al<sub>2</sub>O<sub>3</sub> as the main constituents. A reduction in scanning speed to  $v = 0.14$  m/s, as seen in Fig. 9.5, develop a grain structure in which the pores have been largely disappeared (in comparison with previous figures), and semi-particulate phases have been developed almost all over the matrix (Fig. 9.5a). The size and morphology of these semi-particles lead to a microstructure including grain boundaries and relevant interiors (Fig. 9.5b-c). For example, the boundaries (around spectrum 1) may contain large particulate solids bonded together (Fig. 9.5b), having a general higher oxygen content. In contrast, the interior shows a smoother appearance, less oxygen (Fig. 9.5a), minimum segregation and firmly enclosed particles (e.g. Fig. 9.5c). The XRD pattern (Fig. 9.5d) identifies Al and Fe<sup>2+</sup>Al<sub>2</sub>O<sub>4</sub> (iron aluminium oxide),  $\alpha$ -Al<sub>2</sub>O<sub>3</sub> (alumina) and finally Al<sub>13</sub>Fe<sub>4</sub>.



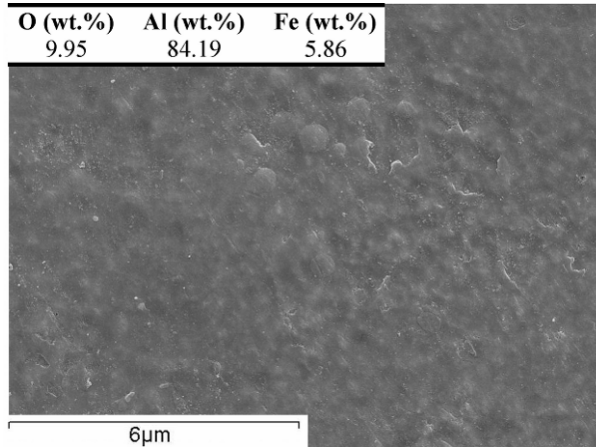
**Fig. 9.4:** (a) Microstructural overall view, (b) mixture of coralline-like feature and fine particles developing in matrix, and (c) XRD pattern of the Al/5wt%Fe<sub>2</sub>O<sub>3</sub> part when  $P = 82$  W and  $v = 0.5$  m/s.



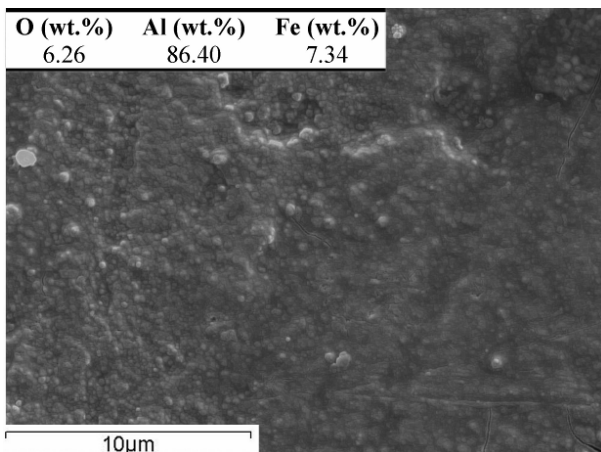
**Fig. 9.5:** (a) Overall view of microstructure, (b) large semi-particulate features around spectrum 1, (c) smooth area around spectrum 3, and (d) XRD pattern of the Al/5wt%Fe<sub>2</sub>O<sub>3</sub> part when  $P = 82$  W and  $v = 0.14$  m/s.

### 9.2.2.2 Al/10wt%Fe<sub>2</sub>O<sub>3</sub>

Fig. 9.6 shows another appearance of microstructure looking like orange peel, being in fact particles firmly embedded in matrix and covered by a thin film (the relatively high oxygen content in this area is evident), revealed in Al/10wt%Fe<sub>2</sub>O<sub>3</sub> when  $P = 39$  W and  $v = 0.5$  m/s. Fig. 9.7 also shows that the matrix embeds fine particles and appears as coarse orange peel when  $P = 51$  W and  $v = 0.14$  m/s.



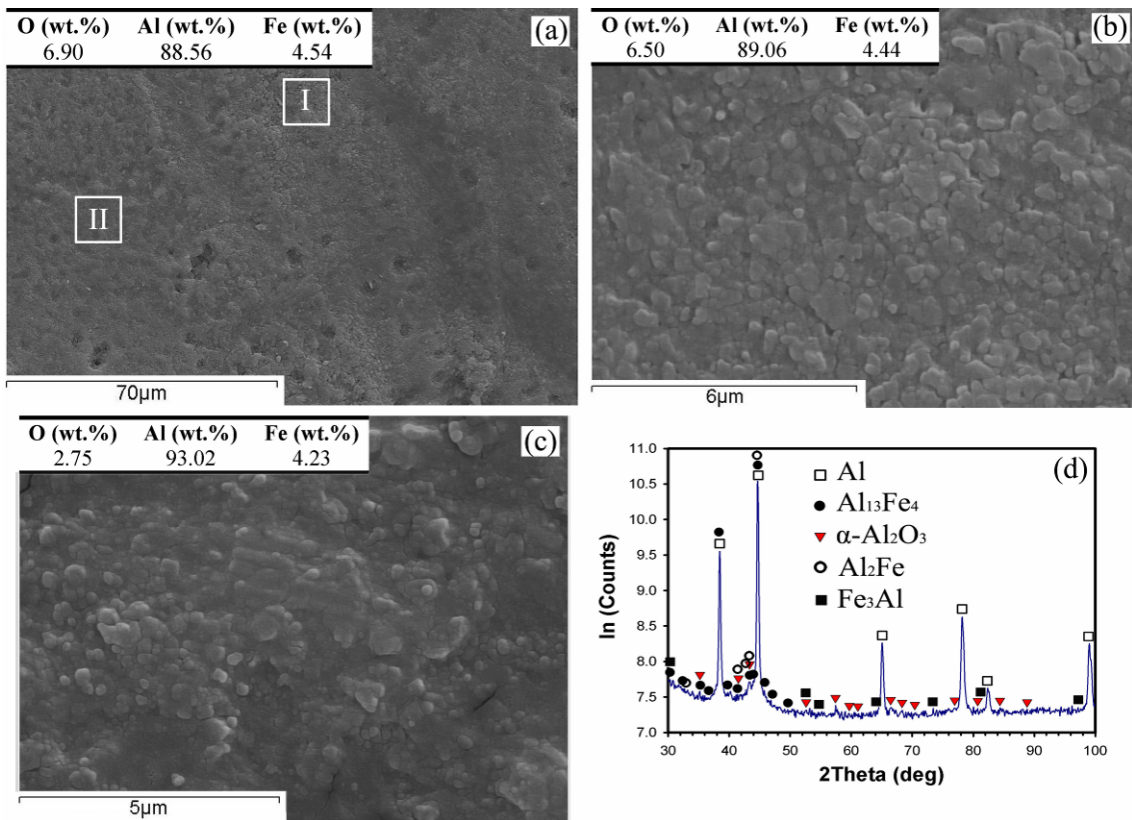
**Fig. 9.6:** The SEM micrographs of Al/10wt%Fe<sub>2</sub>O<sub>3</sub> (when  $P = 39$  W and  $v = 0.5$  m/s) showing a single phase matrix having an orange peel appearance.



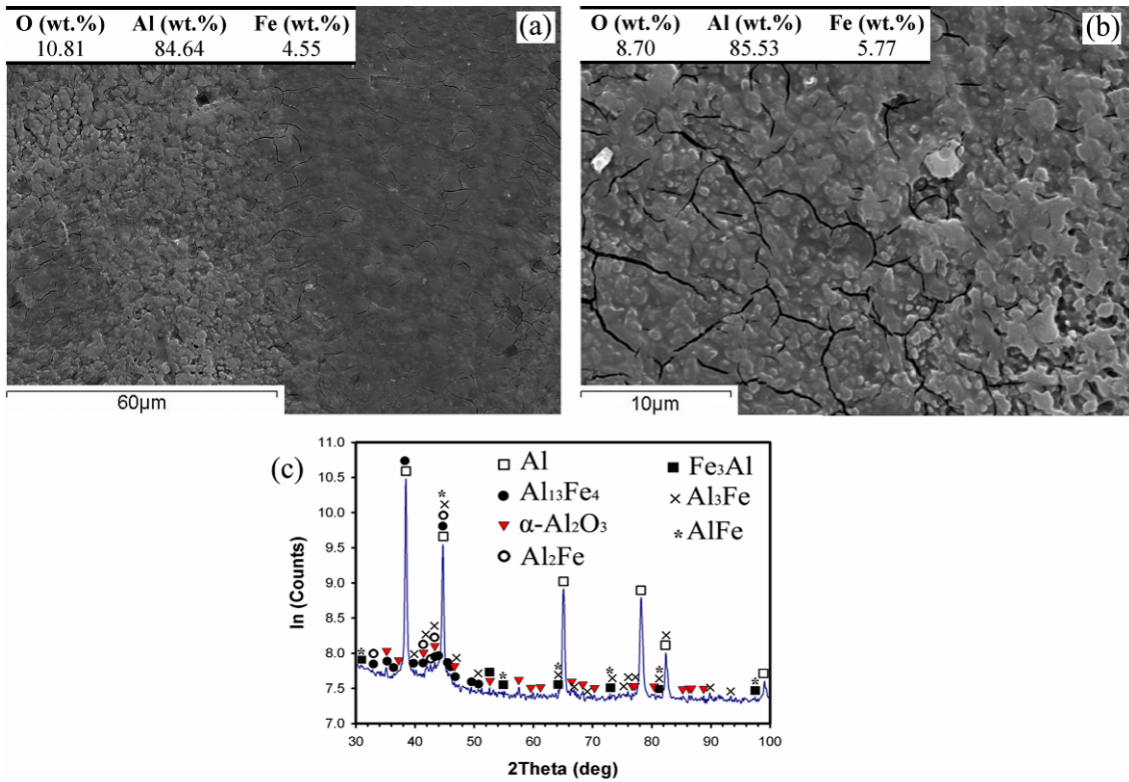
**Fig. 9.7:** The typical microstructure of Al/10wt%Fe<sub>2</sub>O<sub>3</sub> when  $P = 51$  W and  $v = 0.14$  m/s showing a coarse orange peel appearance.

The microstructure of Al/10wt%Fe<sub>2</sub>O<sub>3</sub> part made by using  $P = 82$  W and  $v = 0.5$  m/s seems to be relatively uniform, composed of very fine particles, with grain boundaries hardly distinguishable from interior (Fig. 9.8a). The relatively coarser appearance (around zone I) is composed of particles, somehow below 1 μm in size (submicron size) and firmly

attached to each other (Fig. 9.8b), but slightly finer particles (around zone II) seem to be placed (or resolved) in matrix in such a manner no significant segregation can be observed (Fig. 9.8c). The present phases in matrix (identified by XRD (Fig. 9.8d)) are Al, Al-Fe intermetallics such as  $\text{Al}_{13}\text{Fe}_4$ ,  $\text{Al}_2\text{Fe}$ ,  $\text{Fe}_3\text{Al}$ , and oxides such as  $\alpha\text{-Al}_2\text{O}_3$ . However, a change in SLM parameters to  $P = 91$  W and  $v = 0.14$  m/s creates cracked areas and agglomerated combinations in microstructure (heterogeneous distribution of combination is evident in Fig. 9.9a). As seen from Fig. 9.9b, cracks appear in an area embedding many fine particles which are distributed uniformly with an excellent interface with matrix. The XRD result in Fig. 9.9c demonstrates the presence of Al,  $\text{Al}_{13}\text{Fe}_4$ ,  $\text{Al}_3\text{Fe}$ ,  $\text{Al}_2\text{Fe}$ ,  $\text{AlFe}$ ,  $\text{Fe}_3\text{Al}$ , and  $\alpha\text{-Al}_2\text{O}_3$  in microstructure.



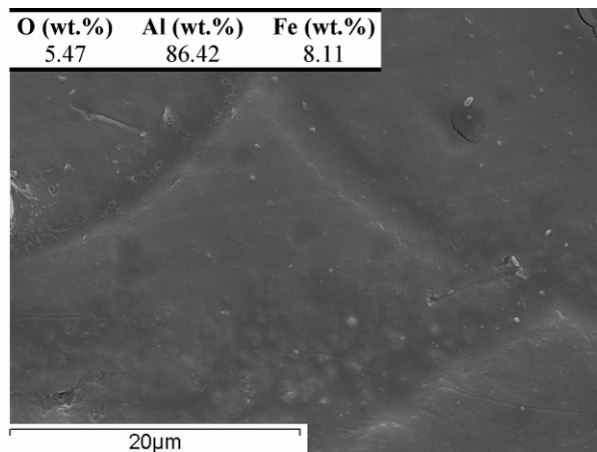
**Fig. 9.8:** (a) Microstructural overall view, (b) particulate format of coarser area around zone I, (c) firmly adhered particles forming around zone II, and (d) XRD pattern of the Al/10wt% $\text{Fe}_2\text{O}_3$  part when  $P = 82$  W and  $v = 0.5$  m/s.



**Fig. 9.9:** a) Microstructural overall view, (b) particles formed on cracked area, and (c) XRD pattern of the Al/10wt% $\text{Fe}_2\text{O}_3$  part when  $P = 91$  W and  $v = 0.14$  m/s.

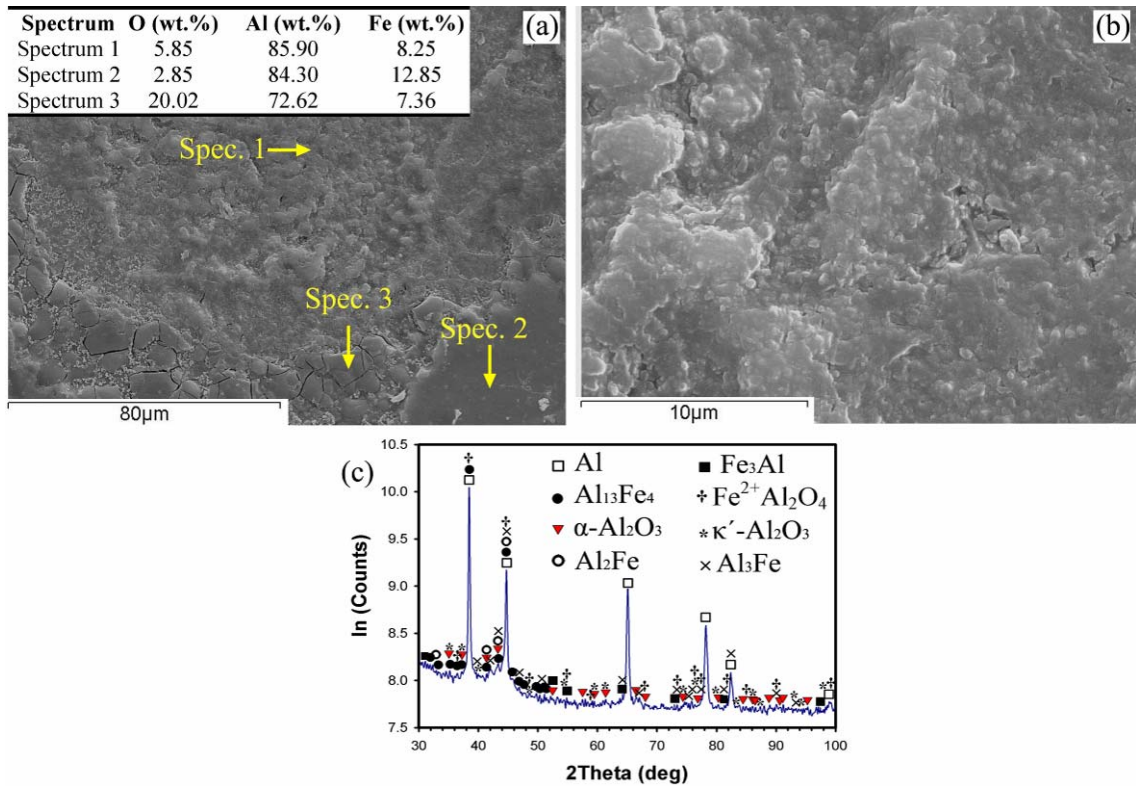
### 9.2.2.3. Al/15wt%Fe2O3

Fig. 9.10 shows the microstructure of the part fabricated from Al/15wt% $\text{Fe}_2\text{O}_3$  using  $P = 39$  W and  $v = 0.5$  m/s, exhibiting the matrix with an orange peel appearance, i.e. being generally smooth while some very fine particles are growing in matrix.



**Fig. 9.10:** Relatively smooth appearance of microstructure embedding tiny particles in Al/15wt% $\text{Fe}_2\text{O}_3$  part when  $P = 39$  W and  $v = 0.5$  m/s.

A rough feature (around spectrum 1), cracked zones (around spectrum 3 with a high oxygen content of  $\sim 20$  wt%), and a relatively smooth area (around spectrum 1 with the lowest oxygen content of  $\sim 2.8$  wt%) can be seen in the SEM micrograph of the Al/15wt%Fe<sub>2</sub>O<sub>3</sub> part when  $P = 61$  W and  $v = 0.14$  m/s (Fig. 9.11a). The rough feature, better shown in Fig. 9.11b, is composed of very fine particles which seem to develop throughout the matrix by mainly fragmenting cracked zones into very fine and well-bonded particles. The XRD results (Fig. 9.11c) reveal the presence of various combinations of Al, Al-Fe intermetallics (such as Al<sub>13</sub>Fe<sub>4</sub>, Al<sub>3</sub>Fe, Al<sub>2</sub>Fe, Fe<sub>3</sub>Al), and oxides (such as  $\alpha$ -Al<sub>2</sub>O<sub>3</sub>,  $\kappa'$ -Al<sub>2</sub>O<sub>3</sub> and Fe<sup>2+</sup>Al<sub>2</sub>O<sub>4</sub> (iron aluminium oxide)). Operation of the SLM by using  $P = 70$  W and  $v = 0.5$  m/s piles up the particulate features on cracked zones (which exist in some positions) (Fig. 9.12a). The XRD results show Al, Al<sub>13</sub>Fe<sub>4</sub>, Al<sub>3</sub>Fe, Al<sub>2</sub>Fe, Fe<sub>3</sub>Al and  $\alpha$ -Al<sub>2</sub>O<sub>3</sub> as the main combinations found in matrix (Fig. 9.12b).



**Fig. 9.11:** (a) Overall view of microstructure showing a rough area developing throughout the matrix, (b) very fine particulate nature of the rough area (around spectrum 1) and (c) XRD pattern of the Al/15wt%Fe<sub>2</sub>O<sub>3</sub> part when  $P = 61$  W and  $v = 0.14$  m/s.

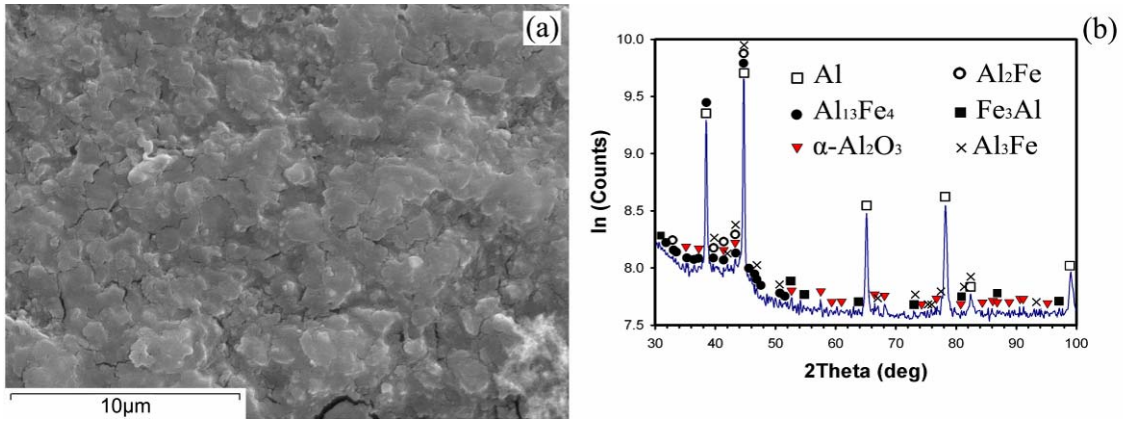


**Fig. 9.12:** (a) Microstructure containing agglomerated and piled up particulate phases on cracks, and (b) XRD pattern of the Al/15wt%Fe<sub>2</sub>O<sub>3</sub> part when  $P = 70$  W and  $v = 0.5$  m/s.

## 9.3. Discussion

### 9.3.1. In-situ combined SLM reaction

The reaction in the mixture of Al/Fe<sub>2</sub>O<sub>3</sub> is ignited by an external energy source (Durães et al., 2007). In the present work, the SLM ignites the exothermic reaction besides manufacturing 3D parts from the mixture. The SLM variables to control the process and reaction are laser power and scanning speed. Higher laser power and lower scanning speed are associated with higher energy input. Moreover, higher scanning speed represents higher solidification and cooling rate affecting the microstructure. The material variable is Fe<sub>2</sub>O<sub>3</sub> content, that although was far lower than that of a stoichiometric thermite mixture ( $\sim 70$  wt%), it has a significant contribution to laser melting and energy input by releasing heat during SLM process.

The low laser energy (due to low laser power of 39 W and high scanning speed of 0.5 m/s) can partially initiate the reaction/melting in the presence of low Fe<sub>2</sub>O<sub>3</sub> content (i.e. 5 wt%). As seen from Fig. 9.2, the grain boundaries have been formed with a fuzzy and coralline-like appearance and relatively high oxygen content due to this low laser energy. Perhaps, these boundaries are primary Al/Fe<sub>2</sub>O<sub>3</sub> interfaces containing primary oxide layers (formed on aluminium powder surfaces) plus in-situ products. In fact, in-situ reaction ignites from the powders interfaces, forming porous coralline-like intermetallics e.g. Fe<sub>3</sub>Al intermetallics regarding the Eq. 3.1) and oxides, and propagates into interior. The smooth interior with lower oxygen seems to be the results of insufficient melting/reaction degree leaving mainly Al inside. The gap between solid areas carries much of oxygen as a sign of

existence of oxides and leftover Fe<sub>2</sub>O<sub>3</sub> (leftover Fe<sub>2</sub>O<sub>3</sub> (Fig. 9.2c) exists due to insufficient laser energy which can not fully accomplish the reaction). However, the higher laser energy to execute SLM propagates the coralline-like feature (such as Al<sub>13</sub>Fe<sub>4</sub> - a hard intermetallic, very similar to Al<sub>3</sub>Fe, being in fact rapidly solidified eutectics which appears in Al-Fe equilibrium phase diagram (Griger and Stefániay, 1996)) mixed with fine oxide particles (e.g.  $\alpha$ -Al<sub>2</sub>O<sub>3</sub>), as shown in Fig. 9.4, and enhances the hardness (Fig. 9.1).

### 9.3.2. Microstructures, phases, and microhardness

Lowering the scanning speed from 0.5 m/s (Fig. 9.2) to 0.14 m/s (Fig. 9.3) to SLM of Al/5wt%Fe<sub>2</sub>O<sub>3</sub> provides more laser energy and longer processing time to facilitate melting/reaction and leads to fragmentation of corallines into particles, changing the microstructure from coralline-like to particulate format. The particles are Al<sub>13</sub>Fe<sub>4</sub>, and  $\kappa$ -Al<sub>2</sub>O<sub>3</sub> (a hard intermediate oxide (Levin and Brandon, 1998)) in this case. These hard particles reinforce the Al matrix, and therefore an increase in hardness is expected from this particulate microstructure being confirmed by that observed in Fig. 9.1 (hardness is higher in lower scanning speed). However, the bonding of particles/matrix interface seems to be not very strong due to evident segregation. In fact, particles can be pulled apart easily from the matrix. A higher laser power seems to succeed to achieve a better particles/matrix interface (Fig. 9.5). As seen, the boundaries are formed from coarser particles (Fig. 9.5b) and possessed high oxide level (high oxygen content) as primary interface of Al/Fe<sub>2</sub>O<sub>3</sub> powders. The interior contains lower oxygen showing a smoother appearance (e.g. around spectrum 3 in Fig. 9.5a) and less segregation (Fig. 9.5c). Accordingly, it seems that higher oxygen (associated to Al oxides) leads to particles with more gaps and segregation. The larger interfacial energy of Al<sub>2</sub>O<sub>3</sub>/solid-Al than that of the Al<sub>2</sub>O<sub>3</sub>/liquid-Al can be a reason for this segregation (Yu et al., 2003). However, a general strong bonding between matrix and secondary phases (hard and stable particles such as  $\alpha$ -Al<sub>2</sub>O<sub>3</sub>, Fe<sup>2+</sup>Al<sub>2</sub>O<sub>4</sub> and Al<sub>13</sub>Fe<sub>4</sub>) can be observed (especially in Fig. 9.5c) leading to a better hardness (which is confirmed by microhardness results). Furthermore, the pores (attributed to the gas entrapped in powders forming voids during SLM processing) significantly disappear in high laser powers and low scanning speeds of Fig. 9.5, despite many pores observed in Figs. 9.2-9.4.

Enhancing the iron oxide to 10 wt% incorporates extra secondary phases and manipulates the material microstructure. The ultrafine formation of particles (which can be easily resolved in matrix or masked by an oxide layer) leads to a smooth orange peel appearance in microstructure of Al/10wt%Fe<sub>2</sub>O<sub>3</sub> part made by low laser power and low scanning speed (Fig. 9.6). Decreasing the scanning speed coarsens the secondary phases in such a manner that fine particles in microstructure are more evident (Fig. 9.7).

As seen from Fig. 9.8, the higher laser power in SLM of Al/10wt%Fe<sub>2</sub>O<sub>3</sub> part (when the scanning speed is high ~ 0.5 m/s) converts the smooth, featureless and orange peel appearance of microstructure (Fig. 9.6) into numerous hard particles (from Al-Fe intermetallics such as Al<sub>13</sub>Fe<sub>4</sub>, Al<sub>2</sub>Fe, Fe<sub>3</sub>Al, and oxides such as  $\alpha$ -Al<sub>2</sub>O<sub>3</sub>) firmly placed in matrix (Fig. 9.8b-d). It seems that increasing the laser power fragments, breaks and tears oxide layers, enlarges particles produced via in-situ reaction, and establishes proper bonding between matrix and particulate reinforcements. Fig. 9.8 represents a desirable composite microstructure leading to high microhardness for Al/10wt%Fe<sub>2</sub>O<sub>3</sub> (Fig. 9.1). Reduction of scanning speed to 0.14 m/s in high laser power agglomerates and piles up secondary phases and forms cracked zones around numerous fine particles (Fig. 9.9a-b). It seems that oxides can flow and agglomerate during SLM (in high laser power and low scanning speed), spread unevenly, and appear like cracked zones or dross (agglomerated components) settled on Al matrix. However, fine particles from Al-Fe intermetallics and Al oxides can still establish an excellent interface with matrix. Despite these proper reinforcing particles in matrix, existence of cracks is a drawback and can be the main reason for reduction of the hardness curve of Al/10wt%Fe<sub>2</sub>O<sub>3</sub> in  $v = 0.14$  m/s (Fig. 9.1).

Smooth microstructure (with some orange peel appearance) can form even in the presence of high Fe<sub>2</sub>O<sub>3</sub> content of 15 wt% when low laser power (39 W) and high scanning speed (0.5 m/s) is used, according to Fig. 9.10. In fact, secondary phases forming during in-situ reaction are extremely fine when laser power is low, while high laser speed contributes to provide a very rapid solidification resolving the fine products inside matrix. This microstructure leads to highest hardness in the corresponding curve of Fig. 9.1, attributed to solution hardening and fine dispersion strengthening (Tong and Fang, 1998b). However, higher laser power (70 W) in the same scanning speed (0.5 m/s) produces piled up components being settled on cracked zones (i.e. thick oxide layers), while particulate feature is still recognisable (Fig. 9.12). This inhomogeneity in microstructure, i.e. crack

zones and piling up of secondary phases, is obviously undesirable. This is why the increasing the laser power has led to a decrease in hardness (Fig. 9.1).

Fig. 9.11 (Al/15wt%Fe<sub>2</sub>O<sub>3</sub>,  $P = 61$  W,  $v = 0.14$  m/s) shows the cracked zones (which are thick oxide layers regarding their high oxygen content) which can be fragmented to fine particles inside matrix and act as excellent reinforcements after fragmentation. In other words, the crack zones diminish with the fragmentation phenomena and transform to ultrafine (or even nano-size) particles having lower oxygen content (Fig. 9.11a-b). The ultrafine particles have been formed from various range of oxides (such as  $\alpha$ -Al<sub>2</sub>O<sub>3</sub>,  $\kappa'$ -Al<sub>2</sub>O<sub>3</sub> and Fe<sup>2+</sup>Al<sub>2</sub>O<sub>4</sub>) and Al-Fe intermetallics (such as Al<sub>13</sub>Fe<sub>4</sub>, Al<sub>3</sub>Fe, Al<sub>2</sub>Fe, Fe<sub>3</sub>Al) and have efficiently increased the hardness (maximum microhardness in Fig. 9.1 belongs to this specimen), by acting as efficient obstacles restricting movement of dislocations. However, Fig. 9.11a also demonstrates a smooth area; seeming to be a solid saturated Al matrix, and locally formed after removal of much of oxide layers (the low oxygen content around spectrum 2 is evident).

### 9.3.3. Effect of Fe<sub>2</sub>O<sub>3</sub> content, laser power, and scanning speed on microstructural evolution

The microstructures presented in the results are largely different from those in typical Al parts. This is because of the combined mechanisms involving both exothermic in-situ reaction and laser rapid consolidation. However, the microstructural evolution with Fe<sub>2</sub>O<sub>3</sub> content, laser power and scanning speed can be summarised in Table 9.1 on the basis of the results presented in this work. As summarised, the laser initiates the reaction from the Al/Fe<sub>2</sub>O<sub>3</sub> interface, forming the coralline-like feature from rapidly solidified eutectic Al-Al<sub>13</sub>Fe<sub>4</sub> phases (e.g. Fig. 9.2), as discussed in chapter 8, and propagates it throughout the part with increasing the laser power (e.g. Fig. 9.4). The reduction in laser speed provokes the fragmentation of the corallines and also increases the formation of particulate alumina, leading to a particulate feature (e.g. Figs. 9.3 and 9.5) with a higher hardness. It appears that Al-Fe particulate intermetallics creates less segregation than that of oxide particles e.g. the low oxygen level in Fig. 9.8c leads to a smoother appearance than that of higher oxygen content in Fig. 9.8b. The microstructure especially in low Fe<sub>2</sub>O<sub>3</sub> contents (5 wt%) may contain some pores and voids (see Figs. 9.2-9.4), attributed to entrapped gas in powders.

Increasing the  $\text{Fe}_2\text{O}_3$  contents to 10-15 wt% diminishes this feature, perhaps due to increasing the eruption and temperature of molten powders with increase in iron oxide content and facilitating the passage of entrapped gas to outside. Furthermore, grain boundaries somehow disappear at higher  $\text{Fe}_2\text{O}_3$  contents (e.g. 10-15 wt%), attributed to numerous particles reinforcing the Al matrix. In fact, small particles may disturb the primary  $\alpha$ -Al dendrites, for instance by acting as potent nucleus facilitating the solidification phenomenon, or by being pushed into interdendritic spaces along solidification interface and suppress the dendritic growth (Zhang and Chen, 2000).

Table 9.1: Summary of microstructural evolution in dependence of  $\text{Fe}_2\text{O}_3$  content, laser power and scanning speed

	Al / 5 wt% $\text{Fe}_2\text{O}_3$	Al / 10 wt% $\text{Fe}_2\text{O}_3$	Al / 15 wt% $\text{Fe}_2\text{O}_3$
Morphology (appearance)	coralline-like/particulate feature inside grains and boundaries	Fine or coarse orange peel /particulate/pile up of secondary phases	Orange peel/particulate/pile up of secondary phases
Predominant phases	Al ; Al-Fe intermetallics being mainly $\text{Al}_{13}\text{Fe}_4$ ; Oxides (like $\text{Al}_2\text{O}_3$ and $\text{Fe}^{2+}\text{Al}_2\text{O}_4$ )	Al ; Al-Fe intermetallics such as $\text{Al}_{13}\text{Fe}_4$ ( $\text{Al}_3\text{Fe}$ ), $\text{Al}_2\text{Fe}$ , $\text{Fe}_3\text{Al}$ ; Oxides (mainly $\alpha$ - $\text{Al}_2\text{O}_3$ plus metastable Al(-Fe)-O oxides such as $\kappa'$ - $\text{Al}_2\text{O}_3$ and $\text{Fe}^{2+}\text{Al}_2\text{O}_4$ )	Al ; Al-Fe intermetallics such as $\text{Al}_{13}\text{Fe}_4$ ( $\text{Al}_3\text{Fe}$ ), $\text{Al}_2\text{Fe}$ , $\text{Fe}_3\text{Al}$ ; Oxides (mainly $\alpha$ - $\text{Al}_2\text{O}_3$ plus metastable Al(-Fe)-O oxides such as $\kappa'$ - $\text{Al}_2\text{O}_3$ and $\text{Fe}^{2+}\text{Al}_2\text{O}_4$ )
Pores and voids	Evident	Not evident	Not evident
Increasing laser power	Development of corallines (mainly Al-Fe intermetallics) mixed with oxide particles from primary Al/ $\text{Fe}_2\text{O}_3$ interface – improving bonding of particles/matrix – creation of stable alumina i.e. $\alpha$ - $\text{Al}_2\text{O}_3$	Growth of particles to form particulate reinforced matrix – piling up and agglomeration of secondary phases may occur in high laser powers	Coarsening the smooth orange peel appearance and converting it to particulate reinforced matrix – piling up and agglomeration of secondary phases may occur in high laser powers
Lowering scanning speed	Fragmentation of the corallines mixed with oxide particles leading to particulate reinforced matrix	Improved dispersion of secondary phases though piling up and agglomeration of secondary phases may occur	Fragmentation of the thick oxide films to be mixed with secondary phase particles leading to particulate reinforced matrix

Overall, the higher laser energies (e.g. higher powers) may coarsen the resolved and very fine particles (e.g. Figs. 9.6-9.7) to an optimum size and enhance the bonding of particles with matrix, which increases the hardness (e.g. Fig. 9.8). However, excessive powers may lead to agglomeration of the secondary phases, reducing the hardness (e.g. Figs. 9.9 and 9.12). This is why one optimum laser power might be observed in microhardness curves as presented in Fig. 9.1. However, a homogeneous distribution of hard particles can be achieved in high  $\text{Fe}_2\text{O}_3$  contents (e.g. 15 wt%) by using an optimum SLM parameters (e.g. see Fig. 9.11b). These abundant particles are very fine and stable with good interfacial bonding, reinforcing the matrix. This reduces the multiple slip-band

piles. In addition, the relatively equiaxed particle morphology reduce the stress concentration associated with corners. These improve the toughness of the composite (Lu et al., 1997) and efficiently enhance the hardness of soft aluminium.

### **9.3.4. In-situ combined SLM mechanisms in dependence of Fe<sub>2</sub>O<sub>3</sub> content, laser power, and scanning speed**

To interpret the above phase evolution as a function of Fe<sub>2</sub>O<sub>3</sub> content, one shall consider the mechanism involved thermite reaction between Al and Fe<sub>2</sub>O<sub>3</sub> (which most efficiently happens when mass ratio of Fe<sub>2</sub>O<sub>3</sub>/Al ~ 2.2 according to stoichiometric ratio in Eq. 3.1). A reaction mechanism can be postulated on the basis of what Durães et al. (2007) proposed, as follows: Fe<sub>2</sub>O<sub>3</sub> reduces to Fe<sub>3</sub>O<sub>4</sub> and FeO. Al at the same time combines with O and tends to transform to thermodynamically stable  $\alpha$ -Al<sub>2</sub>O<sub>3</sub> with further progress of reaction at higher temperatures, though intermediate and non-stable alumina such as  $\kappa$ -Al<sub>2</sub>O<sub>3</sub> (as a common metastable Al<sub>2</sub>O<sub>3</sub> polymorphs) or even  $\kappa'$ -Al<sub>2</sub>O<sub>3</sub> (as an unstable intermediate phase) are most likely to be formed (Levin et al., 1997, Levin and Brandon, 1998). The interaction of the remaining Al with Fe<sub>3</sub>O<sub>4</sub> and FeO leads to formation of iron-aluminium-oxide (Fe<sup>2+</sup>Al<sub>2</sub>O<sub>4</sub>) and also iron (Fe). The formation of Fe<sup>2+</sup>Al<sub>2</sub>O<sub>4</sub> phase is well reported from the decomposition of Fe<sub>2</sub>O<sub>3</sub> in high reaction temperature and inert atmosphere (Mei et al., 1999). However, regarding the over aluminised mixtures in this work, the Al incorporates into the Fe<sup>2+</sup>Al<sub>2</sub>O<sub>4</sub> and also reacts with Fe (Fe can be resolved in Al matrix as well), forming Al-Fe intermetallics. The primary Al-Fe intermetallic is Fe<sub>3</sub>Al regarding Eq. 3.1 (e.g. Fig. 9.2c), but it transforms to Al<sub>13</sub>Fe<sub>4</sub> (very similar to Al<sub>3</sub>Fe) due to a great deal of remained Al, to achieve equilibrium condition (the Al-Al<sub>13</sub>Fe<sub>4</sub> or Al-Al<sub>3</sub>Fe are equilibrium phases (forming eutectics) in these compositions (Allen et al., 2001, Griger and Stefániay, 1996)). However, the higher Fe<sub>2</sub>O<sub>3</sub> content (e.g. 10 and 15 wt%) allows the formation of other Al-Fe intermetallics such as Al<sub>2</sub>Fe, AlFe, Al<sub>3</sub>Fe, and Fe<sub>3</sub>Al besides Al<sub>13</sub>Fe<sub>4</sub>. Obviously, higher laser powers and lower scanning speeds assist these mechanisms to achieve more equilibrium and stable products (e.g.  $\alpha$ -Al<sub>2</sub>O<sub>3</sub> is achieved in Fig. 9.5d in comparison with  $\kappa$ -Al<sub>2</sub>O<sub>3</sub> in Fig. 9.3c).

## 9.4. Conclusions

The mixture of Al with 5, 10, and 15 wt% of  $\text{Fe}_2\text{O}_3$  was subjected to SLM process in order to control particles formation using an in-situ reaction within fabrication of net shape parts. This may lead to a low-cost, energy-saving and net-shape manufacturing technique to fabricate Al composite materials in which the use of expensive submicron and nano-sized reinforcements can be avoided. The following conclusions can be drawn from this chapter:

- The specific process conditions, i.e. in-situ reaction and rapid solidification, lead to unique microstructures for Al matrix parts depending on  $\text{Fe}_2\text{O}_3$  content and SLM parameters such as laser power and scanning speed.
- Increasing the  $\text{Fe}_2\text{O}_3$  contents mitigate the pores originating from entrapped gas. This was attributed to the more eruptions and temperatures in higher iron oxide contents.
- The low laser energy (due to high scanning speed and low laser power) might lead to the formation of  $\text{Fe}_3\text{Al}$  as the primary intermetallics. But, however, equilibrium  $\text{Al}_{13}\text{Fe}_4$  (in these chemical compositions) has the greatest chance to be formed with the progress of reaction.
- The metastable Al oxides such as  $\kappa$ - and  $\kappa'$ - $\text{Al}_2\text{O}_3$  are likely to form, but they tend to transform to stable  $\alpha$ - $\text{Al}_2\text{O}_3$ .
- The higher iron oxide content enhances the formation of other Al-Fe combinations such as  $\text{Al}_2\text{Fe}$ ,  $\text{AlFe}$ , and  $\text{Fe}_3\text{Al}$  in addition to equilibrium  $\text{Al}_{13}\text{Fe}_4$  ( $\text{Al}_3\text{Fe}$ ). These intermetallics are hard and can contribute to strengthening.
- The laser initiates the process with formation of the coralline-like Al-Fe intermetallics and propagates them throughout the SLM part made from Al/5wt% $\text{Fe}_2\text{O}_3$ . The corallines tend to be fragmented in lower laser speeds and higher  $\text{Fe}_2\text{O}_3$  contents appearing as particles, and mixed up with Al oxide particles, providing a particulate microstructural feature. This particulate reinforced microstructure can contribute to further material strengthening.
- Very high laser energies may weaken the material due to excessive microstructural coarsening, large agglomeration of secondary phases and formation of oxide cracked zones, and increasing the microstructural inhomogeneity, despite its ability to enhance material bonding.

- A very fine, well-bonded, and homogeneous distribution of hard particles can be achieved even in high Fe<sub>2</sub>O<sub>3</sub> contents (using appropriate SLM parameters), efficiently enhances the hardness of material and provide a proper in-situ Al matrix composite.

---

# **Chapter 10: Effect of Hot Isostatic Pressing (HIP) on Al Composite Parts Made from Laser Consolidated Al/Fe<sub>2</sub>O<sub>3</sub> Powder Mixtures**

---

## **10.1. Introduction**

Most of SLM studies reported a high content of porosity in Al SLM parts. However, there is little report on the post-processing of Al SLM (composite) parts through the usage of hot isostatic pressing (HIP) which is considered as an effective process to densify various materials. The HIP is a well-recognised process to mitigate porosity and obtaining relatively large, bulk and dense materials in a wide range of metal and non-metal parts. It applies a high pressure gas (usually inert) at elevated temperature to a specimen in a specially constructed vessel. The pressure is isostatic (since applied using gas) and therefore keeps the component geometry (at least to a first approximation). The simultaneous heat and pressure collapse and weld up internal pores or defects. This process can be directly used to consolidate powder or it can be utilised as a post-treatment to further densify cold pressed, sintered (and SLS processed), or cast parts (Agarwala et al., 1995, Atkinson et al., 1997, Billard et al., 2006, Bocanegra-Bernal, 2004, Filho et al., 1998, Loh and Sia, 1992).

As mentioned, despite wide applications of the HIP process to densify metals and metal matrix composites, it has not been used as a post-treatment to improve Al SLM parts. On the other hand, promising researches producing in-situ Al matrix composites (from the mixture of Al/Fe<sub>2</sub>O<sub>3</sub> by common medium power lasers) may suffer from high percentage of porosity. Therefore, this chapter investigates the influence of HIP treatment on physical and mechanical properties of laser assisted in-situ Al matrix composite parts. The effects of HIP treatment are illustrated by the changes in microstructures, hardness and porosity of the various SLM parts made from Al/5wt%Fe<sub>2</sub>O<sub>3</sub> (with layer thicknesses (*t*) of 75 and 50 μm), Al/10wt%Fe<sub>2</sub>O<sub>3</sub> (*t* = 50 μm) and Al/15wt%Fe<sub>2</sub>O<sub>3</sub> (*t* = 50 μm).

## 10.2. Materials and Experiments

SLM samples with dimensions of  $60\text{ mm} \times 10\text{ mm} \times 8\text{ mm}$  were fabricated from Al/5-15wt%Fe<sub>2</sub>O<sub>3</sub>. The parameters such as laser power ( $P$ ) and scanning speed ( $v$ ) were set  $P = 70\text{ W}$  and  $v = 0.25\text{ m/s}$  for Al/5wt%Fe<sub>2</sub>O<sub>3</sub> when layer thickness ( $t$ ) was set at  $75\text{ }\mu\text{m}$ ,  $P = 82\text{ W}$  and  $v = 0.25\text{ m/s}$  for Al/5wt%Fe<sub>2</sub>O<sub>3</sub> when  $t = 50\text{ }\mu\text{m}$ ,  $P = 82\text{ W}$  and  $v = 0.20\text{ m/s}$  for Al/10wt%Fe<sub>2</sub>O<sub>3</sub> when  $t = 50\text{ }\mu\text{m}$ , and  $P = 70\text{ W}$  and  $v = 0.20\text{ m/s}$  for Al/15wt%Fe<sub>2</sub>O<sub>3</sub> when  $t = 50\text{ }\mu\text{m}$  (these parameters were selected from the SLM operation windows to produce suitable net shape specimens).

The HIP post-treatment was carried out through a commercial service. First the samples were wrapped in foil and then processed under pressure of  $\sim 98\text{ MPa}$  at  $\sim 500\text{ }^{\circ}\text{C}$  for  $\sim 2$  hrs, being in the common range for HIP of Al alloys (Bocanegra-Bernal, 2004). The porosity formation (before and after HIP treatment) was revealed in three dimension using a  $\mu\text{CT}$  scanning system. In addition, the samples were examined using various techniques such as SEM, XRD, and hardness and microhardness.

## 10.3. Results

### 10.3.1. Density, hardness and microhardness

Fig. 10.1 illustrates the effects of HIP on the alternation of density as well as hardness and microhardness of the SLM samples made from Al/5wt%Fe<sub>2</sub>O<sub>3</sub> ( $t = 75$  and  $50\text{ }\mu\text{m}$ ), Al/10wt%Fe<sub>2</sub>O<sub>3</sub>, and Al/15wt%Fe<sub>2</sub>O<sub>3</sub>. As seen from Fig. 10.1a, the density slightly increases after HIP post-treatment, but surprisingly this improvement is not significant. Fig. 10.1b shows an obvious drop in the hardness and microhardness of SLM parts due to HIP treatment. For example, the hardness of Al/15wt%Fe<sub>2</sub>O<sub>3</sub> falls around 25 HV after HIP post-treatment. Or the microhardness (which is mainly associated to microstructure) drops about 10-20 HV for most samples. Also, the scatter of hardness is commonly smaller after HIP.

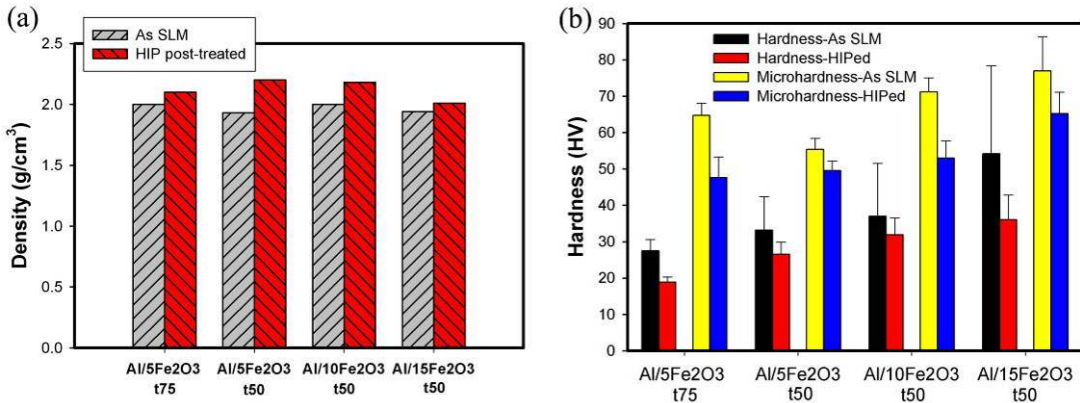


**Fig. 10.1:** (a) Density, and (b) hardness and microhardness of the SLM parts fabricated from Al/5wt%Fe<sub>2</sub>O<sub>3</sub> ( $t = 50$  and  $75 \mu\text{m}$ ), Al/10wt%Fe<sub>2</sub>O<sub>3</sub> and Al/15wt%Fe<sub>2</sub>O<sub>3</sub> powder mixtures.

### 10.3.2. CT scan observations

Fig. 10.2 shows the CT scanning images of the SLM pieces (made from Al/15wt%Fe<sub>2</sub>O<sub>3</sub>) illustrating the propagation of porosity before and after HIP treatment in three dimensions. As seen from Fig. 10.2a, cross section of the sample before HIP treatment is composed of numerous solid areas. Gaps have been developed in an interconnected manner between solid regions, though in some positions they might split and allow the solids join together. This inter-solid regions appear in all sections, showing gap developed through additive layers. In contrast, as seen from Fig. 10.2b, the format of porosity within HIP post-treated part has remained almost untouched, but the gaps look somehow wider.

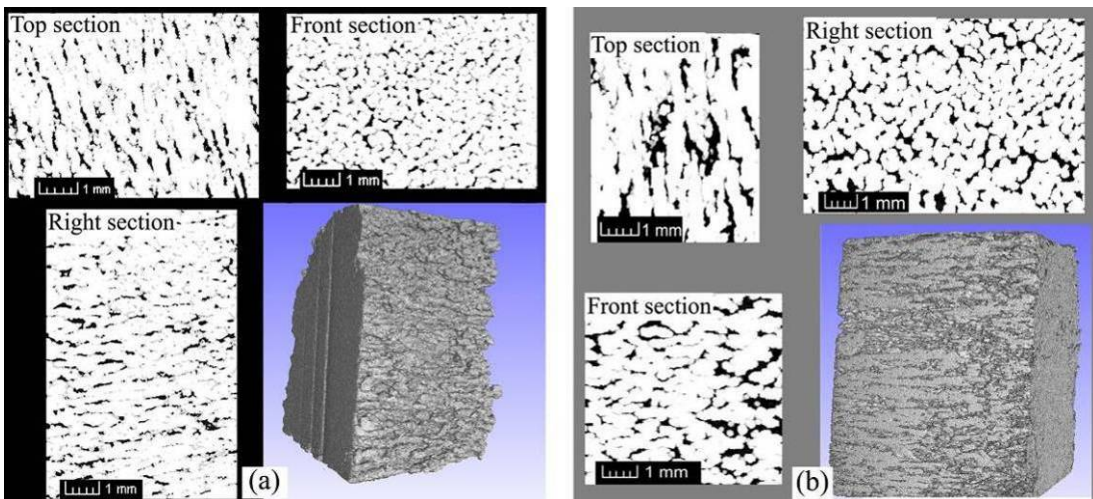


**Fig. 10.2:** CT scan exhibition of the part (made from Al/15wt%Fe<sub>2</sub>O<sub>3</sub>) (a) before and (b) after HIP post-treatment.

### 10.3.3. Microstructural characterisation and phase identification using XRD

#### 10.3.3.1. As manufactured SLM parts (before HIP treatment)

The microstructural details of as manufactured SLM sample made from Al/5wt%Fe<sub>2</sub>O<sub>3</sub> ( $t = 75 \mu\text{m}$ ) shows that the part is composed of circular shaped solids (in x-y cross section), separated by tiny interconnected bands or inter-solid regions (Fig. 10.3a). These solids contain a combination of fine coralline-like and particulate phases developed all over the sample. These features are very tiny (below micron in scale) (Fig. 10.3b-c). The XRD experiment identifies Al, Al<sub>13</sub>Fe<sub>4</sub>, and  $\alpha$ -Al<sub>2</sub>O<sub>3</sub> as the main constituent of microstructure (Fig. 10.3d). Reducing the layer thickness to 50  $\mu\text{m}$  (Fig. 10.4) makes the microstructure more particulate-shape (particles are attached to each other and show some coralline-like feature as well) developed in individual solids surrounded by relatively thick and interconnected bands. The main microstructural phases are Al, Al<sub>13</sub>Fe<sub>4</sub>, and  $\alpha$ -Al<sub>2</sub>O<sub>3</sub> according to XRD results presented in Fig. 10.4d.

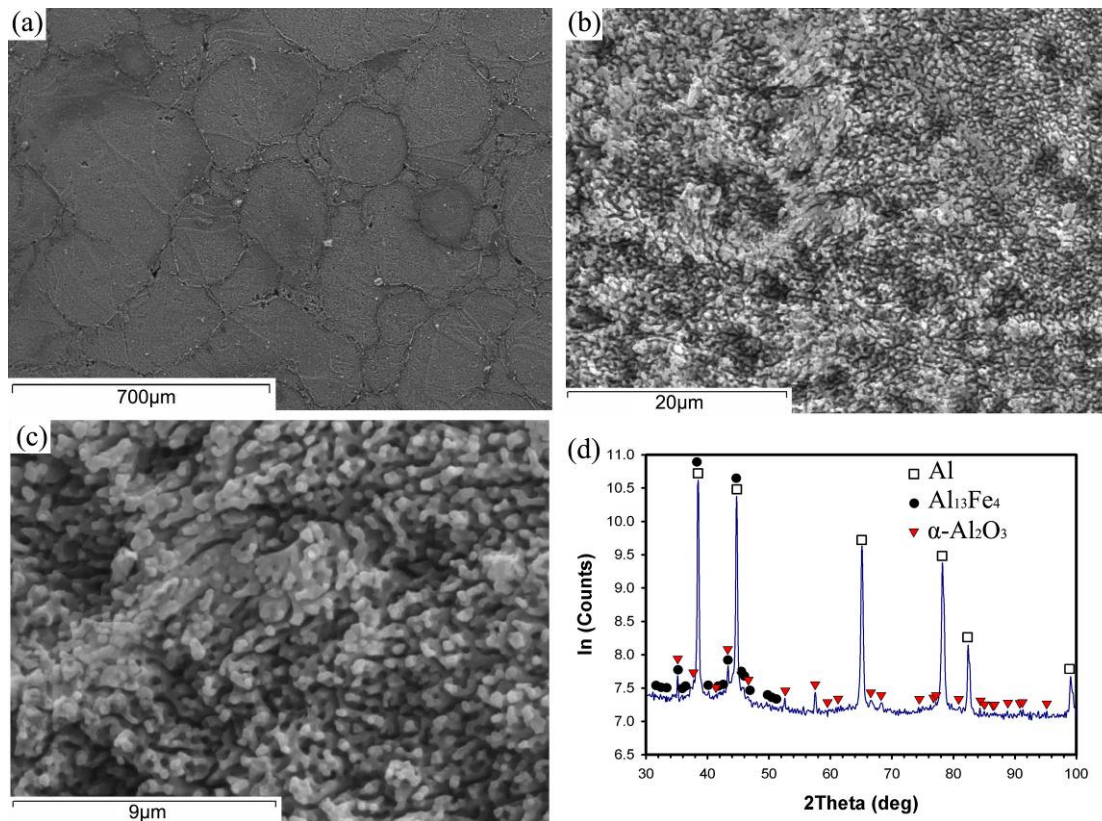


**Fig. 10.3:** As-manufactured Al/5wt%Fe<sub>2</sub>O<sub>3</sub> SLM part when  $t = 75 \mu\text{m}$ ; (a) overall view of solids, (b) typical microstructure with a mixture of coralline-like and particulate appearance, and (c) higher magnification of tiny features. (d) XRD pattern of the corresponding part.

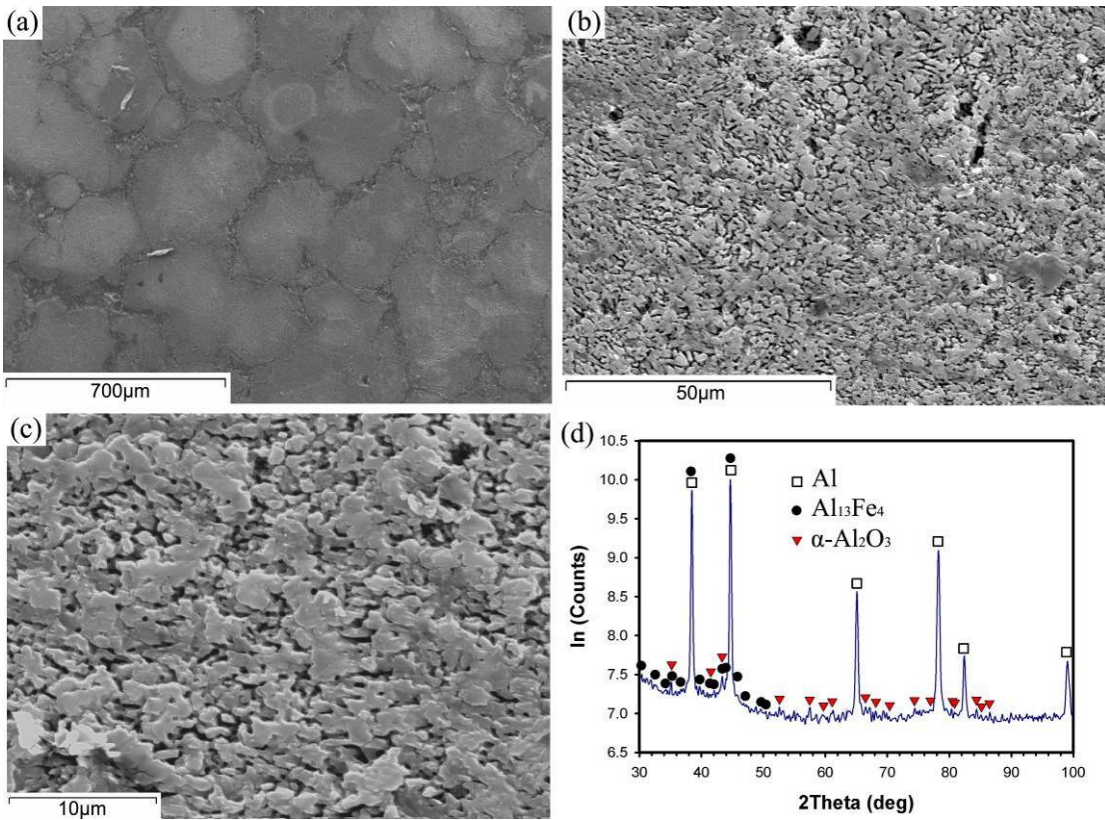


**Fig. 10.4:** As-manufactured Al/5wt%Fe<sub>2</sub>O<sub>3</sub> SLM part when  $t = 50 \mu\text{m}$ ; (a) overall view of solids, (b) microstructure composed of semi-particulate phases, and (c) higher magnification of the attached phases with a semi-particulate appearance. (d) XRD pattern of the corresponding part.

The individual solids separated by an interconnected band (Fig. 10.5a) in Al/10wt%Fe<sub>2</sub>O<sub>3</sub> SLM part are composed of very fine particles (below 1  $\mu\text{m}$ ) which seem to be resolved or placed inside matrix. These particles (such as Al<sub>13</sub>Fe<sub>4</sub>, Al<sub>2</sub>Fe, AlFe, and  $\alpha$ -Al<sub>2</sub>O<sub>3</sub> regarding Fig. 10.5d) can establish a strong interface with matrix (Fig. 10.5b-c). The microstructure of Al/15wt%Fe<sub>2</sub>O<sub>3</sub> SLM part (Fig. 10.6) also contains very fine particles (below 1  $\mu\text{m}$  in size) which are uniformly distributed in matrix (as seen from Fig. 10.6b). The increasing the iron oxide to 15 wt% (in this case) may provide a chance that solid zones fuse together over thick bands. There are some evidence of small amount of inner-solid porosity (located within solid areas), seeming to have a gas origination. Regarding XRD results presented in Fig. 10.6c, secondary phases are mainly Al-Fe intermetallics (such as Al<sub>13</sub>Fe<sub>4</sub>, Al<sub>5</sub>Fe<sub>2</sub>, Al<sub>2</sub>Fe, and Fe<sub>3</sub>Al) plus oxides (such as  $\alpha$ -Al<sub>2</sub>O<sub>3</sub> and  $\gamma$ -Al<sub>2</sub>O<sub>3</sub>) formed in Al matrix.

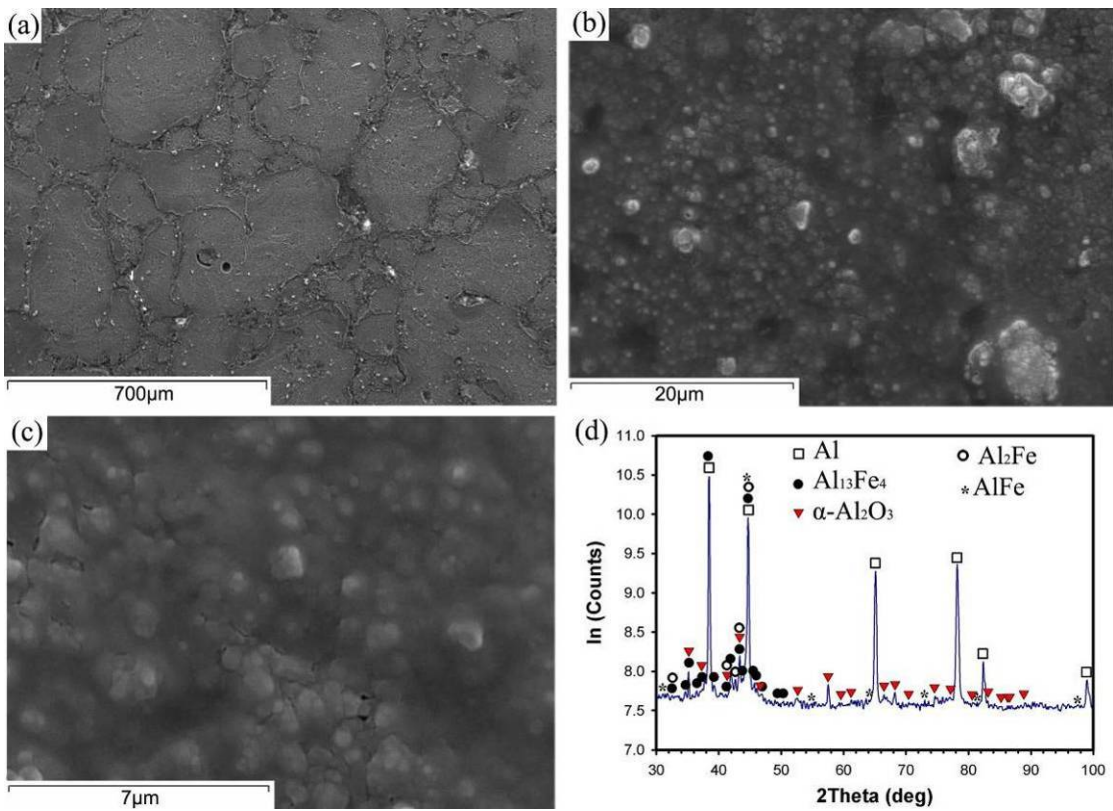


**Fig. 10.5:** (a) Overall view of solids, (b) microstructure with a particulate appearance, (c) higher magnification of the particles resolved in matrix, and (d) XRD pattern of as-manufactured Al/10wt%Fe<sub>2</sub>O<sub>3</sub> SLM part.

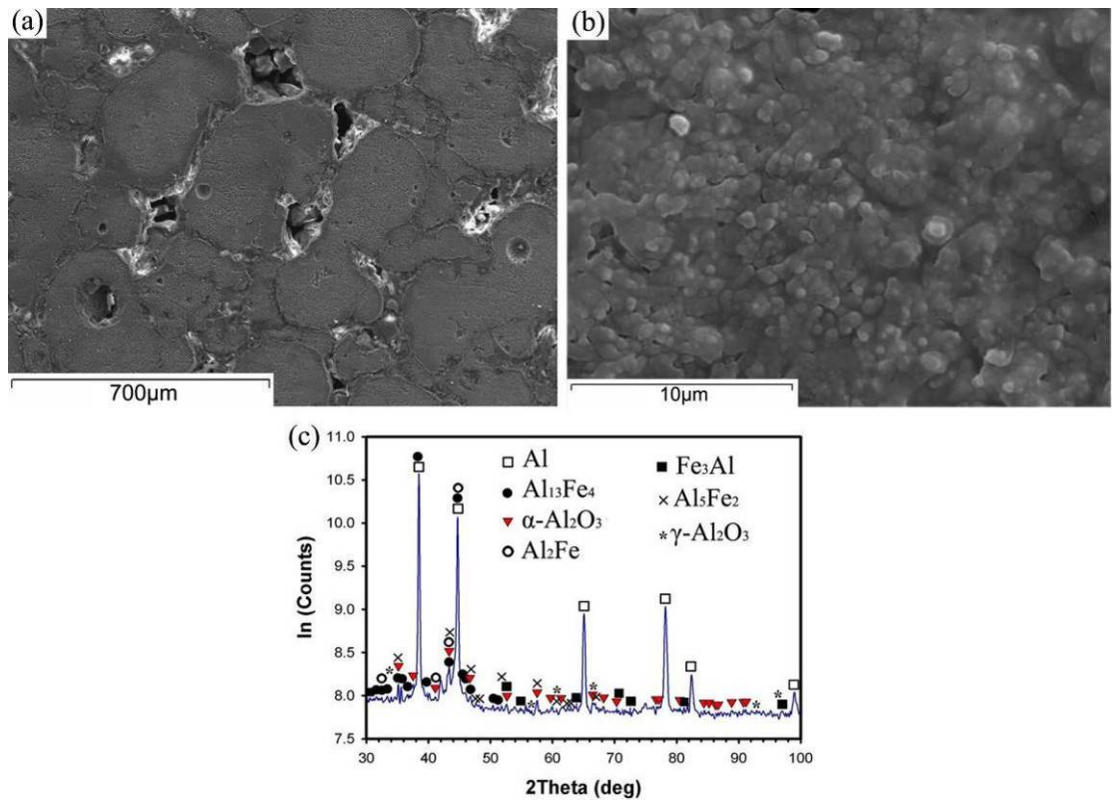


**Fig. 10.6:** (a) Overall view of solids, (b) microstructure showing fine particles placed in matrix, and (c) XRD pattern of as-manufactured Al/15wt%Fe<sub>2</sub>O<sub>3</sub> SLM part.

### 10.3.3.2. HIP post-treated SLM parts

The cross-sectional detail of the Al/5wt%Fe<sub>2</sub>O<sub>3</sub> part ( $t = 75$ ) after HIP treatment is presented in Fig. 10.7 and show the interconnected gaps between solids (Fig. 10.7a). The microstructure is composed of large agglomeration of secondary phases adhered together (Fig. 10.7b). These agglomerated phases can be rough corallines containing very fine particles (perhaps in nano-size scale), as seen from Fig. 10.7c. The XRD identified Al, Al<sub>13</sub>Fe<sub>4</sub> and  $\alpha$ -Al<sub>2</sub>O<sub>3</sub> as the main elements forming the microstructure (Fig. 10.7d). The cross section of HIP post-treated Al/5wt%Fe<sub>2</sub>O<sub>3</sub> part when  $t = 50 \mu\text{m}$  is too composed of clearly interconnected gaps surrounding solids (Fig. 10.8a). The microstructure contains a porous formation of very tiny particles attached together (Fig. 10.8b). The phases are Al, Al<sub>13</sub>Fe<sub>4</sub>, and  $\alpha$ -Al<sub>2</sub>O<sub>3</sub> according to the XRD results (Fig. 10.8c).

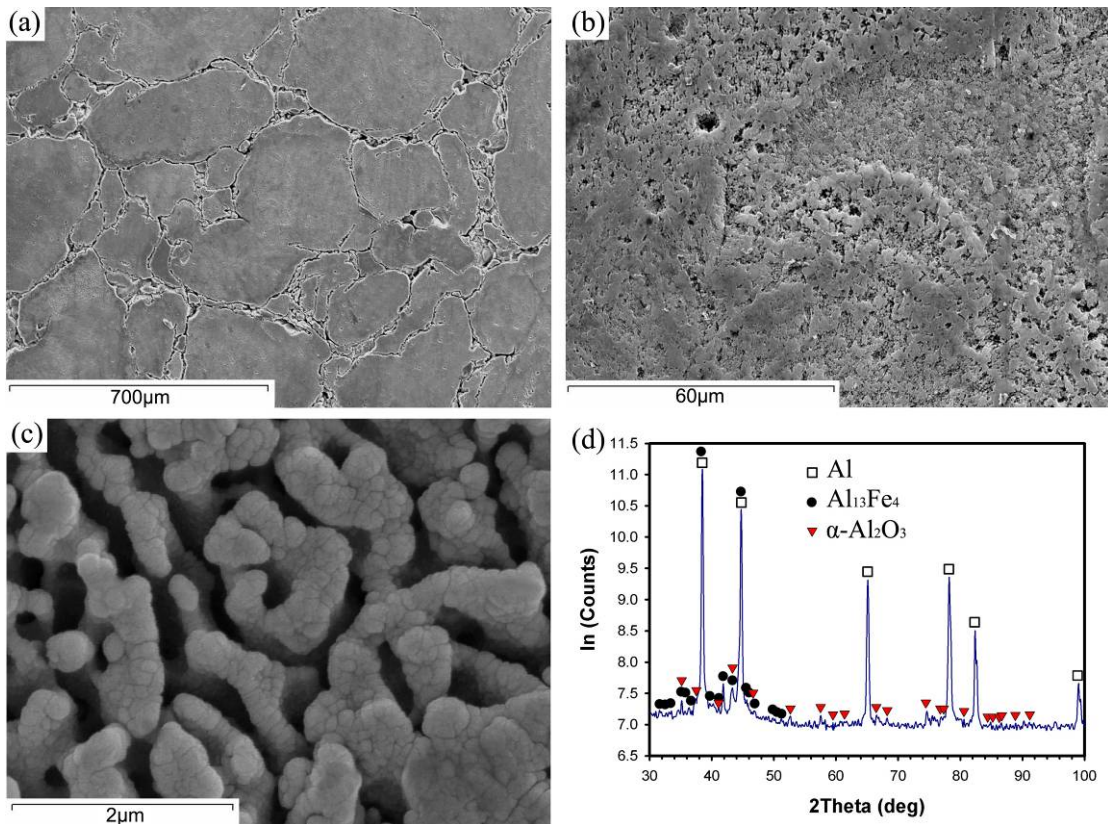


**Fig. 10.7:** (a) Overall view of solids, (b) microstructure with a rough and coarse coralline-like appearance, (c) higher magnification of rough and coarse corallines, and (d) XRD pattern of HIP treated Al/5wt%Fe<sub>2</sub>O<sub>3</sub> SLM part when  $t = 75 \mu\text{m}$ .

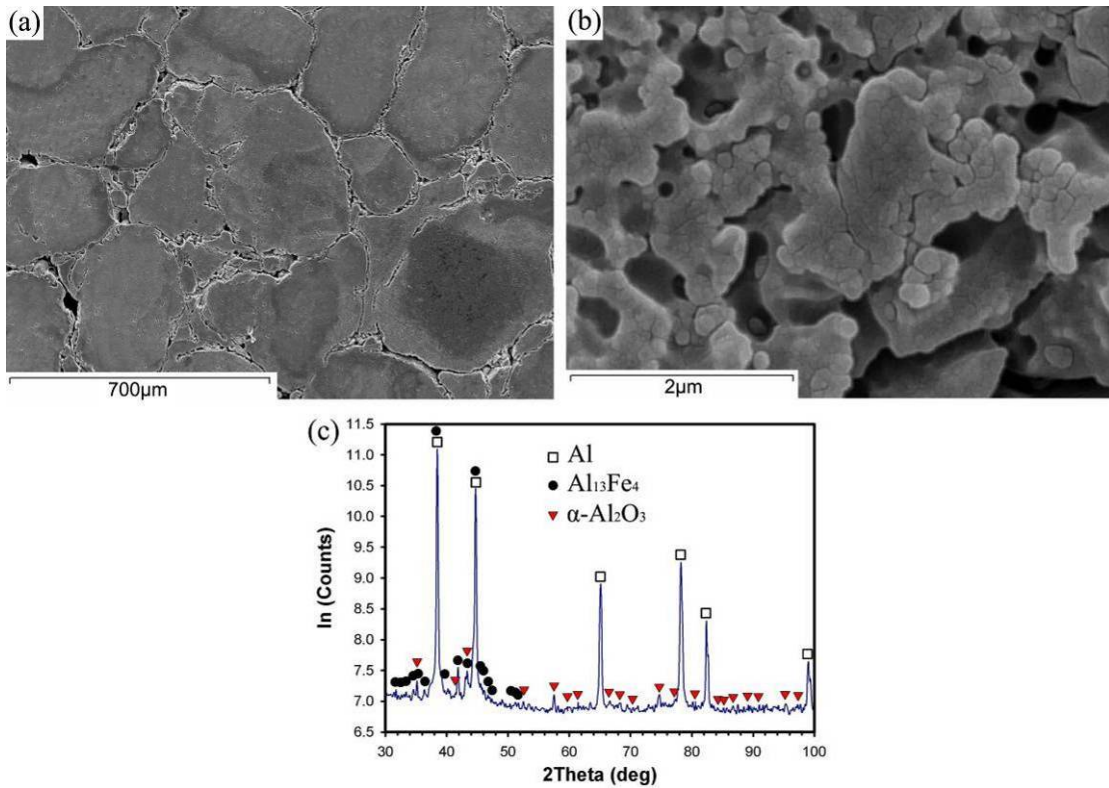


**Fig. 10.8:** (a) Overall view of cross section, (b) porous microstructure composed of very tiny particles, and (c) XRD pattern of HIP treated Al/5wt%Fe<sub>2</sub>O<sub>3</sub> SLM part when  $t = 50 \mu\text{m}$ .

The gaps between solids seem to become larger in HIP treated Al/10wt%Fe<sub>2</sub>O<sub>3</sub> SLM part in comparison with lower Fe<sub>2</sub>O<sub>3</sub> contents (Fig. 10.9a). The microstructure seems to be porous colonies of fine particles (Fig. 10.9b). The XRD once again shows Al, Al<sub>13</sub>Fe<sub>4</sub>, and α-Al<sub>2</sub>O<sub>3</sub> as the main constituents (Fig. 10.9c). Increasing the Fe<sub>2</sub>O<sub>3</sub> to 15wt% slightly affects the mentioned large gaps and connects them in some positions (Fig. 10.10a), and also agglomerates abundant mixture of particles in microstructure (Fig. 10.10b). Once again, the phases are Al, Al<sub>13</sub>Fe<sub>4</sub>, and α-Al<sub>2</sub>O<sub>3</sub> (Fig. 10.10c).

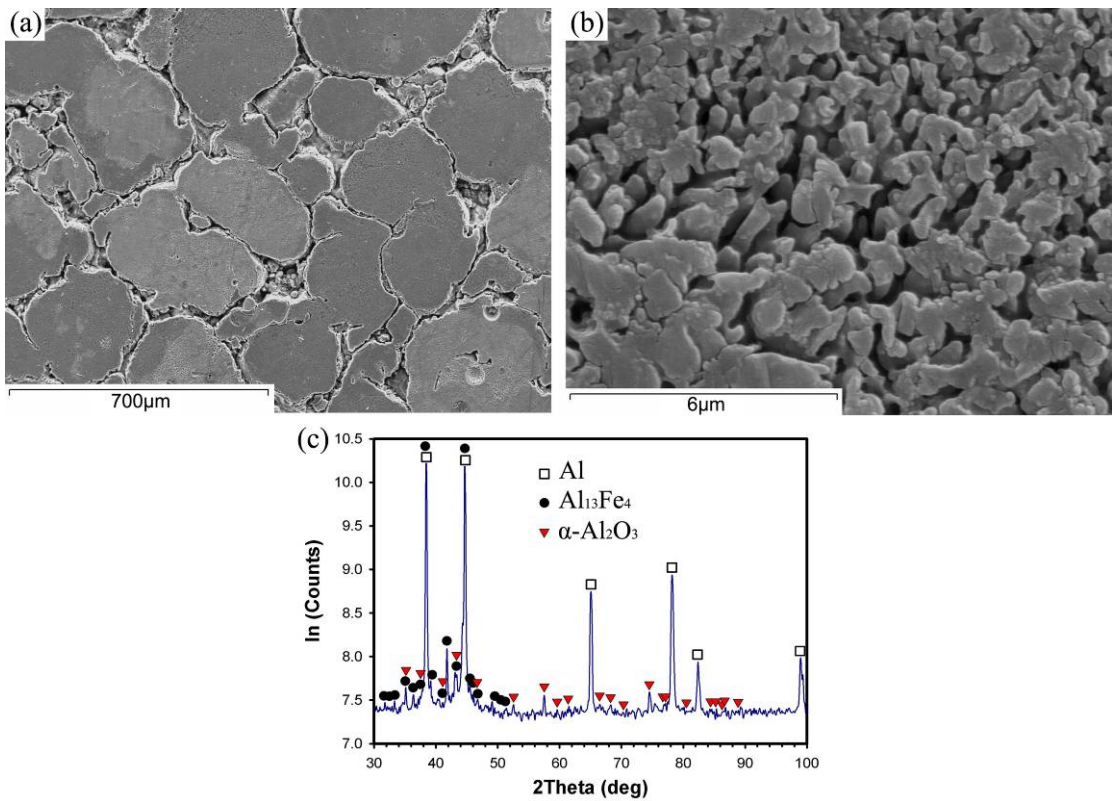


**Fig. 10.9:** (a) The cross section, (b) porous microstructure composed of agglomerated fine particles, and (c) XRD pattern of HIP treated Al/10wt%Fe<sub>2</sub>O<sub>3</sub> SLM sample.

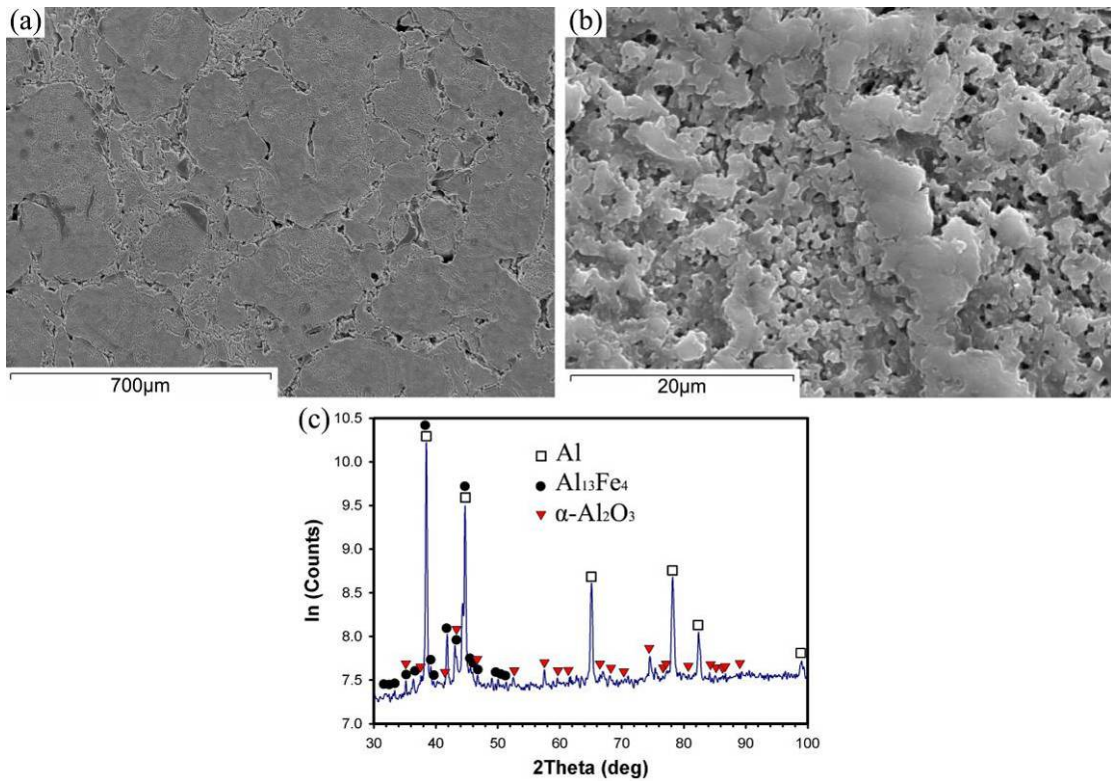


**Fig. 10.10:** (a) The cross section, (b) microstructure resulting from abundant, coarse and mixed phases, and (c) XRD pattern of HIP treated Al/15wt%Fe<sub>2</sub>O<sub>3</sub> SLM sample.

## 10.4. Discussion

The results of microstructural characteristics have been summarised in Table 10.1 which reveals major changes occurring due to HIP post-treatment. The microstructure of Al/5wt% Fe<sub>2</sub>O<sub>3</sub> made using  $t = 75 \mu\text{m}$  is composed of tiny coralline-like phases (associated with rapidly solidified Al-Fe intermetallics such as Al<sub>13</sub>Fe<sub>4</sub>) mixed with some particles (e.g.  $\alpha$ -Al<sub>2</sub>O<sub>3</sub>) (see Fig. 10.3). The Al<sub>13</sub>Fe<sub>4</sub> is an equilibrium Al-Fe combination, as described by (Griger and Stefániay, 1996) for equilibrium intermetallic phases in Al-Fe alloys, which is formed in thermite reaction between Al and Fe<sub>2</sub>O<sub>3</sub> in presence of excessive Al powders, and the  $\alpha$ -Al<sub>2</sub>O<sub>3</sub> is an equilibrium oxide existing on Al powder (in the form of thin films) or produced within in-situ reaction. These secondary phases (Al<sub>13</sub>Fe<sub>4</sub> and  $\alpha$ -Al<sub>2</sub>O<sub>3</sub>) show very good hardness, strength and modulus of elasticity, themselves alone or as composite mixtures (Mukherjee and Bandyopadhyay, 1997), significantly enhance the microhardness. Lowering the layer thickness to  $t = 50 \mu\text{m}$  produces a mass of attached particulate phases from Al<sub>13</sub>Fe<sub>4</sub> and  $\alpha$ -Al<sub>2</sub>O<sub>3</sub> in microstructure (Fig. 10.4), formed due to increasing the remelting of ex-layers (breaking and separating the corallines), the cooling rate (refining the microstructure), and the oxide contents (as pointed out in chapter 8). The HIP post-treatment changes the microstructure of these samples, e.g. coarsens, roughens, and piles up the coralline-like phase (when  $t = 75 \mu\text{m}$  - Fig. 10.7), or in the case of  $t = 50 \mu\text{m}$  converts the attached particles to porous colonies of very tiny particles (Fig. 10.8). In both cases, the elementary composition of secondary phases remains Al<sub>13</sub>Fe<sub>4</sub> and  $\alpha$ -Al<sub>2</sub>O<sub>3</sub> (since they are stable in these chemical compositions).

**Table 10.1:** Summary of microstructural characteristics before and after HIP post-treatment

SLM part	As-manufactured		HIP post-treated	
	Morphology	Phases	Morphology	Phases
Al/5wt%Fe <sub>2</sub> O <sub>3</sub> ( $t = 75 \mu\text{m}$ )	Mainly coralline-like phases mixed with some particles	Al ; Al <sub>13</sub> Fe <sub>4</sub> ; $\alpha$ -Al <sub>2</sub> O <sub>3</sub>	Rough and coarse coralline-like phases containing particles	Al ; Al <sub>13</sub> Fe <sub>4</sub> ; $\alpha$ -Al <sub>2</sub> O <sub>3</sub>
Al/5wt%Fe <sub>2</sub> O <sub>3</sub> ( $t = 50 \mu\text{m}$ )	Firmly attached particles	Al ; Al <sub>13</sub> Fe <sub>4</sub> ; $\alpha$ -Al <sub>2</sub> O <sub>3</sub>	Porous formation of firmly attached and fine particles	Al ; Al <sub>13</sub> Fe <sub>4</sub> ; $\alpha$ -Al <sub>2</sub> O <sub>3</sub>
Al/10wt%Fe <sub>2</sub> O <sub>3</sub> ( $t = 50 \mu\text{m}$ )	Fine particles resolved in matrix	Al ; Al <sub>13</sub> Fe <sub>4</sub> , Al <sub>2</sub> Fe, AlFe ; $\alpha$ -Al <sub>2</sub> O <sub>3</sub>	Porous colonies of fine particles	Al ; Al <sub>13</sub> Fe <sub>4</sub> ; $\alpha$ -Al <sub>2</sub> O <sub>3</sub>
Al/15wt%Fe <sub>2</sub> O <sub>3</sub> ( $t = 50 \mu\text{m}$ )	Uniform distribution of very fine particles (below 1 $\mu\text{m}$ in size)	Al ; Al <sub>13</sub> Fe <sub>4</sub> , Al <sub>2</sub> Fe, Al <sub>5</sub> Fe <sub>2</sub> , Fe <sub>3</sub> Al ; Oxides (mainly $\alpha$ -Al <sub>2</sub> O <sub>3</sub> plus metastable oxides such as $\gamma$ -Al <sub>2</sub> O <sub>3</sub> )	Abundant, coarse and mixed agglomerated particles	Al ; Al <sub>13</sub> Fe <sub>4</sub> ; $\alpha$ -Al <sub>2</sub> O <sub>3</sub>

The microstructural changes due to HIP post-treatment (coarsening as well as formation of porous colonies of particles (Table 10.1)) can be encountered as the main reason for reduction of hardness (Fig. 10.1b). The microstructural changes can be mainly attributed to the influence of high temperature and annealing effects of HIP, activating coarsening and coalescence mechanisms. In some cases e.g. Al/5wt%Fe<sub>2</sub>O<sub>3</sub> when  $t = 50 \mu\text{m}$ , microporosity appears between particulate features. Perhaps, the particles have coalesced and agglomerated together and formed bigger particle colonies instead (under high temperature). Another postulation can be based on the highly resolved Fe inside Al matrix due to rapid solidification of SLM process (rapid solidification significantly extends the solid solubility of Al matrix (Lavernia and Srivatsan, 2010)). High HIP temperature might permit the Fe atoms to leave the Al matrix and form Al-Fe intermetallics (like equilibrium Al<sub>13</sub>Fe<sub>4</sub>). This transformation could cause micro-porous spaces regarding significantly higher density of new combinations (e.g.  $\rho_{\text{Al13Fe4}} \sim 3.85 \text{ g/cm}^3$ ) than that of Al matrix ( $\rho_{\text{Al}} \sim 2.7 \text{ g/cm}^3$ ).

The HIP post-treatment has led to almost the same impact on the hardness and density of Al/5wt% Fe<sub>2</sub>O<sub>3</sub> SLM samples ( $t = 50$  and  $75 \mu\text{m}$ ) (see Fig. 10.2) in despite of their microstructural differences. Density in both cases has slightly increased while the hardness (both macro- and micro-hardness) has dropped after HIP treatment. These have been accompanied with some changes in cross sections, composed of many circular solid zones (embedding microstructures) separated by a tiny interconnected inter-solid band (Figs. 10.3a and 10.4a). These thin bands are filled by high level of oxides formed during SLM process (Louvis et al., 2011), but seem to appear as gaps surrounding individual solids after HIP treatment (Figs. 10.7a and 10.8a).

The applied pressure at elevated temperature of HIP post-treatment obviously squeezes the part and increases the density, when the motion of small oxide particles has a major contribution to compaction (DeLo and Piehler, 1999). However, unfortunately the changes appear to be small and in fact HIP fails to compress all the porosity to achieve a dense part. This failure can be attributed to inter-solid bands as oxide walls, interrupting the connection of solids (i.e. they serve as barriers for the creep deformation and elemental diffusion as main mechanisms of densification (Swinkels et al., 1983, Tang et al., 2005)) and suppressing the solids fusion. The fragmentation or dissolution of these oxide walls in matrix (which may facilitate the fusion of solids) seems to be unlikely as well, due to their

high strength and stability. However, the HIP pressure, which failed to join solid regions over oxide walls, just forces the solids to be further compressed at the HIP elevated temperature. At this point, the solids might shrink, or even loose their inner-porosity (if they have any). After releasing the pressure, the compressed oxide walls normally tend to move back and expand (which may slightly enhance the gap between solids). The oxides accumulated in bands are now loose due to subsequent displacements and can be easily removed during polishing stages and hence larger gaps appear in SEM pictures (Figs. 10.7a and 10.8a).

The effect of higher iron oxide contents can be observed in Figs. 10.5-10.6 where the Al matrix of SLM parts (made from Al/(10-15)wt%Fe<sub>2</sub>O<sub>3</sub>) are heavily reinforced by particles below 1 μm in size. These particles are resolved or firmly placed in matrix and are composed of equilibrium phases such as Al<sub>13</sub>Fe<sub>4</sub> and α-Al<sub>2</sub>O<sub>3</sub> plus non- and meta-stable phases such as Al<sub>5</sub>Fe<sub>2</sub>, Al<sub>2</sub>Fe, AlFe, Fe<sub>3</sub>Al, and γ-Al<sub>2</sub>O<sub>3</sub> (see Table 10.1). In fact, higher iron oxide enables the existence of meta-stable phases in addition to equilibrium ones, e.g. Fe<sub>3</sub>Al is one primary thermite reaction product which were not detected in 5 wt% Fe<sub>2</sub>O<sub>3</sub> because of its transformation to equilibrium Al<sub>13</sub>Fe<sub>4</sub> (Al<sub>3</sub>Fe) in presence of excessive Al reminder. The higher Fe<sub>2</sub>O<sub>3</sub> content also enhances the oxides accumulated in inter-solid regions and, therefore, thickens the oxide bands between solid zones; becoming large gaps after HIP treatment (compare Fig. 10.9a to Figs. 10.7a and 10.8a). The HIP post-treatment affect the constituents' elementary compositions, by transforming the intermediate phases into equilibrium features, i.e. only Al<sub>13</sub>Fe<sub>4</sub> and α-Al<sub>2</sub>O<sub>3</sub> remains after HIP (Table 10.1). In fact, high temperature of HIP allows the elements to diffuse and transform the products to stable and equilibrium combinations. These changes in secondary phases may be followed by segregation between particles (due to coarsening, coalescence and etc), converting the appearance of former smooth microstructure (due to resolved particles or uniform distribution of very fine particles) to numerous particles agglomerated and segregated in matrix (Figs. 10.9-10.10). However, the coarsening and coalescence of phases due to annealing effects of HIP post-treatment weaken the material and lead to a drop in hardness.

The higher Fe<sub>2</sub>O<sub>3</sub> content of 15 wt% has also provided an extra energy to break the inter-solid oxide bands during SLM process and succeeded to partially fuse some solids (Fig. 10.6a). The connection of solids may mitigate the enlargement of gaps after HIP treatment, though the inter-solid bands in cross section might still become thicker (e.g. see

Fig. 10.10a). The corresponding CT scan results (Fig. 10.2) confirms the growth of gaps after HIP process especially where the solids are not fused.

Overall, despite the benefits of HIP process such as integrating the microstructure and reducing the hardness scatter (Fig. 10.1b), similar to the previous study (Ran et al., 2006), the HIP was failed to produce a dense material as its primary task. The reason was attributed to oxide bands which act as barriers to disconnect solid zones suppressing diffusion and failing the densification. This oxide bands can be thickened with increasing the  $\text{Fe}_2\text{O}_3$  contents resulting in a larger gap between solids after HIP post-treatment. The HIP post-treatment does not only fail to efficiently densify the parts, but also negatively reduces the hardness due to the influences of annealing (which lead to coarsening and coalescence of microstructure accompanied with development of local microporosity between microstructural phases). Furthermore, the intermediate phases could transform to equilibrium and stable phases i.e.  $\text{Al}_{13}\text{Fe}_4$  and  $\alpha\text{-Al}_2\text{O}_3$  after HIP treatment.

## 10.5. Conclusions

The SLM of Al mixed with 5, 10 and 15 wt%  $\text{Fe}_2\text{O}_3$  was carried out to produce Al composites reinforced by Al-Fe intermetallics and Al oxides. The influence of HIP post-treatment on density, hardness and microstructure of the products was investigated. The main results can be summarised as:

- Although HIP post-treatment slightly increased the density, it failed to achieve a dense material. This was attributed to formation of oxide bands surrounding the solid areas in cross section. The oxide bands act as a barrier and suppress diffusion and bonding.
- These oxide bands can expand with increasing the iron oxide content, and further restrict the densification by HIP.
- The hardness drops after HIP as a result of high temperature annealing effects of HIP post-treatment leading to coarsening and coalescence of microstructure.
- The HIP post-treatment affects the microstructure and change the phase features from corallines, particles, and particles firmly resolved or placed in matrix into coarse corallines, porous colonies of particles, or coarse particles with a rough appearance.

- In addition to main and equilibrium  $\text{Al}_{13}\text{Fe}_4$  and  $\alpha\text{-Al}_2\text{O}_3$ , the non-equilibrium intermetallics and oxides may form within samples especially those made by high  $\text{Fe}_2\text{O}_3$  contents. The non-equilibrium and intermediate combinations tend to convert to equilibrium and stable phases i.e.  $\text{Al}_{13}\text{Fe}_4$  and  $\alpha\text{-Al}_2\text{O}_3$  after HIP post-treatment.
- The SLM layer thickness can influence the properties of as-manufactured SLM parts, though it does not seem to have a significant effect on HIP-induced densification.

---

# **Chapter 11: Effect of Al Alloys on the Selective Laser Melting of In-Situ Formed Particle Reinforced Composites**

---

## **11.1. Introduction**

The attractive properties of Al alloys have been a great motivation for their development in powder based advanced techniques. Two important but different material examples of Al alloys containing Al, Mg, and Si can be introduced as Al6061 and AlSi10Mg. The former (Al6061) contains low percentage of alloying elements, which makes its casting behaviour more or less similar to pure Al. In contrast, AlSi10Mg contains high percentage of alloying element, especially for casting purposes (Seyed Reihani, 2006, Triveño Rios et al., 2010).

The SLM of in-situ formed particle reinforced Al-Mg-Si matrix composite represents a promising future, but there is little understanding of the effect of different Al alloys on the SLM consolidation behaviour and in-situ formed microstructure. A comprehensive comparison study is therefore required to illustrate unclear influence of alloy composition on SLM stimulated in-situ interaction, and to build a better knowledge of the phenomena governing the in-situ formation of particle reinforced MMCs in presence of rapid solidification. Hence, this chapter presents a comparative study on the SLM of Al, Al6061, AlSi10Mg alloys mixed with 15 wt% Fe<sub>2</sub>O<sub>3</sub> powders, investigating the differences between the resultant MMCs in terms of microstructural features, hardness properties, and consolidation conditions.

## **11.2. Materials and Experiments**

The powder mixtures of Al/15wt%Fe<sub>2</sub>O<sub>3</sub>, Al6061/15wt%Fe<sub>2</sub>O<sub>3</sub>, and AlSi10Mg/15wt%Fe<sub>2</sub>O<sub>3</sub> were provided. Multilayer SLM samples were fabricated using scan line spacing of 0.05 mm, layer thickness of 0.075 mm, laser power of 74 W, and scanning speed of 0.20 m/s. The samples were examined using various techniques such as computed tomography (CT) scanning, SEM, XRD, compression test, and hardness and

microhardness. For SEM, a Hitachi S-3200N scanning electron microscope (SEM) and also an xT Nova Nanolab 200 high resolution SEM were used.

## 11.3. Results and Discussion

### 11.3.1. Visual observation of SLM behaviour and physical phenomena

The processing of various Al alloys mixed with 15 wt%  $\text{Fe}_2\text{O}_3$  to form three-dimensional samples was successfully carried out with recorded visual observation of SLM process. Examples of the visual observation of SLM process to produce parts from Al/15wt% $\text{Fe}_2\text{O}_3$ , Al6061/15wt% $\text{Fe}_2\text{O}_3$ , and AlSi10Mg/15wt% $\text{Fe}_2\text{O}_3$  are shown in Fig. 11.1. The images demonstrate a strong spark, appropriate melting pool, and shiny appearance of parts following SLM. This implies a suitable laser and material interaction characteristics, allowing the construction of successive layers to form parts. However, it seems that the spark gradually becomes somehow larger and the surface becomes shinier when Al/15wt% $\text{Fe}_2\text{O}_3$  is replaced with Al6061/15wt% $\text{Fe}_2\text{O}_3$  and AlSi10Mg/15wt% $\text{Fe}_2\text{O}_3$ . This indicates a larger melting and consolidation for AlSi10Mg/15wt% $\text{Fe}_2\text{O}_3$  powder mixture during SLM in comparison with other alloy mixtures. The enhanced melting pool can be attributed to the alternation in thermal characteristics due to increasing of alloying composition. In fact, increasing the alloying elements shift the chemical composition to eutectic point (e.g. in Al-Si phase diagram, a eutectic system exists about 12.6 wt% Si), leading to a decrease in melting temperature. More importantly, the present changes in the used Al alloy significantly influence thermal conductivity and subsequently cooling rate. In fact, the thermal conductivity of pure Al is larger than Al6061 which is larger than AlSi10Mg (e.g. thermal conductivity (at room temperature) of Al, Al6061, and AlSi10Mg are about 234 W/(m.K), 180 W/(m.K), and 113 W/(m.K) respectively (ASM International Handbook Committee, 1992)). This leads to lowest cooling rate for AlSi10Mg which improves melting condition.

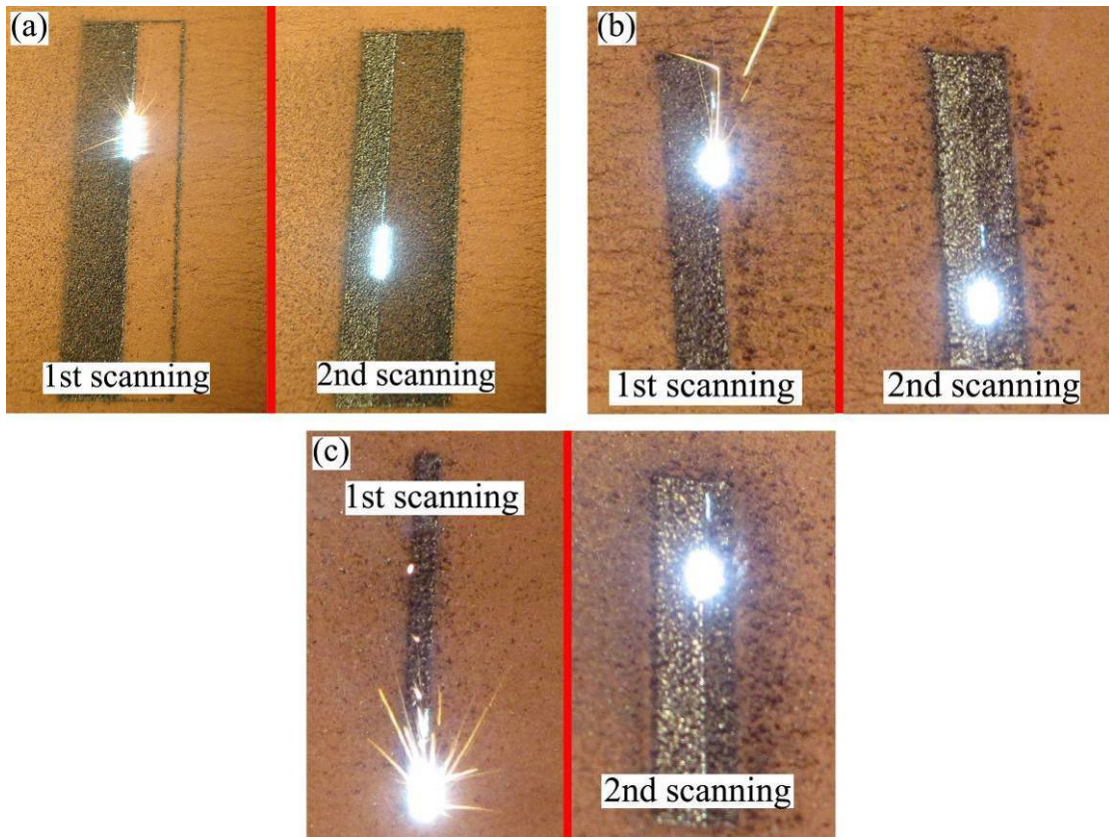


**Fig. 11.1:** The visual appearance of SLM process during first and secondary scanning of each layer for (a) Al/15wt%Fe<sub>2</sub>O<sub>3</sub>, (b) Al6061/15wt%Fe<sub>2</sub>O<sub>3</sub>, and (c) AlSi10Mg/15wt%Fe<sub>2</sub>O<sub>3</sub>.

### 11.3.2. Porosity analysis using CT scanning

After SLM of different powder mixtures, the influence of Al alloy on porosity formation was studied using CT scanning images. Fig. 11.2a shows broad spread of porosity in the SLM parts made from Al/15wt%Fe<sub>2</sub>O<sub>3</sub>. The extensive porosity can be associated with the SLM process pushing the oxide layers into inter-solid regions (Louvis et al., 2011). The accumulated oxides act as barriers suppressing diffusion and melting fusion (which joins the solids together) and thus leaving much porosity within the part. The change of the Al alloy can manipulate the porosity formation. The usage of Al6061 instead of pure Al mixed with 15wt% Fe<sub>2</sub>O<sub>3</sub> seems to slightly mitigate the porosity formation (Fig. 11.2b). This reduction in porosity becomes even more evident when the AlSi10Mg/15wt%Fe<sub>2</sub>O<sub>3</sub> is used (Fig. 11.2c). These changes in porosity formation and growth of solids with changing the Al alloy can be attributed to improvement of melting in presence of higher content of alloying elements (as mentioned in Fig. 11.1), tearing the oxide barriers (accumulated in inter-solid regions) apart and establishing better bonding

between solids. In addition to porosity accumulated in inter-solid regions, micropores can form in microstructure as well. These tiny pores (being more evident in Fig. 11.2c) may be formed when excessive hydrogen is rejected from solution and it recombines as molecular gas which may be entrapped in the solid structure (Polmear, 2005).

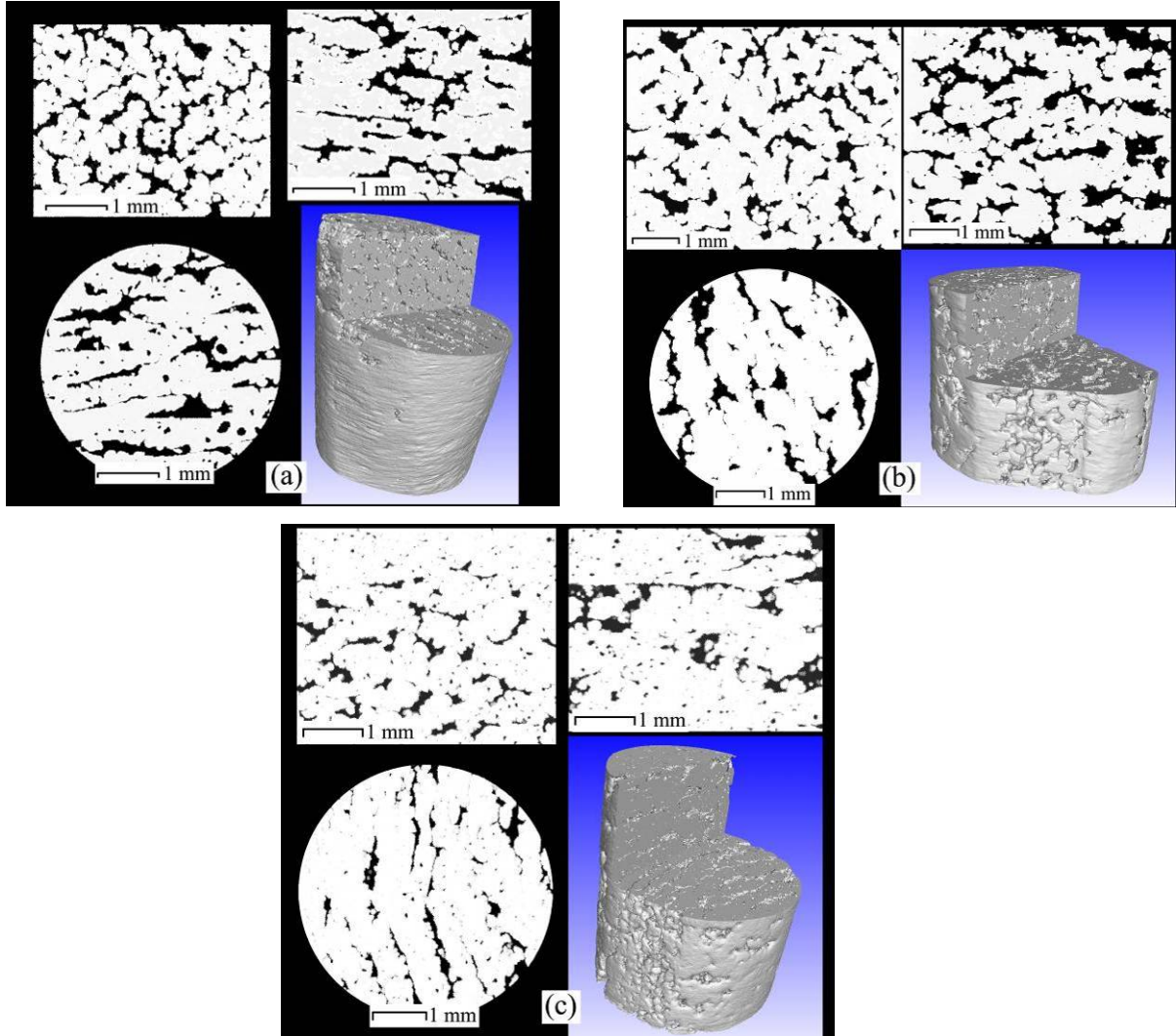


**Fig. 11.2:** The CT scan exhibition of the SLM part made from (a) Al/15wt% $\text{Fe}_2\text{O}_3$ , (b) Al6061/15wt% $\text{Fe}_2\text{O}_3$ , and (c) AlSi10Mg/15wt% $\text{Fe}_2\text{O}_3$ .

### 11.3.3. Density, hardness and microhardness, and compressive strength

Density and relative density of the SLM samples made from Al/15wt% $\text{Fe}_2\text{O}_3$ , Al6061/15wt% $\text{Fe}_2\text{O}_3$ , and AlSi10Mg/15wt% $\text{Fe}_2\text{O}_3$  are shown in Fig. 11.3. As seen, increasing the alloying elements in Al alloy has a positive influence to improve density, i.e. the density gradually increases from pure Al to Al6061 and finally to AlSi10Mg mixed

with 15 wt%  $\text{Fe}_2\text{O}_3$ . As mentioned, this can be attributed to reduction in thermal conductivity and subsequently cooling rate with increasing the alloying elements which improves the melting during SLM process.

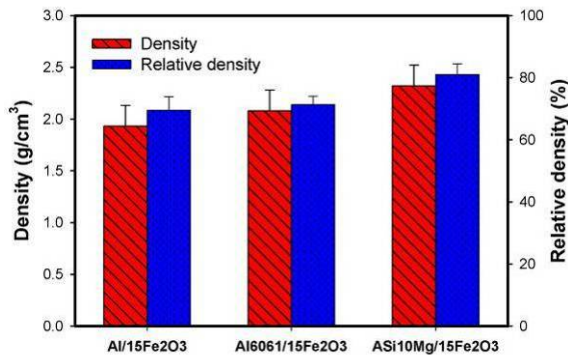


**Fig. 11.3:** Density and relative density of the SLM parts. The density was measured by dimensional method while relative density was achieved according to CT scanning experiments.

The hardness and microhardness comparison shown in Fig. 11.4 exhibits that the SLM formed Al alloy composites (even in the presence of high percentage of porosity) are significantly harder than those of relevant Al alloys reported in previous studies (ASM International Handbook Committee, 1992). This becomes more comprehensible when the microhardness (taken from dense areas) of the SLM formed composites is compared to the hardness of Al alloys. For example, the microhardness of SLM part made from Al6061/15wt% $\text{Fe}_2\text{O}_3$  is about 110 HV which is significantly higher than the hardness of Al6061 in annealed state (~ 30 HV) (ASM International Handbook Committee, 1992) or after SLM (~ 50 HV) (Jerrard et al., 2011). This considerable improvement in hardness could be attributed to the modification in microstructure as a result of in-situ secondary combinations produced during the SLM of Al alloys and  $\text{Fe}_2\text{O}_3$  mixtures. Increasing in the alloying elements of Al alloy is accompanied with the increasing in the hardness as well, e.g. the highest microhardness belongs to the SLM part made from AlSi10Mg/15wt% $\text{Fe}_2\text{O}_3$  (~ 165 HV) which possesses the highest alloying composition. Obviously, the alloy composition plays a significant role in the hardening of these in-situ formed Al MMCs.

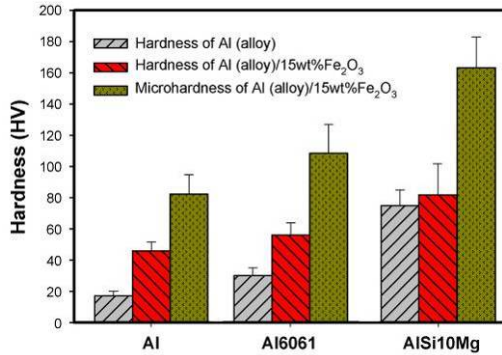


**Fig. 11.4:** Hardness and microhardness of the Al alloy and Al matrix composite parts. The hardness of Al alloys (Al and Al6061 in their annealed state, and AlSi10Mg (comparable to A360.0) in die casting state) was picked from references.

The compressive strength of the Al composite samples is shown in Fig. 11.5, demonstrating the influence of the alloy on the strength and bonding conditions. The results indicate that shifting the Al matrix to eutectic composition of alloy matrix can improve the compressive strength for the in-situ formed composites, i.e. the strength of AlSi10Mg/15wt%Fe<sub>2</sub>O<sub>3</sub> SLM sample is higher than that of Al/15wt%Fe<sub>2</sub>O<sub>3</sub> and Al6061/15wt%Fe<sub>2</sub>O<sub>3</sub>. In fact, eutectic compositions may improve the bonding between solids or strengthening the microstructure. It is noted that the overall compressive strengths of the parts are low due to porosity extended along inter-solid areas (see Fig. 11.2). This harms the compressive strength by facilitating the movement of solids towards each other without actual deformation within solids.

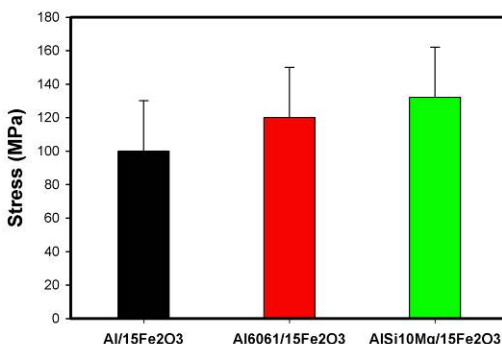


**Fig. 11.5:** Compressive strength of the SLM parts made from Al alloy mixed with 15 wt% Fe<sub>2</sub>O<sub>3</sub>.

#### 11.3.4. Microstructural characterisation and phase identification using XRD

Fig. 11.6 shows the microstructural characteristics of Al/15wt%Fe<sub>2</sub>O<sub>3</sub> SLM part. The Al matrix (containing Al, Fe, and O) embeds very fine (~ 500 nm) and homogenously

distributed particulate phases (Fig. 11.6a-b). These fine secondary phases are composed of hard particles including Al-Fe intermetallics (such as  $\text{Al}_{13}\text{Fe}_4$ ,  $\text{Al}_5\text{Fe}_2$ ,  $\text{Al}_2\text{Fe}$ , and  $\text{Fe}_3\text{Al}$ ) and Al oxides (such as  $\alpha\text{-Al}_2\text{O}_3$ ) according to the XRD results presented in Fig. 11.6c.  $\text{Al}_{13}\text{Fe}_4$  is an equilibrium intermetallic (in present chemical composition), and  $\text{Fe}_3\text{Al}$  could be one of the primary in-situ reaction products, which tend to transform to equilibrium state (i.e.  $\text{Al}_{13}\text{Fe}_4$ ). Through this transformation, some intermediate phases such as  $\text{Al}_5\text{Fe}_2$  and  $\text{Al}_2\text{Fe}$  may form. These homogeneously distributed, fine and hard particles are the most responsible for hardness improvement in comparison with pure Al (Fig. 11.4 shows the microhardness of Al/15wt% $\text{Fe}_2\text{O}_3$  which is about 5 times of pure Al hardness). It should be noted that grain or dendritic structure can not be seen in Al matrix and in fact it appears featureless because of grain refinement due to the high cooling rate together with heterogeneous nucleation (the abundant in-situ reinforcements catalyse the heterogeneous nucleation of phases). The featureless zone (i.e. appears featureless after etching) is a reported structure in rapidly solidified Al alloys (Salehi and Dehghani, 2008).

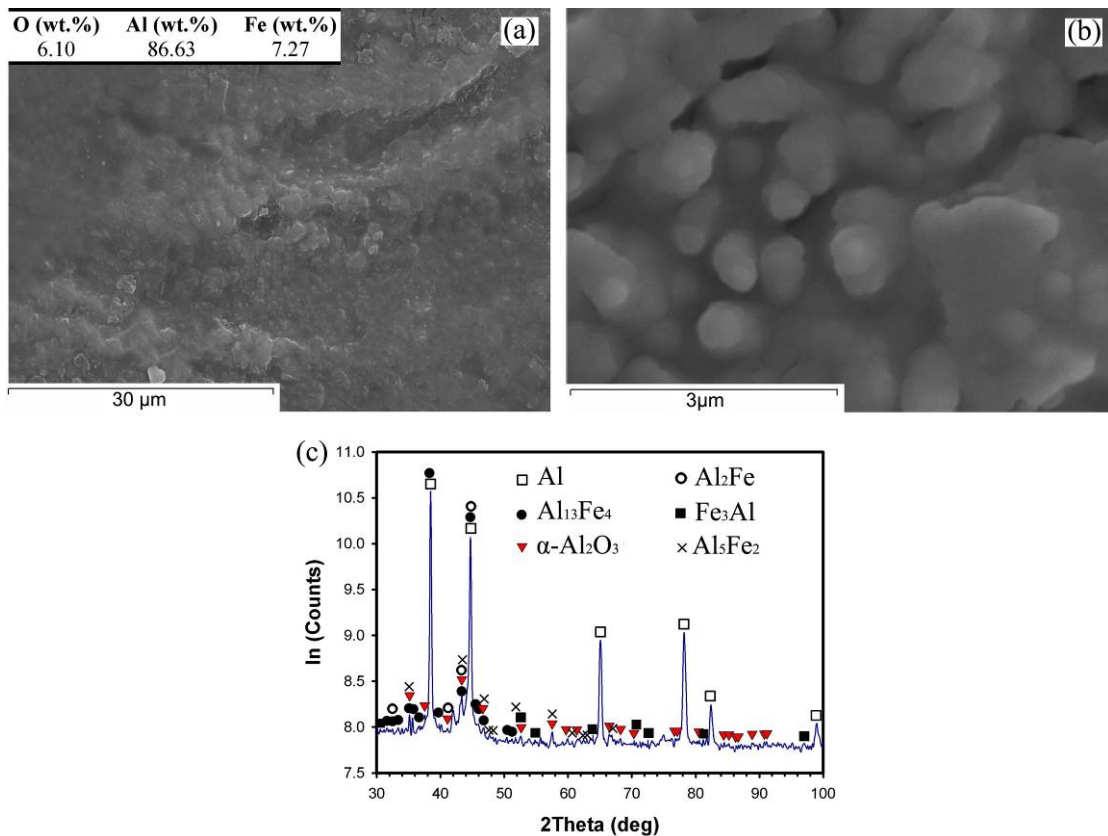


**Fig. 11.6:** (a) Typical microstructure containing (b) very fine particles observed in the SLM part made from Al/15wt% $\text{Fe}_2\text{O}_3$  (the chemical composition was acquired by EDS system). (c) XRD pattern of the corresponding part.

Fig. 11.7 demonstrates the microstructure of Al6061/15wt%Fe<sub>2</sub>O<sub>3</sub> SLM part, composed of very fine particles. In fact, Al6061 powder (which contains low percentage of elements such as Si, Mg, Cu and etc) has not significantly affected the particulate nature of Al matrix, though it has influenced the in-situ combinations reinforcing the part. The XRD results (Fig. 11.7b) shows that the non-equilibrium Al-Fe intermetallics disappear and just equilibrium Al<sub>13</sub>Fe<sub>4</sub> remains. The lower thermal conductivity of Al6061 powders than that of pure Al might have provided a longer time for diffusion and transformation of Fe<sub>3</sub>Al and other intermediate phases to Al<sub>13</sub>Fe<sub>4</sub> at SLM elevated temperatures. Among Al oxides,  $\alpha$ -Al<sub>2</sub>O<sub>3</sub> is stable and appears again after replacing Al with Al6061. Moreover, the Si may limitedly appear in the form of a ternary phase of Al<sub>0.5</sub>Fe<sub>3</sub>Si<sub>0.5</sub>. Hence, these combinations enhance the hardness of the Al MMCs. In addition, the new elements can significantly harden the material by formation of solid solution. For example, the absence of Mg and Cu in XRD result, attributed to high SLM solidification rates which can easily resolve them in Al matrix, contributes to solid solution strengthening (Huskins et al., 2010, Lavernia and Srivatsan, 2010). Likewise, Si (in these percentages) tends to resolve in Al matrix due to rapid solidification (there are reports claiming rapid solidification of melt spinning can extend solid solubility of Si in the Al matrix even up to 3.01 wt% (Salehi and Dehghani, 2008)). Therefore, an increase in hardness of SLM part can be observed from Al6061/15wt%Fe<sub>2</sub>O<sub>3</sub> in comparison with Al/15wt%Fe<sub>2</sub>O<sub>3</sub> powder mixture (see Fig. 4).

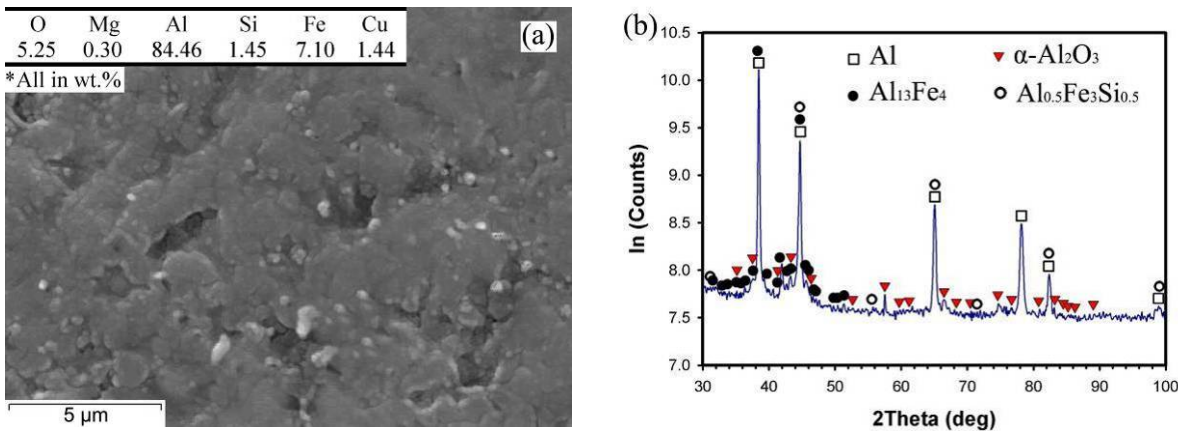


**Fig. 11.7:** (a) Microstructure containing very fine particles with a rough appearance observed in the SLM part made from Al6061/15wt%Fe<sub>2</sub>O<sub>3</sub>. (b) XRD pattern of the corresponding part.

Fig. 11.8 shows the microstructure of AlSi10Mg/15wt%Fe<sub>2</sub>O<sub>3</sub> SLM part which contains very fine particles forming in Al alloy matrix (Fig. 11.8a). The particles are very fine especially when they are observed from a close view. Fig. 11.8b reveals the particles

around 100 nm attached to matrix. The matrix (better shown in Fig. 11.8c) also shows a very fine dendritic appearance which can be encountered in the range of ultrafine or even nanoscale. The XRD result (Fig. 11.8d) reveals the phases reinforcing Al matrix as: i) hard Al-Fe intermetallics which still exist in the form of equilibrium  $\text{Al}_{13}\text{Fe}_4$ , ii) Si based particles alone or in combination with other elements such as  $\text{Al}_{0.5}\text{Fe}_3\text{Si}_{0.5}$ ,  $\text{Al}_{0.7}\text{Fe}_3\text{Si}_{0.3}$  and  $\text{Al}_3\text{FeSi}_2$  formed due to the high percentage of Si element, and iii) stable  $\alpha\text{-Al}_2\text{O}_3$  which is another hard reinforcement to improve the hardness of material.

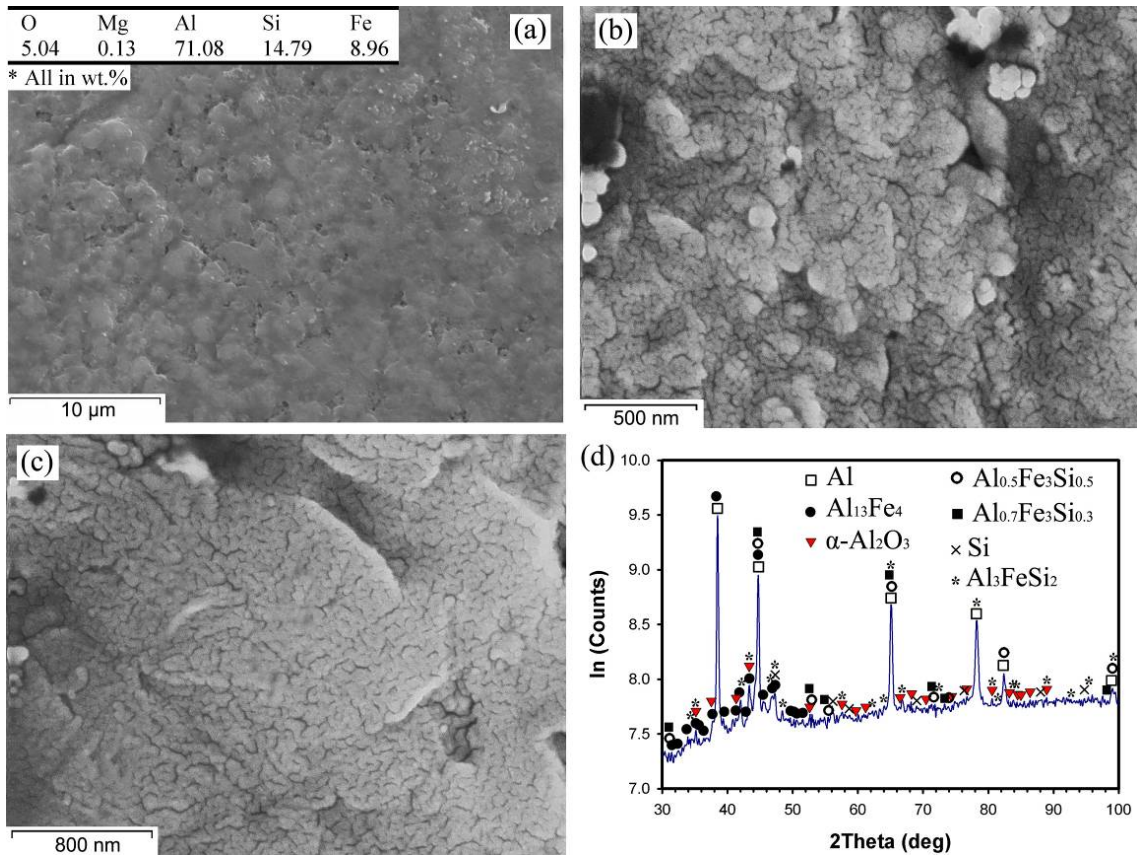


**Fig. 11.8:** SEM micrographs of  $\text{AlSi10Mg}/15\text{wt\%Fe}_2\text{O}_3$ ; (a) microstructure containing very fine particles with a rough appearance, (b) close view of microstructure containing particles around 100 nm, and (c) clear view of ultrafine (or even nanoscale) dendritic nature of matrix. (d) XRD pattern of the corresponding part.

To explain the microstructural details presented in Fig. 11.8 (produced from  $\text{AlSi10Mg}/15\text{wt\%Fe}_2\text{O}_3$ ), rapid solidification phenomena should be considered. In common casting methods, the solidification of  $\text{Al10SiMg}$  usually begins with nucleation and growth of primary Al alloy dendrites and then formation of binary Al-Si eutectics. Also, other binary, ternary and quarternary precipitates like  $\text{Al}_5\text{FeSi}$ ,  $\text{Al}_8\text{Si}_6\text{Mg}_3\text{Fe}$ ,  $\text{Mg}_2\text{Si}$  and even others with more complex structures may be formed due to the low solid solubility of Fe, Si

and Mg in Al, during conventional casting (Ran et al., 2006, Triveño Rios et al., 2010). In contrast, the condition of the SLM facilitated in-situ formation (i.e. rapid solidification and the presence of in-situ reinforcements) can alter the solidification behaviour of AlSi10Mg alloy mixed with Fe<sub>2</sub>O<sub>3</sub>. For example, rapid solidification can considerably extend solid solubility of  $\alpha$ -Al (Triveño Rios et al., 2010), suppressing the precipitation of phases such as Mg<sub>2</sub>Si or replacing the commonplace casting Al-Fe-Si precipitates (like Al<sub>5</sub>FeSi) with precipitates having lower Al in their elementary compositions such as Al<sub>0.5</sub>Fe<sub>3</sub>Si<sub>0.5</sub>, Al<sub>0.7</sub>Fe<sub>3</sub>Si<sub>0.3</sub> and Al<sub>3</sub>FeSi<sub>2</sub>. Rapid solidification also restricts the growth of these particles, leading to their extreme small size (may be  $\sim 100$  nm, as seen in Fig. 11.8b), or forms the Si eutectics with spheroidised shape rather than flake-like appearance (Ran et al., 2006). The presence of alloying elements may also contribute to the small size of these particles by enhancing the heterogeneous nucleation sites (Salehi and Dehghani, 2008)). The lower thermal conductivity of this alloy may replace the featureless zones formed in the SLM part from Al/15wt%Fe<sub>2</sub>O<sub>3</sub> with an ultrafine (or nanoscale) dendritic structure (better shown in Fig. 11.8c). The ultrafine dendritic zones has been previously reported in rapidly solidified Al alloys (it forms in presence of somehow lower solidification rates than that of what needed for featureless zones), presenting Al-rich dendrites (Salehi and Dehghani, 2008). Hence, the ultrafine microstructural characteristics (nanoscale/ultrafine particles and dendrites along with enhanced solid solubility) lead to superior mechanical properties e.g. the high microhardness observed for AlSi10Mg/15wt%Fe<sub>2</sub>O<sub>3</sub> SLM part (Fig. 4).

Overall, the comparison of Figs. 11.6-11.8 shows that composition of the base Al alloy does not significantly alter the particulate appearance of the resultant composites, but it can manipulate the formation of phases, their sizes and even the structure of matrix. For example, non-equilibrium Al-Fe intermetallics do not form in Al6061/15wt%Fe<sub>2</sub>O<sub>3</sub> and AlSi10Mg/15wt%Fe<sub>2</sub>O<sub>3</sub>, or more nucleation sites for heterogeneous nucleation may decrease the size of particles e.g. to about  $\sim 100$  nm in the case of AlSi10Mg/15wt%Fe<sub>2</sub>O<sub>3</sub>. Moreover, the featureless appearance of Al matrix in the case of Al/15wt%Fe<sub>2</sub>O<sub>3</sub> seems to be replaced with ultrafine/nanoscale dendritic structure in the case of AlSi10Mg/15wt%Fe<sub>2</sub>O<sub>3</sub>, attributed to a decrease in thermal conductivity and mitigation of rapid solidification.

## 11.4. Conclusions

The research presented in this Chapter shows that the alloying composition of Al, Al6061 and AlSi10Mg can significantly affect the SLM facilitated in-situ interaction with 15 wt% Fe<sub>2</sub>O<sub>3</sub> to form particle reinforced MMCs. The research provides major following findings:

- The alloy composition directly influenced the SLM consolidation performance, i.e., AlSi10Mg showed the best performance while Al6061 was more comparable to pure Al due to its lower content of alloying elements.
- Inter-solid regions in Al6061 derived SLM part appeared comparable to that in Al derived part, while AlSi10Mg improved the density and reduced inter-solid porosity due to its lower thermal conductivity and enhanced SLM consolidation.
- In-situ composites made from all Al(-Mg-Si) alloys were reinforced by abundant and very fine particles, e.g., AlSi10Mg matrix contained particles around 100 nm scale.
- In-situ formed particles were Al oxides (i.e. stable  $\alpha$ -Al<sub>2</sub>O<sub>3</sub>), Al-Fe intermetallics (i.e. equilibrium Al<sub>13</sub>Fe<sub>4</sub> and other non-equilibrium Al-Fe phases), and Si crystals (alone or in combination such as Al<sub>0.5</sub>Fe<sub>3</sub>Si<sub>0.5</sub>, Al<sub>0.7</sub>Fe<sub>3</sub>Si<sub>0.3</sub> and Al<sub>3</sub>FeSi<sub>2</sub>), depending on the used Al alloy composition. The lower thermal conductivity of Al6061 or AlSi10Mg could transform non-equilibrium Al-Fe intermetallics into equilibrium Al<sub>13</sub>Fe<sub>4</sub>.
- Solubility of elements such as Mg, Si, and Cu in Al matrix can be extended under SLM rapid solidification. This should contribute to hardening through solid solution strengthening mechanisms.
- The matrix appeared featureless in the case of Al/15wt%Fe<sub>2</sub>O<sub>3</sub>, while it was observed with an ultrafine/nanoscale dendritic structure in the case of AlSi10Mg/15wt%Fe<sub>2</sub>O<sub>3</sub>.
- The microstructural characteristics (i.e. ultrafine/nanoscale particles in featureless or ultrafine/nanoscale dendritic matrix, and also enhanced solid solubility) led to significant superior microhardness of composites than that of Al Alloy, indicating the promising prospective of SLM facilitated in-situ reaction to produce advanced Al MMCs.

## **Part Four: Industrial Case Studies and Applications**

---

# **Chapter 12: SLM Case Studies and Industrial Applications**

---

This PhD study is associated with an industrial collaborative project funded by UK Technology Strategy Board which aims to develop laser assisted additive manufacture methods for the rapid prototyping and manufacturing of new classes of high value metallic components. This provides an opportunity to investigate practical applications of SLM and characterise important properties of metallic components. This chapter presents the result of some industrial collaborative studies developing ALM processes.

## **12.1. Surface Finish Improvement of LMD Samples Using Laser Polishing**

### **12.1.1. Introduction**

One exciting collaborative project was manufacturing and polishing of parts using Laser Metal Deposition (LMD). The LMD manufactured parts are almost fully dense with good metallurgical properties, which arise from rapid solidification, meeting the requirement for direct usage (Long et al., 2008, Toyserkani and Khajepour, 2006, Wen et al., 2009). In LMD processes, powder is usually fed into a laser-heated spot to form a melt pool, being solidified quickly after the laser beam moves away (Wen et al., 2009).

Laser polishing is a new technique, and appears to be an attractive alternative for conventional abrasive methods. This method is a non-contact process and would facilitate the automation of the polishing process. To date, laser polishing has been mainly used for the polishing of diamond and optical articles (such as glasses, lens, fibres etc.) (Bol'shepaev and Katomin, 1997, Wang et al., 2003), but it has rarely been used for polishing of metals (Lamikiz et al., 2007, Perry et al., 2009, Shao et al., 2005, Ukar et al., 2010). However, some of these researches on metallic materials showed promising results for laser polishing.

The objective of this study is to examine the feasibility and effects of LMD laser system and corresponding processing parameters on the surface polishing. On the other hand, Inconel alloys are very hard and difficult to be polished by conventional techniques, while their production using LMD techniques is increasing. Accordingly, the surface polishing of the Inconel samples using laser ability was the subject of this study. To do so, a series of block samples of Inconel 718 was produced using the LMD process. The top surface of the samples was laser scanned using a combination of laser power, scanning speed and beam spot size. The surface roughness of the samples was evaluated and subsequently, optimum process parameters for laser polishing were predicted using analytical experimental design (DoE) software.

### 12.1.2. Material and experimental procedure

Commercially available gas-atomised Inconel 718 powder was supplied with a particle size range of 20-50  $\mu\text{m}$ . An array of test blocks of 15 mm  $\times$  15 mm  $\times$  2 mm was deposited onto a stainless steel substrate. The deposition trials and laser polishing were carried out using a Trumpf DMD505 laser deposition system with a 1.8 kW HQ CO<sub>2</sub> laser unit, installed at TWI Ltd (UK). During processing, the powder was uniformly fed into a co-axial nozzle, deposition is undertaken from the inverted apex of the powder stream leaving the nozzle, between the annulus of the inner and outer cones. This is schematically shown in Fig. 12.1. This process was carried out using localised argon shielding to prevent oxidation.

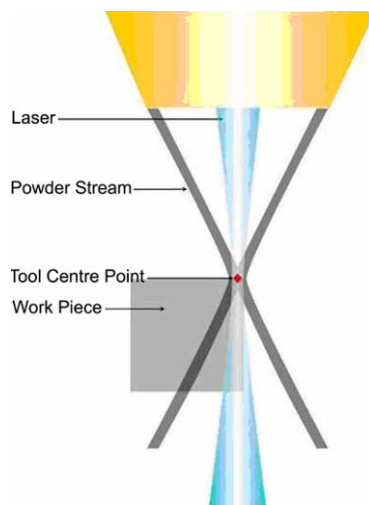


**Fig. 12.1:** The schematic of LMD process, in which the deposition is undertaken at the tool centre point, courtesy of TWI.

There are many variables in the DMD machine influencing the microstructure and mechanical properties of the resulting part, such as laser power, powder feed rate, beam feed rate (laser scanning speed), laser beam spot diameter and etc. A combination of DMD parameters of laser power = 450 W (340 W at the work-piece), beam feed rate = 1200 mm/min, and powder feed rate = 2.5 g/min, beam spot diameter = 0.5 mm, and track spacing = 0.4 mm (35% overlap) were used to deposit an array of 18 Inconel blocks. After that, laser scanning was carried out on the deposited parts, using the parameters shown in Table 12.1, and each block received two scans. Among all the deposited parts, one part was not laser scanned to remain as the reference or as-deposited state. The visual image of deposited parts after the polishing operation is shown in Fig. 12.2 (sample 18 is the reference with no surface polishing).

**Table 12.1:** The laser parameters used for surface polishing of LMD parts

Test No.	Power (W)	Beam feed rate (mm/min)	Beam spot size (mm)
1	400	1263	0.7
2	400	1000	0.3
3	500	800	1.0
4	400	1000	0.7
5	300	1200	0.5
6	300	800	0.5
7	400	1000	1.1
8	500	1200	0.5
9	300	800	1.0
10	400	1000	0.7
11	532	1000	0.7
12	500	1200	1.0
13	268	1000	0.7
14	500	800	0.5
15	300	1200	1.0
16	400	1000	0.7
17	400	737	0.7
18 (Ref.)	-	-	-

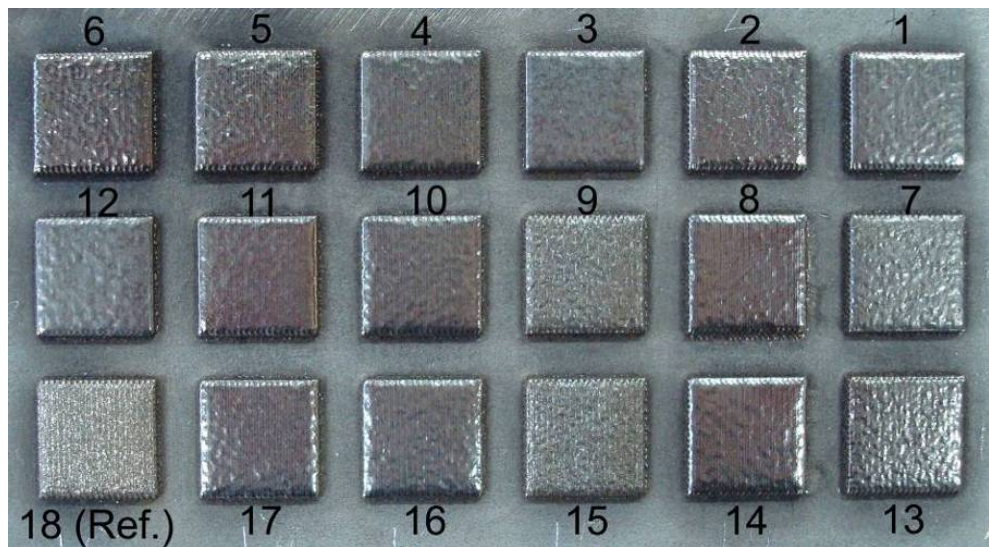


**Fig. 12.2:** Visual appearance of the surface finish after laser polishing of Inconel LMD parts (sample 18 is the reference with no surface polishing).

The surface roughness was measured in both 2D and 3D mode, providing profiles and roughness parameters of  $R_a$  and  $S_a$  respectively. Finally, a statistical design of experiments (based on analytical software Design Expert®) was used to assess the effect of different processing parameters on the laser polishing of the laser deposited samples.

### 12.1.3. Results and discussion

The parts produced by commercial LMD machines such as DMD often require further post-processing operations to reach acceptable part surface finish. The surface finish of a part can even be critical in many applications because it can induce catastrophic failure from surface initiated cracking (Mumtaz and Hopkinson, 2010) and may be required to achieve adequate geometrical accuracy (Brinksmeier et al., 2004). Generally, the top surface of a solidified melt pool may exhibit an undulating and rough texture (see sample 18 [reference for as-deposited state] in Fig 12.2). Repetition of laser scanning can influence the surface finish since the surface of material can be remelted, evaporated, or fused, depending on the material itself and the laser parameters (Bol'shepaev and Katomin, 1997, Lamikiz et al., 2007). With regard to this phenomenon, a repeated scanning on the surface of Inconel samples was performed which changed the surface quality, in contrast with sample 18 (Ref.), which was untouched sample after LMD fabrication: the latter shows a clearly rougher surface compared to other samples shown in Fig. 12.2. To be clearer, Fig. 12.3 presents the surface roughness parameters of the parts after laser polishing. As

expected, the overall surface roughness of the samples after additional laser scanning is effectively lower than that of the as-deposited one (sample 18), showing the effectiveness of polishing process using additional laser scanning. For example, it can be seen that the roughness parameters of the initial surface (sample 18),  $R_a$  (X) = 9.85  $\mu\text{m}$ ,  $R_a$  (Y) = 7.41  $\mu\text{m}$  and  $S_a$  = 23.5  $\mu\text{m}$ , are respectively 374%, 286% and 185% higher than those of sample 3. The corresponding profiles of these samples are shown in Fig. 12.4 for giving a comparative physical idea in 2D and 3D between the mentioned samples.

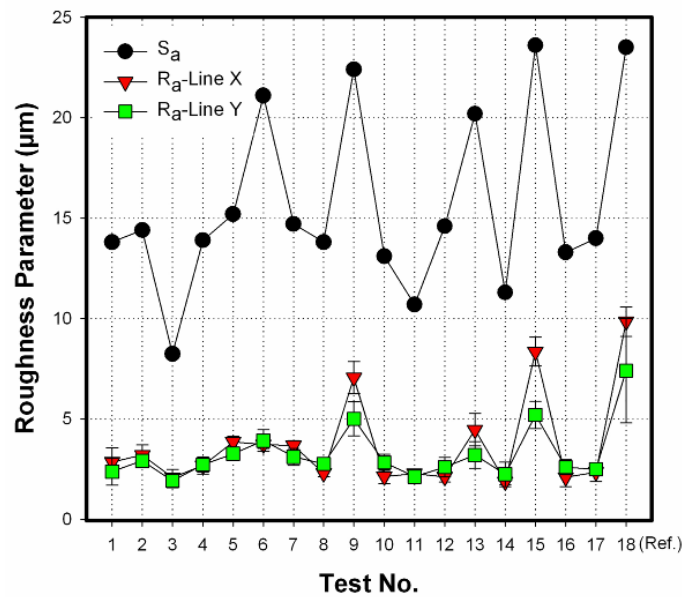


**Fig. 12.3:** 2D ( $R_a$ ) and 3D ( $S_a$ ) roughness parameters of laser polished surface (sample 18 (Ref.) is the sample that was untouched after fabrication).

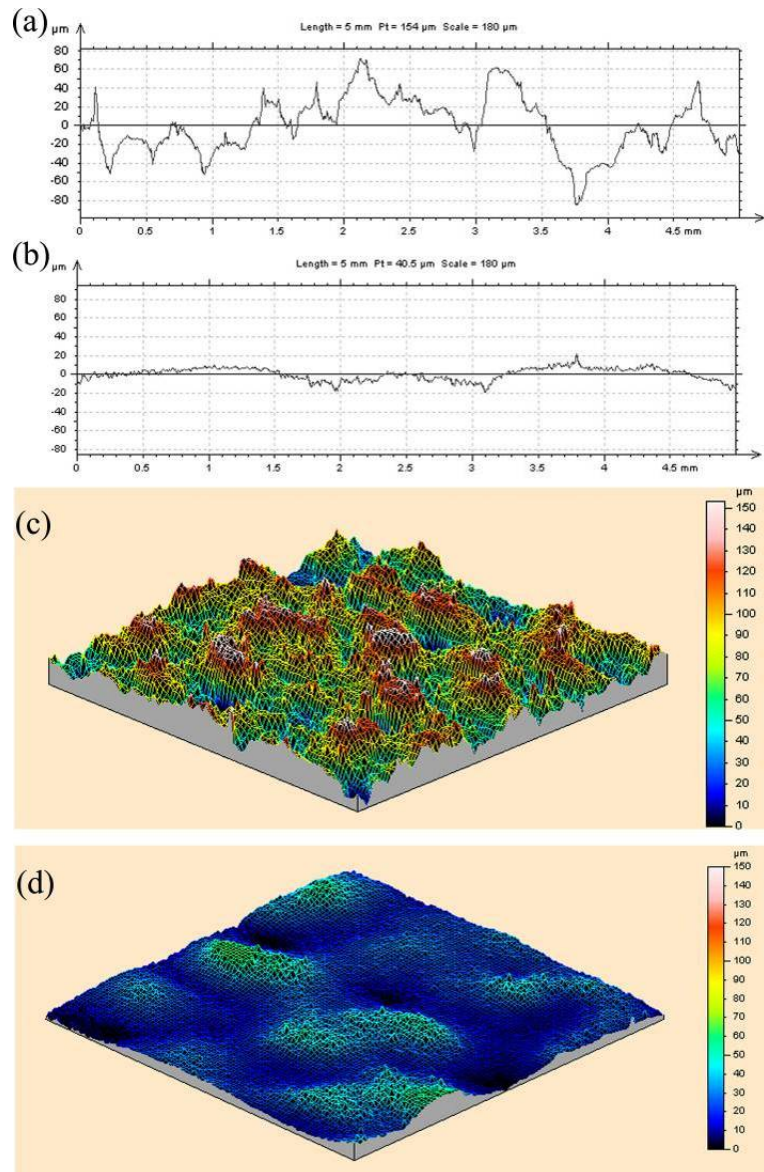


**Fig. 12.4:** Typical 2D and 3D roughness profiles of (a) and (c) sample 18 (Ref.), and (b) and (d) sample 3, respectively.

The results of these tests produced a good basis for DoE generation to investigate the trend of  $R_a$  responses to laser polishing. So, the DoE diagrams for  $R_a$  (X-direction) were obtained using factors of laser power and scanning speed with different beam spot sizes of 1.0, 0.7 and 0.3 mm, respectively. The results, shown in Fig. 12.5, illustrate that the surface quality is improved using 500 W laser power and 800 mm/min speed. Comparison of Figs. 12.5a to 12.5c shows that the beam spot size (in the range of 0.3-1.0 mm) is not a very critical factor for surface polishing as compared to stronger factors like laser power and scanning speed. However, it does affect the surface quality, e.g. beam spot size of 0.7 mm

(Fig. 12.5b) may lead to a better surface finish which means there is an optimum value for spot size. This is in confirmation with the work of Aiyiti et al. (2006) on micro-plasma arc welding, emphasising overlapping influence the surface roughness. They explained that not only big distance between tracks increases the surface roughness, but also too close tracks lead to a greater thickness of the latter tracks than former tracks resulting in a poor surface finish. Therefore, there is an optimum overlap to form a smooth finish. However, the optimum process parameters, predicted using the DoE, are a laser power of at least 500 W and speed of 800-850 mm/min, achieving a  $R_a$  below 2  $\mu\text{m}$  or so.

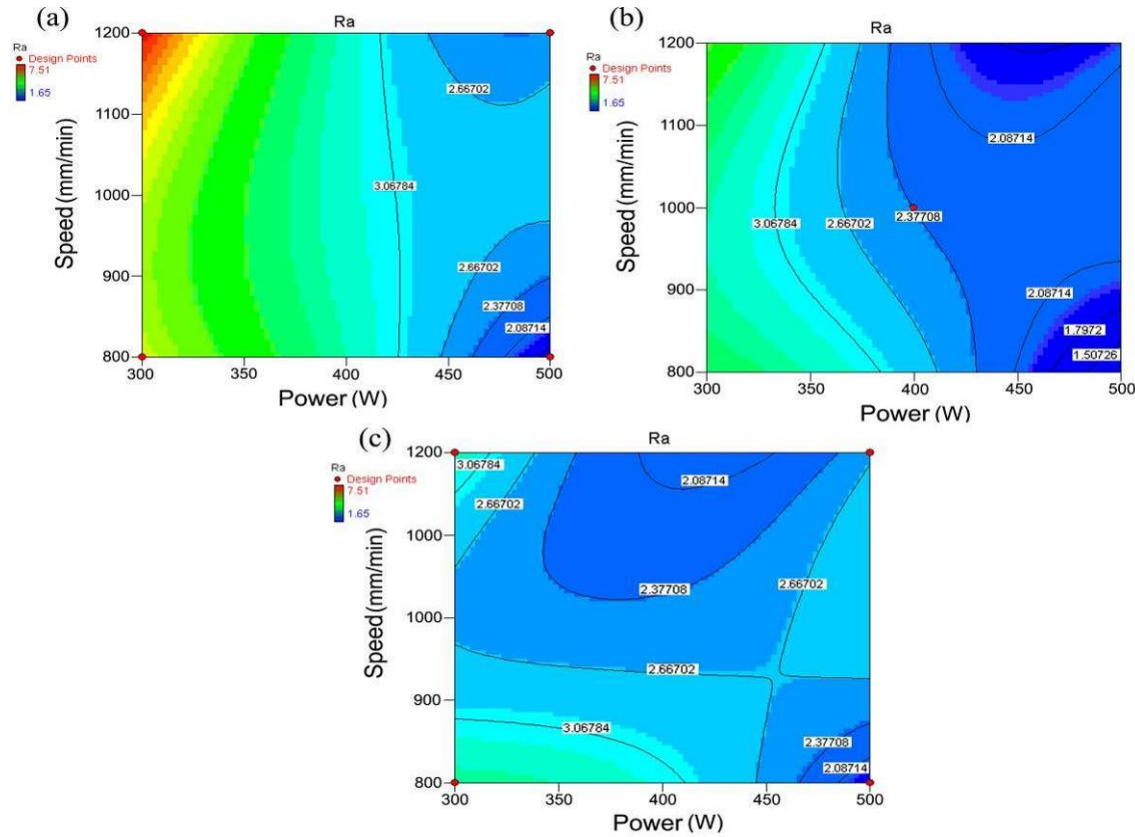


**Fig. 12.5:** Linear roughness predicted using Design Expert software, using beam spot size of (a) 1.0 mm, (b) 0.7 mm and (c) 0.3 mm

The laser-polishing process is based on superficial melting (and/or vaporisation) on a microscopic scale followed by a rapid re-solidification. This leads to filling the microvalleys through flowing molten material. However, to achieve a smoother surface, the molten material should be sufficient to fill the roughness peaks, but not so much as to destroy the surface quality. Thus, the laser beam energy must be carefully studied and controlled to successfully melt a microscopic layer without damaging the surface. The laser energy density ( $\text{J/cm}^2$ ) can be calculated through the following equation:

$$E = \frac{6000P}{DV_f} \quad (\text{Eq. 12.1})$$

where P is the laser power (W), D is the beam diameter (mm) and V<sub>f</sub> is the beam feed rate (laser speed) (mm/min) (Lamikiz et al., 2007, Marinescu et al., 2008, Ukar et al., 2010). Fig. 12.6 plots the experimental surface roughness measurements vs. the energy density, calculated from Eq. 12.1 using the parameters of Table 12.1. The results show that the increase of laser energy is first accompanied with sharp reduction in surface roughness until it reaches a relatively constant level. This is particularly significant since the laser parameters such as feed rate, laser power and beam diameter can be selected to obtain the maximum productivity, while they satisfy the optimum laser energy as well. However, some dispersion in the results can be observed. This dispersion is natural since the initial surface topography (as one of the main parameters) can be slightly different from one sample to another after deposition process.

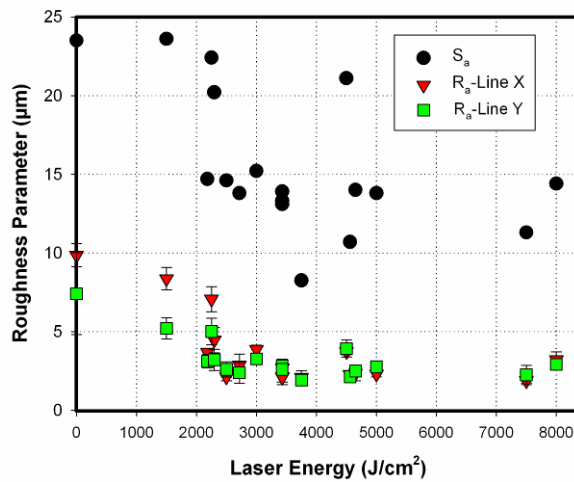


**Fig. 12.6:** Roughness characteristics of the surface as a function of laser energy density

To explain the trend of surface roughness with increase of laser energy, seen in Fig. 12.6, the mechanisms involved interaction of laser with surface should be studied. Two main mechanisms taking place during laser processing are i) Surface Shallow Melting (SSM) and ii) Surface Over Melting (SOM), occurring in different levels according to material and laser parameters such as power and feed rate. In the SSM, a thin material layer is melted (happening with high laser speed). So, the peaks and aggregated spheres of particles are melted filling valleys in between, resulting in a smoother surface. SOM, but, happens due to too high energy density. This melts the layers deep down the surface

valleys, resulting in an increase in surface roughness (Lamikiz et al., 2007, Marinescu et al., 2008). However, in this work the surface of high melting temperature Inconel has been scanned using high laser speed. The relatively high laser speed plus high melting temperature of the material can restrict the melting to the surface layers. So, the laser has melted peaks and smoothes valleys of surface (SSM mechanism), and increasing the laser energy has been useful to an extent to complete the melting of the surface layers. After that the higher laser energy can not be helpful to further smoothen the surface layer. Further increase in laser speed may even damage the substrate surface under strong laser irradiation as mentioned in SOM mechanism (Hsu and Lin, 2005, Marinescu et al., 2008) (this might be happening with further laser energies which have not been experimented in this work).

This study has proved the feasibility of laser surface polishing of ALM/LMD Inconel parts. It should be theoretically applicable to a wide range of metals and alloys, though material behaviour under laser polishing might be varied. Further development of laser polishing for other metal systems is a subject for future work. Moreover, this work has demonstrated the laser polishing effect using flat upward facing surfaces in order to simplify this study. As laser surface polishing is a non-contact and flexible technique, it will be able to be integrated with robot or 5 axis system to treat complicated surface geometries. This promising result of this study has built a good foundation for future process development.

#### **12.1.4. Conclusions**

This study investigated the feasibility of a laser-polishing process for metallic parts, which opens up promising perspectives for this technology in many applications. The results clearly show that improvements in the surface finish of an Inconel 718 produced by LMD is possible using a proper application of laser to the part surface. The experimental results demonstrated the effective surface improvement by laser polishing, and they provided the basis for DoE experimental procedure. The optimum process parameters developed by DoE showed that a laser power of 500 W and a laser speed of 800-850 mm/min can effectively reduce the surface roughness to below  $R_a = 2 \mu\text{m}$  (an acceptable level for many applications, including those in aerospace), which is about 80% less than that of the initial surface roughness. It also seems that there is an optimum value for beam spot diameter depending on applied track spacing to form a smoother surface finish.

The laser energy was shown as a strong factor influencing surface finish in laser polishing. It was established that surface roughness reduced significantly with the energy density reaching a minimum and relatively constant level. However, the results indicated that after choosing optimum energy density, parameters such as feed rate, laser power and spot diameter can be selected to meet at the optimum laser energy and obtain the maximum overall productivity.

Although the laser polishing was only applied to Inconel 718 alloy in this work, in principle it should be applicable to a wide range of metals and alloys. There is much promising research regarding parameters and mechanisms involved in laser polishing of different materials. Moreover, this study only investigated the laser polishing of flat surfaces, while the effect of laser polishing on different geometries, as well as sharp edges and corners, represents another rewarding area for future study.

## Future Work Recommendations

The following titles, suggestions, recommendations, and directions are outlined for improving the present work:

- *In-situ thermal phenomena studies facilitated by infrared camera:* Infrared camera inside SLM machine can be used to map the temperature and subsequently cooling rate during the process. This can give a clear idea of the effect of additive composition on melting and solidification during SLM. This facilitates the understanding of in-situ thermal phenomena and unique microstructures that form due to laser assisted in-situ reaction.
- *Modelling of melting, solidification and microstructural evolution of in-situ SLM processes using numerical methods such as FDM and FEM:* Modelling of processes is nowadays very common to predict the effect of variables or to describe the unexamined systems by generalisation. The numerical tools (e.g. FEM) can be used to model the thermal phenomena (such as melting and solidification) or the resultant properties (such as microstructure) of in-situ assisted SLM processes in pre-described material systems. Such model can be very helpful for engineers to successfully apply the SLM for fabricating parts from different powder systems.
- *Usage of high laser power SLM machine to achieve dense in-situ formed particle Al matrix composites for aerospace/automotive applications:* The main drawback of the produced in-situ formed particle Al matrix composites was high porosity which restricts its applications in various sectors including aerospace and automotive industries. This drawback should be resolvable by the use of new high laser power SLM machines. The production of dense in-situ formed particle Al matrix composites using SLM process opens numerous industrial applications in such a manner that it may become a common product in future.
- *Experimental and analytical investigations to describe the behaviour of in-situ formed particle Al matrix composites under impact and deformation in light of crystal plasticity:* The in-situ formed particle Al matrix composites made by SLM process appear with unique microstructures. The behaviour of these novel microstructures under deformation (e.g. impact, fatigue, tension, compression, torsion, etc) should be tested and studied. The crystal plasticity knowledge can

facilitate these scientific studies. Such knowledge greatly assists development of such components in various industries.

- *Further studies on heterogeneous nucleation, during SLM production of in-situ formed particle MMCs, and resultant amorphous/nanoscale/ultrafine microstructures:* The present research showed the ability of the process to produce nanoscale/ultrafine in-situ formed particles inside featureless/nanoscale Al matrix. This is a good start for manufacturing actual net shape MMC parts with amorphous/nanoscale/ultrafine microstructures. Further studies can be directed to development of these microstructures which nowadays is of great interest of researchers/engineers.
- *Investigation of new in-situ material systems to produce novel advanced composites:* In this research, we introduced Al/Fe<sub>2</sub>O<sub>3</sub> as materials system which could lead to production of in-situ composites after SLM process. In addition to this system, there are many other systems composing of different base metals (e.g. Al, Ti, etc) and additives (e.g. metallic and nonmetallic oxides, intermetallics, etc) which have the potential to be combined and produce new in-situ composites. The constituents can be selected regarding the aim of the research which can be a composite with certain physical properties such as low thermal coefficient or with desirable mechanical properties such as high strength.

## References

- Abe, F., Osakada, K., Shiomi, M., Uematsu, K. & Matsumoto, M. (2001) The manufacturing of hard tools from metallic powders by selective laser melting. *Journal of Materials Processing Technology*, 111, 210-213.
- Agarwala, M., Bourell, D., Beaman, J., Marcus, H. & Barlow, J. (1995) Post-processing of selective laser sintered metal parts. *Rapid Prototyping Journal*, 1, 36-44.
- Aiyiti, W., Zhao, W., Lu, B. & Tang, Y. (2006) Investigation of the overlapping parameters of MPAW-based rapid prototyping. *Rapid Prototyping Journal*, 12, 165-172.
- Allen, C. M., O'Reilly, K. A. Q. & Cantor, B. (2001) Effect of semisolid microstructure on solidified phase content in 1xxx Al alloys. *Acta Materialia*, 49, 1549-1563.
- Ashby, M. F. (2005) Materials selection in mechanical design. 3rd ed. Amsterdam; Boston, Butterworth-Heinemann.
- ASM Handbook (1992) *Nondestructive evaluation and quality control*, Metals Park, Ohio, American Society for Metals.
- ASM International Handbook Committee (1990) *Vol. 1, Properties and selection: irons, steels, and high-performance alloys*, Materials Park, OH, ASM International.
- ASM International Handbook Committee (1992) *Vol.2, Properties and selection: nonferrous alloys and special-purpose materials*, Metals Park, Ohio, American Society for Metals (ASM) International.
- ASM International Handbook Committee (1998) *Powder metal technologies and applications*, Materials Park, OH, ASM International.
- Asta, M., Beckermann, C., Karma, A., Kurz, W., Napolitano, R., Plapp, M., Purdy, G., Rappaz, M. & Trivedi, R. (2009) Solidification microstructures and solid-state parallels: Recent developments, future directions. *Acta Materialia*, 57, 941-971.
- ASTM (2004) *Annual book of ASTM standards. vol. 03.01, Metals-mechanical testing ; elevated and low temperature tests ; metallography section 3 Metals test methods and analytical procedures*, Philadelphia, Pa., American Society for Testing and Materials.
- ASTM Standard B311 (2005) *Test Method for Density Determination for Powder Metallurgy (P/M) Materials Containing Less Than Two Percent Porosity*, West Conshohocken, Pa., ASTM International.
- Atkinson, H. V., Zulfia, A., Lima Filho, A., Jones, H. & King, S. (1997) Hot isostatic processing of metal matrix composites. *Materials & Design*, 18, 243-245.
- Badrossamay, M. & Childs, T. H. C. (2007) Further studies in selective laser melting of stainless and tool steel powders. *International Journal of Machine Tools and Manufacture*, 47, 779-784.
- Bartkowiak, K., Ullrich, S., Frick, T. & Schmidt, M. (2011) New Developments of Laser Processing Aluminium Alloys via Additive Manufacturing Technique. *Physics Procedia*, 12, Part A, 393-401.

- Bergström, D., Powell, J. & Kaplan, A. F. H. (2007) The absorptance of steels to Nd:YLF and Nd:YAG laser light at room temperature. *Applied Surface Science*, 253, 5017-5028.
- Billard, S., Fondère, J. P., Bacroix, B. & Dirras, G. F. (2006) Macroscopic and microscopic aspects of the deformation and fracture mechanisms of ultrafine-grained aluminum processed by hot isostatic pressing. *Acta Materialia*, 54, 411-421.
- Birol, Y. (1996) Microstructural characterization of a rapidly-solidified Al-12 wt% Si alloy. *Journal of Materials Science*, 31, 2139-2143.
- Bocanegra-Bernal, M. H. (2004) Hot Isostatic Pressing (HIP) technology and its applications to metals and ceramics. *Journal of Materials Science*, 39, 6399-6420.
- Bol'shepaev, O. Y. & Katomin, N. N. (1997) Laser polishing of glass articles. *Glass and Ceramics*, 54, 141-142.
- Bourell, D. L. (2006) Materials Issues in Rapid Manufacturing. IN HOPKINSON, N., HAGUE, R. J. M. & DICKENS, P. M. (Eds.) *Rapid manufacturing : an industrial revolution for the digital age*. Chichester, England, John Wiley.
- Brandl, E., Heckenberger, U., Holzinger, V. & Buchbinder, D. (2012) Additive manufactured AlSi10Mg samples using Selective Laser Melting (SLM): Microstructure, high cycle fatigue, and fracture behavior. *Materials & Design*, 34, 159-169.
- Brinksmeier, E., Riemer, O., Gessnerharter, A. & Autschbach, L. (2004) Polishing of Structured Molds. *CIRP Annals - Manufacturing Technology*, 53, 247-250.
- Buchbinder, D., Schleifenbaum, H., Heidrich, S., Meiners, W. & Bültmann, J. (2011) High Power Selective Laser Melting (HP SLM) of Aluminum Parts. *Physics Procedia*, 12, Part A, 271-278.
- Callister, W. D. (2007) *Materials science and engineering : an introduction*, New York, John Wiley & Sons.
- Campbell, J. (2003) *Castings*, Oxford, Butterworth-Heinemann.
- Capello, E. & Previtali, B. (2006) The influence of operator skills, process parameters and materials on clad shape in repair using laser cladding by wire. *Journal of Materials Processing Technology*, 174, 223-232.
- Chang, W. & Na, S. (2002) A study on heat source equations for the prediction of weld shape and thermal deformation in laser microwelding. *Metallurgical and Materials Transactions B*, 33, 757-764.
- Childs, T. H. C., Hauser, C. & Badrossamay, M. (2004) Mapping and Modelling Single Scan Track Formation in Direct Metal Selective Laser Melting. *CIRP Annals - Manufacturing Technology*, 53, 191-194.
- Chowdhury, S., Chen, D., Bhole, S., Powidajko, E., Weckman, D. & Zhou, Y. (2011) Microstructure and Mechanical Properties of Fiber-Laser-Welded and Diode-Laser-Welded AZ31 Magnesium Alloy. *Metallurgical and Materials Transactions A*, 42, 1974-1989.
- Clare, A., Chalker, P., Davies, S., Sutcliffe, C. & Tsopanos, S. (2008) Selective laser melting of high aspect ratio 3D nickel-titanium structures two way trained for

- MEMS applications. *International Journal of Mechanics and Materials in Design*, 4, 181-187.
- DeLo, D. P. & Piehler, H. R. (1999) Early stage consolidation mechanisms during hot isostatic pressing of Ti-6Al-4V powder compacts. *Acta Materialia*, 47, 2841-2852.
- Dieter, G. E. (1986) *Mechanical metallurgy*, New York, McGraw-Hill.
- Dirras, G., Gubicza, J., Tingaud, D. & Billard, S. (2011) Microstructure of Al-Al<sub>2</sub>O<sub>3</sub> nanocomposite formed by in situ phase transformation during Al nanopowder consolidation. *Materials Chemistry and Physics*, 129, 846-852.
- Dong, L., Makradi, A., Ahzi, S. & Remond, Y. (2009) Three-dimensional transient finite element analysis of the selective laser sintering process. *Journal of Materials Processing Technology*, 209, 700-706.
- Durães, L., Costa, B. F. O., Santos, R., Correia, A., Campos, J. & Portugal, A. (2007) Fe<sub>2</sub>O<sub>3</sub>/aluminum thermite reaction intermediate and final products characterization. *Materials Science and Engineering: A*, 465, 199-210.
- Fan, R.-H., Lü, H.-L., Sun, K.-N., Wang, W.-X. & Yi, X.-B. (2006) Kinetics of thermite reaction in Al-Fe<sub>2</sub>O<sub>3</sub> system. *Thermochimica Acta*, 440, 129-131.
- Fan, T., Zhang, D., Yang, G., Shibayanagi, T. & Naka, M. (2003) Fabrication of in situ Al<sub>2</sub>O<sub>3</sub>/Al composite via remelting. *Journal of Materials Processing Technology*, 142, 556-561.
- Filho, A. L., Atkinson, H., Jones, H., De Los Rios, E. & King, S. (1998) Hot isostatic pressing of metal reinforced metal matrix composites. *Journal of Materials Science*, 33, 5517-5533.
- Fischer, P., Romano, V., Weber, H. P., Karapatis, N. P., Boillat, E. & Glardon, R. (2003) Sintering of commercially pure titanium powder with a Nd:YAG laser source. *Acta Materialia*, 51, 1651-1662.
- Foot, C. J. (2006) *Atomic physics*, Oxford [u.a.], Oxford Univ. Press.
- Fox, P., Pogson, S., Sutcliffe, C. J. & Jones, E. (2008) Interface interactions between porous titanium/tantalum coatings, produced by Selective Laser Melting (SLM), on a cobalt-chromium alloy. *Surface and Coatings Technology*, 202, 5001-5007.
- Franco, A., Lanzetta, M. & Romoli, L. (2010) Experimental analysis of selective laser sintering of polyamide powders: an energy perspective. *Journal of Cleaner Production*, 18, 1722-1730.
- Fu, G.-f., Zhang, J.-x., Liu, J. & Wang, Z.-f. (2006a) Wear behavior of Al-Si alloy matrix composites reinforced by  $\gamma$ -Al<sub>2</sub>O<sub>3</sub> decomposed from AACM. *Transactions of Nonferrous Metals Society of China*, 16, 1159-1162.
- Fu, G., Jiang, L., Liu, J. & Wang, Y. (2006b) Fabrication and properties of Al matrix composites strengthened by in situ alumina particulates. *Journal of University of Science and Technology Beijing, Mineral, Metallurgy, Material*, 13, 263-266.
- Gåård, A., Krakhmalev, P. & Bergström, J. (2006) Microstructural characterization and wear behavior of (Fe,Ni)-TiC MMC prepared by DMLS. *Journal of Alloys and Compounds*, 421, 166-171.

- Gao, K. Y. & Liu, B. X. (1997) Surface hardening of Al by high current Fe-ion implantation. *Journal of Applied Physics*, 82, 2209-2214.
- Ghosh, S. K., Saha, P. & Kishore, S. (2010) Influence of size and volume fraction of SiC particulates on properties of ex situ reinforced Al-4.5Cu-3Mg metal matrix composite prepared by direct metal laser sintering process. *Materials Science and Engineering: A*, 527, 4694-4701.
- Gilgien, P., Zryd, A. & Kurz, W. (1995) Microstructure selection maps for Al-Fe alloys. *Acta Metallurgica et Materialia*, 43, 3477-3487.
- Griger, Á. & Stefániay, V. (1996) Equilibrium and non-equilibrium intermetallic phases in Al-Fe and Al-Fe-Si Alloys. *Journal of Materials Science*, 31, 6645-6652.
- Gu, D., Hagedorn, Y.-C., Meiners, W., Wissenbach, K. & Poprawe, R. (2011a) Nanocrystalline TiC reinforced Ti matrix bulk-form nanocomposites by Selective Laser Melting (SLM): Densification, growth mechanism and wear behavior. *Composites Science and Technology*, 71, 1612-1620.
- Gu, D., Hagedorn, Y.-C., Meiners, W., Wissenbach, K. & Poprawe, R. (2011b) Selective Laser Melting of in-situ TiC/Ti<sub>5</sub>Si<sub>3</sub> composites with novel reinforcement architecture and elevated performance. *Surface and Coatings Technology*, 205, 3285-3292.
- Gu, D. & Shen, Y. (2006) Processing and microstructure of submicron WC-Co particulate reinforced Cu matrix composites prepared by direct laser sintering. *Materials Science and Engineering: A*, 435-436, 54-61.
- Gu, D. & Shen, Y. (2009a) Effects of processing parameters on consolidation and microstructure of W-Cu components by DMLS. *Journal of Alloys and Compounds*, 473, 107-115.
- Gu, D. & Shen, Y. (2009b) Balling phenomena in direct laser sintering of stainless steel powder: Metallurgical mechanisms and control methods. *Materials & Design*, 30, 2903-2910.
- Gu, D., Shen, Y. & Lu, Z. (2009c) Preparation of TiN-Ti<sub>5</sub>Si<sub>3</sub> in-situ composites by Selective Laser Melting. *Materials Letters*, 63, 1577-1579.
- Gu, D., Shen, Y., Zhao, L., Xiao, J., Wu, P. & Zhu, Y. (2007) Effect of rare earth oxide addition on microstructures of ultra-fine WC-Co particulate reinforced Cu matrix composites prepared by direct laser sintering. *Materials Science and Engineering: A*, 445-446, 316-322.
- Gu, D., Wang, Z., Shen, Y., Li, Q. & Li, Y. (2009d) In-situ TiC particle reinforced Ti-Al matrix composites: Powder preparation by mechanical alloying and Selective Laser Melting behavior. *Applied Surface Science*, 255, 9230-9240.
- Gu, D. D., Shen, Y. F., Yang, J. L. & Wang, Y. (2006) Effects of processing parameters on direct laser sintering of multicomponent Cu based metal powder. *Materials Science and Technology*, 22, 1449-1455.
- Guduru, R. K., Darling, K. A., Kishore, R., Scattergood, R. O., Koch, C. C. & Murty, K. L. (2005) Evaluation of mechanical properties using shear-punch testing. *Materials Science and Engineering: A*, 395, 307-314.

- Hao, L., Dadbakhsh, S., Seaman, O. & Felstead, M. (2009) Selective laser melting of a stainless steel and hydroxyapatite composite for load-bearing implant development. *Journal of Materials Processing Technology*, 209, 5793-5801.
- Hao, L., Savalani, M. M., Zhang, Y., Tanner, K. E. & Harris, R. A. (2006) Selective laser sintering of hydroxyapatite reinforced polyethylene composites for bioactive implants and tissue scaffold development. *Proceedings of the Institution of Mechanical Engineers, Part H: Journal of Engineering in Medicine*, 220, 521-531.
- Hofmeister, W., Wert, M., Smugeresky, J., Philliber, J. A., Griffith, M. & Ensz, M. (1999) Investigating Solidification with the Laser-Engineered Net Shaping (LENS). *TMS JOM-e*.
- Hosford, W. F. (2005) Mechanical behavior of materials. New York, Cambridge University Press.
- Hsu, C. J., Chang, C. Y., Kao, P. W., Ho, N. J. & Chang, C. P. (2006) Al-Al<sub>3</sub>Ti nanocomposites produced in situ by friction stir processing. *Acta Materialia*, 54, 5241-5249.
- Hsu, H.-T. & Lin, J. (2005) Thermal-mechanical analysis of the surface waves in laser cleaning. *International Journal of Machine Tools and Manufacture*, 45, 979-985.
- Huskins, E. L., Cao, B. & Ramesh, K. T. (2010) Strengthening mechanisms in an Al-Mg alloy. *Materials Science and Engineering: A*, 527, 1292-1298.
- Ibrahim, I. A., Mohamed, F. A. & Lavernia, E. J. (1991) Particulate reinforced metal matrix composites - a review. *Journal of Materials Science*, 26, 1137-1156.
- Ion, J. C. (2005a) Chapter 6 - Laser Processing Diagrams. *Laser Processing of Engineering Materials*. Oxford, Butterworth-Heinemann.
- Ion, J. C. (2005b) Chapter 11 - Surface Melting. *Laser Processing of Engineering Materials*. Oxford, Butterworth-Heinemann.
- Jerrard, P., Hao, L. & Evans, K. E. (2009a) Selective laser melting of pure aluminium powder – A preliminary study. *10th National Conference on Rapid Design, Prototyping and Manufacturing*. UK.
- Jerrard, P. G. E., Hao, L., Dadbakhsh, S. & Evans, K. E. (2011) Consolidation behaviour and microstructural characteristics of Al and mixture of Al-Cu alloy powders following Selective Laser Melting processing. *Lasers in Engineering*, 22, 371-381.
- Jerrard, P. G. E., Hao, L. & Evans, K. E. (2009b) Experimental investigation into selective laser melting of austenitic and martensitic stainless steel powder mixtures. *Proceedings of the Institution of Mechanical Engineers, Part B: Journal of Engineering Manufacture*, 223, 1409-1416.
- Klocke, F. & Wagner, C. (2003) Coalescence behaviour of two metallic particles as base mechanism of selective laser sintering. *CIRP Annals - Manufacturing Technology*, 52, 177-180.
- Koechner, W. (2006) *Solid-state laser engineering*, Berlin; New York, Springer.
- Kruth, J. P., Froyen, L., Van Vaerenbergh, J., Mercelis, P., Rombouts, M. & Lauwers, B. (2004) Selective laser melting of iron-based powder. *Journal of Materials Processing Technology*, 149, 616-622.

- Kruth, J. P., Leu, M. C. & Nakagawa, T. (1998) Progress in Additive Manufacturing and Rapid Prototyping. *CIRP Annals - Manufacturing Technology*, 47, 525-540.
- Kruth, J. P., Levy, G., Klocke, F. & Childs, T. H. C. (2007) Consolidation phenomena in laser and powder-bed based layered manufacturing. *CIRP Annals - Manufacturing Technology*, 56, 730-759.
- Kruth, J. P., Mercelis, P., Van Vaerenbergh, J., Froyen, L. & Rombouts, M. (2005) Binding mechanisms in selective laser sintering and selective laser melting. *Rapid Prototyping Journal*, 11, 26-36.
- Kruth, J. P., Van der Schueren, B., Bonse, J. E. & Morren, B. (1996) Basic Powder Metallurgical Aspects in Selective Metal Powder Sintering. *CIRP Annals - Manufacturing Technology*, 45, 183-186.
- Kurt, A. & Ates, H. (2007) Effect of porosity on thermal conductivity of powder metal materials. *Materials & Design*, 28, 230-233.
- Lamikiz, A., Sanchez, J. A., López de Lacalle, L. N. & Arana, J. L. (2007) Laser polishing of parts built up by selective laser sintering. *International Journal of Machine Tools and Manufacture*, 47, 2040-2050.
- Lavernia, E. & Srivatsan, T. (2010) The rapid solidification processing of materials: science, principles, technology, advances, and applications. *Journal of Materials Science*, 45, 287-325.
- Lavernia, E. J., Ayers, J. D. & Srivatsan, T. S. (1992) Rapid solidification processing with specific application to aluminium alloys. *International Materials Reviews*, 37, 1-44.
- Leong, C. C., Lu, L., Fuh, J. Y. H. & Wong, Y. S. (2002) In-situ formation of copper matrix composites by laser sintering. *Materials Science and Engineering: A*, 338, 81-88.
- Levin, I., Bendersky, L. A., Brandon, D. G. & Rühle, M. (1997) Cubic to monoclinic phase transformations in alumina. *Acta Materialia*, 45, 3659-3669.
- Levin, I. & Brandon, D. (1998) Metastable alumina polymorphs: Crystal structures and transition sequences. *Journal of the American Ceramic Society*, 81, 1995-2012.
- Levy, G. N., Schindel, R. & Kruth, J. P. (2003) Rapid manufacturing and rapid tooling with layer manufacturing technologies: state of the art and future perspectives. *CIRP Annals - Manufacturing Technology*, 52, 589-609.
- Li, R., Shi, Y., Liu, J., Yao, H. & Zhang, W. (2009) Effects of processing parameters on the temperature field of selective laser melting metal powder. *Powder Metallurgy and Metal Ceramics*, 48, 186-195.
- Li, R., Shi, Y., Wang, Z., Wang, L., Liu, J. & Jiang, W. (2010) Densification behavior of gas and water atomized 316L stainless steel powder during selective laser melting. *Applied Surface Science*, 256, 4350-4356.
- Li, X. C., Stampfl, J. & Prinz, F. B. (2000) Mechanical and thermal expansion behavior of laser deposited metal matrix composites of Invar and TiC. *Materials Science and Engineering: A*, 282, 86-90.
- Loh, N. L. & Sia, K. Y. (1992) An overview of hot isostatic pressing. *Journal of Materials Processing Technology*, 30, 45-65.

- Long, R.-s., Liu, W.-j., Xing, F. & Wang, H.-b. (2008) Numerical simulation of thermal behavior during laser metal deposition shaping. *Transactions of Nonferrous Metals Society of China*, 18, 691-699.
- Louvis, E., Fox, P. & Sutcliffe, C. J. (2011) Selective laser melting of aluminium components. *Journal of Materials Processing Technology*, 211, 275-284.
- Lu, L., Fuh, J. Y. H., Chen, Z. D., Leong, C. C. & Wong, Y. S. (2000) In situ formation of TiC composite using selective laser melting. *Materials Research Bulletin*, 35, 1555-1561.
- Lu, L., Lai, M. O. & Chen, F. L. (1997) Al-4 wt% Cu Composite reinforced with in-situ TiB<sub>2</sub> particles. *Acta Materialia*, 45, 4297-4309.
- Maity, P. C., Chakraborty, P. N. & Panigrahi, S. C. (1997) Al-Al<sub>2</sub>O<sub>3</sub> in situ particle composites by reaction of CuO particles in molten pure Al. *Materials Letters*, 30, 147-151.
- Marinescu, N., Ghiculescu, D. & Anger, C. (2008) Correlation between laser finishing technological parameters and materials absorption capacity. *International Journal of Material Forming*, 1, 1359-1362.
- Matsumoto, M., Shiomi, M., Osakada, K. & Abe, F. (2002) Finite element analysis of single layer forming on metallic powder bed in rapid prototyping by selective laser processing. *International Journal of Machine Tools and Manufacture*, 42, 61-67.
- McNulty, T. F., Mohammadi, F., Bandyopadhyay, A., Shanefield, D. J., Danforth, S. C. & Safari, A. (1998) Development of a binder formulation for fused deposition of ceramics. *Rapid Prototyping Journal*, 4, 144-150.
- Mei, J., Halldearn, R. D. & Xiao, P. (1999) Mechanisms of the aluminium-iron oxide thermite reaction. *Scripta Materialia*, 41, 541-548.
- Meiners, W., Wissenbach, K. & Gasser, A. (2001) Selective laser sintering at melting temperature. US 6215093.
- Melchels, F. P. W., Feijen, J. & Grijpma, D. W. (2010) A review on stereolithography and its applications in biomedical engineering. *Biomaterials*, 31, 6121-6130.
- Mercelis, P. & Kruth, J. P. (2006) Residual stresses in selective laser sintering and selective laser melting. *Rapid Prototyping Journal*, 12, 254-265.
- Miracle, D., Senkov, O., Miracle, D. & Firstov, S. (2004) Opportunities and Approaches for Doubling the Structural Efficiency of Metallic Materials. *Metallic Materials with High Structural Efficiency*. Springer Netherlands.
- Mohanty, P. S. & Mazumder, J. (1998) Solidification behavior and microstructural evolution during laser beam-material interaction. *Metallurgical and Materials Transactions B: Process Metallurgy and Materials Processing Science*, 29, 1269-1279.
- Morgan, R., Sutcliffe, C. J. & O'Neill, W. (2004) Density analysis of direct metal laser remelted 316L stainless steel cubic primitives. *Journal of Materials Science*, 39, 1195-1205.

- Mukherjee, S. K. & Bandyopadhyay, S. (1997) Mechanical and interfacial characterisation of Fe<sub>3</sub>Al and Fe<sub>3</sub>Al—Al<sub>2</sub>O<sub>3</sub> intermetallic composite made by mechanical smearing and hot isostatic pressing. *Composites Part B: Engineering*, 28, 45-48.
- Mumtaz, K. A., Erasenthiran, P. & Hopkinson, N. (2008) High density selective laser melting of Waspaloy®. *Journal of Materials Processing Technology*, 195, 77-87.
- Mumtaz, K. A. & Hopkinson, N. (2010) Selective Laser Melting of thin wall parts using pulse shaping. *Journal of Materials Processing Technology*, 210, 279-287.
- Nelson, J. C., Xue, S., Barlow, J. W., Beaman, J. J., Marcus, H. L. & Bourell, D. L. (1993) Model of the selective laser sintering of bisphenol-A polycarbonate. *Industrial & Engineering Chemistry Research*, 32, 2305-2317.
- Neugebauer, R., Mller, B., Gebauer, M. & Tppel, T. (2011) Additive manufacturing boosts efficiency of heat transfer components. *Assembly Automation*, 31, 344-347.
- Nickel, A. H., Barnett, D. M. & Prinz, F. B. (2001) Thermal stresses and deposition patterns in layered manufacturing. *Materials Science and Engineering: A*, 317, 59-64.
- Niu, H. J. & Chang, I. T. H. (1998) Liquid phase sintering of M3/2 high speed steel by selective laser sintering. *Scripta Materialia*, 39, 67-72.
- O'Neill, W., Sutcliffe, C. J., Morgan, R., Landsborough, A. & Hon, K. K. B. (1999) Investigation on Multi-Layer Direct Metal Laser Sintering of 316L Stainless Steel Powder Beds. *CIRP Annals - Manufacturing Technology*, 48, 151-154.
- Osakada, K. & Shiomi, M. (2006) Flexible manufacturing of metallic products by selective laser melting of powder. *International Journal of Machine Tools and Manufacture*, 46, 1188-1193.
- Perry, T. L., Werschmoeller, D., Li, X., Pfefferkorn, F. E. & Duffie, N. A. (2009) Pulsed laser polishing of micro-milled Ti6Al4V samples. *Journal of Manufacturing Processes*, 11, 74-81.
- Polmear, I. J. (2005) Wrought aluminium alloys. *Light Alloys*. Fourth ed. Oxford, Butterworth-Heinemann.
- Prabhakaran, R., Burkes, D. E., Wachs, D. M., Cole, J. I. & Charit, I. (2008) Small-Scale Specimen Testing of Monolithic U-Mo Fuel Foils. *RERTR 2008 Annual Meeting*. Washington, DC.
- Qi, H. B., Yan, Y. N., Lin, F. & Zhang, R. J. (2007) Scanning method of filling lines in electron beam selective melting. *Proceedings of the Institution of Mechanical Engineers, Part B: Journal of Engineering Manufacture*, 221, 1685-1694.
- Rajabi, M., Simchi, A., Vahidi, M. & Davami, P. (2008) Effect of particle size on the microstructure of rapidly solidified Al–20Si–5Fe–2X (X = Cu, Ni, Cr) powder. *Journal of Alloys and Compounds*, 466, 111-118.
- Ran, G., Zhou, J. n. & Wang, Q. G. (2006) The effect of hot isostatic pressing on the microstructure and tensile properties of an unmodified A356-T6 cast aluminum alloy. *Journal of Alloys and Compounds*, 421, 80-86.
- Rawal, S. (2001) Metal-matrix composites for space applications. *JOM*, 53, 14-17.

- Ready, J. F. & Farson, D. F. (2001) *LIA handbook of laser materials processing*, Orlando, FL, Laser Institute of America.
- Reeves, P. (2008) Direct Rapid Manufacturing of Metallic Parts - A UK Industry overview. Econolyst,  
[http://www.econolyst.co.uk/pdf/publications/Direct\\_metal\\_RM\\_processes.pdf](http://www.econolyst.co.uk/pdf/publications/Direct_metal_RM_processes.pdf).
- Rider, M. (1977) The shear strength of enamel - composite bonds. *Journal of Dentistry*, 5, 237-244.
- Rieker, C. & Morris, D. G. (1990) Heterogeneous nucleation during rapid solidification by laser surface melting. *Acta Metallurgica et Materialia*, 38, 1037-1043.
- Rombouts, M., Kruth, J. P., Froyen, L. & Mercelis, P. (2006) Fundamentals of Selective Laser Melting of alloyed steel powders. *CIRP Annals - Manufacturing Technology*, 55, 187-192.
- Salehi, M. & Dehghani, K. (2008) Structure and properties of nanostructured aluminum A413.1 produced by melt spinning compared with ingot microstructure. *Journal of Alloys and Compounds*, 457, 357-361.
- Sánchez-Amay, J. M., Delgado, T., González-Rovira, L. & Botana, F. J. (2009) Laser welding of aluminium alloys 5083 and 6082 under conduction regime. *Applied Surface Science*, 255, 9512-9521.
- Santos, E. C., Osakada, K., Shiomi, M., Kitamura, Y. & Abe, F. (2004) Microstructure and mechanical properties of pure titanium models fabricated by selective laser melting. *Proceedings of the Institution of Mechanical Engineers, Part C: Journal of Mechanical Engineering Science*, 218, 711-719.
- Sastray, K. Y., Froyen, L., Vleugels, J., Bentefour, E. H. & Glorieux, C. (2004) Effect of porosity on thermal conductivity of Al-Si-Fe-X alloy powder compacts. *International Journal of Thermophysics*, 25, 1611-1622.
- Savalani, M., Hao, L. & Harris, R. A. (2006) Evaluation of CO<sub>2</sub> and Nd:YAG lasers for the selective laser sintering of HAPEX. *Proceedings of the Institution of Mechanical Engineers, Part B: Journal of Engineering Manufacture*, 220, 171-182.
- Scaravetti, D., Dubois, P. & Duchamp, R. (2008) Qualification of rapid prototyping tools: proposition of a procedure and a test part. *The International Journal of Advanced Manufacturing Technology*, 38, 683-690.
- Sercombe, T. B. & Schaffer, G. B. (2004) On the role of magnesium and nitrogen in the infiltration of aluminium by aluminium for rapid prototyping applications. *Acta Materialia*, 52, 3019-3025.
- Sexton, L., Lavin, S., Byrne, G. & Kennedy, A. (2002) Laser cladding of aerospace materials. *Journal of Materials Processing Technology*, 122, 63-68.
- Seyed Reihani, S. M. (2006) Processing of squeeze cast Al6061–30vol% SiC composites and their characterization. *Materials & Design*, 27, 216-222.
- Shao, T. M., Hua, M., Tam, H. Y. & Cheung, E. H. M. (2005) An approach to modelling of laser polishing of metals. *Surface and Coatings Technology*, 197, 77-84.

- Shiomi, M., Osakada, K., Nakamura, K., Yamashita, T. & Abe, F. (2004) Residual Stress within Metallic Model Made by Selective Laser Melting Process. *CIRP Annals - Manufacturing Technology*, 53, 195-198.
- Silfvast, W. T. (1996) *Laser fundamentals*, Cambridge, Cambridge University Press.
- Silva, E. M. R., Monteiro, W. A., Rossi, W. & Lima, M. S. F. (2000) Absorption of Nd:YAG laser beam by metallic alloys. *Journal of Materials Science Letters*, 19, 2095-2097.
- Simchi, A. (2006) Direct laser sintering of metal powders: Mechanism, kinetics and microstructural features. *Materials Science and Engineering: A*, 428, 148-158.
- Simchi, A. & Pohl, H. (2003) Effects of laser sintering processing parameters on the microstructure and densification of iron powder. *Materials Science and Engineering: A*, 359, 119-128.
- Simchi, A. & Pohl, H. (2004) Direct laser sintering of iron-graphite powder mixture. *Materials Science and Engineering A*, 383, 191-200.
- Slocombe, A. & Li, L. (2001) Selective laser sintering of TiC-Al<sub>2</sub>O<sub>3</sub> composite with self-propagating high-temperature synthesis. *Journal of Materials Processing Technology*, 118, 173-178.
- Smallman, R. E. & Bishop, R. J. (1999) *Modern physical metallurgy and materials engineering*, Oxford, Butterworth-Heinemann.
- Soboyejo, W. O. (2003) *Mechanical properties of engineered materials*, New York, Marcel Dekker.
- Steen, W. M. (1991) *Laser material processing*, London, Springer.
- Steen, W. M. & Mazumder, J. (2010) Laser material processing. Fourth ed. London; New York, Springer.
- Subramanian, R., McKamey, C. G., Schneibel, J. H., Buck, L. R. & Menchhofer, P. A. (1998) Iron aluminide-Al<sub>2</sub>O<sub>3</sub> composites by in situ displacement reactions: processing and mechanical properties. *Materials Science and Engineering: A*, 254, 119-128.
- Surappa, M. K. (2003) Aluminium matrix composites: Challenges and opportunities. *Sadhana - Academy Proceedings in Engineering Sciences*, 28, 319-334.
- Swinkels, F. B., Wilkinson, D. S., Arzt, E. & Ashby, M. F. (1983) Mechanisms of hot-isostatic pressing. *Acta Metallurgica*, 31, 1829-1840.
- Takeshita, K. & Matsunawa, A. (2001) Numerical simulation of the molten-pool formation during the laser surface-melting process. *Metallurgical and Materials Transactions B*, 32, 949-959.
- Tang, F., Hagiwara, M. & Schoenung, J. M. (2005) Formation of coarse-grained interparticle regions during hot isostatic pressing of nanocrystalline powder. *Scripta Materialia*, 53, 619-624.
- Thijs, L., Verhaeghe, F., Craeghs, T., Humbeeck, J. V. & Kruth, J.-P. (2010) A study of the microstructural evolution during selective laser melting of Ti-6Al-4V. *Acta Materialia*, 58, 3303-3312.

- Tjong, S. C. & Ma, Z. Y. (2000) Microstructural and mechanical characteristics of in situ metal matrix composites. *Materials Science and Engineering R: Reports*, 29, 49-113.
- Tjong, S. C., Wang, G. S., Geng, L. & Mai, Y. W. (2004) Cyclic deformation behavior of in situ aluminum-matrix composites of the system Al-Al<sub>3</sub>Ti-TiB<sub>2</sub>-Al<sub>2</sub>O<sub>3</sub>. *Composites Science and Technology*, 64, 1971-1980.
- Tong, X. C. & Fang, H. S. (1998a) Al-TiC composites in situ-processed by ingot metallurgy and rapid solidification technology: Part I. Microstructural evolution. *Metallurgical and Materials Transactions A: Physical Metallurgy and Materials Science*, 29 A, 875-891.
- Tong, X. C. & Fang, H. S. (1998b) Al-TiC composites in situ-processed by ingot metallurgy and rapid solidification technology: Part II. Mechanical behavior. *Metallurgical and Materials Transactions A: Physical Metallurgy and Materials Science*, 29 A, 893-902.
- Toyserkani, E. & Khajepour, A. (2006) A mechatronics approach to laser powder deposition process. *Mechatronics*, 16, 631-641.
- Toyserkani, E., Khajepour, A. & Corbin, S. (2005) *Laser cladding*, Boca Raton, Fl., CRC Press.
- Triveño Rios, C., Peres, M. M., Bolfarini, C., Botta, W. J. & Kiminami, C. S. (2010) Microstructure and mechanical properties of Al-Si-Mg ribbons. *Journal of Alloys and Compounds*, 495, 386-390.
- Ukar, E., Lamikiz, A., López de Lacalle, L. N., del Pozo, D. & Arana, J. L. (2010) Laser polishing of tool steel with CO<sub>2</sub> laser and high-power diode laser. *International Journal of Machine Tools and Manufacture*, 50, 115-125.
- Uklejewski, R., Winiecki, M., Rogal, P. & Mielniczuk, J. (2011) Selective laser melted prototype of original minimally invasive resurfacing hip endoprosthesis. *Rapid Prototyping Journal*, 17, 76-85.
- Vandenbroucke, B. & Kruth, J. (2007) Selective laser melting of biocompatible metals for rapid manufacturing of medical parts. *Rapid Prototyping Journal*, 13, 196-203.
- Vandenbroucke, B. & Kruth, J. P. (2008) Direct Digital Manufacturing of Complex Dental Prostheses. IN BÁRTOLO, P. J. & BIDANDA, B. (Eds.) *Bio-Materials and Prototyping Applications in Medicine*. Springer US.
- Verhaeghe, F., Craeghs, T., Heulens, J. & Pandelaers, L. (2009) A pragmatic model for selective laser melting with evaporation. *Acta Materialia*, 57, 6006-6012.
- Wang, H. Y., Bourell, D. L. & Beaman Jr, J. J. (2003) Laser polishing of silica slotted rods. *Materials Science and Technology*, 19, 382-387.
- Wen, S. Y., Shin, Y. C., Murthy, J. Y. & Sojka, P. E. (2009) Modeling of coaxial powder flow for the laser direct deposition process. *International Journal of Heat and Mass Transfer*, 52, 5867-5877.
- Wong, T. T. & Liang, G. Y. (1997) Effect of laser melting treatment on the structure and corrosion behaviour of aluminium and AlSi alloys. *Journal of Materials Processing Technology*, 63, 930-934.

- Wong, T. T., Liang, G. Y. & Tang, C. Y. (1997) The surface character and substructure of aluminium alloys by laser-melting treatment. *Journal of Materials Processing Technology*, 66, 172-178.
- Wu, J. M. & Li, Z. Z. (2000) Nanostructured composite obtained by mechanically driven reduction reaction of CuO and Al powder mixture. *Journal of Alloys and Compounds*, 299, 9-16.
- Xie, J. W., Fox, P., O'Neill, W. & Sutcliffe, C. J. (2005) Effect of direct laser re-melting processing parameters and scanning strategies on the densification of tool steels. *Journal of Materials Processing Technology*, 170, 516-523.
- Yadroitsev, I., Thivillon, L., Bertrand, P. & Smurov, I. (2007) Strategy of manufacturing components with designed internal structure by selective laser melting of metallic powder. *Applied Surface Science*, 254, 980-983.
- Yan, C., Lifeng, W. & Jianyue, R. (2008) Multi-functional SiC/Al Composites for Aerospace Applications. *Chinese Journal of Aeronautics*, 21, 578-584.
- Yan, X. & Gu, P. (1996) A review of rapid prototyping technologies and systems. *Computer-Aided Design*, 28, 307-318.
- Yan, Y., Li, S., Zhang, R., Lin, F., Wu, R., Lu, Q., Xiong, Z. & Wang, X. (2009) Rapid Prototyping and Manufacturing Technology: Principle, Representative Techniques, Applications, and Development Trends. *Tsinghua Science & Technology*, 14, Supplement 1, 1-12.
- Yang, J., La, P., Liu, W. & Hao, Y. (2004) Microstructure and properties of Fe<sub>3</sub>Al-Fe<sub>3</sub>AlC<sub>0.5</sub> composites prepared by self-propagating high temperature synthesis casting. *Materials Science and Engineering: A*, 382, 8-14.
- Yasa, E., Deckers, J. & Kruth, J.-P. (2011) The investigation of the influence of laser re-melting on density, surface quality and microstructure of selective laser melting parts. *Rapid Prototyping Journal*, 17, 312-327.
- Yu, P., Deng, C.-J., Ma, N.-G. & Ng, D. H. L. (2004) A new method of producing uniformly distributed alumina particles in Al-based metal matrix composite. *Materials Letters*, 58, 679-682.
- Yu, P., Deng, C.-J., Ma, N.-G., Yau, M.-Y. & Ng, D. H. L. (2003) Formation of nanostructured eutectic network in  $\alpha$ -Al<sub>2</sub>O<sub>3</sub> reinforced Al-Cu alloy matrix composite. *Acta Materialia*, 51, 3445-3454.
- Zaeh, M. & Branner, G. (2010) Investigations on residual stresses and deformations in selective laser melting. *Production Engineering*, 4, 35-45.
- Zhang, K. & Chen, G. N. (2000) Effect of SiC particles on crystal growth of Al-Si alloy during laser rapid solidification. *Materials Science and Engineering A*, 292, 229-231.
- Zhu, H. H., Fuh, J. Y. H. & Lu, L. (2007) The influence of powder apparent density on the density in direct laser-sintered metallic parts. *International Journal of Machine Tools and Manufacture*, 47, 294-298.